

**BIOLOGICAL, ROBOTIC, AND PHYSICS STUDIES TO DISCOVER  
PRINCIPLES OF LEGGED LOCOMOTION ON GRANULAR MEDIA**

A Thesis  
Presented to  
The Academic Faculty

by

Chen Li

In Partial Fulfillment  
of the Requirements for the Degree  
Doctor of Philosophy in the  
School of Physics

Georgia Institute of Technology  
December 2011

Copyright © 2011 by Chen Li

**BIOLOGICAL, ROBOTIC, AND PHYSICS STUDIES TO DISCOVER  
PRINCIPLES OF LEGGED LOCOMOTION ON GRANULAR MEDIA**

Approved by:

**Dr. Daniel I. Goldman**, Advisor  
School of Physics  
*Georgia Institute of Technology*

**Dr. Michael Schatz**  
School of Physics  
*Georgia Institute of Technology*

**Dr. Jennifer Curtis**  
School of Physics  
*Georgia Institute of Technology*

**Dr. Alberto Fernandez-Nieves**  
School of Physics  
*Georgia Institute of Technology*

**Dr. Young-Hui Chang**  
School of Applied Physiology  
*Georgia Institute of Technology*

Date Approved: 1st November 2011

*To my family*

## ACKNOWLEDGEMENTS

I am deeply grateful to my advisor, Prof. Dan Goldman, for taking the “risk” to recruit me as a graduate student even before he arrived on site at Georgia Tech. His passion and dedication to science has been a motivator and guide to helping me improve my abilities as a researcher and communicator of my research. I thank him for the opportunity to work on the fascinating projects presented here, for teaching me the right way to do science, and for the kind advice on how to do things right in general. Being able to help him set up a laboratory has also been an invaluable learning experience.

I am also deeply grateful to Prof. Paul Umbanhowar of Northwestern University and Prof. Tonia Hsieh of Temple University, for their critical contributions to some of these projects, and for their continuing help and support both intellectually and personally over the years. I would also like to thank my robotics collaborators, Dr. Hal Komsuoglu and Prof. Dan Koditschek of University of Pennsylvania, and Dr. Aaron Hoover, Paul Birkmeyer, and Prof. Ron Fearing of UC Berkeley, for providing the robots to work with, and troubleshooting and repairing them when situation required.

I would like to thank many members of the CRAB Lab—Dr. Ryan Maladen, Dr. Yang Ding, Sarah Sharpe, Nick Gravish, Nicole Mazouchova, Andrei Savu, Feifei Qian, Tingnan Zhang, Jeff Aguilar, Mateo Garcia, Loretta Lau, Jeff Shen, Lionel London, Andrew Slatton, and Adam Kamor, for making this a fun group to work with. Special thanks to Ryan for all the help and advice ever since we started building the first crab trackway together. Special thanks to Yang for always being able to enlighten me on theoretical questions I struggle with. Special thanks to Sarah for always being ready to answer my questions on muscle and neural physiology. Special thanks to Nick for help and discussions on physics experiments. Special thanks to Loretta, Mateo, and Jeff Shen for their assistance during some of the projects.

I would also like to thank my committee members, Prof. Mike Schatz, Prof. Jennifer Curtis, Prof. Alberto Fernandez-Nieves, and Prof. Young-Hui Chang for their support and read of my dissertation. Special thanks to Prof. Young-Hui Chang and Prof. Boris Prilutsky of the School of Applied Physiology, for their advice on physiology, neuromechanics, and career development. Special thanks to Prof. Predrag Cvitanović, for encouragement on my class project for his Nonlinear Dynamics class, which eventually led to a published paper.

Thanks to all the staff in the School of Physics, specially Felicia Goolsby, Samantha King, Debbie James, Vicki Speights, Keith Garner, Kevin Carter, Lee Strickland, Stephen Cooke, Sam Mize, and Scott Centers for administrative, financial, and technical assistance. Thanks to all the staff in the Physiology Research Lab for housing and caring the zebra-tailed lizards used in my research. I would also like to acknowledge the Burroughs Wellcome Fund, and the Army Research Lab, and the School of Physics of Georgia Tech, for their financial support over the past six years.

Also thanks to colleagues at other universities, specially Mu Qiao, Prof. Devin Jindrich, Prof. Tim Griffin for career advice; Prof. Bob Full, Prof. Andy Biewener, and Prof. Tom Roberts for helpful discussions. Special thanks to my friends at Georgia Tech, specially Fan Ming, Yang Ding, Yifan Gao, and Lujia Feng, for always being around to listen to me and encourage me. Special thanks to Chris and Rebecca Gray, who hosted me when I first arrived in Atlanta and who have since been great friends.

I would like to dedicate this work to my parents, Danhua Chen, and Xiannian Li, and my twin sister, Li Chen, without whose endless struggles and sacrifices I would not have been able to pursue graduate studies in the US. Thank you for always being there to support me. I would also like to thank my in-laws, Shizao Liao, Daina Chen, and Ze'en Liao, for your kindness to me over the last three years.

Finally, I would like to thank my wife, Jin Liao, whom I met at Georgia Tech, and whom I was so very fortunate to have convinced to marry me. Thank you for always being there for me and making me feel special.

## TABLE OF CONTENTS

|   |              |
|---|--------------|
| <b>DEDICATION</b> . . . . .   | <b>iii</b>   |
| <b>ACKNOWLEDGEMENTS</b> . . . . .   | <b>iv</b>    |
| <b>LIST OF TABLES</b> . . . . .   | <b>xi</b>    |
| <b>LIST OF FIGURES</b> . . . . .  | <b>xii</b>   |
| <b>SUMMARY</b> . . . . .  | <b>xviii</b> |
| <b>I INTRODUCTION</b> . . . . .   | <b>1</b>     |
| 1.1 Motivation and Overview . . . . .   | 1            |
| 1.2 Legged locomotion in biological organisms . . . . .                                 | 10           |
| 1.2.1 Walking and running . . . . .   | 10           |
| 1.2.2 Templates and anchors . . . . .   | 13           |
| 1.3 Model organism . . . . .  | 16           |
| 1.3.1 Zebra-tailed lizard . . . . .   | 16           |
| 1.3.2 An analogy: the water-running basilisk lizard . . . . .                           | 18           |
| 1.4 Physical models of organisms: bio-inspired legged robots . . . . .                  | 21           |
| 1.4.1 RHex . . . . .  | 21           |
| 1.4.2 Smart Composite Manufacturing robots . . . . .                                    | 24           |
| 1.5 Physics of intrusion forces in granular media . . . . .                             | 26           |
| 1.5.1 Horizontal drag . . . . .   | 26           |
| 1.5.2 Vertical penetration . . . . .  | 27           |
| 1.5.3 Vertical impact . . . . .   | 28           |
| 1.6 Experimental techniques . . . . .   | 30           |
| 1.6.1 Control of granular media by a fluidized bed . . . . .                            | 30           |
| 1.6.2 Construction of fluidized beds . . . . .  | 32           |
| 1.6.3 Three-dimensional kinematics capture using Direct Linear Transformation . . . . . | 33           |
| 1.6.4 Intrusion force measurements using a six degree-of-freedom robotics arm . . . . . | 34           |
| 1.6.5 Field collection of lizards . . . . .   | 36           |
| 1.7 Specific aims . . . . .   | 37           |

**II THE EFFECT OF SUBSTRATE ON THE RUNNING MECHANICS  
OF THE ZEBRA-TAILED LIZARD (*CALLISAURUS DRACONOIDES*)**  
**39**

|       |  |    |
|-------|--|----|
| 2.1   | Summary . . . . .  | 39 |
| 2.2   | Introduction . . . . .   | 40 |
| 2.3   | Materials and methods . . . . .                                      | 44 |
| 2.3.1 | Animals . . . . .  | 44 |
| 2.3.2 | Surface treatments . . . . .   | 44 |
| 2.3.3 | Three-dimensional kinematics . . . . .                               | 44 |
| 2.3.4 | Hind limb dissection and hind foot resilience measurements . . . . . | 45 |
| 2.3.5 | Data analysis . . . . .  | 47 |
| 2.3.6 | Statistics . . . . .   | 47 |
| 2.3.7 | Granular penetration force measurements . . . . .                    | 48 |
| 2.4   | Results . . . . .  | 50 |
| 2.4.1 | Morphology . . . . .   | 50 |
| 2.4.2 | Gait and center of mass kinematics . . . . .                         | 51 |
| 2.4.3 | Trunk and hind leg kinematics . . . . .                              | 55 |
| 2.4.4 | Hind foot kinematics . . . . .                                       | 58 |
| 2.4.5 | Principal Component Analysis of kinematics . . . . .                 | 60 |
| 2.4.6 | Hind foot resilience . . . . .                                       | 61 |
| 2.4.7 | Granular penetration force . . . . .                                 | 63 |
| 2.5   | Discussion . . . . .   | 65 |
| 2.5.1 | Comparison of CoM motion with spring-mass model . . . . .            | 65 |
| 2.5.2 | Foot function on solid surface: energy-saving spring . . . . .       | 66 |
| 2.5.3 | Foot function on granular surface: force-generating paddle . . . . . | 69 |
| 2.5.4 | Motor function of upper hind leg . . . . .                           | 72 |
| 2.5.5 | Advantages of a large, elongate foot . . . . .                       | 73 |
| 2.5.6 | Model assumptions and future work . . . . .                          | 74 |
| 2.6   | Conclusions . . . . .  | 76 |
| 2.7   | Appendix . . . . .   | 77 |
| 2.7.1 | Foot curvature on the solid surface . . . . .                        | 77 |
| 2.7.2 | Small relative forward speed oscillation . . . . .                   | 77 |

|            |   |            |
|------------|---|------------|
| 2.7.3      | Estimates of tendon spring deformation and stiffness . . . . .  | 77         |
| 2.7.4      | Elongate foot increases energy saving on solid surface . . . . .  | 78         |
| 2.7.5      | Estimates of vertical force and energy loss on granular surface . . .   | 79         |
| 2.7.6      | Large foot reduces energy loss on granular surface . . . . .  | 80         |
| <br>       |   |            |
| <b>III</b> | <b>SUBSURFACE FOOT KINEMATICS AND FORCE GENERATION<br/>OF THE ZEBRA-TAILED LIZARD (CALLISAURUS DRACONOIDES)<br/>RUNNING ON GRANULAR MEDIA . . . . .</b> | <b>81</b>  |
| 3.1        | Summary . . . . .   | 81         |
| 3.2        | Introduction . . . . .  | 83         |
| 3.3        | Materials and methods . . . . .   | 85         |
| 3.3.1      | Animals . . . . .   | 85         |
| 3.3.2      | X-ray subsurface kinematics capture . . . . .   | 85         |
| 3.3.3      | Kinematics analysis . . . . .   | 86         |
| 3.3.4      | Granular force measurements . . . . .   | 87         |
| 3.4        | Results . . . . .   | 89         |
| 3.4.1      | Gait parameters . . . . .   | 89         |
| 3.4.2      | Foot curvature on the granular surface . . . . .  | 89         |
| 3.4.3      | Foot-ground interaction on the granular surface . . . . .   | 90         |
| 3.4.4      | Granular force measurements . . . . .   | 92         |
| 3.5        | Discussion . . . . .  | 94         |
| 3.5.1      | Reduced energy savings by foot tendons on the granular surface . .  | 94         |
| 3.5.2      | Force generation on granular media . . . . .  | 94         |
| 3.5.3      | Comparison to the water-running basilisk lizard . . . . .   | 96         |
| 3.5.4      | Recapitulation . . . . .  | 98         |
| 3.6        | Conclusions . . . . .   | 100        |
| <br>       |   |            |
| <b>IV</b>  | <b>SENSITIVE DEPENDENCE OF THE MOTION OF A LEGGED ROBOT<br/>ON GRANULAR MEDIA . . . . .</b>   | <b>101</b> |
| 4.1        | Summary . . . . .   | 101        |
| 4.2        | Introduction . . . . .  | 102        |
| 4.3        | Materials and Methods . . . . .   | 104        |
| 4.3.1      | SandBot . . . . .   | 104        |
| 4.3.2      | Limb kinematics . . . . .   | 105        |

|           |  |            |
|-----------|--|------------|
| 4.3.3     | Trackway volume fraction control . . . . .   | 106        |
| 4.3.4     | Kinematics measurements . . . . .  | 107        |
| 4.4       | Results and Discussion . . . . .   | 109        |
| 4.4.1     | Sensitive dependence of speed on volume fraction . . . . .   | 109        |
| 4.4.2     | Rotary walking mode . . . . .  | 110        |
| 4.4.3     | Sensitive dependence of speed on limb frequency . . . . .  | 111        |
| 4.4.4     | Rotary walking model captures robot performance . . . . .  | 113        |
| 4.4.5     | Trigger of swimming mode . . . . .   | 117        |
| 4.5       | Conclusions . . . . .  | 119        |
| 4.6       | Appendix . . . . .   | 120        |
| <b>V</b>  | <b>THE EFFECT OF LIMB KINEMATICS ON THE SPEED OF A LEGGED ROBOT ON GRANULAR MEDIA . . . . .</b>          | <b>123</b> |
| 5.1       | Summary . . . . .  | 123        |
| 5.2       | Introduction . . . . .   | 124        |
| 5.3       | Background and review of previous study . . . . .  | 127        |
| 5.3.1     | Physics of limb-granular media interaction . . . . .   | 127        |
| 5.3.2     | Review of previous observations and model . . . . .  | 127        |
| 5.4       | Methods and Results . . . . .  | 133        |
| 5.5       | Discussion . . . . .   | 137        |
| 5.5.1     | Application of model to slow phase extent and location variation . . . . .                               | 137        |
| 5.5.2     | Anisotropic penetration force law . . . . .  | 139        |
| 5.5.3     | Effect of duty cycle . . . . .   | 144        |
| 5.6       | Conclusions . . . . .  | 147        |
| <b>VI</b> | <b>SYSTEMATIC STUDY OF THE PERFORMANCE OF SMALL ROBOTS ON CONTROLLED LABORATORY SUBSTRATES . . . . .</b> | <b>149</b> |
| 6.1       | Summary . . . . .  | 149        |
| 6.2       | Introduction . . . . .   | 150        |
| 6.3       | Materials and Methods . . . . .  | 152        |
| 6.3.1     | Experiment Design . . . . .  | 152        |
| 6.3.2     | Experimental Setup . . . . .   | 153        |
| 6.4       | Results and Discussions . . . . .  | 156        |

|   |   |            |
|---|---|------------|
| 6.5   | Conclusions . . . . .   | 163        |
| 6.6   | Appendix . . . . .  | 165        |
| 6.6.1   | Performance on closely vs. loosely packed granular media . . . . .              | 165        |
| 6.6.2   | SCM process . . . . .   | 168        |
| 6.6.3   | RoACH . . . . .   | 170        |
| 6.6.4   | DASH . . . . .  | 171        |
| <b>VII TOWARDS A TERRAMECHANICS FOR LEGGED LOCOMOTION<br/>ON GRANULAR MEDIA . . . . .</b> |   | <b>174</b> |
| 7.1   | Summary . . . . .   | 174        |
| 7.2   | Introduction . . . . .  | 176        |
| 7.3   | Previous drag experiments in horizontal plane . . . . .                         | 179        |
| 7.4   | Measuring force on a small plate . . . . .                                      | 182        |
| 7.5   | Force per depth as a function angle of attack and direction of motion . . . . . | 186        |
| 7.6   | Forces on rotating model legs of different geometry . . . . .                   | 189        |
| 7.7   | Application of the RFT to a legged robot . . . . .                              | 192        |
| 7.8   | Conclusions . . . . .   | 196        |
| 7.9   | Appendix . . . . .  | 197        |
| 7.9.1   | CP poppy seeds . . . . .  | 198        |
| 7.9.2   | LP 0.27 mm glass particles . . . . .  | 200        |
| 7.9.3   | CP 0.27 mm glass particles . . . . .  | 202        |
| 7.9.4   | CP 3 mm glass particles . . . . .   | 204        |
| <b>VIII CONCLUSIONS . . . . .</b>   |   | <b>206</b> |
| 8.1   | General remarks . . . . .   | 206        |
| 8.2   | Specific accomplishments . . . . .  | 207        |
| 8.3   | Future directions . . . . .   | 209        |
| 8.4   | Final thoughts . . . . .  | 215        |
| <b>REFERENCES . . . . .</b>   |   | <b>233</b> |
| <b>VITA . . . . .</b>   |   | <b>245</b> |

## LIST OF TABLES

|   |  |     |
|---|--|-----|
| 1 | Morphological measurements of the four individuals reported. . . . .   | 50  |
| 2 | Gait and CoM kinematic variables. . . . .  | 52  |
| 3 | Trunk, hind leg, and hind foot kinematic variables. . . . .  | 55  |
| 4 | Results of principal component analyses on kinematic variables. . . . .  | 61  |
| 5 | Statistics of modified work loop experiments. . . . .  | 62  |
| 6 | Four stages of foot-ground interaction on the granular surface. . . . .  | 90  |
| 7 | Comparison of contributions to total vertical impulse from different phases of<br>foot-ground interaction between the basilisk lizard and the zebra-tailed lizard. | 97  |
| 8 | Granular media used for developing the resistive force theory in the sagittal<br>plane. . . . .  | 183 |

## LIST OF FIGURES

|    |   |    |
|----|---|----|
| 1  | Terrestrial animals move nimbly in complex natural environments. . . . .  | 1  |
| 2  | The Mars rover Spirit stuck in soft, loose Martian soil. . . . .  | 2  |
| 3  | Principles of legged locomotion gained from biological studies provides inspiration for legged robots. . . . .        | 3  |
| 4  | Forces during locomotion in Newtonian fluids can in principle be obtained by solving Navier-Stokes Equations. . . . . | 4  |
| 5  | A model substrate–granular media. . . . .   | 5  |
| 6  | Solid and fluid behavior of granular media. . . . .   | 6  |
| 7  | Granular media are relevant to many desert-dwelling legged animals. . . . .   | 7  |
| 8  | Overview of the objective, approach, and outcome of this dissertation. . . . .  | 8  |
| 9  | The simplest models for walking and running. . . . .  | 10 |
| 10 | Walk-to-run transition in legged animals on solid surfaces. . . . .   | 11 |
| 11 | Gait parameters during walk-to-run transitions. . . . .   | 12 |
| 12 | Templates and anchors of legged locomotion. . . . .   | 13 |
| 13 | Neural and mechanical aspects of locomotion control. . . . .  | 14 |
| 14 | A zebra-tailed lizard sitting on a granular surface in the wild. . . . .  | 16 |
| 15 | Zebra-tailed lizard and its closely-related desert lizards. . . . .   | 17 |
| 16 | Three phases of foot-water interaction during water-running in the basilisk lizard. . . . .                           | 18 |
| 17 | Detailed flow and forces during water-running obtained from PIV and CFM. . . . .                                      | 20 |
| 18 | Recent bio-inspired legged robots. . . . .  | 22 |
| 19 | SandBot, a RHex class legged robot. . . . .   | 23 |
| 20 | SandBot’s clock signal that controls leg rotation. . . . .  | 23 |
| 21 | Milli-robots. . . . .   | 24 |
| 22 | Force during horizontal drag of a cylinder in granular media at low speeds. . . . .                                   | 27 |
| 23 | Force during vertical penetration of a sphere into granular media at low speeds. . . . .                              | 28 |
| 24 | Force during vertical impact of a sphere into granular media at high speeds. . . . .                                  | 29 |
| 25 | Granular media of different volume fractions in nature. . . . .   | 30 |
| 26 | Diagram and principles of a fluidized bed. . . . .  | 31 |
| 27 | Fluidized beds constructed for this study. . . . .  | 32 |

|    |  |    |
|----|--|----|
| 28 | Direct Linear Transformation for three-dimensional kinematics capture. . .                             | 34 |
| 29 | A six degree-of-freedom robotic arm for intrusion physics studies. . . . .                             | 35 |
| 30 | Field collection of the zebra-tailed lizards. . . . .  | 36 |
| 31 | A zebra-tailed lizard resting on sand in the wild. . . . .   | 42 |
| 32 | Experimental setup for three-dimensional kinematics capture. . . . .                                   | 45 |
| 33 | Experimental setup for hind foot resilience measurements. . . . .                                      | 46 |
| 34 | Experimental setup for granular penetration force measurements. . . . .                                | 49 |
| 35 | Ventral anatomy of a dissected hind limb. . . . .  | 51 |
| 36 | Gait parameters. . . . .   | 53 |
| 37 | Center of mass kinematics. . . . .   | 54 |
| 38 | Lateral views of representative runs on solid and granular surfaces. . . . .                           | 56 |
| 39 | Kinematic variables of the trunk and hind leg. . . . .   | 57 |
| 40 | Closer views of foot posture at touchdown. . . . .   | 58 |
| 41 | Foot-ground interaction on the solid surface. . . . .  | 59 |
| 42 | Representative passive work loops of the hind foot. . . . .  | 62 |
| 43 | Hind foot resilience. . . . .  | 62 |
| 44 | Granrce as a function of depth. . . . .  | 63 |
| 45 | A two-dimensional strut-spring model of the hind foot. . . . .   | 67 |
| 46 | Normalized tendon spring deformation on the solid surface. . . . .                                     | 68 |
| 47 | Ground reaction force and CoM vertical speed. . . . .  | 70 |
| 48 | Hypothesized subsurface foot rotation in the sagittal plane. . . . .                                   | 72 |
| 49 | The sand-running zebra-tailed lizard and the water-running basilisk lizard.                            | 83 |
| 50 | Experimental setup for subsurface foot kinematics capture using high speed<br>x-ray imaging. . . . .   | 86 |
| 51 | Experimental setup for granular force measurements. . . . .  | 87 |
| 52 | X-ray high speed videos revealed the lizard’s subsurface foot kinematics on<br>granular media. . . . . | 89 |
| 53 | Comparison of foot curvature on solid and granular surfaces. . . . .                                   | 90 |
| 54 | Subsurface foot kinematics during stance. . . . .  | 91 |
| 55 | Vertical forces as a function of depth. . . . .  | 92 |
| 56 | Peak impact force as a function of impact speed. . . . .   | 93 |
| 57 | Ground reaction force and CoM vertical speed. . . . .  | 99 |

|    |   |     |
|----|---|-----|
| 58 | The six-legged robot, SandBot. . . . .  | 104 |
| 59 | Experimental setup. . . . .   | 108 |
| 60 | Locomotion of SandBot on granular media is sensitive to substrate packing and limb frequency. . . . .                                   | 109 |
| 61 | Schematic of a single robot leg rotary walking during a step in granular media. . . . .   | 111 |
| 62 | Average robot forward speed as a function of limb frequency. . . . .  | 112 |
| 63 | Signatures of phase transitions in robot performance. . . . .   | 112 |
| 64 | Step length as a function of penetration depth. . . . .   | 113 |
| 65 | Vertical force balance during rotary walking. . . . .   | 114 |
| 66 | Granular penetration force measurements. . . . .  | 115 |
| 67 | Measured yield stress per depth as a function of volume fraction for poppy seeds. . . . .   | 116 |
| 68 | Step length as a function of limb frequency. . . . .  | 117 |
| 69 | Vertical force balance during rotary walking from the full model. . . . .   | 121 |
| 70 | Comparison of full model predicted speed with simple model and experiment. . . . .  | 122 |
| 71 | SandBot, a six-legged insect inspired robot, moves with an alternating tripod gait. . . . .   | 125 |
| 72 | Schematic of single-leg representation of SandBot. . . . .  | 128 |
| 73 | Vertical forces on SandBot during locomotion. . . . .   | 130 |
| 74 | Schematic of rotary walking. . . . .  | 131 |
| 75 | SandBot's intra-cycle limb kinematics. . . . .  | 133 |
| 76 | SandBot's speed depends sensitively on intra-cycle limb kinematics. . . . .   | 135 |
| 77 | SandBot's speed as a function of slow phase extent and location. . . . .  | 136 |
| 78 | Schematic of overlap of the slow phase and the rotary walking range. . . . .  | 137 |
| 79 | Model prediction of speed as a function of slow phase extent and location using the original penetration force law. . . . .             | 138 |
| 80 | Asymmetry of speed as a function of slow phase location. . . . .  | 139 |
| 81 | Anisotropic penetration force. . . . .  | 140 |
| 82 | Anisotropic penetration force law better predicts speed as a function of slow phase extent and location. . . . .                        | 142 |
| 83 | Comparison of overlap of the slow phase and the rotary walking phase between Soft Ground Kinematics and Hard Ground Kinematics. . . . . | 142 |
| 84 | Speed as a function of slow phase extent. . . . .   | 143 |

|     |   |     |
|-----|---|-----|
| 85  | Speed as a function of duty cycle. . . . .  | 144 |
| 86  | RoACH and DASH standing on loosely packed poppy seeds. . . . .  | 151 |
| 87  | Experimental setup. . . . .   | 153 |
| 88  | Average speed as a function of stride frequency. . . . .  | 156 |
| 89  | Mean mechanical power as a function of stride frequency. . . . .  | 158 |
| 90  | Mean mechanical cost of transport as a function of frequency. . . . .                                     | 159 |
| 91  | Mean mechanical cost of transport as a function of frequency. . . . .                                     | 160 |
| 92  | Mean mechanical cost of transport as a function of frequency. . . . .                                     | 161 |
| 93  | Comparison of minimal mechanical cost of transport to animals and other legged robots. . . . .            | 162 |
| 94  | Average speed as a function of stride frequency. . . . .  | 165 |
| 95  | Mean mechanical power as a function of stride frequency. . . . .  | 166 |
| 96  | Mean mechanical cost of transport as a function of frequency. . . . .                                     | 166 |
| 97  | Mean mechanical cost of transport as a function of frequency. . . . .                                     | 167 |
| 98  | Mean mechanical cost of transport as a function of frequency. . . . .                                     | 167 |
| 99  | Step-by-step illustration of the posterboard link and hinge fabrication process.                          | 169 |
| 100 | The RoACH robot shown with component parts of onboard power and electronics highlighted. . . . .          | 171 |
| 101 | Linkage kinematics for RoACH’s alternating tripod gait. . . . .   | 171 |
| 102 | The DASH robot with component parts of onboard power and electronics. .                                   | 172 |
| 103 | Linkage kinematics of DASH. . . . .   | 172 |
| 104 | Relevance of rotational intrusion in locomotion. . . . .  | 176 |
| 105 | Granular resistive force theory in the horizontal plane. . . . .  | 178 |
| 106 | Representative total drag force as a function of time. . . . .  | 179 |
| 107 | Drag force as a function of the angle between segment orientation and direction of motion. . . . .        | 180 |
| 108 | Granular resistive force theory in the sagittal plane. . . . .  | 182 |
| 109 | Representative force vs. depth measurements on the plate. . . . .   | 184 |
| 110 | Lift force per depth as a function of angle of attack and direction of motion for LP poppy seeds. . . . . | 186 |
| 111 | Drag force per depth as a function of angle of attack and direction of motion for LP poppy seeds. . . . . | 187 |

|     |   |     |
|-----|---|-----|
| 112 | Experimental setup for rotation force measurements of model legs of five geometries into granular media. . . . .              | 190 |
| 113 | Net lift and drag on the model legs of five geometries during rotation in LP poppy seeds. . . . .                             | 190 |
| 114 | The Xplorer robot. . . . .  | 192 |
| 115 | Robot performance on poppy seeds using C-shaped legs of positive and negative curvatures. . . . .                             | 193 |
| 116 | Lift force per depth as a function of angle of attack and direction of motion for CP poppy seeds. . . . .                     | 198 |
| 117 | Drag force per depth as a function of angle of attack and direction of motion for CP poppy seeds. . . . .                     | 199 |
| 118 | Net lift and drag on the model legs of five geometries during rotation in CP poppy seeds. . . . .                             | 199 |
| 119 | Lift force per depth as a function of angle of attack and direction of motion for LP 0.27 mm glass particles. . . . .         | 200 |
| 120 | Drag force per depth as a function of angle of attack and direction of motion for LP 0.27 mm glass particles. . . . .         | 201 |
| 121 | Net lift and drag on the model legs of five geometries during rotation in LP 0.27 mm glass particles. . . . .                 | 201 |
| 122 | Lift force per depth as a function of angle of attack and direction of motion for CP 0.27 mm glass particles. . . . .         | 202 |
| 123 | Drag force per depth as a function of angle of attack and direction of motion for CP 0.27 mm glass particles. . . . .         | 203 |
| 124 | Net lift and drag on the model legs of five geometries during rotation in CP 0.27 mm glass particles. . . . .                 | 203 |
| 125 | Lift force per depth as a function of angle of attack and direction of motion for CP 3 mm glass particles. . . . .            | 204 |
| 126 | Drag force per depth as a function of angle of attack and direction of motion for CP 3 mm glass particles. . . . .            | 205 |
| 127 | Net lift and drag on the model legs of five geometries during rotation in CP 3 mm glass particles. . . . .                    | 205 |
| 128 | Artist’s concept of future legged robots that traverse granular surfaces, inspired from studies in this dissertation. . . . . | 214 |
| 129 | The ghost crab project. . . . .   | 217 |
| 130 | Calibration objects. . . . .  | 218 |
| 131 | Natural beauty of the Mojave Desert. . . . .  | 219 |

|     |  |     |
|-----|--|-----|
| 132 | A physical model of the lizard foot to test the hypothesis of reduced foot curvature due to distribution of ground reaction force on granular media. . . . . | 220 |
| 133 | Measurements and modeling of the damping properties a hind foot of the zebra-tailed lizard during free vibration. . . . .                                    | 221 |
| 134 | Enhancement of SandBot's performance by increasing leg rigidity. . . . .   | 222 |
| 135 | Enhancement of SandBot's performance by increasing leg area. . . . .   | 223 |
| 136 | SandBot's performance in wheel-leg transition. . . . .   | 224 |
| 137 | SandBot's leg strain during locomotion on granular media. . . . .  | 225 |
| 138 | Mean drag force as a function of depth and speed in 0.27 mm diameter glass particles. . . . .  | 226 |
| 139 | Mean drag force as a function of depth and speed in 3 mm diameter glass particles. . . . .   | 227 |
| 140 | Influence of volume fraction on cratering. . . . .   | 228 |
| 141 | Force fluctuations during vertical penetration as a function of volume fraction. . . . .   | 229 |
| 142 | Granular force as a function of air flow through the fluidized bed. . . . .  | 230 |
| 143 | Effect of grain inertial force during intrusion at high speeds. . . . .  | 231 |
| 144 | Granular Particle Imaging Velocimetry to capture the flow field during slow intrusion. . . . .   | 232 |

## SUMMARY

Terrestrial animals encounter natural surfaces which comprise materials that can yield and flow such as sand, rubble, and debris, yet appear to nimbly walk, run, crawl, or climb across them with great ease. In contrast, man-made devices on wheels and treads suffer large performance loss on these surfaces. Legged locomotion thus provides an excellent source of inspiration for creating devices of increased locomotor capabilities on natural surfaces. While principles of legged locomotion on solid ground have been discovered, the mechanisms by which legged animals move on yielding/flowing surfaces remain poorly understood, largely due to the lack of fundamental understanding of the complex interactions of body/limbs with these substrates on the level of the Navier-Stokes Equations for fluids. Granular media (e.g., sand) provide a promising model substrate for discovering the principles of legged locomotion on yielding/flowing surfaces, because they can display solid- and fluid-like behaviors, are directly relevant for many desert-dwelling animals, can be repeatedly and precisely controlled, and the intrusion force laws can be determined empirically.

In this dissertation, we created laboratory devices to prepare granular media in well-controlled states, and integrated biological, robotic, and physics studies to discover principles of legged locomotion on granular media. For both animals and bio-inspired robots, legged locomotion on granular surfaces must be achieved by limb intrusion to generate sufficient vertical ground reaction force (lift) to balance body weight and inertial force. When limb intrusion was slow (speed  $< 0.5$  m/s), granular forces were independent of intrusion speed (dominated by grain-grain and grain-intruder friction) and generally increased with intrusion depth (due to granular hydrostatic pressure). Locomotor performance (speed) depended sensitively on limb kinematics, limb morphology, and the strength of the granular media, which together determined vertical force balance (or lack thereof). Based on these findings, we developed a granular resistive force theory in the sagittal plane as a general model for calculating forces during low-speed intrusions relevant to legged locomotion.

# CHAPTER I

## INTRODUCTION

### 1.1 Motivation and Overview

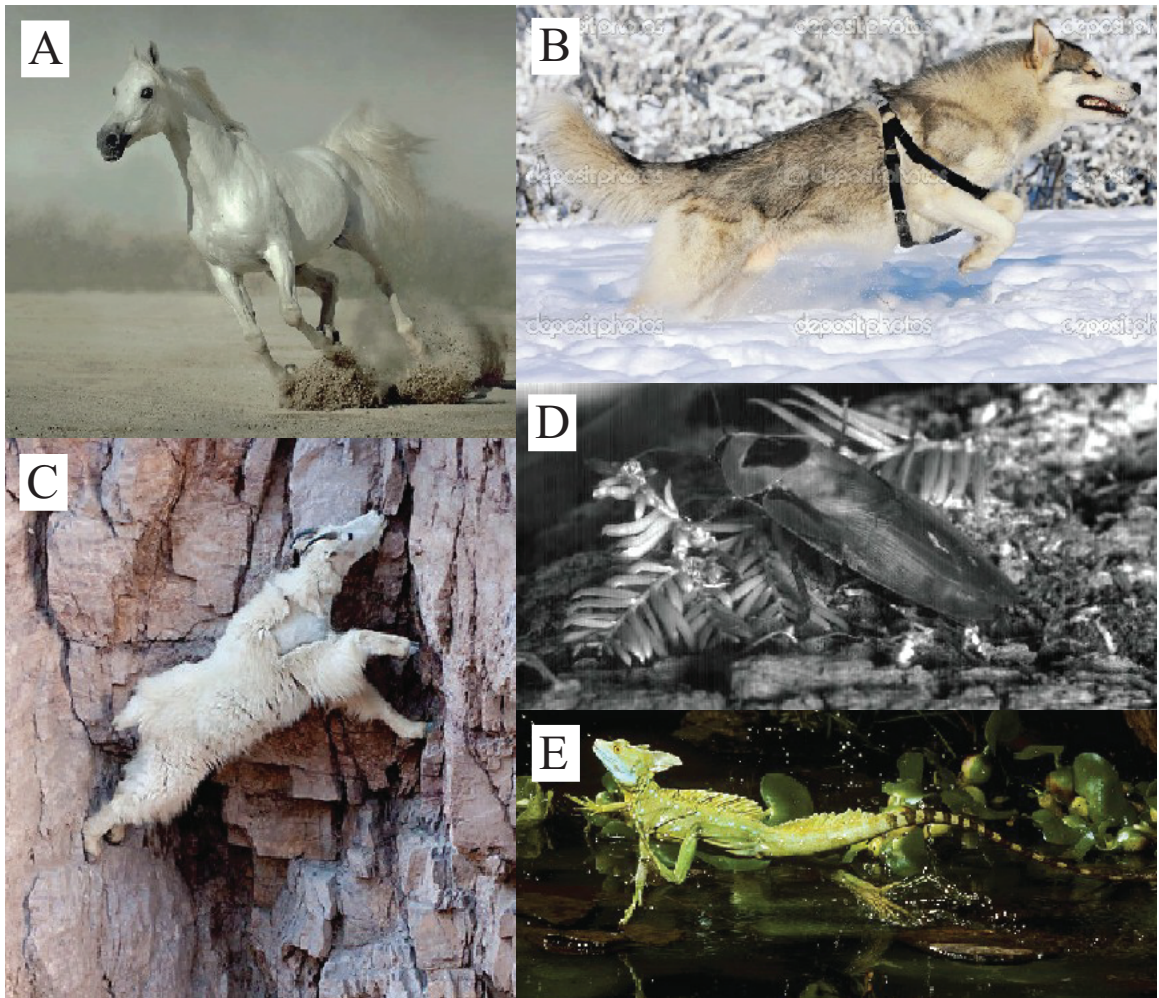


**Figure 1:** Terrestrial animals move nimbly on complex natural substrates. (A) A horse galloping on loose soil. (B) A husky hopping on thick snow. (C) A mountain goat descending a sheer rock wall to lick exposed salt. (D) A cockroach climbing over a pile of leaf litter. (E) A basilisk lizard running on the surface of water. Images courtesy of (A) Wojtek Kwiatkowski, (B) shutterstock.com, (C) National Geographic, (D) Daniel I. Goldman, and (E) National Geographic.

The natural surfaces that terrestrial animals encounter in the wild are often highly complicated [1, 2]. They are often uneven [3, 4], inclined [5], and dispersed [6], and comprise heterogeneous materials like dirt, mud, sand, rubble, snow, and debris, which display various elastic [7, 8] and damping [9] properties. In particular, these materials can often yield and flow during footsteps and display both solid- and fluid-like properties [10], and thus present great locomotor challenges. Terrestrial animals encounter such surfaces on a daily basis yet appear to nimbly walk, run, jump, crawl, or climb across them with ease [1, 2] (Fig. 1).

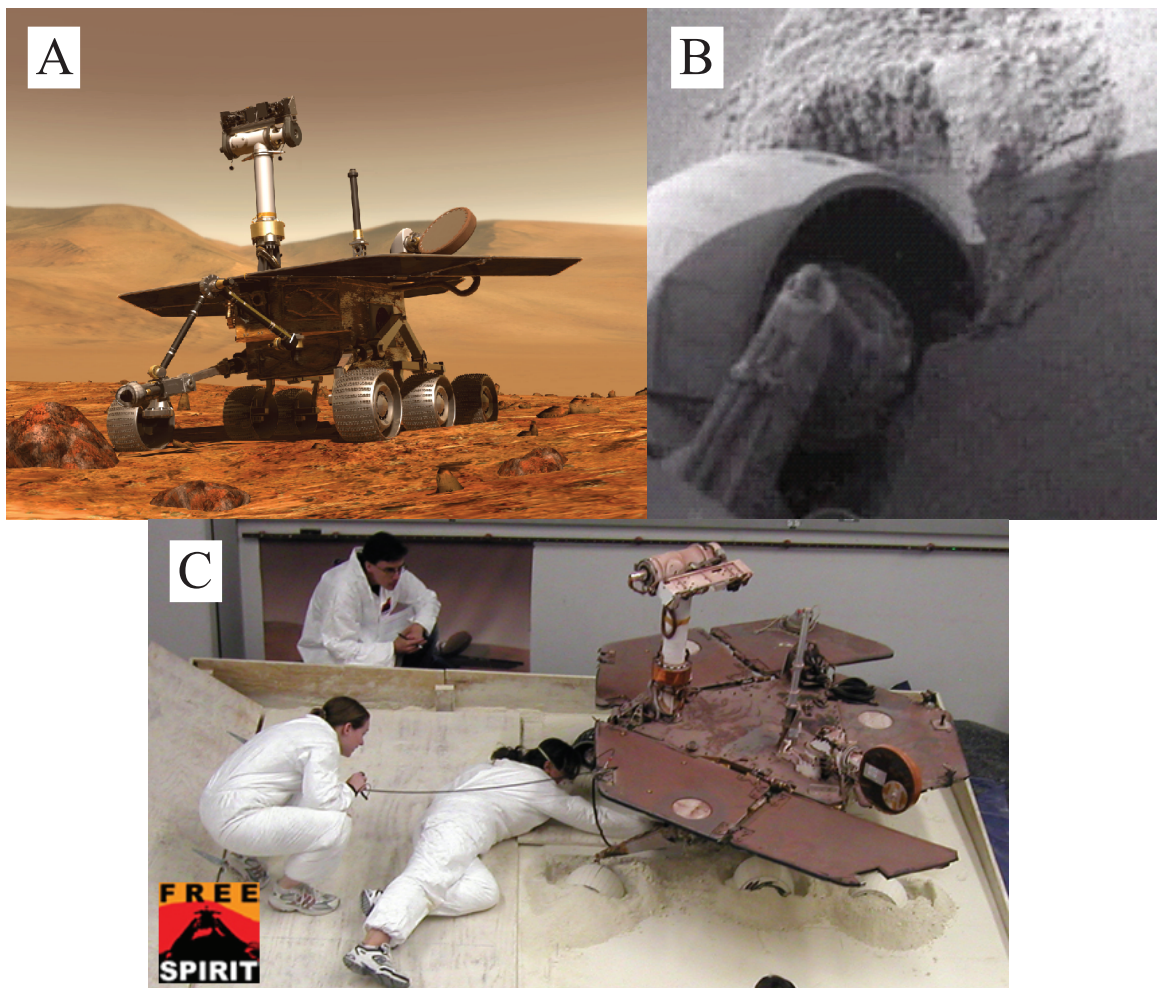


**Figure 2:** The Mars rover Spirit stuck in soft, loose Martian soil. (A) Artist's concept of the rover on Mars. (B) Spirit's wheel stuck in soft, loose Martian soil. (C) NASA's scientists and engineers working hard to free a copy of Spirit stuck in Mars soil simulant in the laboratory. Images courtesy of NASA Jet Propulsion Laboratory.

In contrast, while wheeled and treaded vehicles demonstrate excellent locomotor performance and low cost of transport on rigid or close-to-rigid grounds like paved roads and hard-packed soil, the mobility of most man-made terrestrial devices is still generally poor to non-existent on natural surfaces, particularly substrates that can yield and flow (hereafter referred to as yielding/flowing substrates) like mud and sand [11]. An excellent example is NASA’s Mars rover Spirit, which is permanently stuck in soft, loose Martian soil [12] (Fig. 2).

Legged locomotion therefore provides an excellent source of inspiration for creating engineering devices that have increased locomotor capabilities on natural surfaces. A frontier in robotics is to work out the principles of biological systems and transfer the principles gained

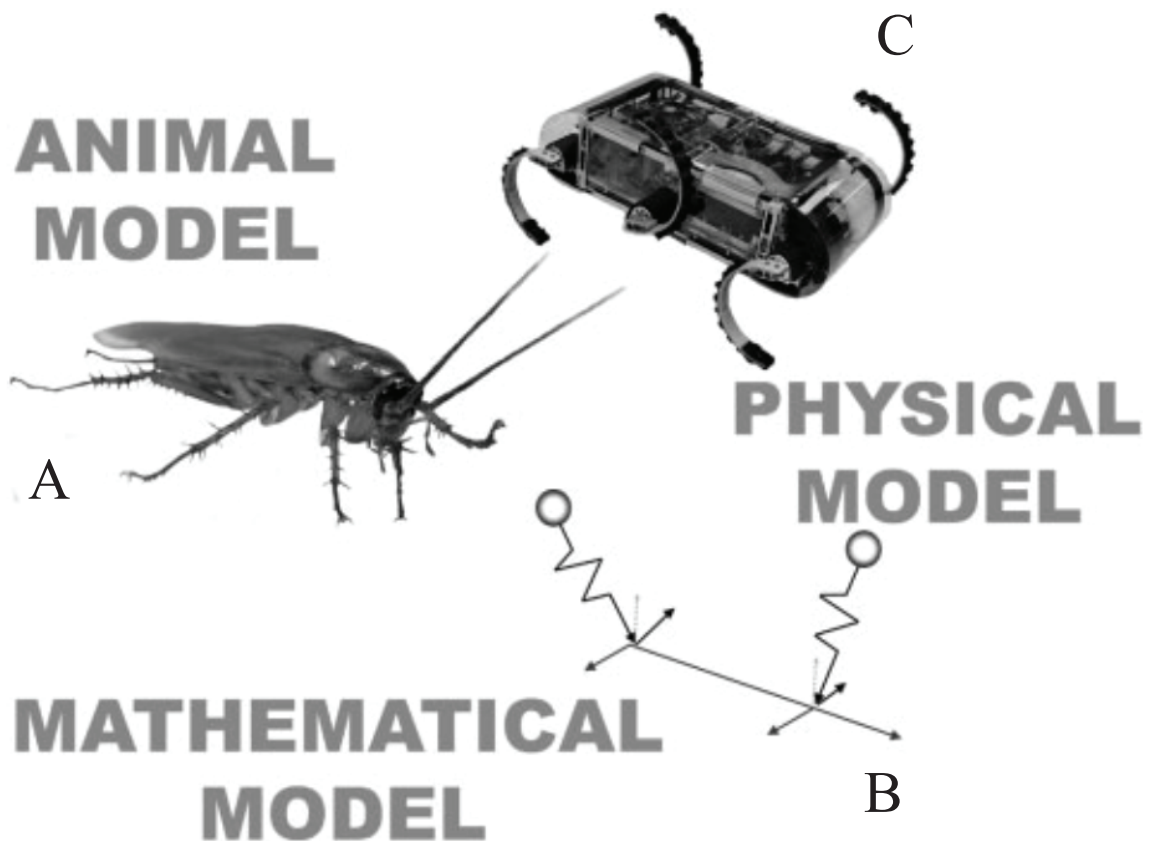


**Figure 3:** Principles of legged locomotion on solid surfaces gained from biological studies provides inspiration for legged robotics. (A) The American cockroach *Periplaneta Americana*. (B) The Spring-Loaded Inverted Pendulum (SLIP) model for running and hopping. (C) The RHex robot. Reproduced from [13].

to robotic design [14]. For example, the discovery of spring-mass like bouncing dynamics in cockroaches and other legged animals has inspired a class of legged robots, the Robot Hexapod (RHex) ( $\sim 0.5$  m long), which uses compliant, c-shaped legs and an alternating tripod gait to bounce rapidly ( $\sim 1$  bodylength/s) on solid ground and even some rugged off-road terrain like hard compact soil [15] (Fig. 3). Similar to the improvements of airplanes and submarines aided by a comprehensive knowledge of hydrodynamics, a principled understanding of legged locomotion on complex natural surfaces promises to accelerate the creation of legged devices capable of traversing natural terrain.

While principles of legged locomotion have been discovered by studying model organisms walking and running on rigid, level, flat, non-slip surfaces such as treadmills and running tracks, the mechanisms by which terrestrial animals locomote on natural surfaces remain poorly understood [1, 2]. In addition to the complication presented by the highly

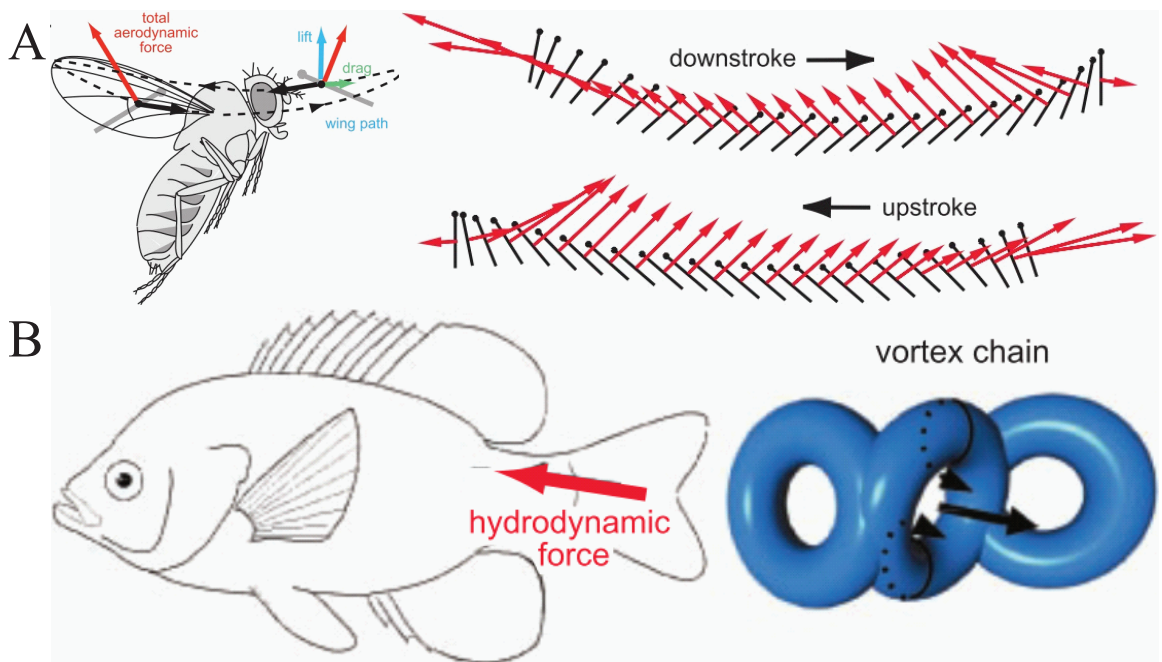


**Figure 4:** Forces during locomotion in Newtonian fluids can in principle be obtained by solving Navier-Stokes Equations. (A) Aerodynamic forces created by a fruit fly wing during hovering flight measured on a dynamically scaled model insect. Diagram on the right shows wing motion (black) and the total aerodynamic force (red) generated throughout the stroke. (B) Reconstruction of vortex wake behind a swimming fish. As the tail sweeps back and forth, it creates a series of alternating vortices. Each stroke of the fin creates a single donut-shaped vortex that is linked to the vortices of previous strokes. Reproduced from [2].

complex, many degree-of-freedom nervous and musculoskeletal systems of an animal [16], a major challenge in locomotion studies has been to gain principled understanding how animals’s bodies and limbs interact with the complex surrounding environment [2]. Recent studies of terrestrial locomotion have begun to investigate surfaces that are elastic [7, 8], damped [9], inclined [5], uneven [3, 4], or dispersed [6]; however, the possible complication of substrate yielding and flow has been largely neglected (but see [17, 18, 19, 20]). Unlike for flight and swimming where complex interaction can in principle be understood by solving Navier-Stokes Equations in the presence of moving boundary conditions [21] (Fig. 4), no fundamental theory yet exists to describe the interactions between the complex interaction of the body and limbs of legged locomotors with yielding/flowing substrates.

Granular media provide a promising model substrate for studying and revealing principles of legged locomotion on yielding/flowing substrates. Granular media (e.g., sand),



**Figure 5:** A model substrate—granular media. Image courtesy of Sean O’Flaherty.

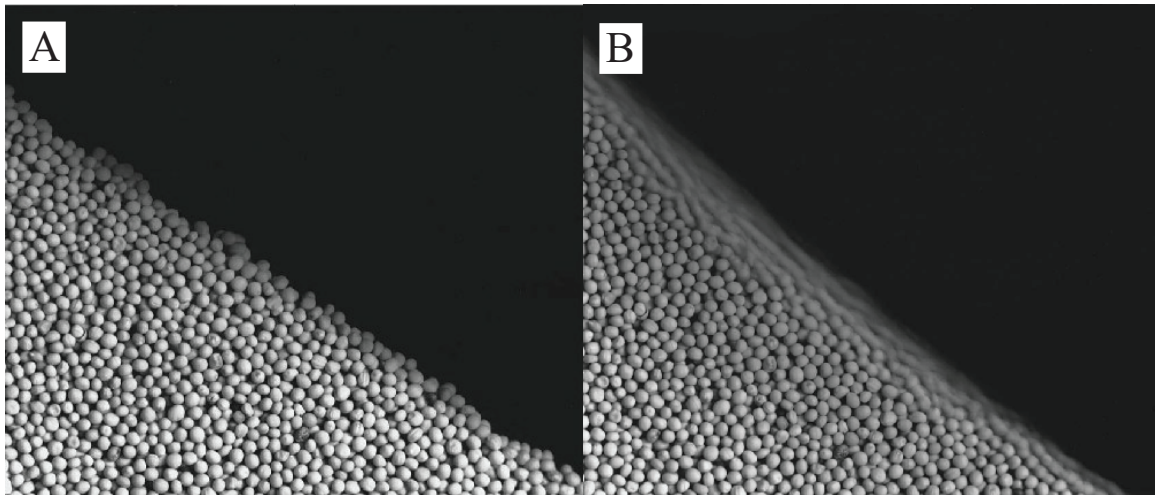


**Figure 6:** Solid- and fluid-like behavior of granular media. (A) A pile of granular medium (mustard seeds) that is tilted to an angle lower than the angle of repose. (B) The same pile after the slope has been increased slightly to create an avalanche. Note that the flow occurs only along the surface and that the seeds deeper within the pile remain stationary. Modified from [22].

generically defined as collections of discrete particles that interact through dissipative, repulsive contact forces [22] (Fig. 5), are representative of such substrates because forced granular media remain solid below the yield stress, but can flow like a fluid when the yield stress is exceeded [10] (Fig. 6). At the same time, granular materials like sand are relatively homogeneous compared to other natural materials and are simple enough that fundamental understanding of the collective physics may be achieved through interplay of experiment and theory [10, 22, 23]. In addition, granular media are readily and precisely controlled by setting the volume fraction (i.e., packing fraction) [24] to mimic natural surfaces of various strengths which animals encounter in nature. Furthermore, the study of legged locomotion on granular media is directly relevant for a large variety of desert-dwelling animals ranging including insects, arachnids, reptiles, and mammals (Fig. 7). Deserts, common in nature and occupying a significant portion of the land surface on Earth [25, 26], consist largely of granular media. Many desert-dwelling animals such as insects, arachnids, reptiles, and mammals must contend with granular media like sand and gravel on a daily basis [27, 28, 29, 30, 31].

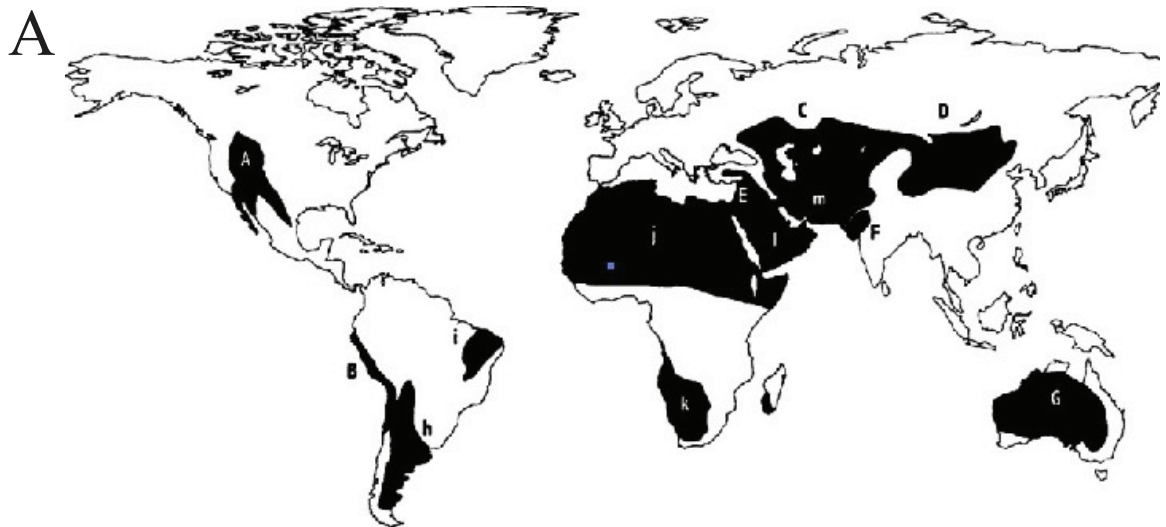


**Figure 7:** Granular media are relevant to many desert-dwelling legged animals. (A) Map of the world's desert regions (black). Reproduced from [26]. (B) Examples of desert-dwelling legged animals, including insects, arachnids, reptiles, and mammals (clockwise). Images courtesy of Moongateclimber, Tim Flash, Garwin Kim Sing, and itsnature.org (clockwise).

In this dissertation, we use granular media as a model substrate for yielding/flowing substrates, and integrate biological, robotic, and physics studies to discover principles of legged locomotion on granular media (Fig. 8). We create laboratory devices to prepare granular media in well-controlled states (yellow box). We study biological organisms (red box) and bio-inspired legged robots (blue box) moving on these substrates to reveal relevant physics of forces during legged locomotion on granular media (blue arrows). We study the physics of forces (green box) in granular media to reveal mechanisms of effective legged locomotion (or lack thereof) on these surfaces (red arrows). These studies result in predictive models which describe the complex interactions (gray arrows) of limb/foot with granular media and capture locomotion performance. Such models are leading us towards a principled understanding of legged locomotion on natural surfaces that can yield and flow. The design

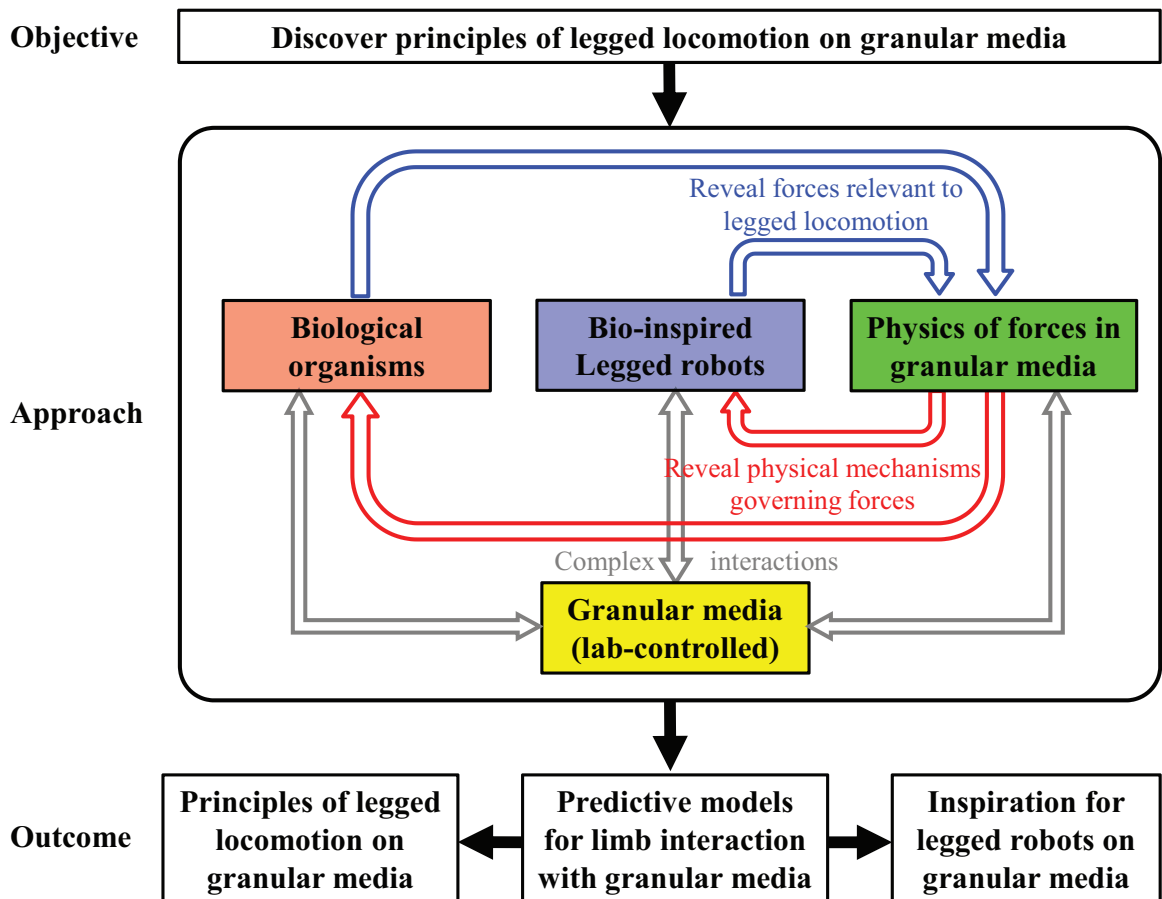


**Figure 8:** Overview of the objective, approach, and outcome of this dissertation.

principles from such studies promise to accelerate the development of the next generation legged robots capable of traversing multiple terrains.

Within this framework, Chapters II–VII are categorized into:

- Biological studies: **Chapters II and III.**
- Robotic studies: **Chapters IV, V, and VI.**
- Physics studies: Portions of **Chapters II–V**, and **Chapter VII.**

In the following sections of this Chapter, we review previous work and describe experimental techniques that provide the scientific and technical basis of this dissertation.

## 1.2 Legged locomotion in biological organisms

### 1.2.1 Walking and running

Walking and running (among others) are two basic gaits (the pattern of limb movement during locomotion) for most legged animals. Studies of model animals in controlled, simplified laboratory conditions on rigid, level, flat, and non-slip ground (i.e., solid ground), such as treadmills and running tracks, have revealed the fundamental mechanics of walking and running. Walking can be modeled as an “inverted pendulum”, in which the animal body (represented by the center of mass) vaults over a rigid leg during each step (Fig. 9A). Running can be modeled as a spring-mass system (or “Spring-Loaded Inverted Pendulum”, SLIP), in which the animal body (represented by the center of mass) bounces like a pogo stick on the compliant leg (represented by a spring) during each step (Fig. 9B). In both cases, the foot exerts point contact on the solid ground.

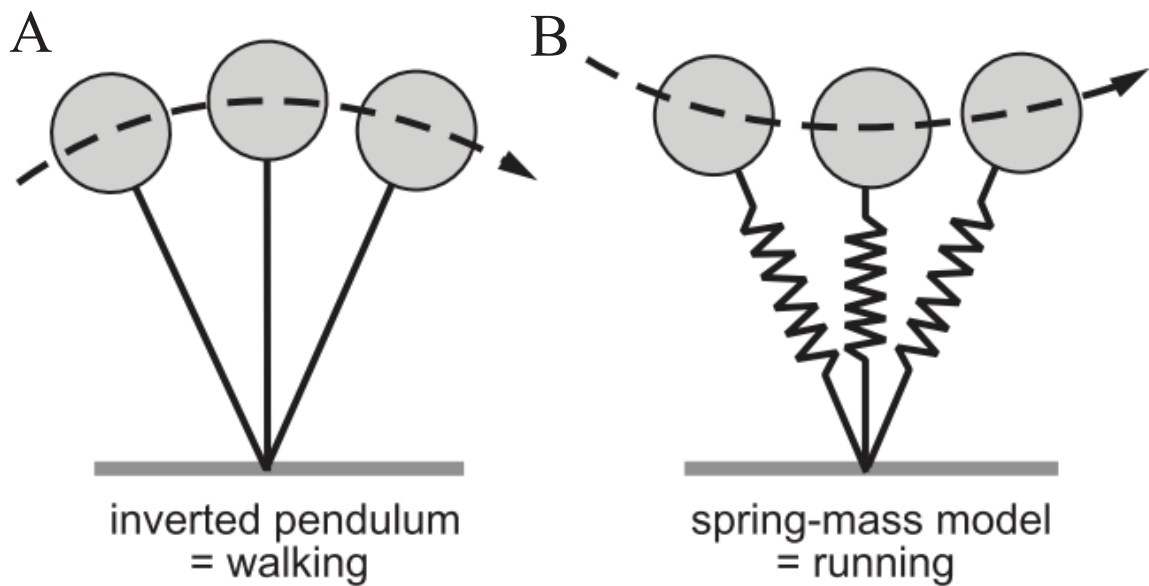
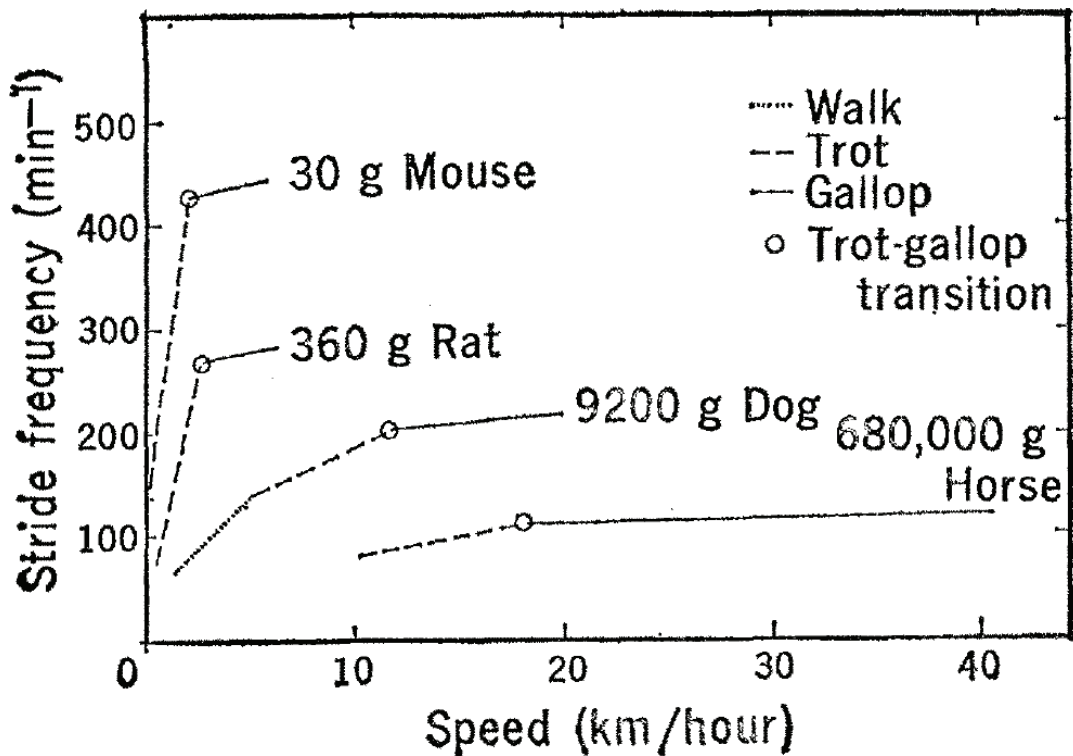


**Figure 9:** The simplest models for walking and running. (A) The Inverted Pendulum model for walking. (B) The Spring-Loaded Inverted Pendulum (SLIP) model for running. Reproduced from [2].

Both the inverted pendulum and the SLIP indicate that walking and running gaits are energetically efficient and do not require energy input. For walking, the kinetic energy and gravitational potential energy of the center of mass interchange; for running, the mechanical

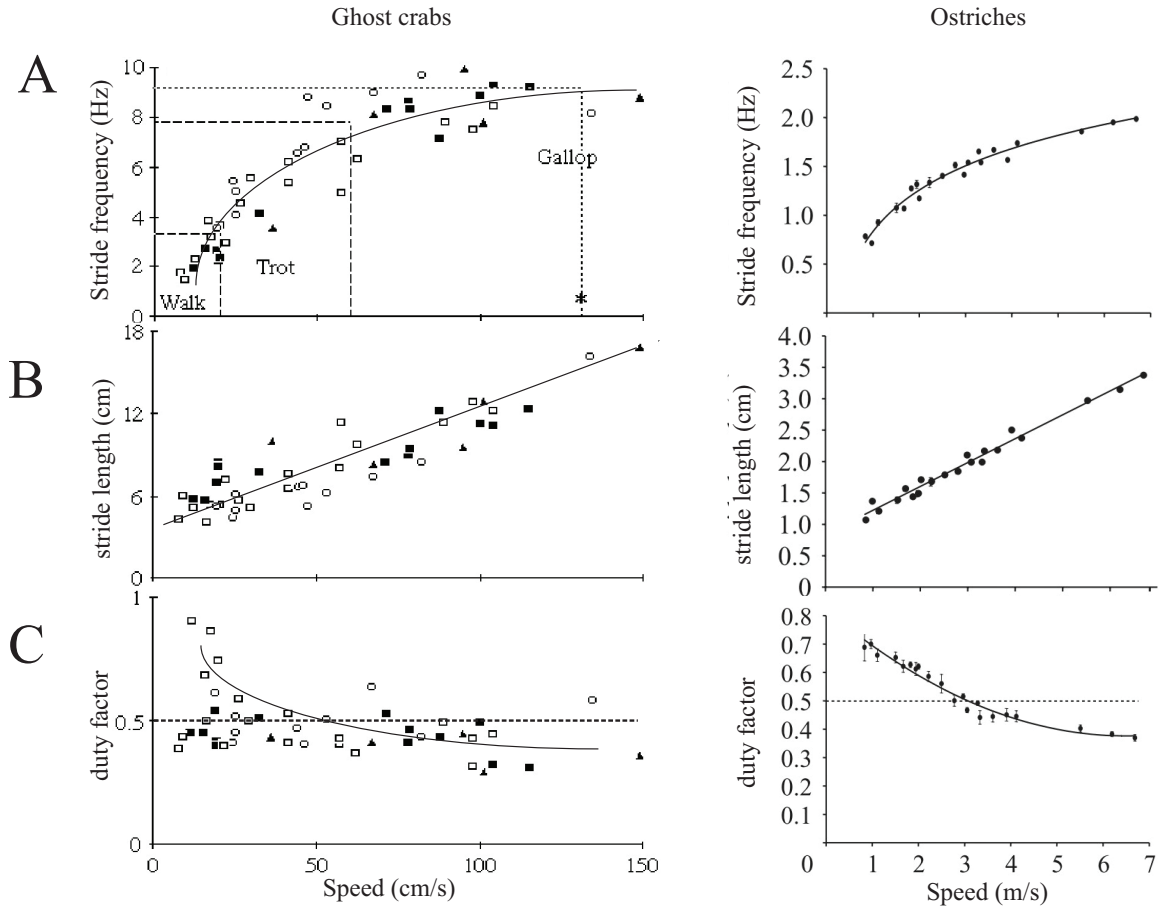
energy (kinetic plus gravitational potential energy) of the center of mass interchanges with elastic energy of the leg spring. In these models, the spring-mass system and the interaction with the solid ground are perfectly elastic and do not dissipate energy; thus no net work is performed.

However, in the natural world, as animals move across complex surfaces, energy is dissipated both within the body and limbs [32] and to the environment [1]. Thus mechanisms to minimize energy loss during locomotion can be important. For example, the limbs of many organisms possess elastic elements such as tendons and ligaments (most notably, the ankle extensor tendons in the lower leg) that can function as springs during rapid locomotion to save energy [33]. Furthermore, different limb-ground interaction strategies may be utilized depending on the dissipative properties of the substrate to minimize energy loss.



**Figure 10:** Walk-to-run transition in legged animals on solid surfaces. Stride frequency of mouse, rat, dogs, and horse as a function of speed. The relation between speed and stride frequency changes from gait to gait. The trot-gallop transition is marked with a circle. Reproduced from [34].

In many legged animals, as speed increases, gait changes from walking to trotting to galloping on solid surfaces (Fig. 10). During a walk or a trot, stride frequency increases approximately linearly with speed although the slope is larger for trotting [34]. Over the range of walking and trotting, higher speed is achieved by increasing stride frequency and stride length together. However, during a gallop (i.e., running) as speed increases, stride frequency remains almost unchanged (i.e., maximal sustained stride frequency, which is constraint by the physiology of the animal), and increased stride length is the dominant factor responsible for increase in speed [34].



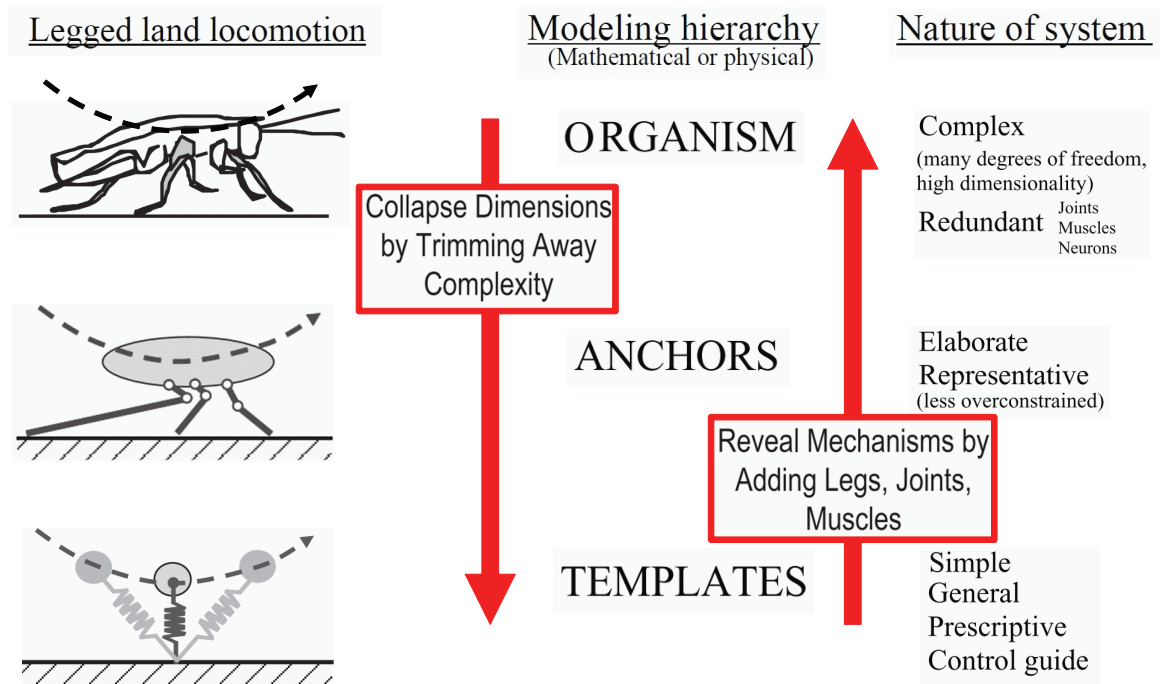
**Figure 11:** Gait parameters during walk-to-run transitions. (A) Stride frequency, (B) stride length, and (C) duty factor as a function of speed in ghost crabs (left) and ostriches (right). Modified from [35, 36].

Fig. 11 shows stride frequency  $f$ , stride length  $\lambda$ , and duty factor  $D$  as a function of speed  $v$  on solid surfaces for two model animals, ghost crab and ostriches [35, 36]. The

sub-linear increase of  $f$  with  $v$  (i.e., super-linear increase of  $v$  with  $f$ ) is also observed (Fig. 11A). Because  $\lambda$  increases approximately linearly with  $v$  as  $\lambda = kv + b$  (Fig. 11B) and  $v = \lambda f$ ,  $v = \frac{bf}{1-kf}$ . Since  $\frac{1}{1-kf}$  increases with  $f$ ,  $v$  increases super-linearly with  $f$  (or  $f$  increases sub-linearly with  $v$ ). Duty factor usually decreases from above 0.5 to below 0.5 as gait changes from walking to running (Fig. 11C).

### 1.2.2 Templates and anchors

Animal locomotion results from complex, high-dimensional, nonlinear, dynamically coupled interactions between an organism, which has highly complex, many degree-of-freedom nervous and musculoskeletal systems, and its complicated environment [16, 2]. The simplest models (also known as “templates” [16]) of legged locomotion such as the Inverted Pendulum and the SLIP were identified by constraining locomotion on solid surfaces and trimming away the complexity of the animal (e.g., joints, muscles, and neurons) [16] (Fig. 12,



**Figure 12:** Templates and anchors of legged locomotion. A template is a pattern that describes and predicts the behavior of the body in pursuit of a goal. It serves as a guide or target for the control of locomotion. An anchor is a more realistic model fixed firmly or grounded in the morphology and physiology of an animal. It adds degrees of freedom to better represent the animal of interest such. Modified from [16].

downward arrow).

However, a template does not reveal the mechanisms of how an animal’s nervous and musculoskeletal systems operate and interact with its environment to achieve the template behavior (or lack thereof). It is crucial to create more realistic, elaborate models (also known as “anchors” [16]) which incorporate the morphology and physiology of an animal, but at the same time display the general behaviors captured by the corresponding templates [16] (Fig. 12, upward arrow). For example, while the SLIP model predicts that an animal could run with no energy input, in animals running on natural surfaces, energy is dissipated both within the body and limbs [32] and to the environment [1]. Only part of the required mechanical energy can be saved by elastic stretch and recoil of tendons and ligaments [33].

Similarly, to understand the mechanisms of effective locomotion on natural surfaces, it is critical to add the complexity of natural surfaces. In this spirit, recent laboratory experiments have begun to reveal the mechanisms of running on non-solid surfaces, including surfaces that are elastic [7, 8], damped [9], inclined [5], or uneven [3, 4]; surfaces with few footholds [6]; and the surface of water [19, 20]. While spring-mass-like CoM motion is observed only in some of these studies [7, 9, 8], a common finding is that on non-solid

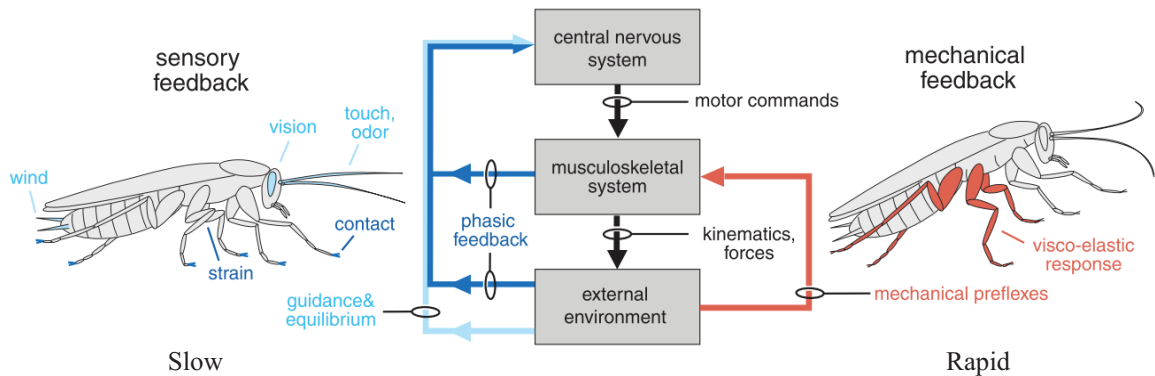


**Figure 13:** Neural and mechanical aspects of locomotion control. Both sensory feedback from the nervous system and mechanical feedback from the musculoskeletal system play a role in locomotion control. The nervous system processes the sensory feedback (light blue) and modifies the motor commands (dark blue). In parallel, viscoelastic mechanical reflexes (red) of the musculoskeletal system act rapidly to resist perturbations. Sensory feedback is dominant during slow running (left); mechanical feedback becomes important as running becomes faster (right). Modified from [2].

surfaces animal's limbs do not necessarily behave like springs to save energy. In addition, these studies suggest that both the active control of body and limb movement through the animal's neural system, and the passive mechanical responses of the animal's viscoelastic limbs and feet with the environment, play important roles in the control of rapid terrestrial locomotion [16, 2, 37] (Fig. 13). In particular, to understand how terrestrial animals move on yielding/flowing substrates like granular media, it is important to create models of foot-ground interaction that incorporate not only the morphology and physiology of an animal, but also the appropriate physics of interaction with the surrounding yielding and flowing media.

### 1.3 *Model organism*

#### 1.3.1 Zebra-tailed lizard



**Figure 14:** A zebra-tailed lizard sitting on a granular surface in the wild. Photo courtesy of Thomas C. Brennan.

The zebra-tailed lizard (*Callisaurus draconoides*, SVL  $\sim 10$  cm, mass  $\sim 10$  g, Fig. 14) provides an excellent model animal for studying the mechanics of running on natural surfaces, because of its high locomotor performance over diverse terrain. It is the fastest running lizard among desert lizards of similar size [38] (Fig. 15). As a desert generalist,

this lizard lives in a large range of desert habitats including flat land, washes, and sand dunes [39, 40], and encounters a great variety of substrates ranging from rocks, gravel, closely-packed coarse sand, and loosely-packed fine sand [41, 40]. Although these substrates can range from solid surfaces to yielding/flowing substrates, the zebra-tailed lizard can achieve high running speeds of up to  $\sim 4$  m/s ( $\sim 50$  bl/s) both on solid (treadmill [38]) and on granular (in the wild [42]) surfaces. It was also observed in the field that the zebra-tailed lizard's maximal acceleration and running speed do not differ significantly when the substrate changes from coarse wash sand to fine dune sand [40]. Previous studies found that two other species of lizards run like a spring-mass system (pogo stick) on solid surfaces [43]; however, it is not clear whether this is true on granular surfaces.

Of particular interest is whether and how the zebra-tailed lizard's large, elongate hind foot contributes to its high locomotor capacity. In addition to a slim body, a long, tapering tail, and slender legs, the zebra-tailed lizard has an extremely large, elongate hind foot,

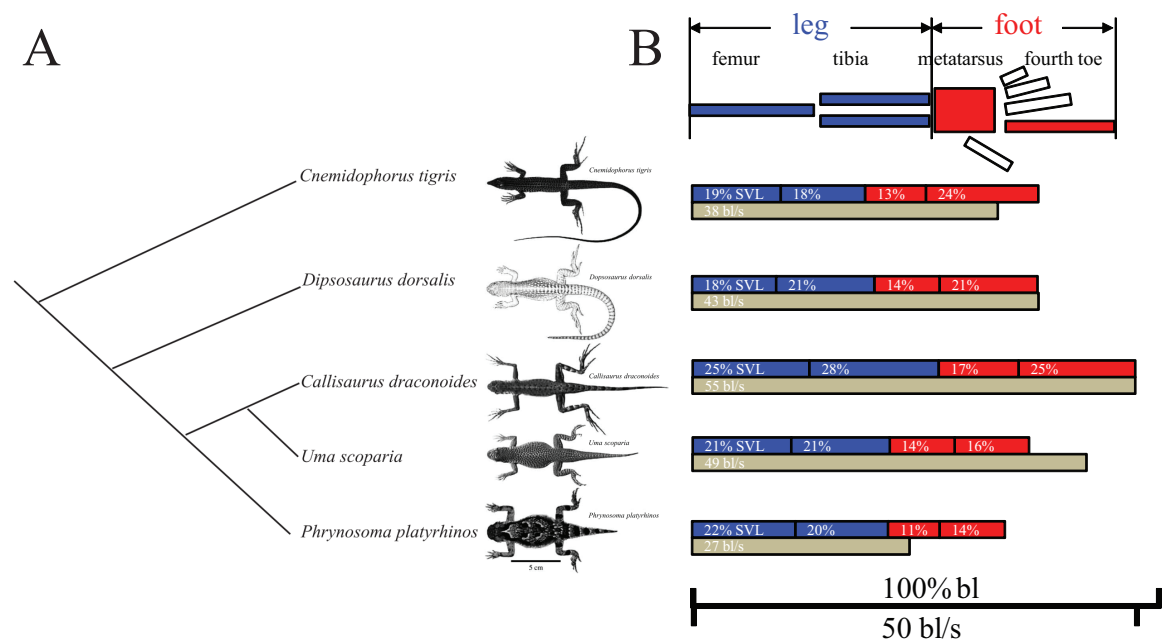


**Figure 15:** Zebra-tailed lizard and its closely-related desert lizards. (A) Phylogeny of five closely-related desert lizards. The zebra-tailed lizard is in the middle. Modified from [38]. (B) Hind limb segment lengths and running speed (in bodylength/s) of these five lizards. Produced using data from [38].

the largest (40% SVL) among lizards of similar size [38] (Fig. 15). Recent studies in insects, spiders, and geckos [44, 45, 46, 6] suggested that animals largely rely on appropriate morphology and material properties of their bodies and limbs to accommodate variable, uncertain conditions during locomotion. Despite proposals that the large foot area [27] and increased stride length via elongate toes may confer locomotor advantages [38], the mechanisms of how the large, elongate hind foot contributes to the zebra-tailed lizard’s high running capacity remain to be uncovered.

### 1.3.2 An analogy: the water-running basilisk lizard

From morphological and locomotor perspectives, the zebra-tailed lizard resembles the water-running basilisk lizard (*Basiliscus* species) [19, 47]. Both lizards have elongate body and limbs, and an large, elongate hind foot, and are capable of rapid running on a deformable surface that can flow during footsteps.

The foot-ground (water surface) interaction of the basilisk lizard consists of three phases with distinct forces [19]. First, an upward impulse (slap impulse) is produced as the lizard foot impacts the water surface and suddenly accelerates a volume of water downwards (Fig. 16A). Next, after impact, an air cavity is produced as the lizard strokes downwards

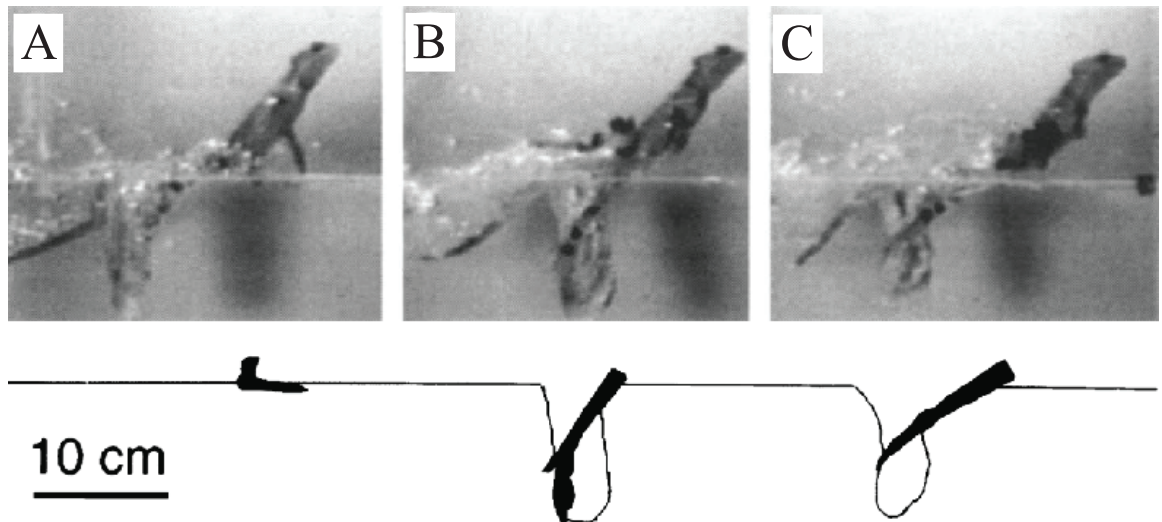


**Figure 16:** Three phases of foot-water interaction during water-running in the basilisk lizard. (A) Slap. (B) Stroke. (C) Retraction. Modified from [19].

and backwards while plantar-flexing the foot. Integrated over time, the upward component of the drag force helps to support the lizard's body weight (stroke impulse) (Fig. 16B). Finally, the lizard minimizes the downward forces associated with foot protraction by pulling its foot upwards before the cavity collapses. Protraction drag is further minimized by the feathering of the lateral toe fringes and the reorientation of the foot such that its long axis is parallel with the direction of movement (Fig. 16C).

The total vertical force (impulse) on the basilisk lizard's foot results from three sources. During slap, when foot depth is small, force is dominated by the inertia of the water under the foot being accelerated downward rapidly (up to 3 m/s). This hydrodynamic impact force during slap contributes approximately 18% of the total vertical impulse needed to balance the weight of the lizard. During stroke, as the foot penetrates deeper ( $\sim 10$  cm) into water, both hydrodynamic force (due to the water under the foot being accelerated downwards and backwards at  $\sim 1$  m/s) and hydrostatic force (due to the pressure difference between the water surface and the bottom of the air cavity) contribute to total thrust. Impact experiments of discs and foot models [48, 49] and calculations using hydrostatic and hydrodynamic equations show that these forces together contribute a total of 84% of the required vertical thrust [19], with 22% from hydrostatic force, and 62% from hydrodynamic force.

For water-running, techniques like Particle Imaging Velocimetry (PIV) and Computational Fluid Dynamics (CFD) can be employed to capture the details of water flow vortices and compute the resulting thrust [47] (Fig. 17). However, these methods are difficult to apply for running on granular media due to the opacity of the grains.

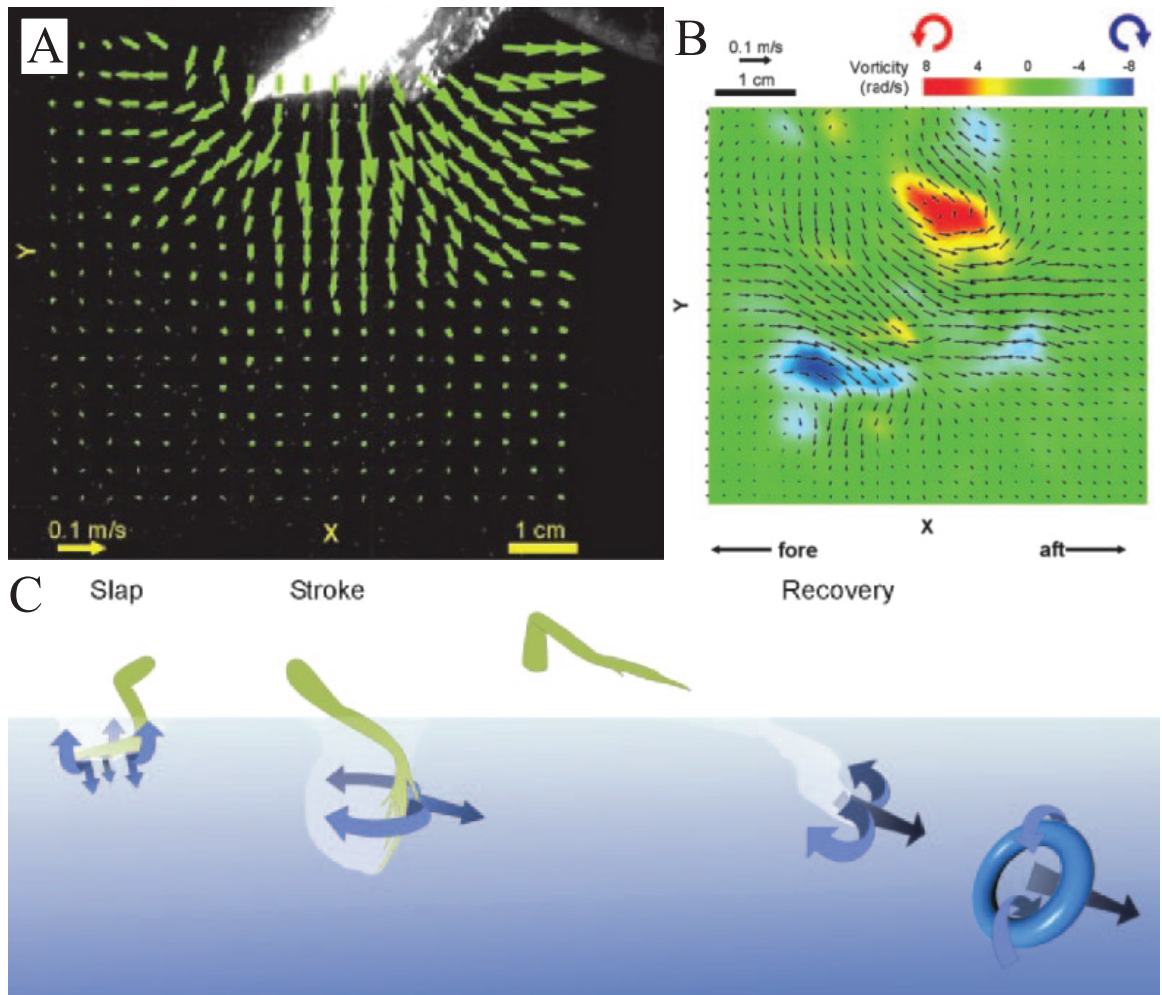


**Figure 17:** Detailed flow and forces during water-running obtained from PIV and CFD. (A) Velocity field of the water during foot slap (sagittal view) obtained from Particle imaging velocimetry. (B) Counter-rotating centers of vorticity shed from the foot after the stroke (sagittal view) obtained from Computational Fluid Dynamics. (C) A schematic of vortex ring formation during the three phases of a stride. Modified from [47].

## ***1.4 Physical models of organisms: bio-inspired legged robots***

In addition to high performing biological organisms, researchers have begun to bio-inspired robots (physical models of biological organisms) to study legged locomotion on granular media. Recently developed bio-inspired robots begin to display mobility approaching that of terrestrial animals. Using these robots as opposed to animals to study locomotion has a few advantages. First, the robots have relatively simple morphology and kinematics compared to the highly complex, many degree-of-freedom nervous and musculoskeletal systems of animals, and are thus easier to observe and model. In addition, the kinematics of robots can be systematically and precisely controlled over a large range of parameter space, as opposed to animals which behave on their own and are often limited by environmental and physiological constraints. Furthermore, the morphology of robots are more readily modified for test of hypotheses.

### **1.4.1 RHex**

The first robot we study, SandBot, is the smallest descendent in a successful series of hexapedal robots, the RHex (Robot Hexapod) (Fig. 18A) [15]. The RHex class of robots take inspiration from the dynamically stable spring-mass like locomotion of a cockroach (Fig. 3) [50]. RHex employs an alternating tripod gait, and uses compliant, c-shaped legs whose stiffnesses are tuned to bounce on rigid surfaces. RHex was the first legged machine to achieve autonomous locomotion at speeds of  $\sim 1$  body length per second [15] and it and its “descendants” such as Edubot/Sandbot (Fig. 19), iSprawl [51] (Fig. 18B), and Whlegs [52] (Fig. 18C) are still the leaders in legged mobility (roughly, speed and efficacy) on general terrain. In fact, prior to the recent development of BigDog [53] (Fig. 18D), RHex remained the only class of legged machine with documented ability (at  $\sim 1$  body length/s) to navigate complex, natural, outdoor terrain, and has been used as the standard platform in comparisons with commercial wheeled and tracked vehicles like Packbot [54] (Fig. 18E). The RHex class of model locomotors (robots) has also proved useful to test hypotheses of limb use in biological organisms on hard ground [55] and recently on more complex ground with few footholds [6].

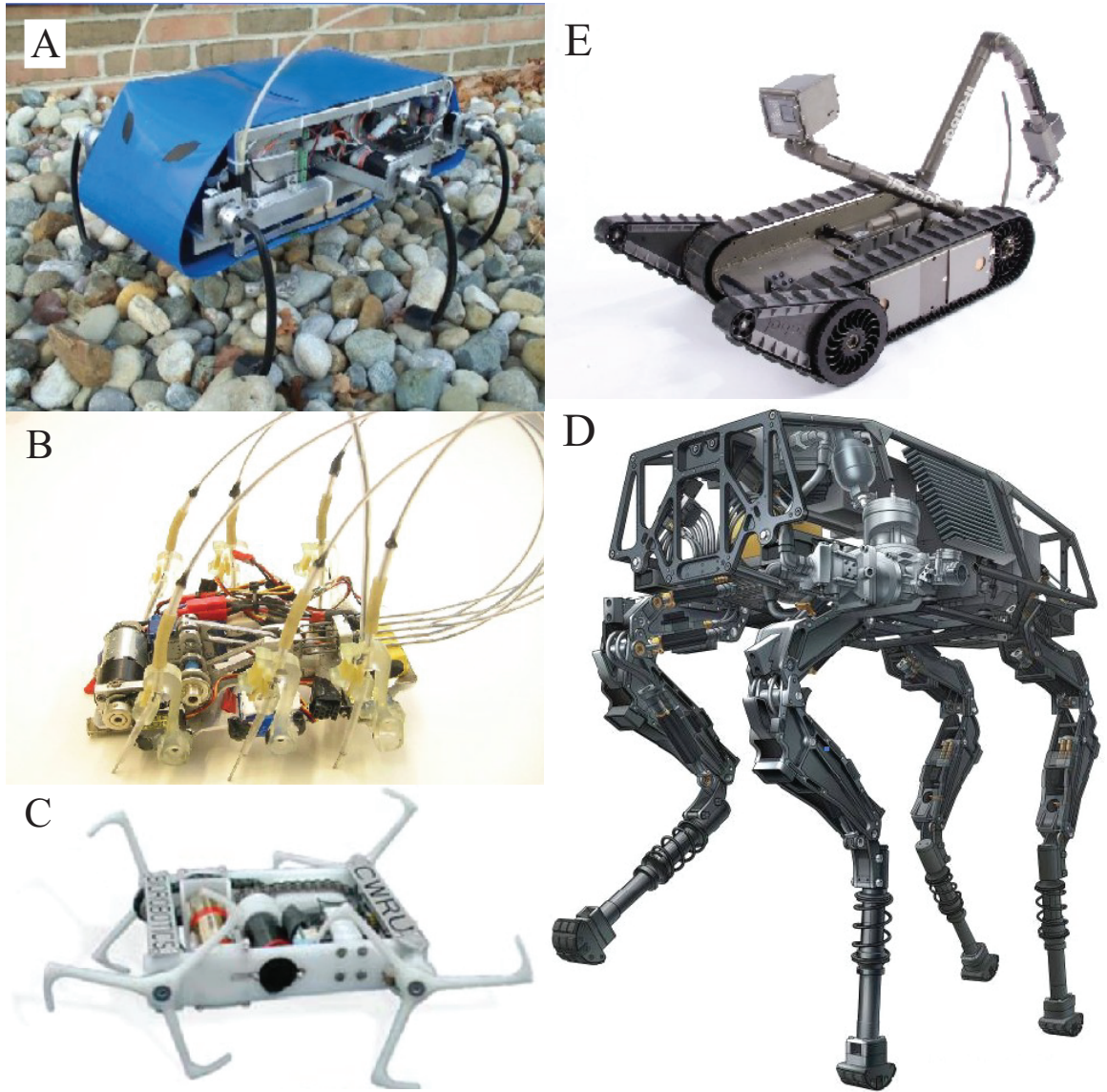


**Figure 18:** Recent bio-inspired legged robots. (A) RHex. (B) iSprawl. (C) Whigs. (D) BigDog. (E) Packbot. (A–D) are reproduced from [15, 51, 52, 53]. (E) courtesy of iRobot.

SandBot\* (Fig. 19, 30 cm long, 2.3 kg) moves using an alternating tripod gait such that two sets of three approximately c-shaped limbs rotate synchronously and  $\pi$  out of phase (Fig. 19). In these devices, complexity in limb motion is pared down to a few biologically relevant parameters controlling intra-cycle ‘slow ‘stance’ and fast ‘swing’ phases of 1-dof rotating limbs (referred to as ‘gait’ parameters hereafter). A controlling signal called the

---

\*This robot was developed by Haldun Komsuoglu and Daniel E. Koditschek.

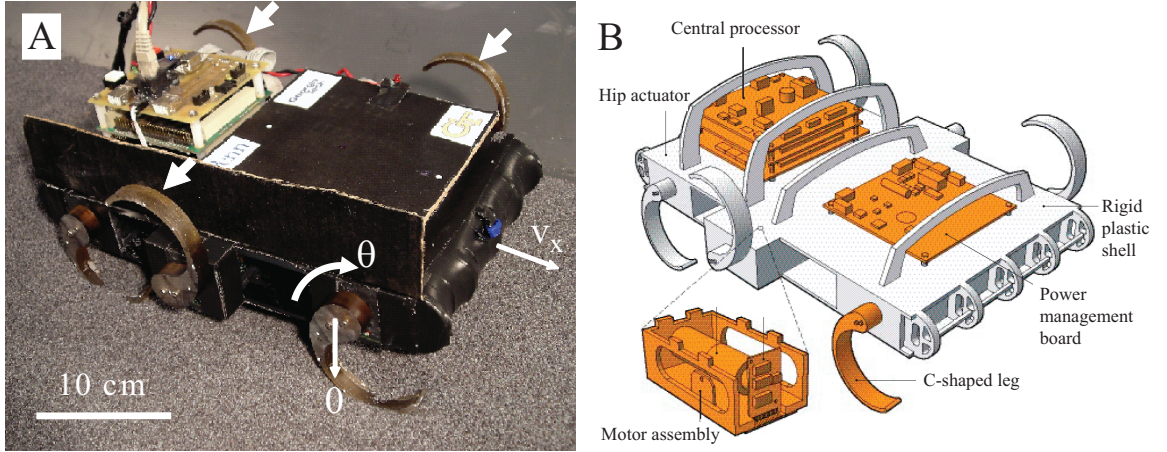


**Figure 19:** SandBot, a RHex class legged robot. (A) SandBot standing on granular media ( $\sim 1$  mm diameter poppy seeds). Arrows indicate a tripod of three c-shaped limbs rotating in phase. (B) Design diagram of SandBot. Modified from [56].

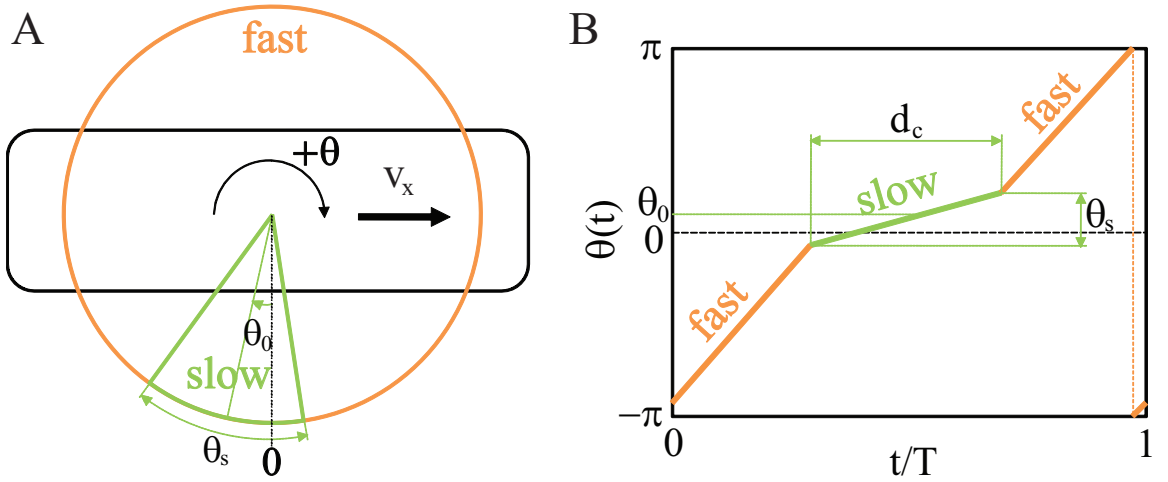


**Figure 20:** SandBot's clock signal that controls leg rotation. (A) Each leg rotation is composed of a fast phase (orange) and a slow phase (green).  $\theta_s$  and  $\theta_0$  define the angular extent and center of the slow phase, respectively. (B) Leg angle  $\theta$  as a function of time  $t$  during one cycle (normalized to period  $T$ ).  $\theta(t)$  of the other tripod is shifted by  $T/2$  but otherwise identical.  $d_c$  is the duty cycle of the slow phase, i.e. fraction of the period spent in the slow phase.

clock signal (Fig. 20) prescribes the angular trajectory of each tripod. On rigid, no-slip ground RHex's limb trajectories are tuned to create a bouncing locomotion that generates speeds up to  $\sim 1$  bodylengths/s [15]. When these gait parameters are appropriately

adjusted, RHex shows performance comparable in speed and stability to organisms on a diversity of terrain [15]. However, because of the scarcity of existing models of limb interaction with complex substrates, gait parameters have been determined empirically [57, 50].

#### 1.4.2 Smart Composite Manufacturing robots

Another class of robots used in this dissertation is the Smart Composite Manufacturing robots, including RoACH [58] and DASH [59]<sup>†</sup> (Fig. 21). These are small, lightweight ( $\sim 10$  cm,  $\sim 20$  g), biologically inspired six-legged robots that utilize alternating tripod gaits. Their masses are  $\sim 100$  times smaller than earlier top performing devices like the RHex class of robots [15]. They both use a single 6 mm brushed DC motor to drive all six limbs through linkage drive mechanisms. The Smart Composite Manufacturing (SCM) process [60] makes it possible to construct very lightweight robots with complex spatial kinematics that exhibit relatively high power densities, by simply folding a single piece of relatively inexpensive lightweight 2D board into a pre-designed 3D structure. In addition, robots created with this process can survive collisions with the ground at their terminal velocities [59].

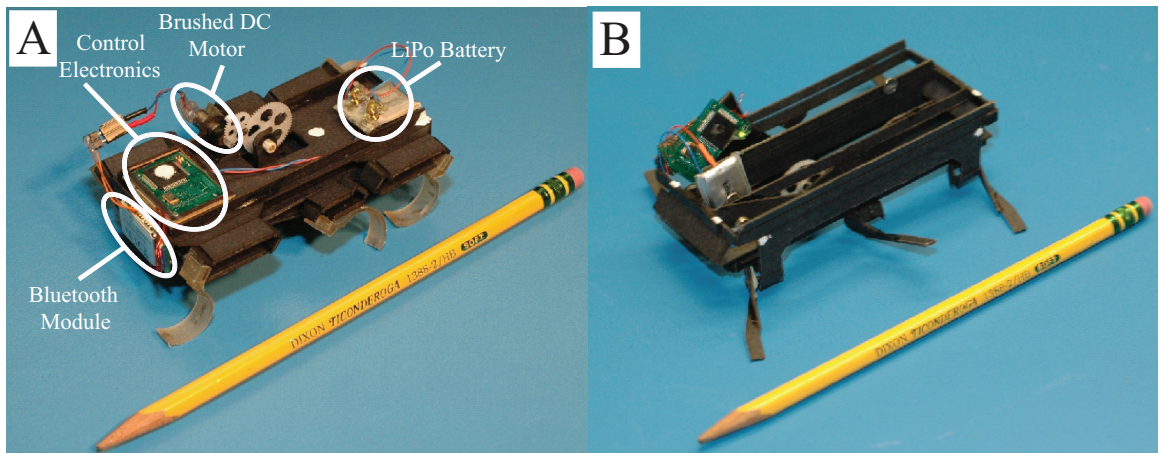


**Figure 21:** Smart Composite Manufacturing robots. (A) The RoACH robot shown with component parts of onboard power and electronics highlighted. (B) The DASH robot.

While DASH and RoACH are similar in size, components, manufacturing process, and

---

<sup>†</sup>These robots were developed by Aaron M. Hoover, Paul Birkmeyer, and Ronald S. Fearing.

an alternating tripod gait, they have distinct limb morphology and kinematics. The most notable among these differences is their posture. RoACH has an upright posture with its legs directed almost vertically downward; whereas DASH has a sprawled posture, with its legs directed outward nearly horizontally. As a result, they provide excellent test platforms for assessing benefits and tradeoffs of these factors on a variety of substrates.

## 1.5 *Physics of intrusion forces in granular media*

During legged locomotion on granular media, the bodies, limbs, and feet of animals and robots must intrude into the granular substrate to generate force. These intrusions are localized [61] as opposed to globalized forcing (e.g., avalanche [62], couette flow [63]). While terramechanics has been around for a few decades and has guided the development of off-road vehicles [64, 65, 66, 67], it focused on the study of the overall performance of large wheeled and treaded vehicles with unprepared soil, and the locomotor-ground interaction involved largely concentrates on how normal stresses determine shear stresses. Due to the large size of the vehicle wheels and treads as compared to the size of the grains in a granular medium, this is mainly a global forcing problem. No general models currently exist to predict resistance forces for localized intruder of complex geometry along complex trajectories during footsteps, particularly those relevant to legged locomotion. As such, granular forces during localized intrusion have been measured empirically using simple intruders like spheres, cylinders, discs, and plates (and occasionally complicated shapes [68]) moving along simple paths, such as horizontal drag [69, 70, 71], vertical penetration [72], and vertical impact within granular media [73, 74].

### 1.5.1 **Horizontal drag**

Most studies of forces during horizontal drag in granular media have focused on measuring the horizontal drag force opposing the direction of motion at low speeds (speed  $v < 0.5$  m/s [69], and often  $v \sim 0.001$  m/s [70, 71]). At such low speeds, drag force is approximately independent of speed [69, 70]. This is because at low speeds, granular force is dominated by grain-grain friction and grain-intruder friction, which are approximately rate independent. While the shape of intruders has small effects on the force magnitude [68], drag force scales approximately with the area of the intruder perpendicular to the direction of motion, i.e. the projected area. For example, the drag force on a vertically oriented cylinder scales with the cylinder diameter, which is proportional to the projected area (Fig. 22B).

In addition, for an intruder that extends to the surface such as a vertically oriented cylinder (Fig. 22A), drag force increases approximately quadratically with the maximal

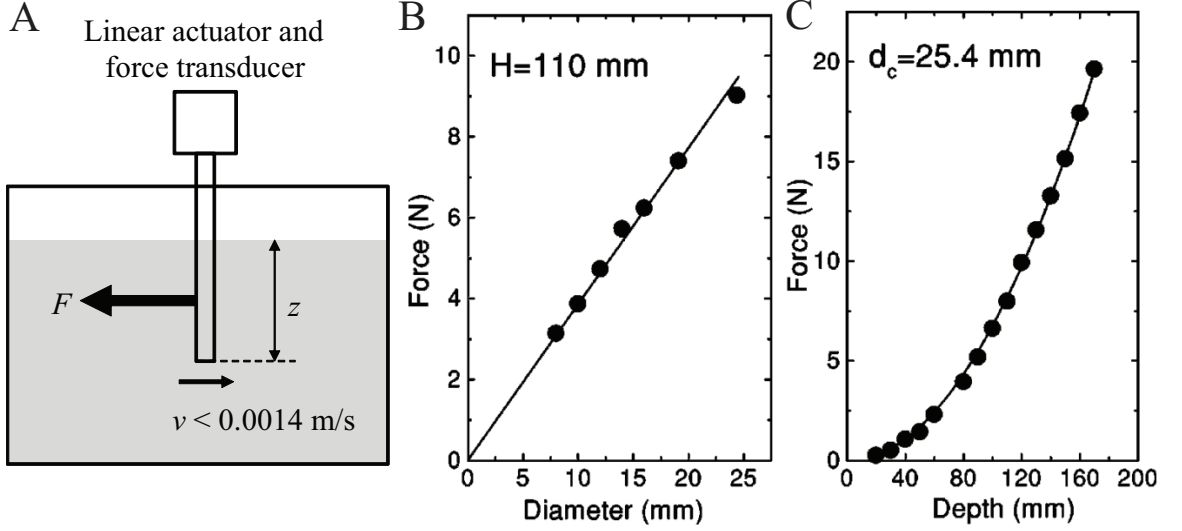


**Figure 22:** Force during horizontal drag of a cylinder in granular media at low speeds. (A) Experimental setup. Produced based on descriptions in [71]. (B) Force as a function of cylinder diameter (i.e., the width of the cylinder into the plane, which scales with the area perpendicular to the direction of motion). (C) Force as a function of the maximal depth of the cylinder. Reproduced from [71].

depth (Fig. 22C). This indicates that the drag force  $dF$  on an infinitesimal element  $dz$  at depth  $z$  increases linearly with  $z$ , because for  $dF = kz dz$ ,  $F = \int_0^{z_{max}} dF = \int_0^{z_{max}} \frac{dF(z)}{dz} dz = \int_0^{z_{max}} kz dz = \frac{1}{2}kz^2$ .

### 1.5.2 Vertical penetration

Similar to horizontal drag, forces during vertical penetration into granular media at low speeds ( $v < 0.5$  m/s) were found to scale approximately with the projected area of the intruder, and increase approximately linearly with depth. For example, the penetration force on a sphere moving vertically into granular media scales as:  $\frac{F}{\rho g V} \propto \frac{z}{l}$  (more accurately,  $F = 21(\frac{z}{l})^{1.2}$ ) (Fig. 23), where  $\rho$  is the density of the granular media,  $g$  is gravitational acceleration,  $l$  is the sphere diameter, and  $V = \frac{1}{6}\pi l^3$  is the sphere volume. Rewriting this equation gives  $F \approx \propto Az$ , where  $A = \pi l^2$  is the projected area of the sphere.

The approximate proportional dependence of granular forces during both horizontal drag and vertical penetration is the result of the hydrostatic-like pressure in granular media, which increases approximately linearly with depth. Because friction is proportional to

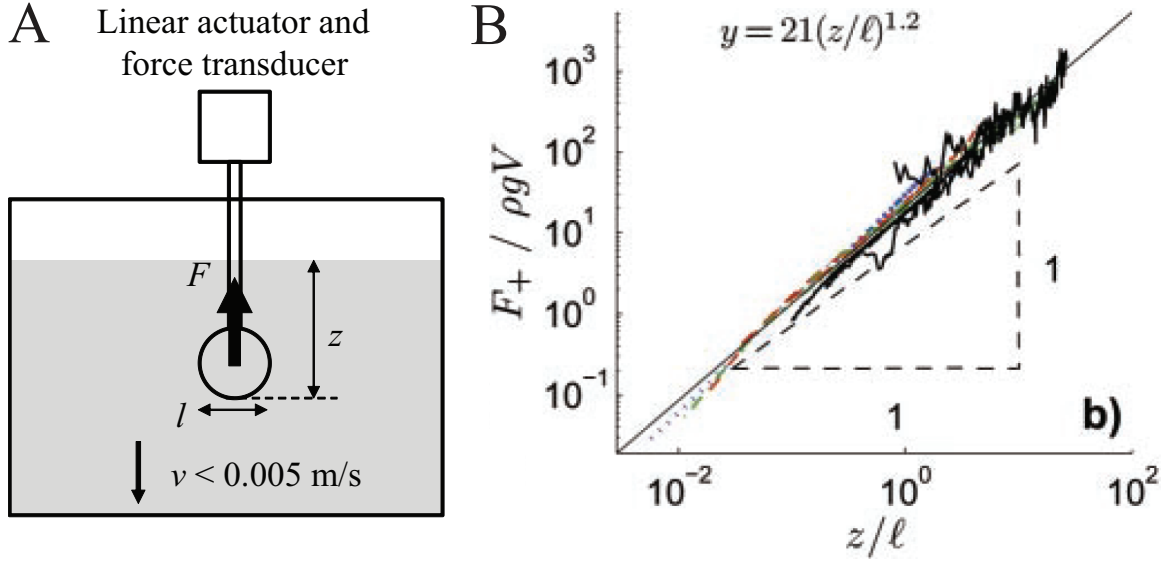


**Figure 23:** Force during vertical penetration of a sphere into granular media at low speeds. (A) Experimental setup. Intruder is a sphere pushed downward by an actuator. Produced based on descriptions in [72]. (B) Force as a function of the maximal depth of the intruder. Note that force is scaled to sphere weight, and depth is scaled to sphere diameter. Reproduced from [72].

normal force and thus pressure, and granular forces are dominated by grain friction at low speeds, it is expected that granular forces increases approximately linearly with depth.

### 1.5.3 Vertical impact

Intrusion forces in granular media at high speeds have been mainly investigated during vertical impact, where an intruder free falls from a height to reach high speeds (often  $v_c > 0.5$  m/s) at the time it impacts the granular surface, penetrates, and stops. These studies show that unlike for low speed intrusion forces which are approximately rate independent, at high speeds ( $v_c > 0.5$  m/s) granular force increases approximately quadratically with the impact speed. This is observed both for force (acceleration) at the time of impact (i.e., peak acceleration on a sphere), and force (acceleration) during the subsequent deceleration phase [73].

The quadratic dependence of high speed impact force on impact speed indicates that at high speeds granular force is instead dominated by the inertia of the grains being accelerated, much like in fluids at high Reynolds number where the inertia of water is

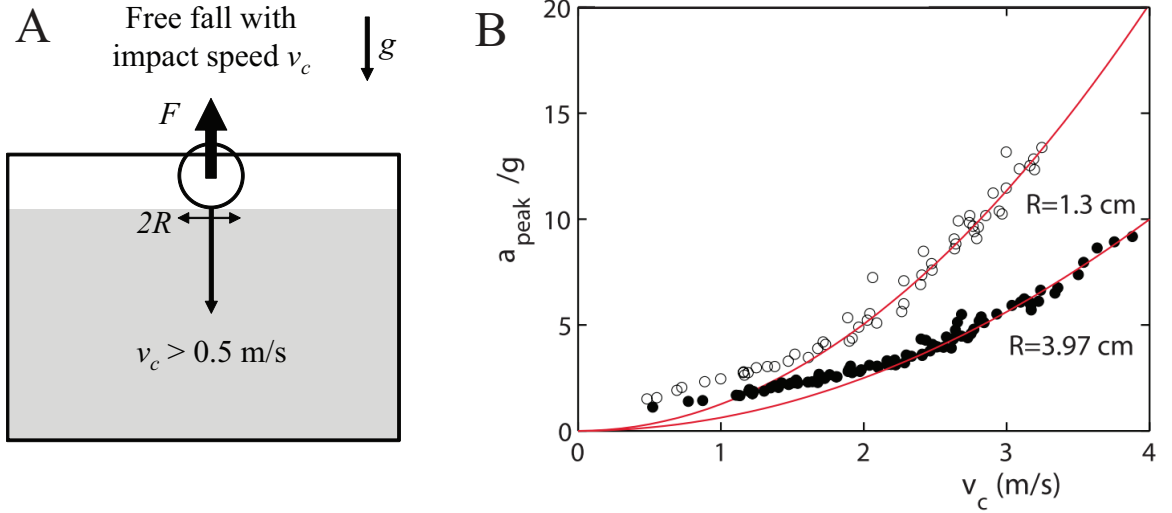


**Figure 24:** Force during vertical impact of a sphere into granular media at high speeds. (A) Experimental setup. Impact speed  $v_c$  is defined as the intruder speed when it impacts the surface. Force is obtained by measuring acceleration using an accelerometer embedded in the intruder. Produced based on descriptions in [74]. (B) Peak acceleration (i.e., acceleration at the time of impact) as a function of the impact speed of the intruder. Reproduced from [74].

dominant. Assuming that at the time of impact, during a time period of  $dt$ , a volume of stationary grains of area  $A$  and thickness  $dx$  in front of the intruder are accelerated from zero speed to the intruder speed  $v$ , the inertial force to accelerate the grains is  $F = \frac{dp}{dt} = \frac{dmv-0}{dt} = \frac{\phi\rho A dx v}{dt} = \phi\rho A v^2 \propto A v^2$ , where  $\phi \approx 0.6$  is the volume fraction of the granular medium, and  $\rho$  is the grain density. Note that acceleration  $a$  is lower for larger sphere radius  $R$  in Fig. 24 since  $a = \frac{F}{m} \propto \frac{R^2}{R^3} \propto \frac{1}{R}$ .

## 1.6 Experimental techniques

### 1.6.1 Control of granular media by a fluidized bed

Granular media like sand can exist in different compactions (Fig. 25). A static granular medium responds differently to shear when it is loosely packed from when it is closely packed [10]. The compaction of a granular medium is measured by the volume fraction, defined as the ratio between the solid volume of the medium and the volume it occupies [10]:

$$\phi = \frac{V_{solid}}{V_{occupied}}. \quad (1)$$

In nature, the volume fraction of stationary dry granular media ranges from  $\phi = 0.55$  to  $\phi = 0.64$  (i.e., the random close packing state  $\phi = 0.64 \pm 0.02$  [75]) [76]. A few percent of increase in volume fraction can increase the forces by a few times [77]. For example, a person's foot would sink much deeper on loose sand than on compact sand (Fig. 25).



**Figure 25:** Granular media of different volume fractions in nature. (A) Loosely packed sand (low  $\phi$ ). (B) Closely packed sand (high  $\phi$ ). Images courtesy of (A) Corbis Images and (B) Getty Images.

In granular physics studies, a device named a fluidized bed [24] have recently been employed to precisely control the volume fraction of a granular medium to generate well-defined, repeatable packing states [78, 79, 80, 77]. A fluidized bed has a flow distributor sandwiched between a upper container and a lower compartment (Fig. 26A). The upper container resembles an aquarium and contains the granular medium to be controlled. Beneath it is the air distributor which is a porous bottom with micro-sized holes serving to distribute air homogeneously. Other than the air distributor above it, the bottom compartment is otherwise sealed. A fluidized bed operates by allowing a flow of air (or fluids in some cases [24]) into the lower compartment, distributed homogeneously by the air distributor, and upward through granular medium.

The volume fraction of a granular medium is controlled by a fluidized bed as follows. For a collection of particles, a flow of air opposite to the direction of gravity exerts buoyant forces

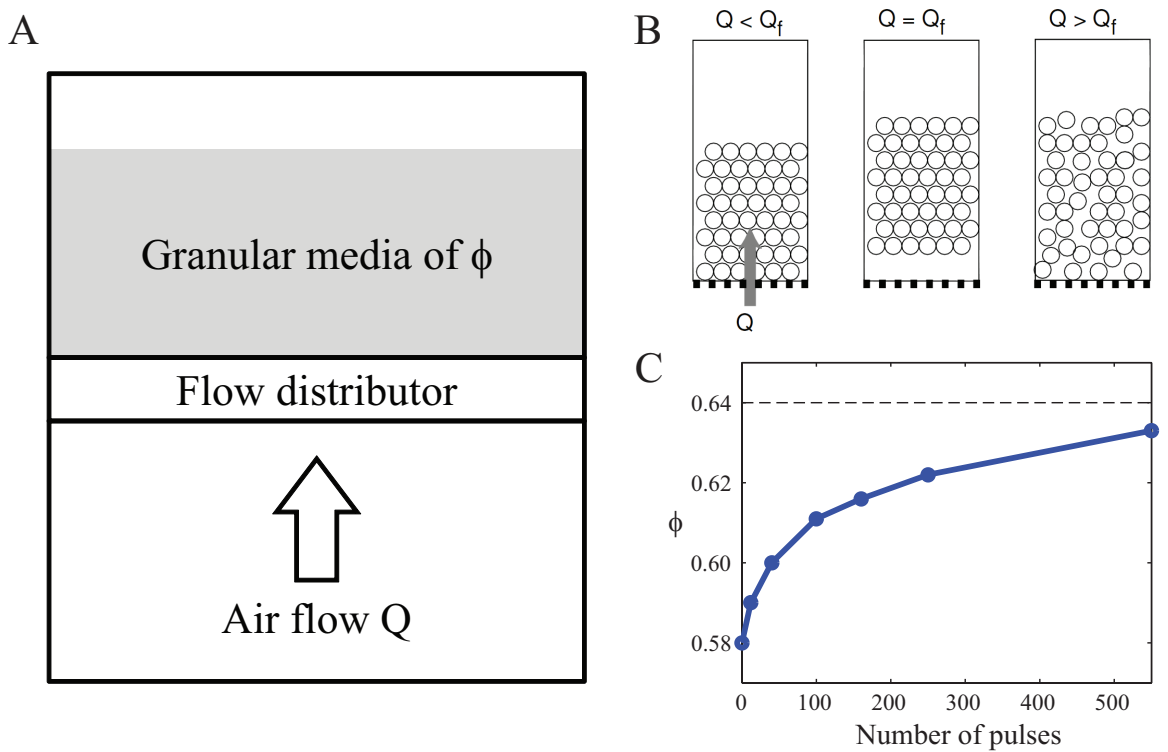


**Figure 26:** Diagram and principles of a fluidized bed. (A) Diagram of the design of a fluidized bed (not to scale). (B) The principle of fluidization process. Reproduced from [78]. (C) Volume fraction as a function of number of air pulses (data from the fluidized bed trackway in Fig. 27A using  $\sim 1$  mm diameter poppy seeds).

on the particles. As air flow reaches and past a critical value (defined as onset of fluidization  $Q_f$ ), the grains become neutrally buoyant and enter a fluidized state (Fig. 26B). As air flow is slowly turned off, the grains settle into a loosely packed state ( $\phi = 0.58$ ). Repeated air pulses or vibrations can then be applied to compact the granular medium [81] into higher volume fraction up to a closely packed state ( $\phi = 0.64$ ). Volume fraction increases approximately logarithmly with the number of air pulses or vibrations and approaches the closely packed state (Fig. 26C). With automated flow control (LabVIEW) and granular surface detection by imaging analysis, volume fraction can be controlled to an accuracy of 0.001.

### 1.6.2 Construction of fluidized beds

Using a fluidized bed to control granular media has not been applied for locomotion studies until very recently [82]. To create well-controlled granular substrates for locomotion studies which mimic natural surfaces with different penetration properties, I built a 250 cm long, 50 cm wide, 100 cm tall fluidized bed trackway (Fig. 27A). Its large size allows animals and robots ( $\sim 10$  cm long) to move across for a substantial distance so as to achieve steady

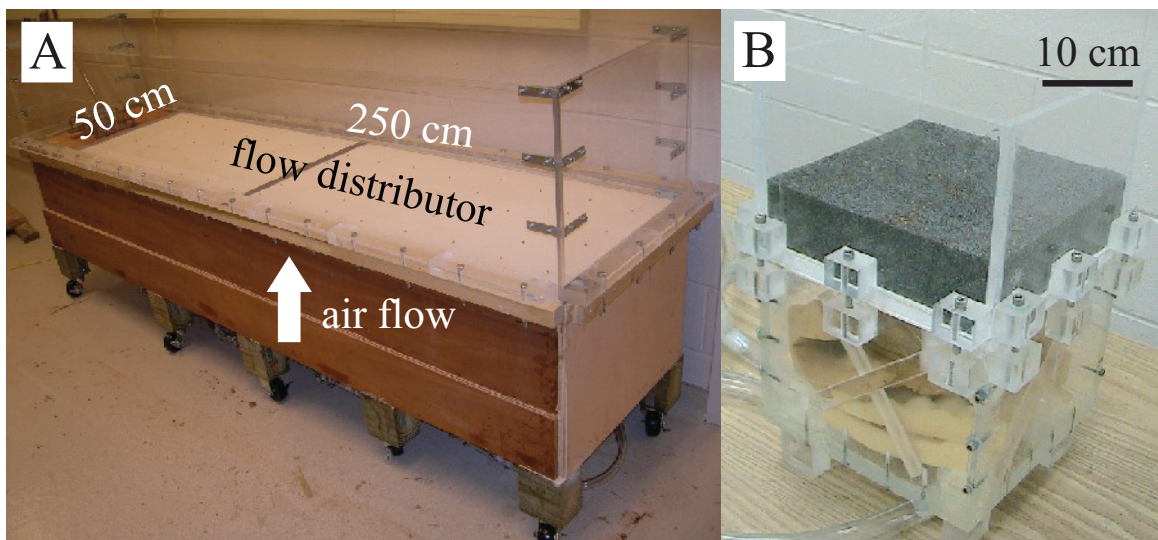


**Figure 27:** Fluidized beds constructed for this study. (A) A large fluidized bed trackway for locomotion studies. (B) A small fluidized bed (containing  $\sim 1$  mm diameter poppy seeds) for physics studies.

state locomotion. For physics studies of forces in granular media, I built another smaller fluidized bed (24 cm  $\times$  22 cm surface area) (Fig. 27B).

Porous plastic plates (Porex Corporation, Fairburn, GA, USA) were used as the flow distributor in both fluidized beds. For the large fluidized bed trackway, a porous plastic plate of 112  $\times$  106  $\times$  0.6 cm<sup>3</sup>, 90 – 130 *µm* pore size was used. The upper container was made from plexiglas. The lower compartment was made from wood. Porous foam filled the bottom compartment to enhance homogeneous air distribution. 64 threaded rods stood vertically underneath the flow distributor to support the weight of the granular media. Guitar strings and pegs were attached from the plate to the bottom to hold down the flow distributor against air flow. Four leaf blowers (340 HP, Tori) provided air into the trackway. Plastic tubing connected the trackway to compressed air as an additional air source.

For the small fluidized bed, a porous plastic plate of 24  $\times$  22  $\times$  1.25 cm<sup>3</sup>, 90–130 *µm* was used. Both the upper container and bottom compartment were made from plexiglas. Porous foam filled the bottom compartment to enhance homogeneous air distribution. Plastic tubing connected the trackway to compressed air source.

### **1.6.3 Three-dimensional kinematics capture using Direct Linear Transformation**

Although commercially available, proprietary systems such as VICON are widely used in studying human locomotion, these systems are often targeted at clinical studies and cannot be easily modified to fit to research needs in other disciplines such as animal studies [83]. As an alternative, we use direct linear transformation [84, 83], to obtain detailed three-dimensional (3-D) kinematics of animal locomotion.

Direct linear transformation (DLT) is a technique well established and widely used in animal studies thanks to its flexible camera placement and acceptable reconstruction accuracy [83]. DLT is essentially an algorithm to transform two-dimensional (2-D) coordinates of the object of interest in multiple camera views to three-dimensional (3-D) coordinates, using a set of prescribed calibration points whose spatial coordinates are known.

We use a freely available software package, DLTcal3 and DLTdv3 (courtesy of Ty Hedrick [83]) (Fig. 28B). We custom made a custom-made 39-point calibration object using

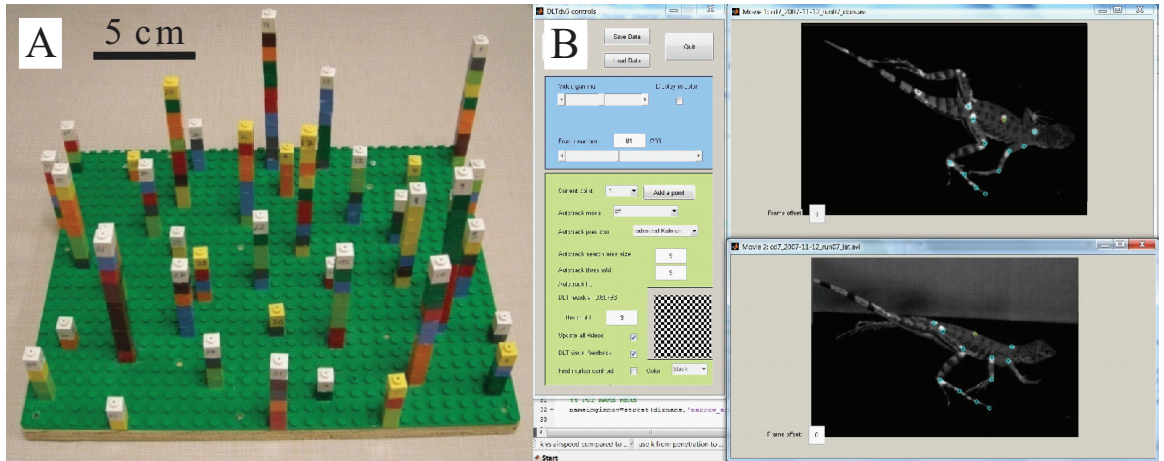


**Figure 28:** Direct Linear Transformation for three-dimensional kinematics capture. (A) A custom made 39-point calibration object using LEGO. (B) A screenshot of the DLTdv3 software [83] showing dorsal and lateral videos of a zebra-tailed lizard running on the solid surface.

LEGO (Fig. 28A). By placing the calibration object in the field of view of two (or more) securely-mounted high-speed cameras, we can obtain still calibration images which yield transformation matrix (via DLTcal3). We can then take simultaneous high-speed video of animal (or robots) of interest moving in the field of view using two (or more) cameras. Digitizing the markers on the animals (or robots) in 2-D videos (Fig. 28B) and transforming them into 3-D coordinates (via DLTdv3) yield 3-D kinematics. This technique can provide sub-millimeter accuracy for a 200 mm  $\times$  200 mm field of view [85].

#### 1.6.4 Intrusion force measurements using a six degree-of-freedom robotics arm

We use a six-degree-of-freedom robotic arm (CRS Robotics) to perform intrusion experiments to study forces in granular media. The robotic arm has six joints and is capable of moving in three-dimensional space within a large work space ( $\sim 1 \text{ m}^3$ ). The distal joint of the robotic arm can translate at speeds up to 1 m/s (with little vibrations below 0.3 m/s) and rotate at angular velocity of up to  $150^\circ/\text{s}$ . The robotic arm can achieve sub-millimeter accuracy during translation and sub-degree accuracy during rotation. A six-axis force/torque transducer (ATI) is mounted on the distal joint of the robotic arm, which can be attached to an intruder to measure force/torque. The accuracy of the transducer is

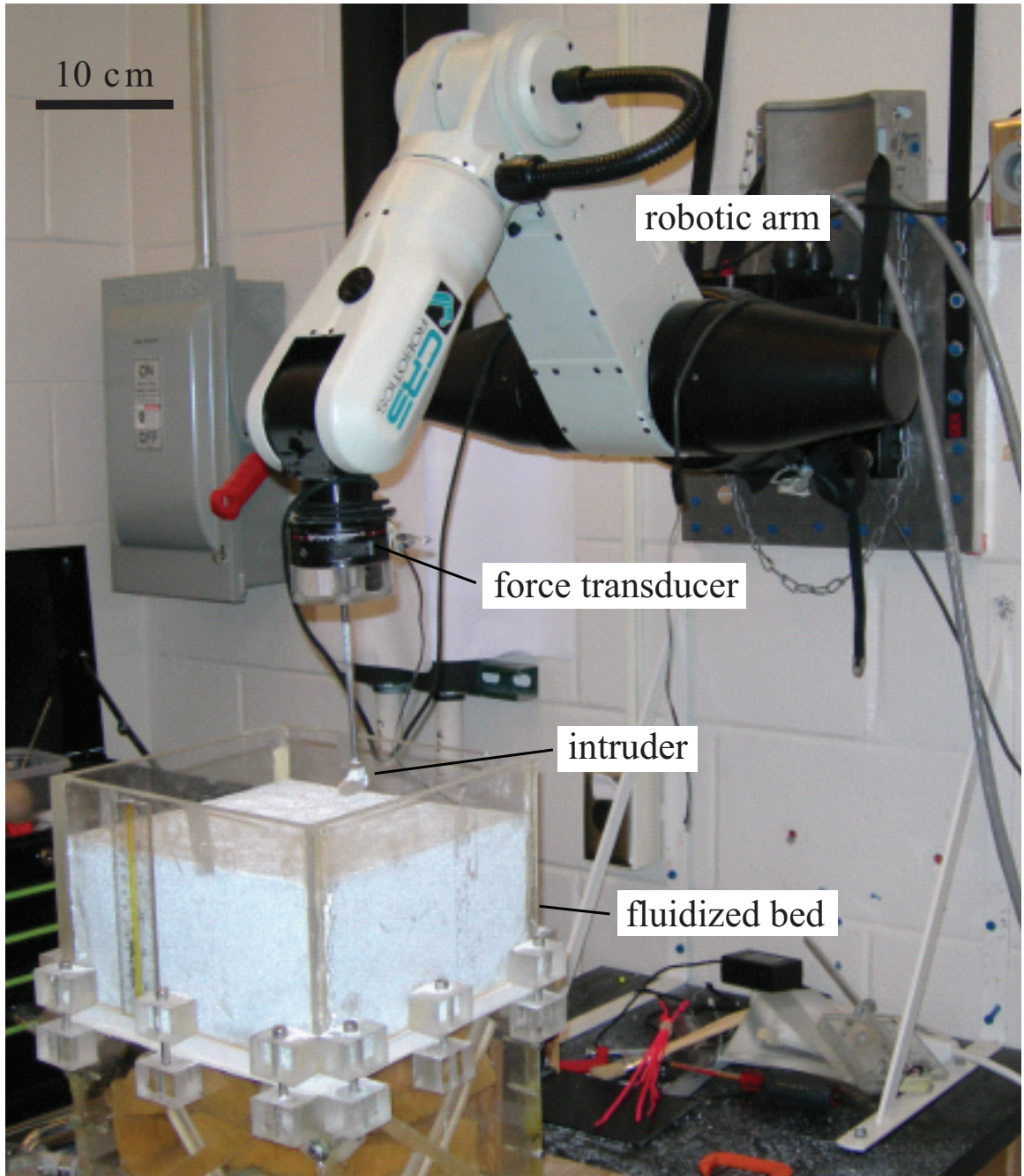


**Figure 29:** A six degree-of-freedom robotic arm (CRS Robotics) for intrusion physics studies. A six-axis force/torque transducer (ATI) is mounted on the last joint and attached to an aluminum rod through a stainless steel support rod. Beneath the robotic arm is a fluidized bed filled with 0.27 mm diameter glass particles. Photo: Daniel I. Goldman.

$\approx 0.05$  N. The range of the transducer is  $\approx 80$  N. A custom made camera tracking system (courtesy of Pushkar Kolhe and Nick Gravish) is dedicated to measure the position of the

robotic arm using an LED light mounted on the distal joint.

### 1.6.5 Field collection of lizards

The zebra-tailed lizards were collected in the field. To spot these lizards, a trained herpetologist's eye (courtesy of Tonia Hsieh) was essential. Two or more people would work better than one person when catching them, as these lizard run extremely fast and would often disappear before a person can approach one closely enough to make the catch. By surrounding and approaching a lizard from several directions slowly, the animal would get confused and usually ran into a bush and stayed put. At this time, one person further approached the lizard tiptoeing, while all kept their eyes on the lizard and be prepared to trace it in case it startled and ran. Within about 5 m from the lizard, the catcher reached a “fishing” pole out slowly, and lowered the tip of the pole with a noose dangling in breeze, trying to position it around the neck of the lizard. At this time, the lizard would usually not know what was going on. Once the noose was around the neck, the catcher quickly raised the pole, and the lizard (or sometimes, a bush branch) would be tied to the noose. With some luck, ten lizards could be caught within a day.

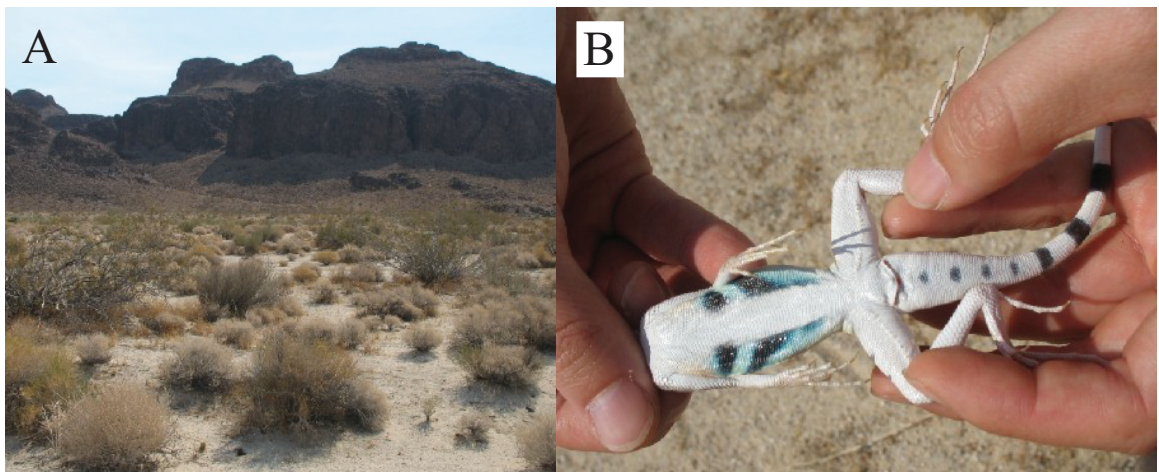


**Figure 30:** Field collection of the zebra-tailed lizards. (A) A site in the Mojave Desert, CA where some of the lizards were collected. (B) A freshly caught lizard with its ventral side shown. Caught by Tonia Hsieh.

## 1.7 *Specific aims*

The overall objective of this dissertation is to discover principles of legged locomotion on granular media. To achieve this goal, we integrate biological, robotic, and physics studies, with specific aims summarized below:

### **Biological studies:**

- Use high-speed imaging to capture three-dimensional kinematics during running of a model organism, the zebra-tailed lizard, on both solid and granular surfaces (**Chapter II**).
- Use high-speed x-ray imaging to capture subsurface kinematics of the lizard's hind foot to reveal foot-ground interaction on granular surface (**Chapter III**).
- Model the foot-ground interaction of the lizard running on both solid and granular surfaces to reveal the functions of the large, elongate hind foot (**Chapters II and III**).

### **Robotic studies:**

- Use high-speed imaging to study how the locomotor performance (speed) of a legged robot, SandBot, depends on the compaction (volume fraction) of granular media and the robot's stride frequency (**Chapter IV**).
- Use high-speed imaging to study how the locomotor performance (speed) of SandBot depends on the intra-cycle limb kinematics, i.e., the relative length and timing of the slow stance and fast swing phases (**Chapter V**).
- Use high-speed imaging to study how the performance (speed and cost of transport) of two small, lightweight, legged robots, RoACH and DASH, depends on the limb frequency and limb morphology (**Chapter VI**).

### Physics studies:

- Use vertical penetration and impact experiments to identify relevant granular forces during running of the zebra-tailed lizard on granular media and reveal and their relative contribution to thrust (**Chapters II and III**).
- Use vertical penetration experiments to measure the granular forces relevant to SandBot's limb-ground interaction, and use these forces with a kinematic model to explain the observations of SandBot's locomotor performance (**Chapters IV and V**).
- Use systematic intrusion experiments and resistive force theory to create models towards a comprehensive theory for granular forces during arbitrary intrusion relevant to legged locomotion on granular media (**Chapter VII**).

## CHAPTER II

### THE EFFECT OF SUBSTRATE ON THE RUNNING MECHANICS OF THE ZEBRA-TAILED LIZARD (*CALLISAURUS DRACONOIDES*)

#### 2.1 Summary

A diversity of animals running on solid, level, flat, non-slip surfaces appear to bounce on their legs; elastic tendons in the limbs can store and return energy during each step. The mechanics of running on natural terrain, particularly surfaces that can yield and flow, is less understood. The zebra-tailed lizard (*Callisaurus draconoides*), a small desert generalist, runs rapidly across substrates ranging from solid to granular surfaces. We use high-speed video to obtain three-dimensional kinematics during running on solid and granular surfaces to reveal how limb, foot, and substrate mechanics contribute to its high locomotor performance. Running at 20 bodylength/s (1.5 m/s), the lizard displays similar gait and center-of-mass kinematics on both substrates, with only 10% reduction in stride length on the granular surface. Based on the anatomy and damping properties of the elongate (40% SVL) hind foot obtained from dissection and resilience measurements respectively, we estimate from kinematics that on the solid surface the tendinous hind foot saves the lizard ( $39 \pm 10$ )% of the total mechanical work per step, a significant portion for its small size. Using measurements and a model of granular penetration force and hypothesized subsurface foot rotation (paddling), we estimate the energy lost on the granular surface due to irreversible deformation of the substrate. The energy lost within the limbs and to the substrate must be compensated by muscle work from the upper hind leg. Our models predict that a large, elongate foot increases elastic energy storage and return on solid surfaces, and reduces energy loss to granular surfaces.\*

---

\*This Chapter is a paper by Chen Li, S. Tonia Hsieh, and Daniel I. Goldman, The Journal of Experimental Biology, in review [85].

## 2.2 Introduction

Rapid locomotion like running and hopping can be modeled as a spring mass system (referred to as a Spring-Loaded Inverted Pendulum, SLIP) [86] bouncing in the sagittal plane. This has been demonstrated in a variety of animals (Holmes et al., 2006) in the laboratory on rigid, level, flat, non-slip surfaces (hereafter referred to as “solid surfaces”) such as running tracks and treadmills [1, 2]. In the SLIP model, the animal body (represented by the center of mass, CoM) bounces like a pogo stick on the leg (represented by a spring) which exerts point contact on the solid ground. The CoM compresses the leg spring during the first half of stance, and the leg spring recoils during the second half of stance. Through this process, the mechanical energy of the CoM (kinetic plus gravitational potential energy) is interchanged with elastic energy stored in the compressed leg spring, saving energy during each step. For animals like insects (e.g., [87]) and reptiles (e.g., [88]) that run with a sprawled limb posture, the CoM also oscillates substantially in the horizontal plane in a similar fashion, as described by the Lateral Leg Spring (LLS) model [89, 90].

In these models, the spring-mass system and the interaction with the solid ground are perfectly elastic and do not dissipate energy; thus no net work is performed. However, in the natural world, as animals move across complex surfaces, energy is dissipated both within the body and limbs [32] and to the environment [1]. Thus mechanisms to minimize energy loss during locomotion can be important. The limbs of many organisms possess elastic elements such as tendons and ligaments (most notably, the ankle extensor tendons in the lower leg) that can function as springs during rapid locomotion to save energy [33]. Furthermore, different limb-ground interaction strategies may be utilized depending on the dissipative properties of the substrate to minimize energy loss.

Recent laboratory experiments have begun to reveal the mechanisms of running on non-solid surfaces, including surfaces that are elastic [7, 8], damped [9], inclined [5], or uneven [3, 4]; surfaces with few footholds [6]; and the surface of water [19, 20]. While spring-mass-like CoM motion is observed only in some of these studies [7, 9, 8], a common finding is that on non-solid surfaces animal’s limbs do not necessarily behave like springs to save energy. In addition, these studies suggest that both the active control of body and

limb movement through the animal's neural system, and the passive mechanical responses of the animal's viscoelastic limbs and feet with the environment, play important roles in the control of rapid terrestrial locomotion (for reviews, see [16, 2, 37]).

Many surfaces found in nature, such as sand, gravel, rubble, dirt, soil, mud, and debris, can yield and flow during footsteps and go through solid-fluid transitions [10], during which energy may be dissipated through plastic deformation [91, 10]. Understanding locomotion on such yielding surfaces is challenging because, unlike for flying and swimming where the flows and forces in fluids can in principle be determined by the Navier-Stokes equations [21], no comprehensive theory yet exists for terrestrial environments that yield and flow. Granular materials like sand provide a good model substrate for studying locomotion on yielding surfaces. Compared to other yielding substrates, granular materials are relatively simple and the intrusion forces within them can be measured empirically [70]. Their mechanical properties can also be readily and repeatedly controlled using a fluidized bed [92]. In addition, locomotion on granular surfaces is directly relevant for many desert-dwelling reptiles and arthropods such as lizards, snakes, insects, etc. [27, 28, 29, 30, 31], which must contend with sand and gravel on a daily basis. Recent advances in the understanding of force and flow laws in granular materials subject to localized intrusion [70, 61, 72, 73, 93, 94] begin to provide insight into the mechanics of locomotion on (and within) granular substrates [92, 95, 96, 97, 94].

The zebra-tailed lizard (*Callisaurus draconoides*, SVL  $\sim 10$  cm, mass  $\sim 10$  g, Fig. 31) provides an excellent model animal for studying the mechanics of running on natural surfaces, because of its high locomotor performance over diverse terrain. It is the fastest running lizard among desert lizards of similar size [38]. As a desert generalist, this lizard lives in a large range of desert habitats including flat land, washes, and sand dunes [39, 40], and encounters a great variety of substrates ranging from rocks, gravel, closely-packed coarse sand, and loosely-packed fine sand [41, 40]. Although these substrates transition from solid surfaces to surfaces that yield and flow during footsteps, the zebra-tailed lizard can achieve high running speeds of up to  $\sim 4$  m/s ( $\sim 50$  bl/s) both on solid (treadmill [38]) and on granular (in the wild [42]) surfaces. It was also observed in the field that the zebra-tailed

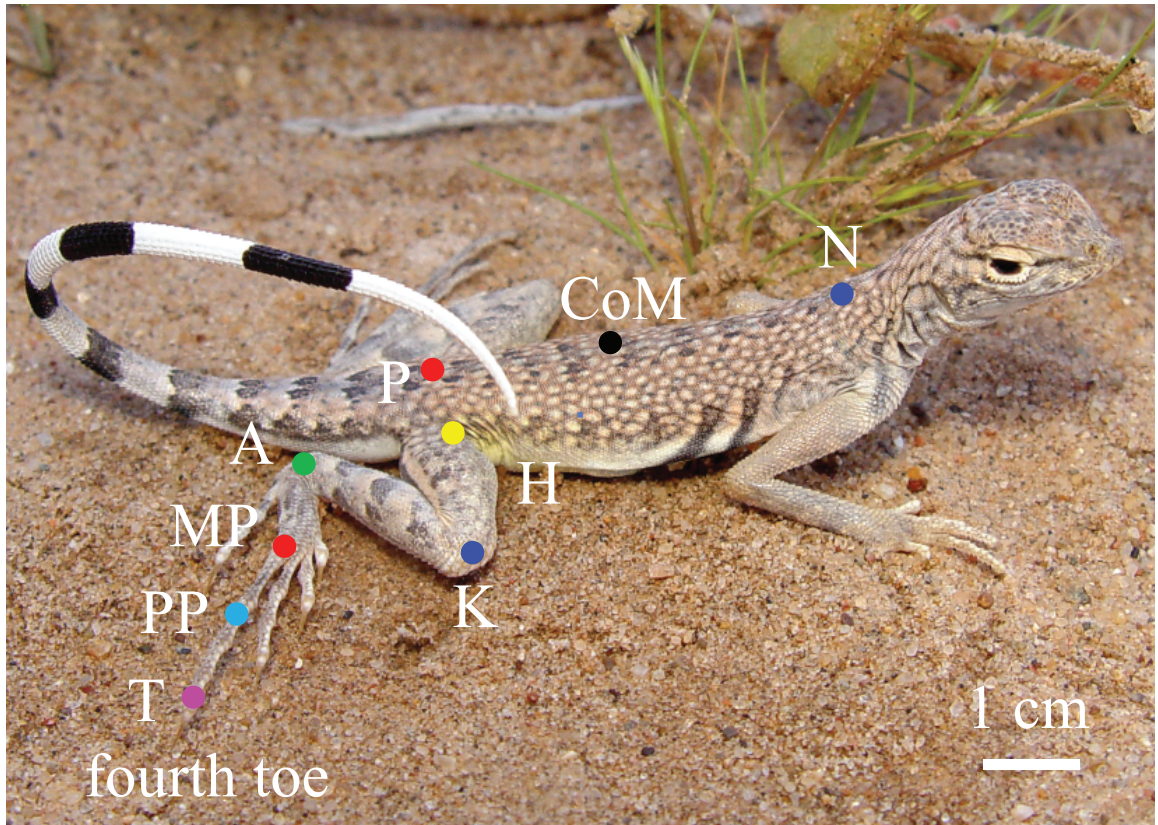


**Figure 31:** A zebra-tailed lizard resting on sand in the wild. Colored circles show digitized points on the midline of the trunk, hind leg, and elongate hind foot. Photo courtesy of Thomas C. Brennan.

lizard’s maximal acceleration and running speed do not differ significantly when substrate changes from coarse wash sand to fine dune sand [40].

Of particular interest is whether and how the zebra-tailed lizard’s large, elongate hind foot contributes to its high locomotor capacity. In addition to a slim body, a long, tapering tail, and slender legs (Fig. 31), the zebra-tailed lizard has an extremely large, elongate hind foot, the largest (40% SVL) among lizards of similar size [38]. Recent studies in insects, spiders, and geckos [44, 45, 46, 6] suggested that animals largely rely on appropriate morphology and material properties of their bodies and limbs to accommodate variable, uncertain conditions during locomotion. Despite proposals that the large foot area [27] and increased stride length via elongate toes may confer locomotor advantages [38], the mechanisms of how the large, elongate hind foot contributes to the zebra-tailed lizard’s

high running capacity remain to be uncovered.

In this study, we investigate the running mechanics of the zebra-tailed lizard on two well-defined surfaces, a solid and a granular surface. These two surfaces lie on opposite ends of the spectrum of substrates that the zebra-tailed lizard encounters in its natural environment, and present distinct conditions for locomotion. For example, previous studies found higher energy cost for locomotion on granular surfaces than on solid surfaces [17, 18, 98], and performance loss (via stride length reduction at a given stride frequency) with reduced substrate compaction on granular surfaces [92].

We use high-speed video to capture three-dimensional kinematics of the lizard running on both solid and granular surfaces, and observe the motion of its body and leg, and particularly, the foot-ground interaction during running. We focus on the hind foot because it is larger than the fore foot (area  $\approx 1 \text{ cm}^2$  vs.  $\approx 0.3 \text{ cm}^2$ ) and likely plays a dominant role for locomotion [27]. We perform dissection and resilience measurements to characterize the anatomy and damping properties of the hind foot, respectively. For running on the solid surface, we estimate the energy storage and return in the hind foot using the observed kinematics and a model of the hind foot. For running on the granular surface, we present an explanation of the observed kinematics using measurements and a model of granular penetration force [72, 92], and estimate the amount of energy lost to the substrate. With the proposed models of foot-ground interaction, we discuss possible advantages of a large, elongate foot for running on both solid and granular surfaces.

## **2.3 Materials and methods**

### **2.3.1 Animals**

We collected seven adult zebra-tailed lizards (*Callisaurus draconoides*) from the Mojave Desert, AZ, USA in 08/2007 (Permit SP591773) for three-dimensional kinematics experiments. Eleven additional adult animals were collected from the Mojave Desert, CA, USA in 09/2009 (Permit SC 10901) for hind foot resilience measurements. Two preserved specimens were used for dissection. The animals were housed in the Physiological Research Laboratory animal facility of The Georgia Institute of Technology. Each animal was housed individually in an aquarium, and fed live crickets and mealworms dusted with vitamin and calcium supplement two to three times a week. The housing room was maintained at 28°C during the day and 24°C during the night. Full-spectrum fluorescent bulbs high in UVB were set to a 12 hour/12 hour light/dark schedule. Ceramic heating elements were provided 24 hours a day to allow the animals to thermo-regulate at preferred body temperature. All experimental procedures were conducted in accordance with The Georgia Institute of Technology IACUC protocols.

### **2.3.2 Surface treatments**

A wood board ( $120 \times 23 \times 1 \text{ cm}^3$ ) covered with sandpaper (grit size  $\sim 0.1 \text{ mm}$ ) for enhanced traction was used as the solid surface. Glass particles (diameter =  $0.27 \pm 0.04 \text{ mm}$  (mean  $\pm 1 \text{ s.d.}$ ), density =  $2.5 \times 10^3 \text{ kg/m}^3$ , Jaygo Incorporated, Union, NJ, USA) were used as the granular substrate, which are of similar size to typical desert sand [76] and are approximately spherical. Before each trial, a fluidized bed trackway (200 cm long, 50 cm wide) prepared the granular substrate (12 cm deep) into a loosely packed state (volume fraction  $\phi = 0.58$ ) for repeatable yielding strength (for details, see [92]).

### **2.3.3 Three-dimensional kinematics**

We used high-speed video to obtain three-dimensional kinematics as the lizard ran across the prepared surface (Fig. 32). Before each session, high-contrast markers (Wite-Out, Garden Grove, CA, USA) were painted on each animal for digitizing at nine joints along the midline

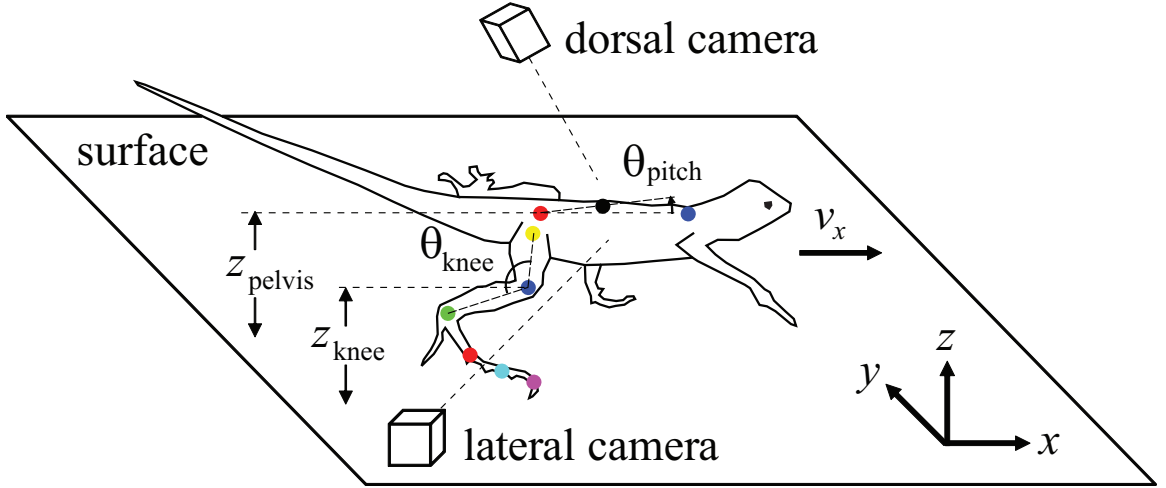


**Figure 32:** Experimental setup for three-dimensional kinematics capture. The diagram shows definitions of kinematic variables including pelvis height ( $z_{pelvis}$ ), knee height ( $z_{knee}$ ), pitch angle of the trunk ( $\theta_{pitch}$ ), and knee angle ( $\theta_{knee}$ ). Colored circles correspond with those in Fig. 31.

of the trunk and the right hind limb (Fig. 31, Fig. 32): neck (N), center of mass (CoM), pelvis (P), hip (H), knee (K), ankle (A); and the metatarsal-phalangeal joint (MP), distal end of the proximal phalanx (PP), and digit tip (T) of the fourth toe. The approximate longitudinal location of the CoM in resting position was determined by tying a thread around the body of an anesthetized lizard and repositioning the thread until the body balanced horizontally. Before each trial, the surface was prepared (for the granular surface treatment only), and calibration images were taken of a custom 39-point calibration object. The animal was then induced to run across the surface by a slight tap or pinch on the tail. Two synchronized high-speed cameras (AOS Technologies, Baden Daettwil, Switzerland) captured simultaneous dorsal and lateral views at 500 frame/s with 300  $\mu s$  shutter time. The ambient temperature was 35°C during the test. Animals were permitted to rest at least five minutes between trials and at least two days between sessions.

#### 2.3.4 Hind limb dissection and hind foot resilience measurements

To aid understanding of the anatomy of the hind limb, the hind limbs of two preserved specimens were dissected, focusing on muscle and tendon arrangements within the lower leg and the foot. To characterize the resilience of the hind foot, a modification of the

work loop technique [99] (Fig. 33) was used, in which the animal is anesthetized (using 2% isoflurane air solution), the limb is kept intact, and forces are applied to the limb instead of a single muscle [100]. The hind foot was pushed down (loading) and then retracted (unloading) on a custom small force platform [101, 102] ( $10.2 \times 7.6 \text{ cm}^2$ , range = 2.5 N, resolution = 0.005 N) bonded with sandpaper (grit size  $\sim 0.1 \text{ mm}$ ), and ground reaction force was measured at 10 kHz sampling rate using a custom LabVIEW program (National Instruments, Austin, TX, USA). A high-speed camera (Vision Research, Wayne, NJ, USA) simultaneously recorded angular displacement of the foot from the side view at 250 frame/s with  $500 \mu\text{s}$  shutter time. High-contrast markers (Wite-Out, Garden Grove, CA, USA) were painted on the joints of the foot (A, MP, PP, T, and a point on the tibia above the ankle). The ambient temperature was  $35^\circ\text{C}$  during the test.

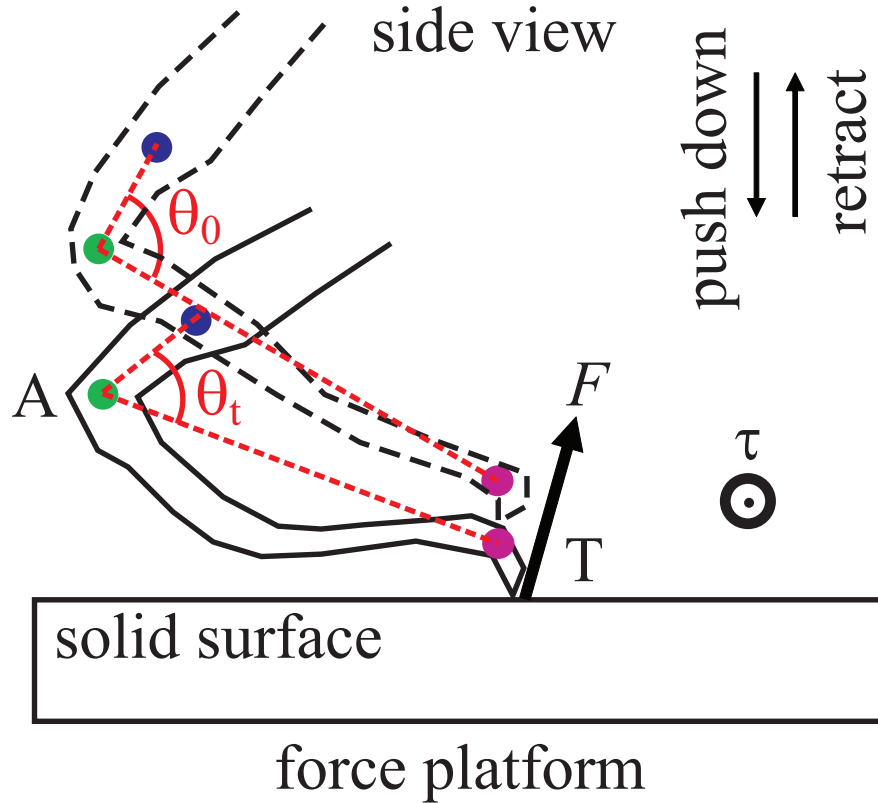


**Figure 33:** Experimental setup for hind foot resilience measurements. Dashed foot tracing indicates the relaxed, straight foot right before touchdown. Solid foot tracing indicates the hyperextended foot during ground contact. The diagram shows angular displacement  $\Delta\theta = \theta_0 - \theta_t$  and the ground reaction force  $F$ . Torque  $\kappa$  about the ankle is measured at the digit tip and is directed out of the plane.

### 2.3.5 Data analysis

We used direct linear transformation (DLT) to reconstruct three-dimensional kinematics from the two-dimensional dorsal and lateral videos by custom software (DLTcal3 and DLTdv3 [83]). The calibration images and two-dimensional point coordinates were digitized and converted to three-dimensional coordinates with DLT. Axes were set according to the right-hand rule such that  $+x$  pointed in the direction of forward motion,  $+z$  pointed vertically upward, and  $y$  was in the medio-lateral direction. Footfall patterns of touchdown (TD) and takeoff (TO) were determined from the videos. On the granular surface, takeoff is determined as when the foot begins moving upward (because a granular substrate exerts little force on the foot during upward retraction, see discussion and Fig. 2 for details). To reduce noise from enable comparisons among different running trials, position data were butterworth-filtered with a low pass cutoff frequency of 75 Hz and scaled to one full stride period  $T$  between two successive touchdowns of the right hind limb, and used to calculate kinematic variables.

Video data from the modified work loop experiments were digitized to obtain angular displacement (measured at the digit tip of the fourth toe) of the foot about the ankle relative to the tibia. Angular displacement was synchronized with the torque about the ankle calculated from the measured ground reaction force to obtain a work loop. The damping ratio (i.e., energy loss ratio) of the hind foot was calculated as the fraction of area within a work loop relative to the area under the higher loading curve [32]. Hind foot resilience (i.e., the percentage of energy returned by the foot after loading and unloading) was one minus the damping ratio [103, 46]. All data analysis was conducted using MATLAB (MathWorks, Natick, MA, USA). Means are reported as mean  $\pm$ 1 s.d. unless otherwise specified.

### 2.3.6 Statistics

To distinguish the effect of different surfaces on running mechanics, we chose a small control group of runs from animals of similar size ( $< 10\%$  variation in SVL) running at similar speeds (mean  $\pm$ 1 s.d.:  $1.5 \pm 0.3$  m/s). In addition, we only included runs that met the following criteria: the animal ran continuously through the field of view, the run was straight

without contacting sidewalls of the trackway, there was a full stride (between two consecutive touchdowns) of the marked right side hind limb in the range of view, all the nine markers were visible throughout the full stride, and the forward speed did not change more than 10% after the full stride.

With these criteria, out of the total of 142 runs collected from seven individuals on both solid and granular surfaces over a period of over three months, we ultimately accepted thirteen runs from four individuals for analyses. These include seven runs from three individuals on the solid surface ( $N = 3$  individuals,  $n = 7$  runs), and six runs from three individuals on the granular surface ( $N = 3$  individuals,  $n = 6$  runs). As a result of using such stringent criteria for selecting our trials, the analyzed trials are representative of unperturbed, constant cycle-averaged speed runs on solid and granular media.

An ANOVA showed no significant effect of individual on measured variables ( $P > 0.05$ , ANOVA). As a result we pooled all data and tested for statistical differences between solid and granular surfaces using a non-parametric Mann-Whitney U test. To determine which variables were responsible for the greatest variance in the data, we ran a principal component analysis (PCA). All principal components (PC) with an eigenvalue greater than unity were investigated further for differences between substrates using a one-way, fixed factor ANOVA. All statistical tests were performed using JMP 8 (JMP, Cary, NC, USA).

### **2.3.7 Granular penetration force measurements**

To aid modeling of the force on a lizard foot during running on the granular surface, we measure the vertical ground reaction force on a plate penetrating vertically into the granular substrate. Figure 8A shows the experimental setup. Before each trial a fluidized bed prepared  $0.27 \pm 0.4$  mm diameter glass particles into a loosely packed state (volume fraction = 0.58) (for details, see [95]). A robotic arm (CRS robotics, Burlington, OT, Canada) pushed an aluminum plate (oriented horizontally) vertically downward into the glass particles to a depth of 7.6 cm at 1 cm/s, paused for 15 s, and then extracted the plate upward along the same path at 1 cm/s. The ground reaction force on the plate was measured

by a force transducer (ATI Industrial Automation, Apex, NC, USA) using a custom LabVIEW program (National Instruments, Austin, TX, USA). The depth of the plate was measured by tracking the position of an LED light marker on the robotic arm from videos (Edmund Optics, Barrington, NJ, USA). Two thin Aluminum plates of different area were used ( $A_1 = 7.6 \times 2.5 \text{ cm}^2$  and  $A_2 = 3.8 \times 2.5 \text{ cm}^2$ ; thickness is 0.6 cm for both plates). Three trials were performed for each of the two plates and force was averaged from the three trials.

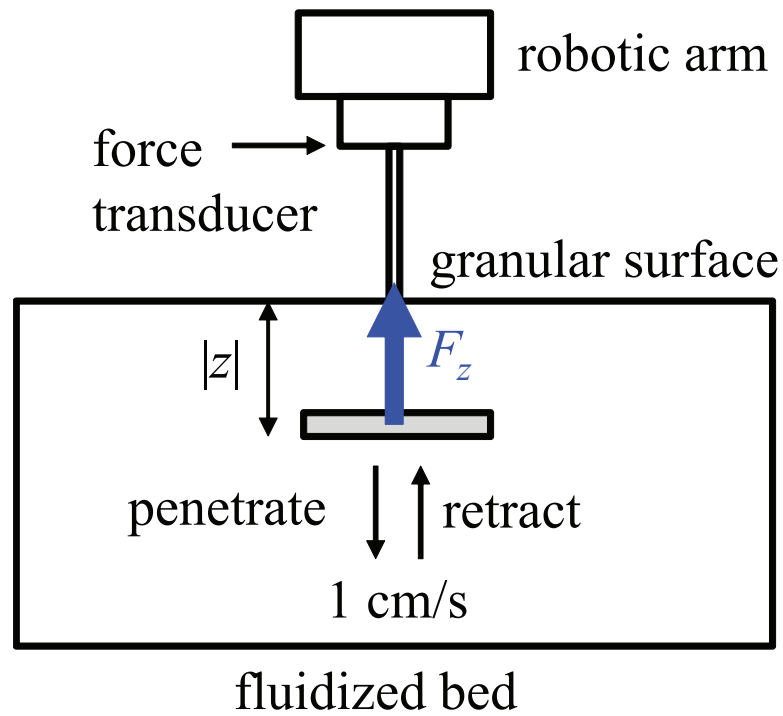


**Figure 34:** Experimental setup for granular penetration force measurements. A fluidized bed prepared the glass particles into loosely packed state, and a robotic arm penetrated a plate into the medium and retracted it, during which force was measured as a function of depth.

## 2.4 Results

### 2.4.1 Morphology

Table 1 presents morphological measurements of the four individuals reported. The hind foot comprised 38% of the hind limb length, and the longest fourth toe alone accounted for 62% of the hind foot length. These ratios are in similar range as previously found in [38]. The foot was slender with a cross-sectional radius of  $r \approx 0.50 - 1.25$  mm tapering distally (joint radii:  $r_K = r_A \approx 1.25$  mm,  $r_{MP} \approx 0.75$  mm,  $r_{PP} = r_T \approx 0.50$  mm).

**Table 1:** Morphological measurements of the four individuals reported. Values are mean  $\pm 1$  s.d.

|                                     |               |
|-------------------------------------|---------------|
| Body length SVL (cm)                | $6.8 \pm 0.3$ |
| Mass $m$ (g)                        | $9.3 \pm 2.0$ |
| Trunk length (cm)                   | $4.1 \pm 0.2$ |
| Pelvic width (cm)                   | $1.3 \pm 0.1$ |
| Hind limb length (cm)               | $5.9 \pm 0.3$ |
| Hind foot length (cm)               | $2.6 \pm 0.2$ |
| Femur length (cm)                   | $1.4 \pm 0.1$ |
| Tibia length (cm)                   | $1.9 \pm 0.1$ |
| Tarsals and metatarsals length (cm) | $1.0 \pm 0.1$ |
| Fourth toe length (cm)              | $1.6 \pm 0.2$ |

Unlike many cursorial mammals in which long tendons of the ankle extensor muscles reside in the lower leg [1], dissection of the zebra-tailed lizard’s hind limb (Fig. 35)<sup>†</sup> revealed that in its lower leg, ankle extensor tendons are nearly non-existent. Instead, layers of elongate tendons are found in both the dorsal and ventral surfaces of the foot. Our anatomical description is therefore focused on the ventral muscle and tendon anatomy in the hind limb. Terms given to muscles and tendons follow [104]. A large, tendinous sheath, the superficial femoral aponeurosis, originates from the femoro-tibial gastrocnemius, stretches across the ventral surface of the foot, and inserts on the metatarsal-phalangeal joints for digits III and IV. The superficial portion of the femoro-tibial gastrocnemius muscle body extends to the base of the ankle, thereby rendering the human equivalent of the ankle extensor tendons (i.e., the “Achilles” tendon) absent. Deep to the superficial femoral aponeurosis lie the

---

<sup>†</sup>This dissection was performed by S. Tonia Hsieh.

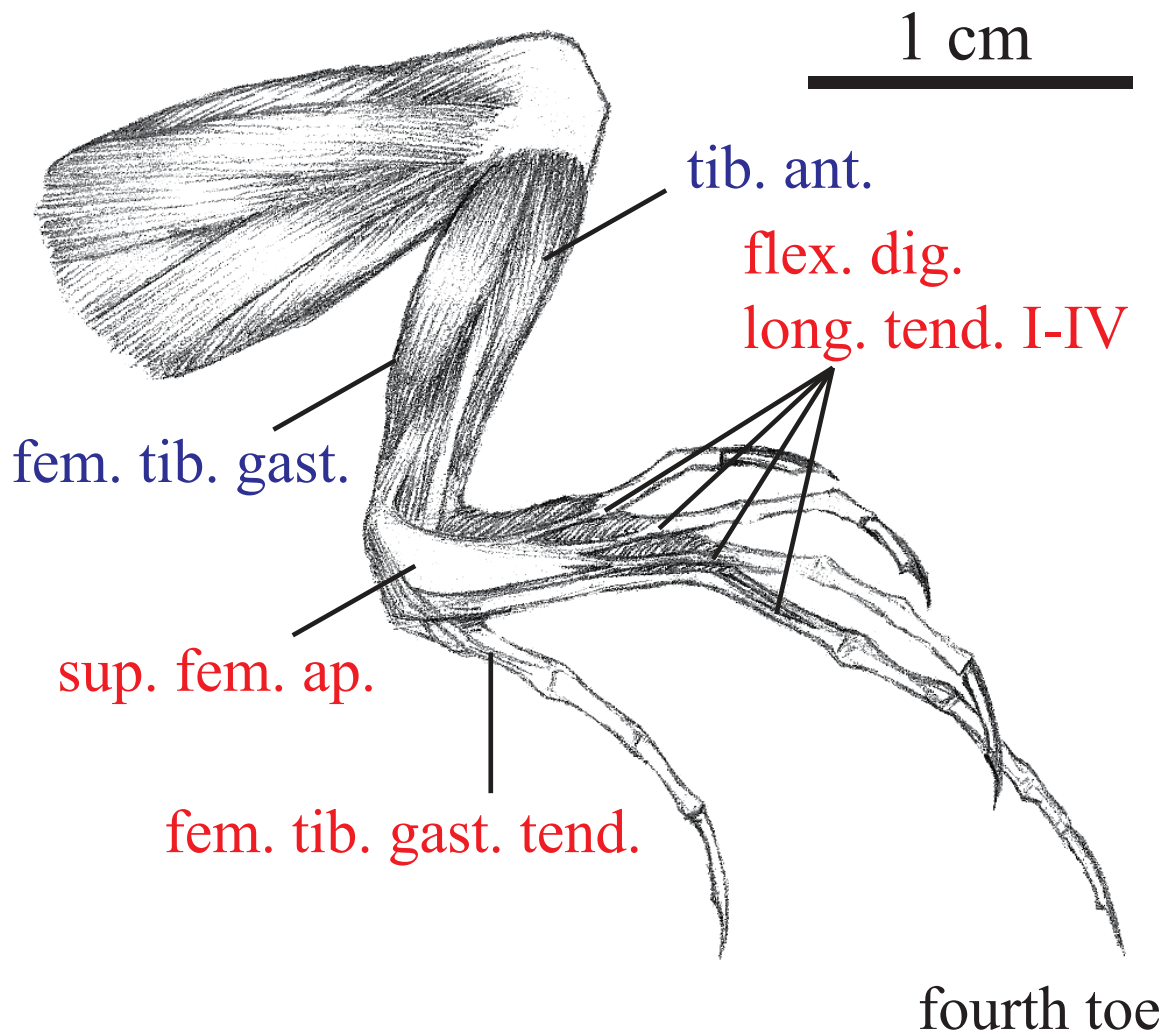


**Figure 35:** Ventral anatomy of a dissected hind limb. Lower hind leg muscles are indicated in blue; foot tendons are indicated in red.

flexor digitorum brevis muscles (not shown) which control the flexion of each of the digits. Tendons from the flexor digitorum longus muscle located on the lower hind leg run deep to the flexor digitorum brevis muscle bodies, and extend to the tips of the digits. No additional tendons are visible deep to the flexor digitorum longus tendons.

#### 2.4.2 Gait and center of mass kinematics

Table 2 compares the gait and center of mass kinematics measurements between solid and granular surfaces. On both solid ( $N = 3$  individuals,  $n = 7$  runs) and granular ( $N = 3$  individuals,  $n = 6$  runs) surfaces, the zebra-tailed lizard ran with a diagonal gait, a sprawled

limb posture, and lateral trunk bending (see Fig. 38). During steady-speed running at average forward speed  $\bar{v}_{x,CoM}$  of approximately 1.5 m/s (Fig. 36A), the lizard ran with similar stride frequency  $f$  of approximately 9 Hz (Fig. 36B) and duty factor  $D$  of approximately 0.4 (Fig. 36C) on both surfaces, with an aerial phase of approximately 10% stride period  $T$  between alternating stances (Fig. 37A). Calculated stride length  $\lambda$  was 11% longer ( $P < 0.05$ , ANOVA) on the solid surface than on the granular surface (Fig. 36D).

On both surfaces, the center of mass (CoM) oscillated vertically at twice the stride frequency (Fig. 37C). The CoM fell during the first half of a stance, reaching the lowest position at mid-stance, and then rose during the second half of a stance, reaching the highest position during the aerial phase (Fig. 37C, black dashed curve). The CoM also oscillated medio-laterally at the stride frequency (Fig. 37D). In frequency (Fig. 37D). In addition, on the solid surface, the CoM forward speed  $v_{x,CoM}$  (Fig. 37B, red curve) showed a modest trend (Fig. 37B, black dashed curve) to decrease during the first of stance and then increase during the second half of stance. This trend was not observed on the granular surface (Fig. 37B, blue curve).

**Table 2:** Gait and CoM kinematic variables. All values on solid and granular surfaces are presented as mean  $\pm$  1 s.d. All significant differences ( $\alpha = 0.05$ ) are in bold.

| Variable                                    | Solid           | Granular        | $\chi^2$ | $P$           |
|---|-----------------|-----------------|----------|---------------|
| Forward speed $v_{x,CoM}$ (m/s)             | 1.5 $\pm$ 0.2   | 1.4 $\pm$ 0.3   | 1.3061   | 0.2531        |
| Stride frequency $f$ (Hz)                   | 9.0 $\pm$ 1.3   | 9.3 $\pm$ 1.8   | 0.0460   | 0.8301        |
| Duty factor $D$ (Hz)                        | 0.42 $\pm$ 0.06 | 0.37 $\pm$ 0.04 | 2.7064   | 0.0999        |
| Stride length ( $\lambda$ ) (m)             | 0.17 $\pm$ 0.01 | 0.15 $\pm$ 0.01 | 4.0000   | <b>0.0455</b> |
| Average CoM height $\bar{z}_{CoM}$ (cm)     | 2.7 $\pm$ 0.3   | 2.6 $\pm$ 0.3   | 0.0204   | 0.8864        |
| Lowest CoM height $z_{CoM}$ (cm)            | 2.5 $\pm$ 0.4   | 2.5 $\pm$ 0.4   | 0.0204   | 0.8864        |
| Time of lowest CoM height ( $T$ )           | 0.18 $\pm$ 0.03 | 0.20 $\pm$ 0.04 | 0.8942   | 0.3443        |
| Highest CoM height $z_{CoM}$ (cm)           | 2.8 $\pm$ 0.3   | 2.8 $\pm$ 0.3   | 0.0204   | 0.8864        |
| Time of highest CoM height ( $T$ )          | 0.44 $\pm$ 0.06 | 0.47 $\pm$ 0.03 | 0.4237   | 0.5151        |
| CoM lateral excursion $\Delta y_{CoM}$ (cm) | 0.73 $\pm$ 0.17 | 0.84 $\pm$ 0.16 | 0.7347   | 0.3914        |

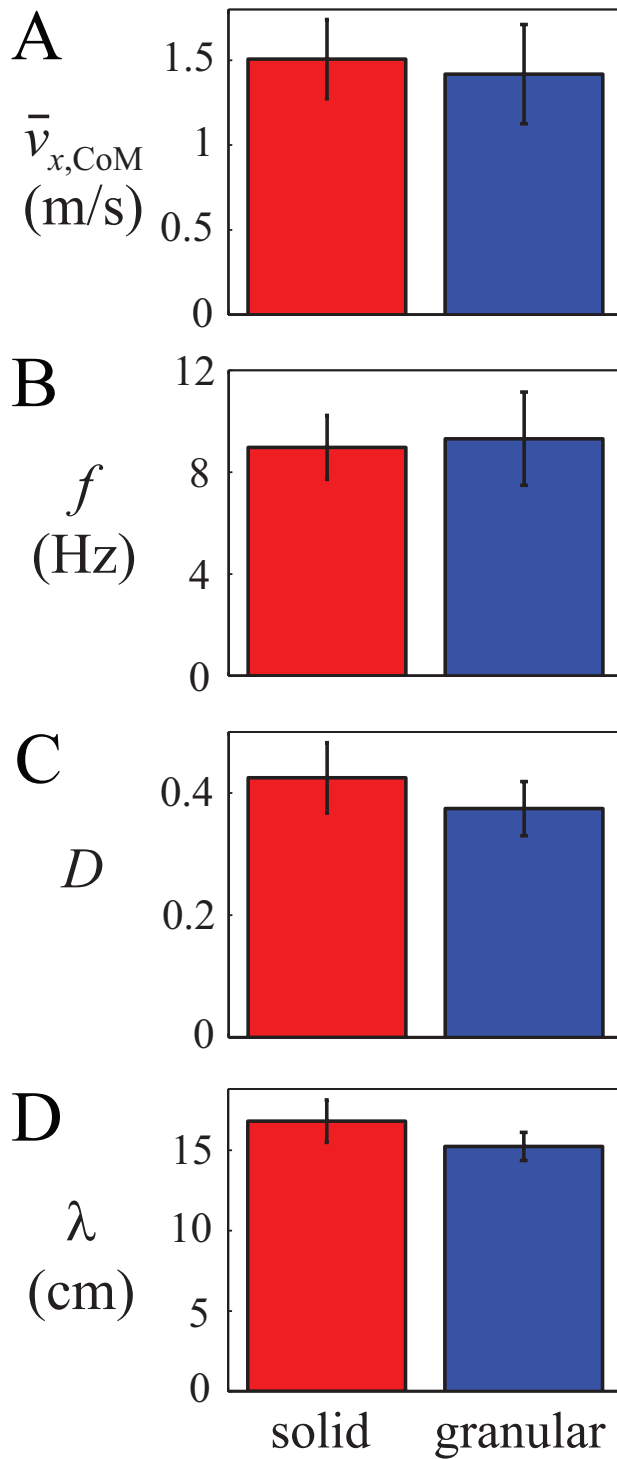


**Figure 36:** Gait parameters. While running at similar (A) average forward speeds of  $\approx 1.5$  m/s, the zebra-tailed lizard displayed similar (B) stride frequency, and (C) duty factor on the solid (red) and the granular (blue) surfaces. (D) Stride length is slightly larger on the solid substrate ( $P < 0.05$ , ANOVA). Error bars and shaded areas denote  $\pm 1$  s.d.

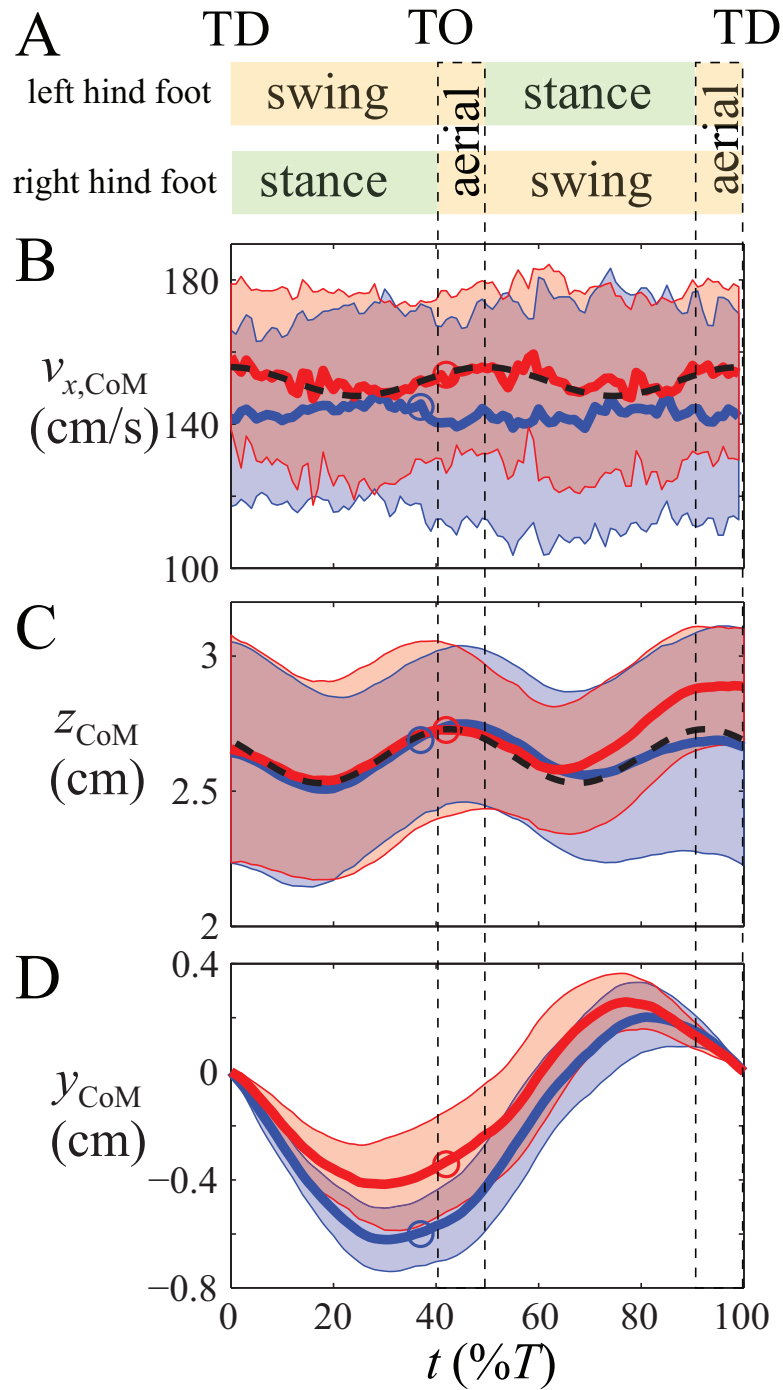


**Figure 37:** Center of mass kinematics. While running at similar (B) forward speeds of  $\approx 1.5$  m/s, the zebra-tailed lizard displayed similar CoM kinematics on the solid (red) and the granular (blue) surfaces including (A) diagonal gait, (C) CoM vertical oscillation, and (D) CoM lateral oscillation. Black dashed curves in (B,C) are sinusoidal patterns expected from the spring-mass SLIP model drawn to guide the eye. Circles in (B-D) indicate takeoff. Error bars and shaded areas denote  $\pm 1$  s.d. TD and TO indicate touchdown and takeoff.

### 2.4.3 Trunk and hind leg kinematics

**Table 3:** Trunk, hind leg, and hind foot kinematic variables. All values on solid and granular surfaces are presented as mean  $\pm$ 1 s.d. All significant differences ( $\alpha = 0.05$ ) are in bold. A direct comparison was not possible between substrates for the leg sprawl angle because it was measured differently between the solid surface (leg orientation measured from the hip to the digit tip) and the granular surface (leg orientation measured from the hip to the ankle).

| Variable  | Solid         | Granular      | $\chi^2$ | $P$           |
|---|---------------|---------------|----------|---------------|
| Average pelvis height $\bar{z}_{pelvis}$ (cm)                               | $2.7 \pm 0.4$ | $2.3 \pm 0.3$ | 5.2245   | <b>0.0223</b> |
| Average pitch angle of the trunk $\theta_{pitch}$ ( $^\circ$ )              | $1 \pm 4$     | $11 \pm 5$    | 9.0000   | <b>0.0027</b> |
| Touchdown knee height $z_{knee}$ (cm)                                       | $2.3 \pm 0.4$ | $2.1 \pm 0.4$ | 0.5102   | 0.4751        |
| Lowest knee height $z_{knee}$ (cm)  | $1.6 \pm 0.3$ | $1.0 \pm 0.2$ | 8.1633   | <b>0.0043</b> |
| Knee vertical displacement during stance $\Delta z_{knee}$ (cm)             | $0.7 \pm 0.5$ | $1.1 \pm 0.4$ | 4.5918   | <b>0.0321</b> |
| Touchdown knee angle $\theta_{knee}$ ( $^\circ$ )                           | $88 \pm 14$   | $98 \pm 13$   | 1.0000   | 0.3173        |
| Largest knee angle $\theta_{knee}$ ( $^\circ$ )                             | $115 \pm 15$  | $156 \pm 3$   | 9.0000   | <b>0.0027</b> |
| Knee joint extension during stance $\Delta\theta_{knee}$ ( $^\circ$ )       | $27 \pm 21$   | $58 \pm 14$   | 5.8980   | <b>0.0152</b> |
| Average leg sprawl angle during stance $\bar{\theta}_{sprawl}$ ( $^\circ$ ) | $46 \pm 2$    | $37 \pm 4$    | N/A      | N/A           |
| Foot angle at touchdown $\theta_{TD}$ ( $^\circ$ )                          | $14 \pm 5$    | $5 \pm 3$     | 8.1633   | <b>0.0043</b> |

Despite similar gait and CoM kinematics, the lizard’s trunk and hind leg kinematics showed differences between the solid and the granular surfaces (Figs. 38, 39). Table 3 summarizes the kinematic variables of the trunk, hind leg, and hind foot. On the solid surface, the trunk assumed a nearly horizontal posture (Fig. 38A-D, dashed line), with average pitch angle of the trunk  $\bar{\theta}_{pitch} \approx 0^\circ$  (Fig. 39A, red). As a result, the average pelvis height  $\bar{z}_{pelvis}$  (Fig. 39B, red) was similar ( $P > 0.05$ , ANOVA) to the average CoM height  $\bar{z}_{CoM}$  (Fig. 37C, red). In contrast, on the granular surface, the trunk was pitched head-up (Fig. 38E-H, dashed line), with  $\bar{\theta}_{pitch} \approx 10^\circ$  (Fig. 39A, blue), and thus  $\bar{z}_{pelvis}$  (Fig. 39B, blue) was 15% lower ( $P < 0.05$ , ANOVA) than  $\bar{z}_{CoM}$  (C, blue). The tail was also often higher away from the surface during running on the solid surface (Fig. 38A-D) the granular surface (Fig. 38E-H).

The hind leg extended by a larger amount during stance on the granular surface. At touchdown, the knee height  $z_{knee}$  (Fig. 39B) and knee angle  $\theta_{knee}$  (Fig. 39D) were not significantly different ( $P > 0.05$ , ANOVA) between solid and granular surfaces. However, at mid-stance,  $z_{knee}$  was significantly lower on the granular surface ( $P < 0.05$ , ANOVA),

and at takeoff,  $\theta_{knee}$  was significantly larger on the granular surface ( $P < 0.05$ , ANOVA). As a result, the vertical displacement of the knee during stance  $\Delta z_{knee}$ , and the total extension of the knee joint during stance  $\Delta\theta_{knee}$ , were significantly larger on the granular surface ( $P < 0.05$ , ANOVA). The sprawl angle of the hind leg  $\theta_{sprawl}$  (defined as the angle between the horizontal plane and the leg orientation in the posterior view) also differed between surfaces ( $P < 0.05$ , ANOVA).

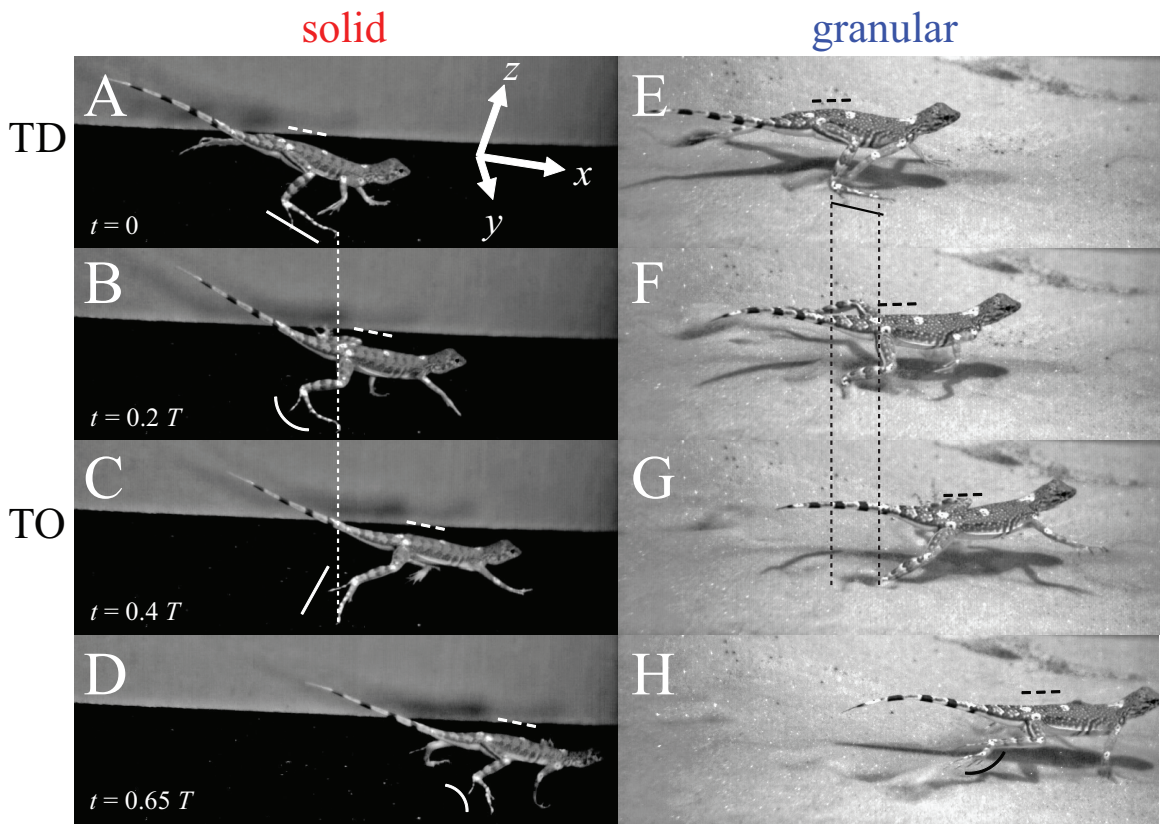


**Figure 38:** Lateral views of representative runs on solid and granular surfaces. (A-D) are on the solid surface and (E-H) are on granular surface. Both runs are shown at  $t = 0, 0.2T, 0.4T$ , and  $0.65T$ . Dashed lines in (A-D) and (E-H) indicate trunk posture. Solid lines/curves in (A-D) and (E) indicate the hind foot posture and shape. Vertical dotted lines in (A-C) and (E-G) indicate foot displacement during stance on the on the solid (measured at the digit tip) and the granular (measured at the ankle) surfaces. Note that the lateral camera was oriented at an angle to the  $x, y, z$  axes such that forward ( $+x$ ) direction appeared to point slightly downwards. TD and TO indicate touchdown and takoff.

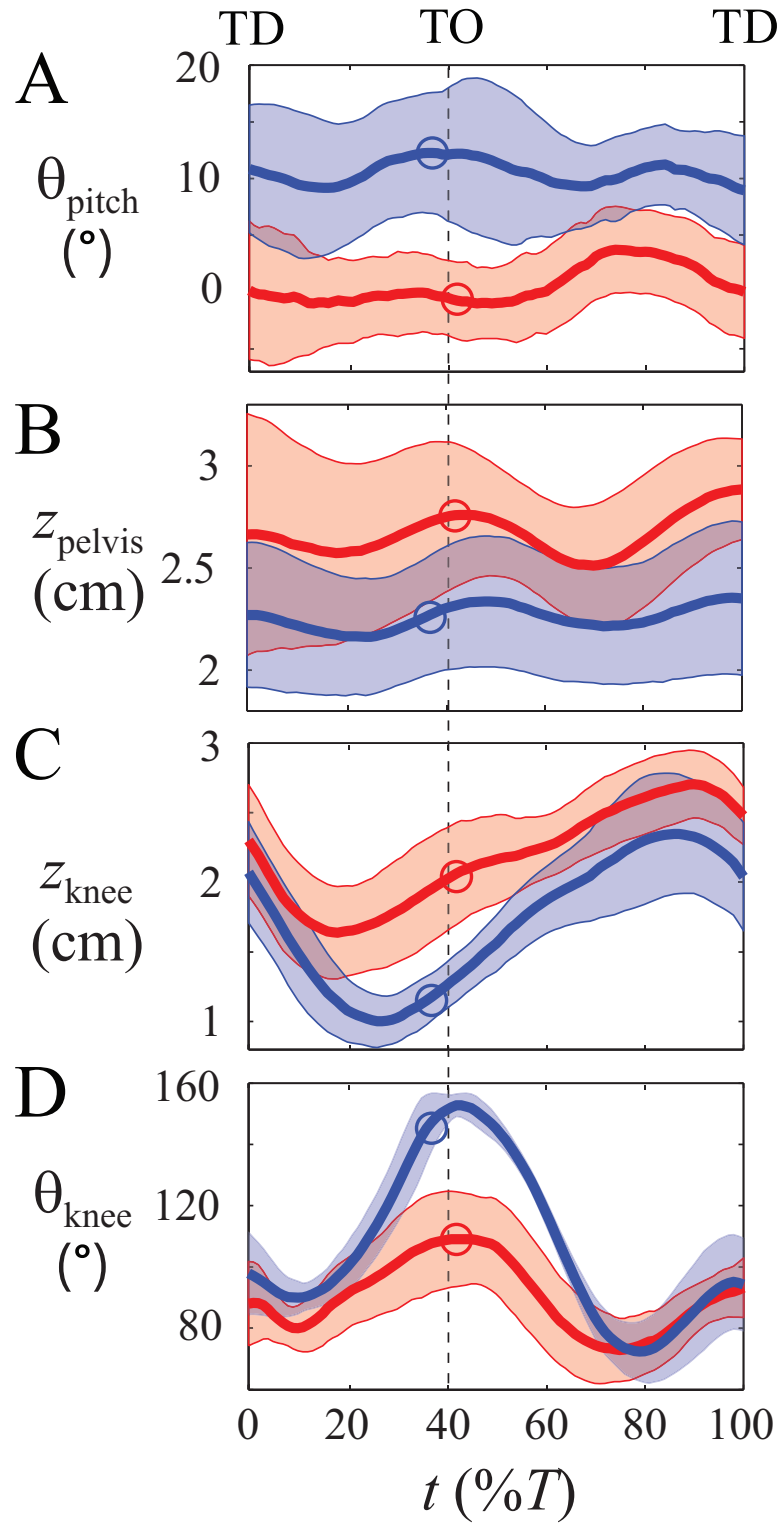


**Figure 39:** Kinematic variables of the trunk and hind leg. (A) Pitch angle of the trunk. (B) Pelvis height. (C) Knee height. (D) Knee angle. Red indicates the solid surface, and blue indicates the granular surface. Circles in (A-D) indicate takeoff. Error bars and shaded areas denote  $\pm 1$  s.d. TD and TO indicate touchdown and takeoff.

#### 2.4.4 Hind foot kinematics

The kinematics of the hind foot differed between the two substrates. On the solid surface, the lizard used a digitigrade foot posture (Fig. 38A-D, Fig. 40A, solid line and curve; Fig. 46A-D). The hind foot touched down only with the digit tips; the toes were spread out, held nearly straight, and pointed slightly downward. The foot angle at touchdown (measured along the fourth toe) was  $\theta_{TD} = (14 \pm 5)^\circ$  relative to the surface (Fig. 40A; Fig. 40C, red). During stance, the digit tips contacting the surface remained fixed in place

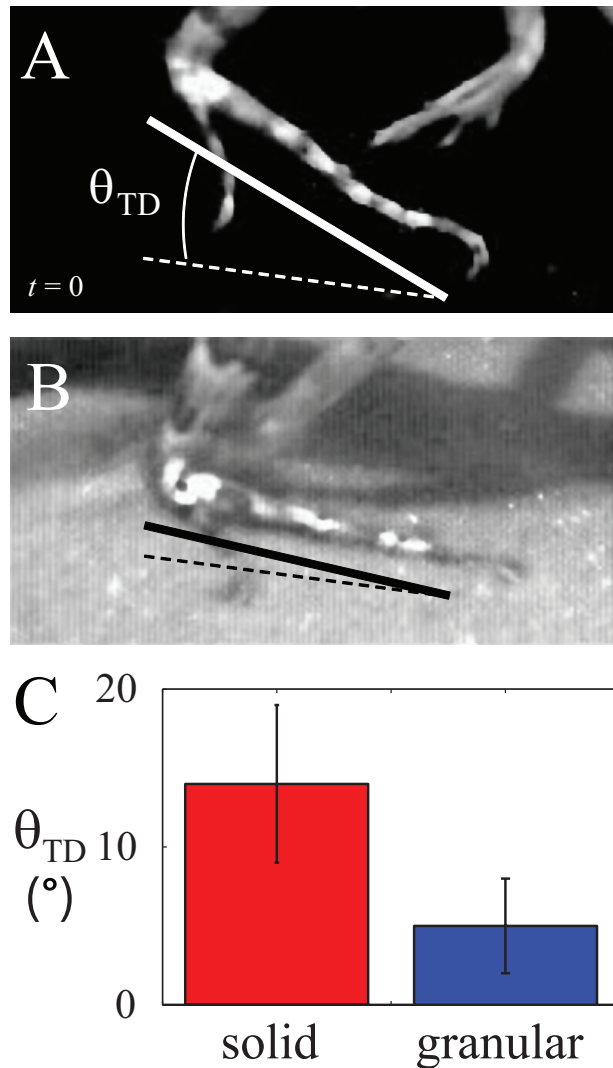


**Figure 40:** Closer views of foot posture at touchdown. (A) Foot posture at touchdown on the solid surface. (B) Foot posture at touchdown on the granular surface. (C) Foot angle at touchdown, as defined in (A,B). Error bars and shaded areas denote  $\pm 1$  s.d.

(Fig. 38A-C, vertical dotted line shows zero displacement). The long toes pivoted over the digit tips and hyperextended into a c-shape (Fig. 38B, solid curve; Fig. 46B). The foot returned to its nearly straight posture at takeoff (Fig. 38C, solid line; Fig. 46C), and then flexed during swing (Fig. 38D, solid curve; Fig. 46D).

We used foot curvature  $\kappa$  (measured along the longest fourth toe) to characterize the foot shape during running on the solid surface (see Appendix for details of the calculation). Calculated  $\kappa$  (Fig. 46E; normalized to maximal positive foot curvature  $\kappa_{max}$ ) showed that the hind foot hyperextended (positive  $\kappa$ ) during stance and flexed (negative  $\kappa$ ) during most of

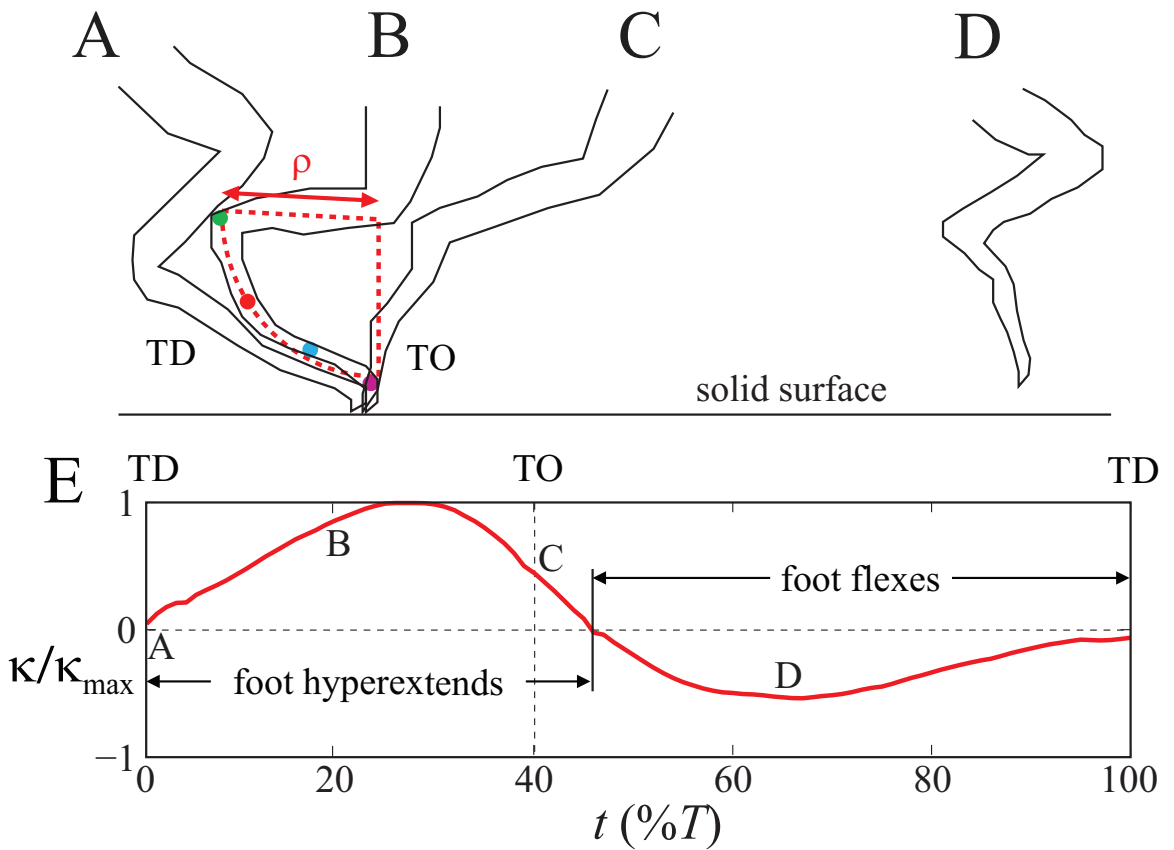


**Figure 41:** Foot-ground interaction on the solid surface. (A-D) The hind foot shape in the lateral view of a representative run (at  $t = 0, 0.2T, 0.4T$ , and  $0.65T$ ) on the solid surface. The diagram in (B) defines the radius of curvature  $\rho$  of the foot. The hind foot shape in the dorsal view is similar because the sprawl angle of the foot plane is approximately constant during stance. (E) Normalized foot curvature over a full stride on the solid surface. The time instants of (A-D) are indicated in (E) and correspond to (A-D) in Fig. 38. TD and TO indicate touchdown and takeoff.

swing. Maximal foot hyperextension occurred at mid-stance, maximal foot flexion occurred at mid swing, and the foot was straight ( $\kappa = 0$ ) at touchdown and shortly after takeoff.

On the granular surface, the lizard used a plantigrade foot posture (Fig. 38E, Fig. 40B, solid line) at touchdown. The entire hind foot touched down, with the toes spread out, held nearly straight, and nearly parallel to the surface. The foot angle at touchdown was  $\theta_{TD} = (5 \pm 3)^\circ$  relative to the surface (Fig. 40B; Fig. 40C, blue), significantly lower ( $P < 0.05$ , ANOVA) than that on the solid surface (Fig. 40A; Fig. 40C, blue). During stance, the entire foot penetrated the substrate and became obscured (Fig. 38F). Only the ankle remained visible at the surface level and moved forward by about a foot length (Fig. 38E-G, vertical dotted line shows displacement). After the foot retracted from the substrate, it flexed during swing (Fig. 38H, solid curve).

#### 2.4.5 Principal Component Analysis of kinematics

To determine which variables were responsible for the greatest variance in the data, two Principal Component Analysis (PCA) models were developed<sup>‡</sup> for variables that described the CoM and stride kinematics (10 variables; stride model), and positional characteristics of the trunk and legs (9 variables; position model). Results for the PCAs and interpretations of the analyses are shown in Table 4. Three PCs were selected for further analysis in the stride and position models, describing 79.3% and 87.8% of the total variance, respectively. Results from these models largely support the results presented above, highlighting the primary variables responsible for the greatest variance between surfaces. For the stride PCA model only PC 3 was significantly different between the surfaces ( $F(1, 11) = 5.20, P = 0.044$ ), highlighting greater stride lengths and lower CoM lateral excursions on solid ground. For the position PCA model, only PC1 was significantly different between solid and granular surfaces (PC1:  $F(1, 11) = 33.64, P < 0.001$ ). Examination of the variable loadings (i.e., eigenvectors) and plots of the principal components showed that on solid ground, lizards ran with a lower average pitch angle of the trunk, higher pelvis and knee at touchdown, as well as less knee extension and a higher foot angle at touchdown.

---

<sup>‡</sup>This analysis was performed by S. Tonia Hsieh.

**Table 4:** Results of principal component analysis on kinematic variables. Significant difference between solid and granular surface. Eigenvector values of variables contributing significantly to the variance along a principal component are in bold.

| CoM and Stride PCA                       |                 |             |                |
|--|-----------------|-------------|----------------|
| Variable                                 | PC1 (42.2%)     | PC2 (26.0%) | PC3* (11.1%)   |
| Forward speed                            | -0.32086        | 0.42308     | 0.15293        |
| Stride frequency                         | -0.38473        | 0.28383     | -0.22067       |
| Duty factor                              | 0.15947         | -0.34855    | 0.34366        |
| Stride length                            | 0.08369         | 0.32794     | <b>0.73969</b> |
| Average CoM height                       | 0.41662         | 0.25651     | -0.15445       |
| Lowest CoM height                        | 0.42393         | 0.23889     | -0.21249       |
| Time of lowest CoM height                | 0.27624         | -0.06351    | 0.34444        |
| Highest CoM height                       | 0.40908         | 0.25343     | -0.25467       |
| Time of highest CoM height               | -0.31806        | -0.16485    | -0.06668       |
| CoM lateral excursion                    | 0.13598         | -0.54140    | -0.07563       |
| Position PCA                             |                 |             |                |
| Variable                                 | PC1* (55.2%)    | PC2 (18.5%) | PC3 (14.2%)    |
| Average pelvis height                    | <b>-0.38982</b> | 0.31808     | 0.12583        |
| Average pitch angle of the trunk         | <b>0.34641</b>  | 0.24463     | -0.23350       |
| Touchdown knee height                    | <b>-0.31606</b> | 0.50144     | 0.22024        |
| Lowest knee height                       | <b>-0.42120</b> | 0.01280     | 0.00332        |
| Knee vertical displacement during stance | 0.17604         | 0.59176     | 0.26297        |
| Touchdown knee angle                     | 0.14902         | 0.44291     | -0.57342       |
| Largest knee angle                       | <b>0.36638</b>  | 0.18523     | 0.27053        |
| Knee joint extension during stance       | 0.29197         | -0.07631    | 0.63194        |
| Foot angle at touchdown                  | <b>0.42197</b>  | -0.02993    | -0.10314       |

#### 2.4.6 Hind foot resilience

Representative work loops (Fig. 42B) showed that the torque  $\tau$  was higher when the foot was pushed down on the solid surface (loading) than when it was retracted (unloading), similar to [103, 46]. Maximal torque was positively correlated with maximal angular displacement ( $P < 0.001$ , ANOVA). The kinks observed in the middle of the loading curve were due to the fifth toe contacting the surface. Average hind foot resilience calculated from the work loops was  $R = 0.44 \pm 0.12$  (Fig. 43,  $N = 3$  individuals,  $n = 64$  runs). Hind foot resilience did not differ between individuals ( $P > 0.05$ , ANOVA), nor did it change significantly with maximal torque (Fig. 43A;  $P > 0.05$ , ANOVA), maximal angular displacement (Fig. 43B;  $P > 0.05$ , ANOVA), or average loading rate (Fig. 43C;  $P > 0.05$ , ANOVA). See Table 5 for details of the statistics.

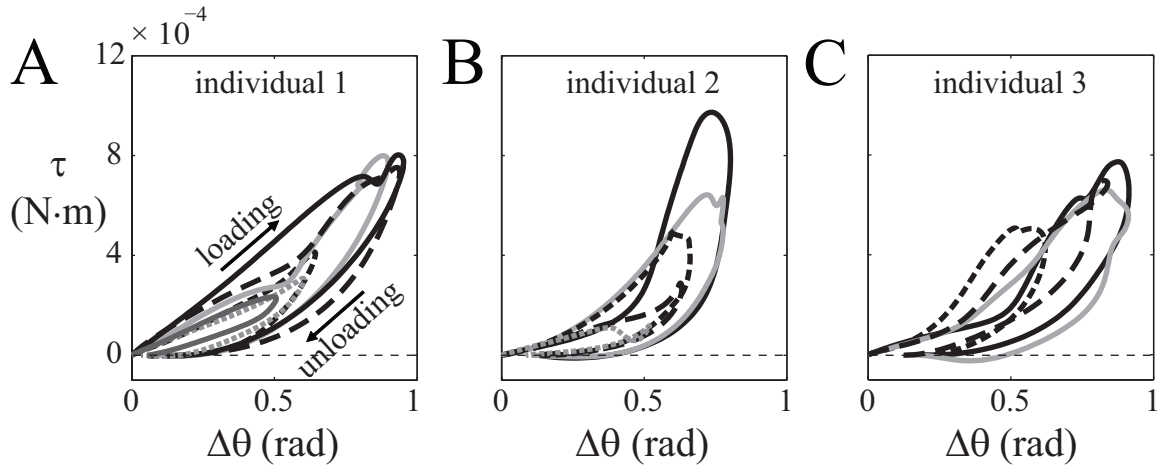


**Figure 42:** Representative passive work loops of the hind foot. (A-C) are representative work loops for three anesthetized lizards tested. Different curves are for different trials. The higher portion of each curve (labeled “loading”) is the torque during push down, and the lower portion of each curve (labeled “unloading”) is the torque during retraction. The area within a work loop is the energy lost within the foot. Both torque and angular displacement were measured at the digit tip.

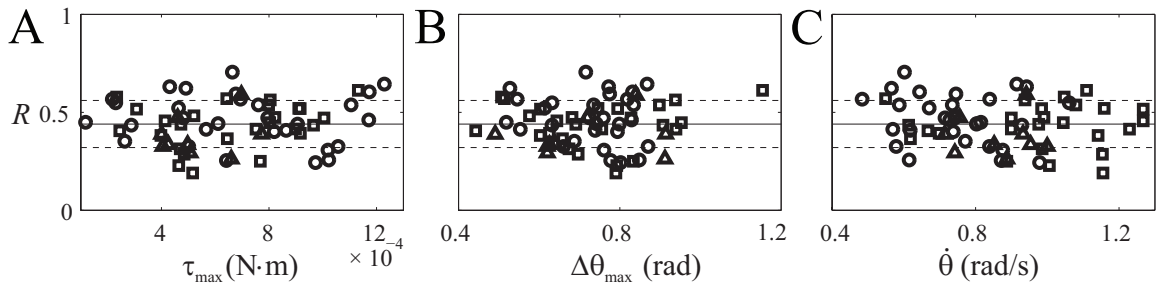


**Figure 43:** Hind foot resilience. (A) Hind foot resilience as a function of maximal torque, (B) Hind foot resilience as a function of maximal angular displacement. (C) Hind foot resilience as a function of average loading rate. Different symbols indicate different individuals. Solid and dashed lines denote mean  $\pm 1$  s.d.

**Table 5:** Statistics of modified work loop experiments. All significant differences ( $\alpha = 0.05$ ) are in bold.

| Variable       | Effect                             | Effect minimum       | Effect maximum       | $F$     | $D.F.$ | $P$            |
|----------------|------------------------------------|----------------------|----------------------|---------|--------|----------------|
| Resilience     | Maximal torque (Nm)                | $0.1 \times 10^{-3}$ | $1.3 \times 10^{-3}$ | 0.5208  | (1,62) | 0.4732         |
| Resilience     | Maximal angular displacement (rad) | 0.4                  | 1.2                  | 0.0164  | (1,62) | 0.8987         |
| Resilience     | Average loading rate (rad/s)       | 0.4                  | 1.3                  | 1.1228  | (1,62) | 0.2934         |
| Resilience     | Individual                         | N/A                  | N/A                  | 2.1025  | (2,61) | 0.1309         |
| Maximal torque | Maximal angular displacement (rad) | 0.4                  | 1.2                  | 64.3188 | (1,62) | < <b>0.001</b> |

### 2.4.7 Granular penetration force

Force data on both plates (Fig. 2; solid curve:  $A_1 = 7.6 \times 2.5 \text{ cm}^2$ ; dotted curve:  $A_2 = 3.8 \times 2.5 \text{ cm}^2$ ) show that during downward vertical penetration, the vertical force ( $F_z$ ) was upward and increased approximately linearly with penetration depth ( $|z|$ ) (higher portion of both curves). During upward retraction, vertical force immediately became negative (downward) and dropped by an order of magnitude (lower portion of both curves). In addition, penetration force scaled with plate area projected into the horizontal plane ( $A$ ): at given depth, the force on the larger plate ( $A_1$ ) was double that on the smaller plate ( $A_2$ ), as  $A_1 = 2A_2$ .

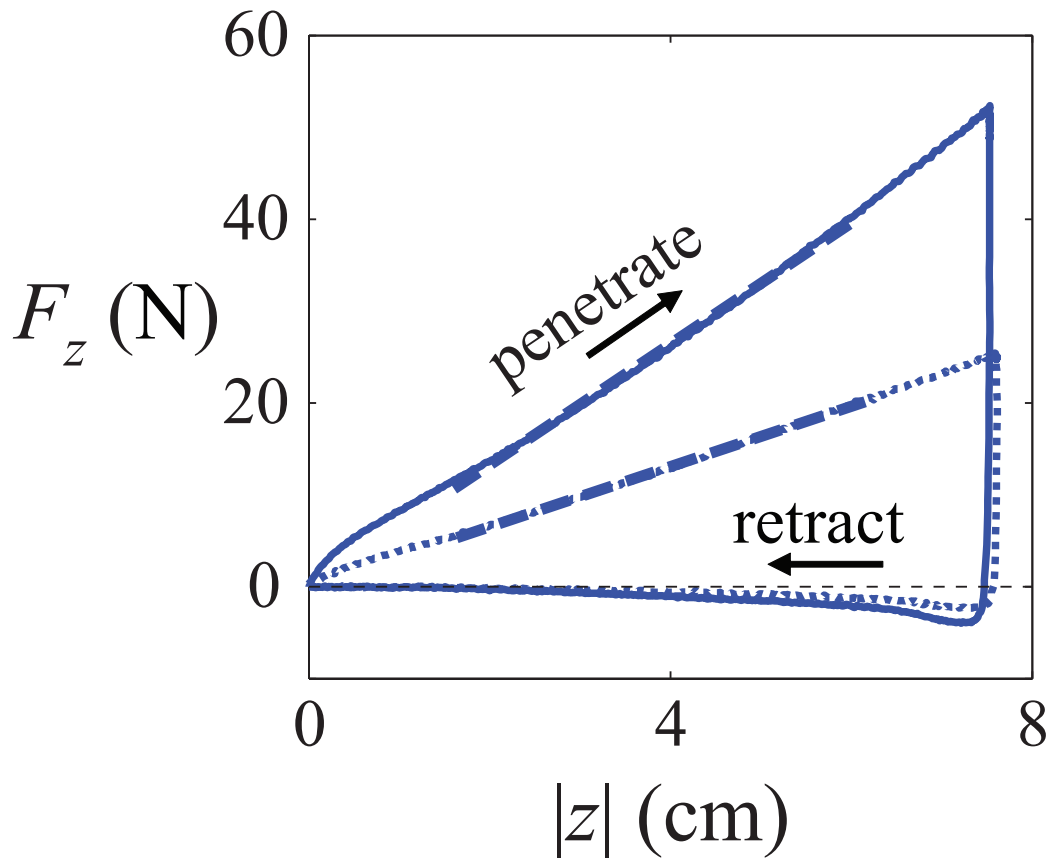


**Figure 44:** Granular penetration force as a function of depth. The solid curve is the force on a plate of area  $7.6 \times 2.5 \text{ cm}^2$ . The dotted curve is the force on a plate of half the area ( $3.8 \times 2.5 \text{ cm}^2$ ). The higher portion of each curve (labeled “penetrate”) is the force during penetration, and the lower portion of each curve (labeled “retract”) is the force during retraction. Dashed lines are linear fits to the forces during penetration using Eqn. 2. The area within each force loop is the energy lost to the granular substrates.

From these measurements and from [72], the granular penetration force can be modeled as:

$$F_z = \begin{cases} \alpha A |z|, & \text{for increasing } |z|, \\ 0, & \text{for decreasing } |z|, \end{cases} \quad (2)$$

where  $\alpha$  is a constant characterizing the penetration resistance of the granular material, which decreases with its compaction (i.e., volume fraction) [92]. Fitting  $Fz = \alpha A |z|$  to the force during penetration (higher portion of the curves in Fig. 2) over steady state region (dashed lines), we obtain  $\alpha A_1 = 660$  N/m, and  $\alpha A_2 = 330$  N/m. Thus  $\alpha \approx 3.5 \times 10^5$  N/m<sup>3</sup> for loosely packed  $0.27 \pm 0.4$  mm diameter glass particles.

## 2.5 Discussion

### 2.5.1 Comparison of CoM motion with spring-mass model

The Spring-Loaded Inverted Pendulum (SLIP) model predicts that both the CoM vertical position ( $z_{CoM}$ ) and forward speed ( $v_{x,CoM}$ ) oscillate within a step, reaching minimum at mid-stance and maximum during the aerial phase [86]. Accordingly, the mechanical energy of the CoM ( $E_{CoM}$ ) also reaches minimum at mid-stance and maximum during the aerial phase (because  $E_{CoM} = \frac{1}{2}mv_{CoM}^2 + mgz_{CoM}$ , where  $\frac{1}{2}mv_{CoM}^2 \approx \frac{1}{2}mv_{x,CoM}^2$  is the kinetic and  $mgz_{CoM}$  the gravitational potential energy of the CoM). In the first half of stance, the reduction in CoM energy ( $\Delta E_{CoM}$ ) is transformed into elastic energy stored in the leg spring, part of which could be released for mechanical work in the second half of stance as the leg spring recoils.

During running on the both solid and granular surfaces, the zebra-tailed lizard's CoM vertical position  $z_{CoM}$  (Fig. 37C, red and blue curves) oscillated in the same pattern as predicted by the SLIP model (Fig. 37C, black dashed curve). The oscillation of the CoM lateral position  $y_{CoM}$  was also in accord with the Lateral Leg Spring (LLS) model predictions [89, 90]. The substantial sprawl of the legs contributes to the medio-lateral bouncing motion of the animal.

On the solid surface, the CoM forward speed  $v_{x,CoM}$  (Fig. 37B, red curve) displayed a modest SLIP-like oscillatory trend (Fig. 37B, dashed curve), whose oscillation magnitude was small compared to the magnitude of forward speed (i.e.,  $v_{x,CoM} \ll v_x$ ) and comparable to the noise in measured speed. This is expected because the Froude number is large at high running speeds (see Appendix for details). Despite the difficulty in detecting the relatively small oscillations in  $v_x$ , a modest SLIP-like oscillatory trend in  $v_{x,CoM}$  was observed in six out of the seven runs on the solid surface (from all three individuals). This indicates that the lizard runs in a SLIP-like fashion on the solid surface.

Further evidence for SLIP-like CoM motion on the solid surface is found by observing the change in the total mechanical energy of the CoM ( $E_{CoM}$ ) during a step. On the solid surface,  $E_{CoM}$  decreased in the first half of stance by  $\Delta E_{CoM} = 1.6 \times 10^{-3}$  J (from  $15.3 \times 10^{-3}$  J to  $13.7 \times 10^{-3}$  J), and then recovers (to  $15.0 \times 10^{-3}$  J) at mid aerial phase,

in accord with spring-mass model predictions. SLIP-like and LLS-like CoM motion was previously observed in other lizards running on solid surfaces [43, 88]. However, it was not clear whether energy-saving by elastic elements played an important role.

On the granular surface, a SLIP-like oscillatory trend in  $v_{x,CoM}$  was not observed (Fig. 37B, blue curve), nor was it observed in any of the six runs. In addition, on the granular surface,  $E_{CoM}$  actually increased during the first half of stance by  $\Delta E_{CoM} = 0.7 \times 10^{-3}$  J (from  $12.7 \times 10^{-3}$  J to  $13.4 \times 10^{-3}$  J), and then recovered (to  $12.9 \times 10^{-3}$  J) at mid-aerial phase, contrary to spring-mass model predictions. This indicates that on the granular surface the lizard is not bouncing like a passive spring-mass system despite the SLIP-like oscillation in  $z_{CoM}$  and LLS-like oscillation in  $y_{CoM}$ . This is likely because the granular substrate yields and dissipates energy at each footstep.

### 2.5.2 Foot function on solid surface: energy-saving spring

In many running and hopping vertebrates, ankle extensor tendons in the lower leg act as the primary elastic elements to store and return energy (for a review, see [1]). The zebra-tailed lizard (and other iguanids [104]) does not have substantial ankle extensor tendons, but rather possesses large, elongate tendons in the foot. These foot tendons are morphologically different from ankle extensor tendons, but may be functionally equivalent during locomotion and serve as an energy-saving spring. This is particularly likely on the solid surface because during stance the lizard used a digitigrade foot posture and displayed substantial foot hyperextension.

Previous studies have demonstrated the strut-like function of ankle extensor muscles and spring-like function of ankle extensor tendons during running (for reviews, see [1, 2]). Specifically, during a footstep, the ankle flexes after touchdown and then extends before takeoff. Ankle flexion occurs as a result of ground reaction force generation. During this time, ankle extensor muscles contract nearly isometrically [105] and act as struts [5], transferring forces that stretch the ankle extensor tendons, but performing little muscle work [105]. Subsequent recoil of these tendons during ankle extension releases part of the elastic energy stored in them and provides a significant portion of the total mechanical work required ( $\Delta E_{CoM}$ ) to

raise and accelerate the CoM to the next step [105].

Inspired by these previous findings and the tendinous foot anatomy, we propose a two-dimensional strut-spring model of the hind foot (Fig. 45) which assumes isometric contraction of the lower leg muscles and incorporates the spring nature of the foot tendons. Rigid segments (Fig. 45, dashed lines), which are free to rotate about joints within a plane, represent the foot skeleton. The ankle extensor muscles in the lower leg are modeled as a rigid strut (muscle strut; Fig. 45, blue line) that runs along the ventral side of the tibia, and contracts isometrically during stance in running. A linear spring (tendon spring; Fig. 45, red lines) originates from the distal end of the muscle strut and extends to the digit tip with the capability of stretching around each joint, models the springy foot tendons. The muscle strut and tendon spring are ventrally offset from the midline of the skeleton at each foot joint by respective joint radii ( $r_K = r_A \approx 1.25$  mm,  $r_{MP} \approx 0.75$  mm,  $r_{PP} = r_T \approx 0.50$

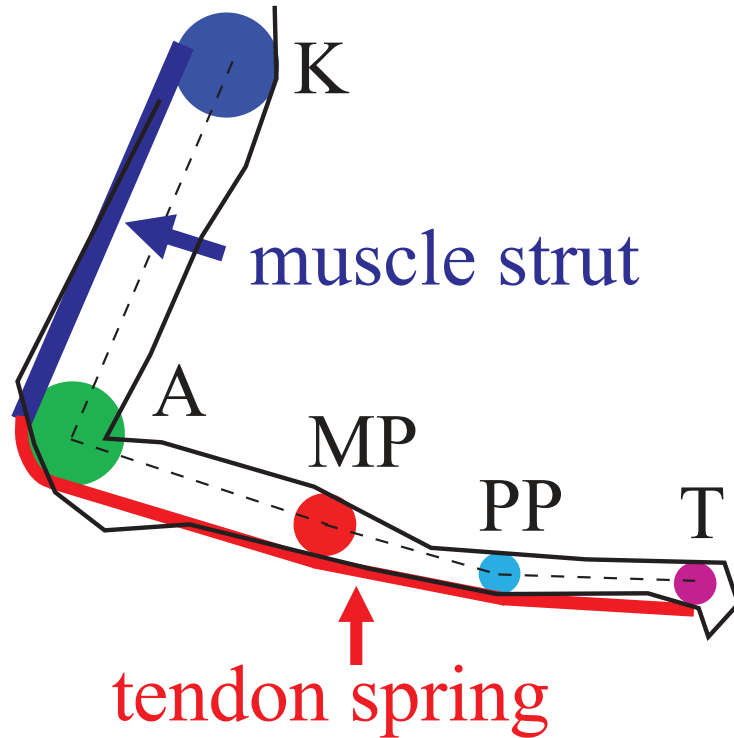


**Figure 45:** A two-dimensional strut-spring model of the hind foot. The model assumes isometric contraction of lower leg muscles (muscle strut) and spring nature of foot tendons (tendon spring). The radii of colored circles correspond to joint radii ( $r_K = r_A \approx 1.25$  mm,  $r_{MP} \approx 0.75$  mm,  $r_{PP} = r_T \approx 0.50$  mm).

mm).

The strut-spring model of the hind foot enables calculation of the deformation  $\Delta l$  of the tendon spring (see Appendix for details of the calculation). Calculated  $\Delta l$  during stance (Fig. 46, dashed curve; normalized to maximal positive deformation,  $l_{max}$ ) shows that the tendon spring stretches during the first half of stance and recoils during the second half of stance, in support of the proposed elastic energy storage and return in the hind foot. With the tendon spring deformation, the stiffness of the tendon spring (defined as the maximal tension divided by the maximal deformation of the tendon spring) is estimated to be  $k_{tendon} = 4.3 \times 10^3$  N/m (see Appendix for details of the calculation).

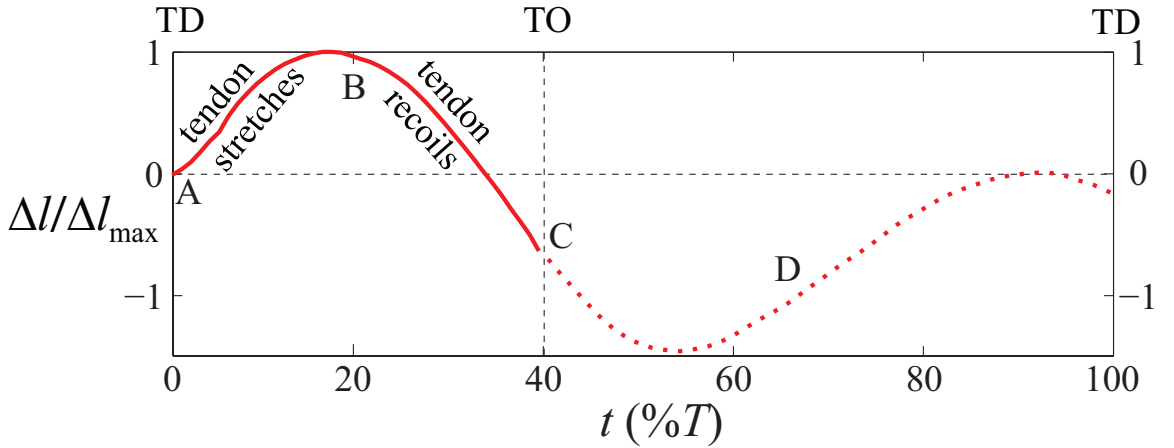


**Figure 46:** Normalized tendon spring deformation on the solid surface. The solid part of the curve is during stance, when the muscle strut assumption is valid. The dotted curve is during swing, when the muscle strut assumption does not hold. The time instants indicated by (A-D) correspond to (A-D) in Fig. 4. TD and TO indicate touchdown and takoff.

Using the estimated deformation and stiffness of the tendon spring, we can calculate the elastic energy savings in the hind foot during running on the solid surface. At mid-stance, the elastic energy stored in the tendon spring is  $\Delta E_{elastic} = \frac{1}{2}k_{tendon}\Delta l_{max}^2 = 1.4 \times 10^{-3}$  J. This is comparable to the reduction in the mechanical energy of the CoM ( $\Delta E_{CoM} = 1.6 \times 10^{-3}$  J) and implies that almost all of the reduced mechanical energy of the CoM is stored in the foot at mid-stance. Using hind foot resilience  $R = 0.44 \pm 0.12$ , the elastic recoil of the foot tendons returns an energy of  $R\Delta E_{elastic} = (0.56 \pm 0.17) \times 10^{-3}$  J per step, and provides (3910)% of the total mechanical work needed ( $\Delta E_{CoM} = 1.6 \times 10^{-3}$

J). We verified that the observed foot flexion during swing induces little energy storage ( $1.0 \times 10^{-4}$  J) because the hind foot is less stiff during flexion ( $0.7 \times 10^3$  N/m) than during hyperextension ( $4.3 \times 10^3$  N/m).

The energy saving by foot tendons is in a similar range (35%–50%) to the energy saving by ankle extensor tendons in larger animals [1], such as kangaroos (50%) [106], wallabies (45%) [107], horses (40%) [105], and humans (35%, with an additional 17% from ligaments in the foot arc) [103]. This is somewhat surprising because energy saving by elastic stretch and recoil of tendons was previously considered less important in small animals [1]. Because the leg tendons of smaller animals are “overbuilt” to withstand large stresses during escape, they usually experience smaller stress during footsteps in steady-speed locomotion [101, 108]. For example, in hopping kangaroo rat (mass  $\sim 100$  g), the gastrocnemius and plantaris tendons saves only 14% of the mechanical work needed [109]. We verified that for the zebra-tailed lizard the maximal stress in the foot tendons during stance is 4.3 MPa, well below the 100 MPa breaking point for tendons [110].

### 2.5.3 Foot function on granular surface: force-generating paddle

On the granular surface, the lizard’s foot penetrated into the substrate to generate force; however, subsurface foot motion could not be observed because of the opacity of the substrate. Based on previous understanding of granular forces and their role in locomotion, as well as the observed above-surface foot kinematics, we assume that the lizard’s foot-ground interaction can be modeled by a granular penetration force model [72]. This enables development of a hypothesis of the subsurface foot motion in the sagittal plane, and reveals the function of the hind foot on the granular surface.

Previous studies of a legged robot moving on granular surfaces demonstrated that it is important for foot penetration to generate sufficient vertical force to prevent body and limbs from sinking into the deformable media; a model incorporating vertical force balance captured the general features of the locomotion [92, 97]. Therefore, we focus on vertical ground reaction force. Before touchdown, the lizard’s hind foot moves downward at speeds close to 1 m/s on both solid and granular surfaces. On the solid surface, the hind foot

stopped moving downward immediately after touchdown (within  $\sim 3$  ms or  $\sim 8\%$  of the stance phase) and then moved slowly upward and forward about the pivot (digit tip) at speeds less than 0.5 m/s. On the granular surface, although the foot became invisible during stance, the ankle remained visible, and also stopped moving downward immediately after touchdown (within  $\sim 3$  ms). Therefore, we assume that the foot moves subsurface at similar speeds ( $< 0.5$  m/s) as on the solid surface. Because at these foot speeds the granular resistance is dominated by grain friction, force is approximately independent of speed [69, 70, 95].

The vertical ground reaction force that the lizard foot generates can then be modeled

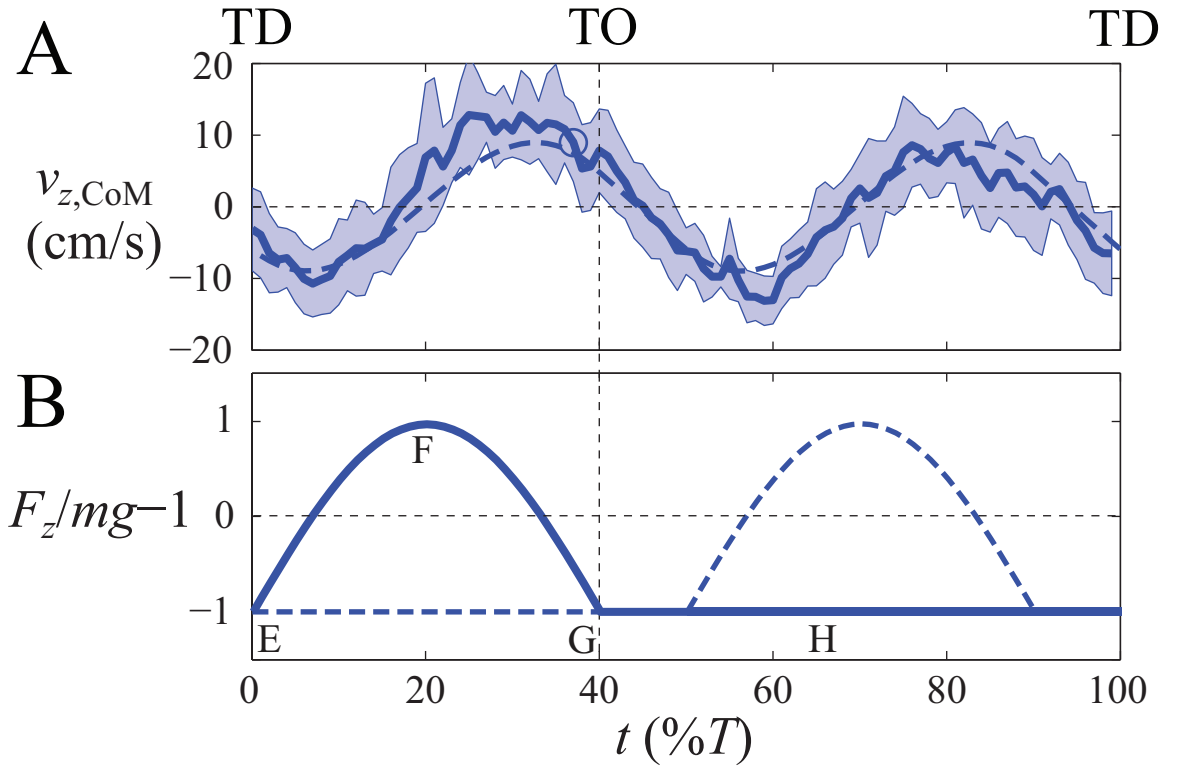


**Figure 47:** Ground reaction force and CoM vertical speed. (A) CoM vertical speed. Solid curve is speed derived from measured CoM vertical position (Fig. 37C). Dashed curve is the CoM vertical speed predicted from the model by integrating vertical acceleration. Shaded area denotes  $\pm 1$  s.d. (B) Vertical acceleration calculated from the vertical ground reaction force  $F_z$  and gravity.  $F_z = \frac{5\pi mg}{8} \sin \frac{5\pi t}{4T}$  is obtained from a granular penetration force model using hypothesized foot rotation (C). Solid and dashed curves are the  $F_z$  on the two alternating hind feet, respectively. The time instants of (E-H) indicated in (B) correspond to (E-H) in Fig. 38. TD and TO indicate touchdown and takeoff.

by the force on a plate penetrating vertically into the granular medium at a given low speed ( $< 0.5$  m/s). The penetration force data and model (Eqn. 2) indicate that as the foot penetrates downward and then retracts upward, a constant foot area  $A$  would result in monotonically increasing  $F_z$  followed by an immediate drop of  $F_z$  to zero. However, during a step, we expect that the vertical force  $F_z$  on a lizard foot is sinusoidal because the observed  $v_{z,CoM}$  oscillated approximately sinusoidally (Fig. 47A, dashed curve). Sinusoidal  $F_z$  has been demonstrated for SLIP-like running on solid surfaces and can be explained by the compression and extension of the leg spring [111]. However, on a granular surface to generate a sinusoidal  $F_z$  which gradually decreases during the second half of stance,  $A$  must decrease over time. (A sinusoidal  $F_z$  is also possible for fixed  $A$  if the foot maintains contact on solidified grains, i.e., a SLIP-like motion with a solid foothold below the surface, but this is unlikely considering the observation that during stance the ankle moves forward at the surface level by a foot length.)

Therefore, we hypothesize that during stance the foot “paddles” through fluidized grains to generate force (Fig. 48). The rotation of the foot about the moving ankle in the sagittal plane enables the projected foot area to decrease with time. Our preliminary data of subsurface foot kinematics using x-ray high-speed video (similar as in [95]) supported this hypothesis. We note that the mechanism for thrust on the lizard foot is different from the utilization of solidification forces observed in previous studies of interaction of the limbs of a legged robot [92, 97] and the flippers of hatchling sea turtles [96] with granular media.

The hypothesized subsurface foot rotation in the sagittal plane explains the observed sagittal CoM kinematics on the granular surface. Assuming that during stance the hind foot rotates at constant angular velocity by  $\frac{\pi}{2}$  in the sagittal plane about the moving ankle, the ground reaction force which each foot generates ( $Fz \approx 2mgsin\frac{5\pi t}{4T}$ ) is sinusoidal during stance (see Appendix for details of the calculation). The net acceleration due to this  $F_z$  and gravity is  $a_z = \frac{F_z}{m} - g$  (Fig. 47B, solid curve; dashed curve is the  $a_z$  from the other hind foot). The CoM vertical speed  $v_{z,CoM}$  predicted from this  $F_z$  on both hind feet (Fig. 47A, dashed curve) agrees well with observations (Fig. 47A, solid curve).

On the granular surface, the substrate yields irreversibly (i.e., plastic deformation [91,

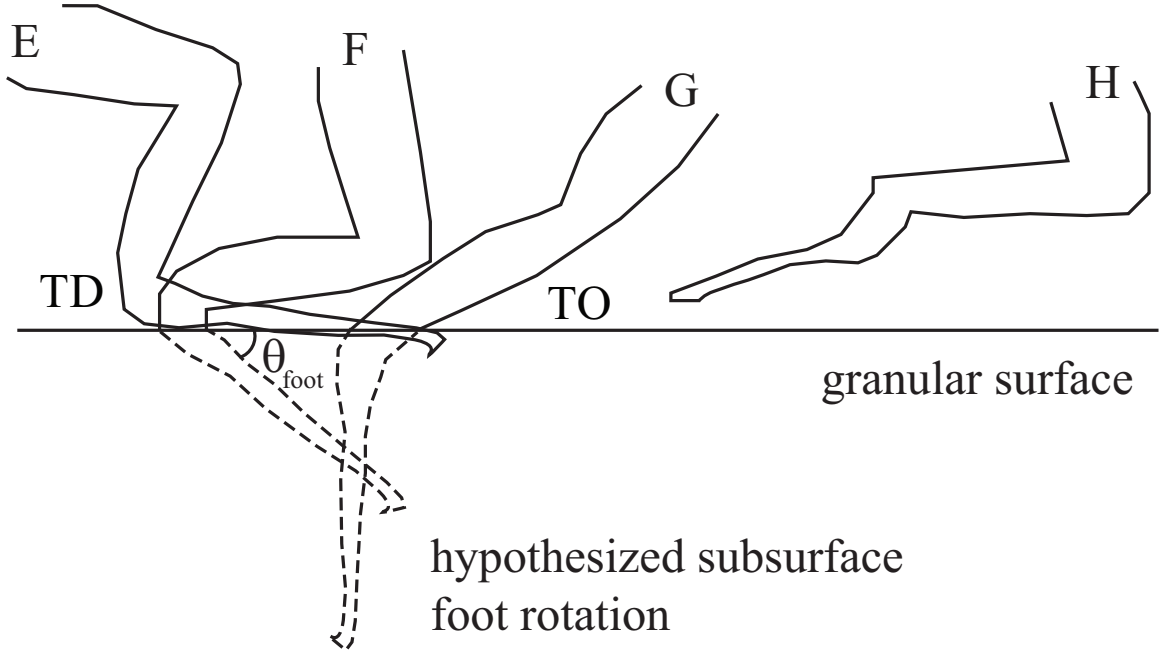


**Figure 48:** Hypothesized subsurface foot rotation in the sagittal plane. Foot tracings indicated by (E-H) are at  $t = 0, 0.2T, 0.4T,$  and  $0.65T$  and correspond to (E-H) in Fig. 38. TD and TO indicate touchdown and takeoff.

10]) at each footstep and energy is dissipated. By integration of  $F_z$  over vertical displacement, the energy lost to the granular substrate per step is  $\Delta E_{loss} = 1.5 \times 10^{-3}$  J (see Appendix for details of the calculation). This energy loss is similar to the amount of elastic energy storage ( $\Delta E_{elastic} = 1.4 \times 10^{-3}$  J) on the solid surface, suggesting that on the granular surface the foot no longer functions as an energy-saving spring.

#### 2.5.4 Motor function of upper hind leg

Despite the passive nature of the leg spring in the spring-mass model, animal limbs do not function purely as passive springs, but also perform muscle work and may actively adjust to accommodate changes in surface conditions [112, 3]. On the solid surface, the lizard's foot saves about 40% of the total mechanical work per step. The remaining 60% is lost either within the foot or to the ground. This loss must be compensated by muscle work ( $W_{muscle} = 1.0 \times 10^{-3}$  J), likely through active extension of the knee joint (Fig. 39D, red curve) powered by the upper leg muscles.

On the granular surface, the lizard's foot penetration results in lower knee (Fig. 39B,

blue curve) and pelvis (Fig. 39A, blue curve) heights at mid-stance than on the solid surface. Because the mechanical energy of the CoM increases ( $\Delta E_{CoM} = 0.7 \times 10^{-3}$  J) during the first half of stance, while substantial energy ( $\Delta E_{loss} = 1.5 \times 10^{-3}$  J) is lost to the substrate per step, the upper leg must perform larger work ( $W_{muscle} = \Delta E_{CoM} + \Delta E_{loss} = 2.2 \times 10^{-3}$  J) than on the solid surface. This is reflected in the larger knee extension during stance on the granular surface (Fig. 39D, blue curve), and possibly the pitch of the trunk (Fig. 39C, blue curve). The larger muscle work on the granular surface is in accord with previous findings of higher energetic cost in human [17, 18] and robot [98] locomotion on granular surfaces.

### 2.5.5 Advantages of a large, elongate foot

Many cursorial animals including mammals [113, 114, 115] and lizards [116] display elongation of distal limb segments. Our model of foot-ground interaction on the solid surface predicts that an elongate foot decreases tendon stiffness and mechanical advantage [117], and thus increases energy saving capacity (see Appendix for details). More generally, elongate distal limb segments such as legs, feet, and toes may be an adaptation for energy saving during rapid locomotion. Indeed, short fascicles and long tendons are often found in ankle extensor muscles and digital flexor muscles in large cursorial ungulates such as horses, camels, and antelopes [1]. A recent study also found significant energy savings (53%) by elongate foot tendons in running ostriches [118].

Our model of foot-ground interaction on the granular surface predicts that for a given animal (constant weight), energy loss to the substrate is proportional to foot penetration, and thus inversely proportional to foot area and substrate strength (see Appendix for details). On a given granular surface, a larger foot would sink less than a smaller foot [82] and lose less energy, serving as a “snowshoe” [119]. In addition, natural surfaces can be stronger than the loosely packed,  $\sim 0.27$  mm diameter glass particles used in this study [76]. For example, increase of packing fraction by a few percent [92], variation of grain size distribution [40], and change in particle roughness [10] can result in a few times of increase in granular penetration resistance. Therefore, on stronger surfaces a foot would lose less

energy and could even save energy-and this would be easier with a large foot than with a small one.

Together, our models of foot-ground interaction on both solid and granular surfaces suggest that the zebra-tailed lizard’s large, elongate hind foot functions differently on different substrates. This multi-functional appendage provides the desert generalist with energetic advantages, and simplify its sensory-neural control tasks during locomotion in natural environments [16].

### **2.5.6 Model assumptions and future work**

Our estimate of elastic energy storage and return on the solid surface assume isometric contraction of lower leg muscles. However, muscles have a finite stiffness and often do lengthen by a small amount under limb tension [105, 5]. In this case, our estimates still hold, because both the lower leg muscles and the foot tendons behave like springs, and the total stiffness remains the same (since external force and total deformation remain the same). In the case where the muscles actively shorten during stance and perform positive work on the tendons (resulting in larger tendon lengthening), the energy storage and return in the tendons would increase. However, the overall energy efficiency would in fact decrease, because apart from energy lost in tendon recoil, energy is further lost in performing muscle work (i.e., muscle work is more expensive than tendon work [120]).

In addition, the hind foot resilience obtained from anesthetized lizards was assumed to provide a good estimate for the hind foot resilience in running lizards. This is based on our observations that hind foot resilience was independent of torque, angular displacement, and loading rate, as well as previous findings that the damping properties of animal limbs are largely intrinsic to their structural and material properties [121, 122, 32, 46]. Future studies using techniques such as tendon buckles [107], sonomicrometry [107], ultrasonography [123], and oxygen consumption measurement [124] during locomotion are needed to confirm these assumptions and estimates.

Our model on the granular surface only considered vertical penetration. However, previous studies of robot locomotion on granular surfaces demonstrated that ground reaction

forces depend sensitively on foot kinematics [97] and foot morphology [98]. More elaborate models are needed to capture granular force generation during intrusion of complex shapes along complex trajectories such as that of a rotating lizard foot. Future studies using high-speed x-ray imaging [95], discrete element simulation [125, 94], and theoretical approaches [23, 94] are needed to better observe complex intrusions relevant to locomotion and model the resulting granular forces.

For running on the granular surface, we assumed that force was dominated by the hydrostatic-like component during intrusion and neglected the additional contribution to force from the inertia of grains being accelerated. This allowed us to assume that the force was dominated by the frictional flow of grains and thus independent of speed. However, since at touchdown the foot impacts the granular substrate at high speeds ( $\sim 1$  m/s) before it slows down (after  $\sim 3$  ms), we do not know if the foot achieves high speeds again during stance. At high speeds ( $\sim 1$  m/s), grain inertial forces may be significant. For example, impact studies showed that at high speeds (1 to a few m/s) force is dominated by grain inertia [73, 74]. Thus our estimates of the granular forces provide a lower bound, and the calculated maximal foot penetration ( $|z|_{max} = 1.1$  cm, see Appendix for details of the calculation) sets a higher bound. The foot rotation hypothesis still holds because grain inertial force also scales with foot area. Future studies are needed to capture detailed subsurface foot-ground interaction and investigate the role of inertial forces of the grains during high speed intrusion in locomotion.

Finally, our models of the hind foot function assume purely passive foot mechanics, and do not consider the role of active sensory-neural control. We observed that when confronted by a substrate which transitions from solid into granular (or *vice versa*), the lizard displayed partial adjustment of foot posture during the first step on the new surface, and full adjustment of foot posture during the second step. Future studies using neuromechanics techniques [13] such as EMG [107, 126] and denervation/reinnervation [127] are needed to determine how sensory feedback mechanisms are involved to control limb function to accommodate changing environments [128, 3].

## 2.6 *Conclusions*

In this study, we found that while running at similar speeds, the zebra-tailed lizard displayed similar gait and center of mass kinematics on both solid and granular surfaces, but used different trunk, hind leg, and hind foot kinematics. The lizard’s vertical CoM motion resembled that of a spring-mass system on both the solid surface and the granular surface. On the solid surface, the lizard’s elongate, tendinous hind foot functioned as an energy-saving spring and saved a significant portion of the mechanical work needed each footstep to recover the mechanical energy of the CoM. On the granular surface, the lizard’s large hind foot paddled through fluidized grains to generate force, and substantial energy was lost due to irreversible deformation of the granular substrate. The energy lost within the foot and to the substrate must be compensated by larger muscle work of the upper leg. Our models predict that the large, elongate hind foot increases energy storage and return on the solid surface, and reduces energy loss to the granular substrate by reducing foot penetration.

These findings increase the understanding of the mechanisms by which animals contend with complex natural environments. In particular, viscoelastic limbs and feet which have appropriate morphology and material properties and passively accommodate various conditions may be beneficial for terrestrial animals [16, 14]. Current robotic devices often suffer performance loss and require high cost of transport on yielding surfaces like granular material [11, 92, 97, 98]. Insights from studies like ours can provide inspiration for future robotic devices [14]. Finally, our study also highlights the need comprehensive theory of forces relevant to locomotion on granular media and yielding and flowing terrestrial environments in general.

## 2.7 Appendix

### 2.7.1 Foot curvature on the solid surface

Three-dimensional kinematics showed that both the tibia and the foot (i.e., from the knee to the digit tip of the fourth toe) remained approximately within a plane during the entire stride (out-of-plane component is 3% on average and  $< 10\%$  during the entire stride). During stance, the orientation of the foot plane remained nearly unchanged, with a foot sprawl angle of  $(53 \pm 4)^\circ$  relative to the sagittal plane in the posterior view. Foot curvature  $\kappa$  could then be obtained by fitting a circle to the foot from the ankle to the digit tip within the foot plane and determining the radius of curvature  $\rho$  of the fit circle (see diagram in Fig. 46B), i.e.,  $\kappa = \pm \frac{1}{\rho}$ , where + sign indicates foot hyperextension, – sign indicates foot flexion, and  $\kappa = 0$  indicates a straight foot shape. Maximal curvature  $\kappa_{max} = 0.8 \pm 0.2 \text{ cm}^{-1}$  occurs at  $t = 0.27T$ .

### 2.7.2 Small relative forward speed oscillation

At 1.5 m/s, the lizard's Froude number in the sagittal plane is  $Fr = v_{x,CoM}^2/gL_0 \approx 6$  (where  $L_0 \approx 4 \text{ cm}$  is the leg length at touchdown), higher than the typical value of 2.5 where most animals transition from trotting to galloping [129]. This means that the kinetic energy ( $\frac{1}{2}mv_{CoM}^2 \approx \frac{1}{2}mv_{x,CoM}^2$ ) of the CoM of the lizard is much larger ( $\approx 6$  times) than its gravitational potential energy ( $mgz_{CoM}$ ) [55]. Because both the oscillation magnitudes in forward ( $\Delta v_{x,CoM}$ ) and vertical ( $\Delta v_{z,CoM}$ ) speeds are determined by the total ground reaction force and the attack angle of the leg spring ( $\beta = \sin^{-1} \frac{v_{x,CoM}DT}{2L_0}$ )  $\approx 0.9 \text{ rad}$ ), they should be of the same order of magnitude [86], i.e.,  $\Delta v_{x,CoM} \sim \Delta v_{z,CoM}$ . From the observed CoM kinematics,  $\Delta v_{z,CoM} < (mgL_0)^{1/2}$ . Therefore,  $\Delta v_{x,CoM} \sim \Delta v_{z,CoM} < (mgL_0)^{1/2} \ll v_{x,CoM}$ , or  $\Delta v_{x,CoM}/v_{x,CoM} \ll 1$  (i.e., the angle of the landing/takeoff velocity is small [86]).

### 2.7.3 Estimates of tendon spring deformation and stiffness

From the two-dimensional strut-spring model of the hind foot, by geometry, the tendon spring deformation  $l$  is related to the observed joint angles changes and the foot joint radii as  $\Delta l = \sum_{i=A,MP,PP} r_i \Delta \theta_i$ , where  $\Delta \theta_i$  is the observed change of joint angles, and  $r_i$  is the

joint radii ( $r_K = r_A \approx 1.25$  mm,  $r_{MP} \approx 0.75$  mm,  $r_{PP} = r_T \approx 0.50$  mm). We observed that the relaxed hind foot of a live animal is approximately straight (Fig. 31), similar to the foot shape at touchdown during running (Fig. 38A, Fig. 40A). Thus we define the relaxed length of the tendon spring as its length when the foot is straight, i.e.,  $\Delta l = 0$  at touchdown. Maximal tendon spring deformation ( $\Delta l_{max} = 0.8$  mm) during stance occurs at  $t = 0.17T$  and corresponds to a 3% strain. We do not consider tendon spring deformation in the swing phase (dashed curve in Fig. 46E) because the assumption of isometric contraction of lower leg muscle only holds in stance phase.

The stiffness of the tendon spring is defined as the maximal tension divided by the maximal deformation of the tendon spring, i.e.,  $k_{tendon} = \frac{T_{max}}{\Delta l_{max}}$ . From the observed CoM kinematics, the total ground reaction force at mid-stance is  $F_{max} \approx 0.3$  N, and lies within the coronal plane and points from the digit tip to the hip. At mid-stance, since the tendon spring stretches to a maximum, torque is balanced at the ankle, i.e.,  $T_{max}r_A = F_{max}\Delta x_{ankle-digittip}$ , where  $\Delta x_{ankle-digittip} = 1.4$  cm is the distance between the ankle and digit tip along the forward direction at mid-stance, and  $r_A \approx 1.25$  mm. Thus  $T_{max} = 3.4$  N and  $k_{tendon} = 4.3 \times 10^3$  N/m. The maximal stress in the foot tendons during stance is  $\sigma_{max} = \frac{T_{max}}{\pi r_{PP}^2} = 4.3$  MPa.

During stance the lizard's lower leg muscles must be activated, because the torsional stiffness of the ankle (defined as maximal torque divided by maximal angular displacement) estimated from running kinematics ( $12 \times 10^{-3}$  Nm/rad) is much larger than found in anesthetized lizards from the modified work loop experiments ( $\sim 1 \times 10^{-3}$  Nm/rad). Higher tension from muscle contraction usually increases limb stiffness [130, 122].

#### 2.7.4 Elongate foot increases energy saving on solid surface

The stiffness of a piece of elastic material (e.g., a tendon) is  $k = \frac{EA}{l}$ , where  $E$  is the Young's modulus of the material,  $A$  is its cross sectional area, and  $l$  is its rest length. Most animal tendons are primarily made of collagen [110] and are of similar Young's modulus. Thus, the stiffness of the tendon spring scales as  $k_{tendon} \propto \frac{r^2}{l}$ , i.e., an elongate tendon is less stiff and stretches more easily than a short, thick tendon. Since elastic energy storage decreases

with tendon stiffness (because  $\Delta E_{elastic} = \frac{1}{2}k_{tendon}\Delta l_{max}^2 = \frac{1}{2}\frac{T_{max}^2}{k_{tendon}} \propto \frac{1}{k_{tendon}}$  for a given  $T_{max}$ ), an elongate tendon can thus store and return more energy.

The elongate foot also reduces the moment arm of tendon tension (small  $r_A$ ) but increases the moment arm of the ground reaction force (large  $\Delta x_{ankle-digittip}$ ) about the ankle (i.e., decreases mechanical advantage [117]), so it increases tension in the foot (because  $T_{max} = \frac{F_{max}\Delta x_{ankle-digittip}}{r_A}$  and  $\Delta x_{ankle-digittip}$  increases with foot length) for a given ground reaction force and amplifies tendon stretch for enhanced energy storage and return.

### 2.7.5 Estimates of vertical force and energy loss on granular surface

Assuming that the hind foot rotates by  $\frac{\pi}{2}$  about the moving ankle at constant angular velocity during stance, i.e.,  $\theta_{foot} = \omega t$  within  $0 \leq \theta_{foot} \leq \frac{\pi}{2}$  (where  $\omega = \frac{\pi}{2DT} = \frac{5\pi}{4T} \approx 40$  rad/s), the projected foot area in the horizontal plane decreases with time as  $A = A_{foot}\cos\omega t$ , where  $A_{foot} = 1$  cm<sup>2</sup> is the hind foot area; the depth of the foot (measured at the center of the foot) increases with time as  $|z| = |z|_{max}\sin\omega t$ . The vertical ground reaction force that the foot generates during stance is then sinusoidal:  $F_z = F_{z,max}\sin 2\omega t$ , where  $F_{z,max} = \alpha A_{foot}|z|_{max}\sin\frac{\pi}{4}\cos\frac{\pi}{4} = \frac{1}{2}\alpha A_{foot}|z|_{max}$ . For steady-state locomotion on a level surface, the  $F_z$  generated by one foot averaged over a cycle must equal half the body weight, i.e.,  $\int_0^T F_{z,max}\sin 2\omega t dt = \frac{1}{2}mg$ . Therefore  $F_{z,max} = \frac{5\pi mg}{8} \approx 2mg$  and thus  $F_z = \frac{5\pi mg}{8}\sin\frac{5\pi t}{4T} \approx 2mg\sin\frac{5\pi t}{4T}$ .

By integration of vertical ground reaction force over vertical displacement, we obtain the energy loss  $\Delta E_{loss} = \int_0^{|z|_{max}} F_z d|z| = \int_0^T F_z \frac{d|z|}{dt} dt = 1.5 \times 10^{-3}$  J, where  $|z|_{max} = 1.1$  cm from  $F_{z,max} = \frac{1}{2}\alpha A_{foot}|z|_{max}$ . The hypothesized foot rotation in the sagittal plane does not take into account possible sprawl of the foot when it is subsurface, which could induce additional energy loss by lateral displacement of the grains. However, a sprawled foot posture does not affect the condition of vertical force balance and thus does not change our estimate of energy dissipation in the sagittal plane. Therefore this estimate provides a lower bound.

### 2.7.6 Large foot reduces energy loss on granular surface

For a given animal (constant weight  $mg$ ),  $F_{z,max} = \frac{1}{2}\alpha A_{foot}|z|_{max} \approx 2mg$  is constant, thus  $\Delta E_{loss} = |z|_{max} \int_0^T F_z \omega \cos \omega t dt \propto |z|_{max} \propto \frac{1}{\alpha A_{foot}}$ . This implies that energy loss to the substrate increases with foot penetration. On a given granular surface (fixed  $\alpha$ ), a larger foot (increased  $A_{foot}$ ) sinks less than a smaller foot, and thus loses less energy to the substrate. For a given foot size (fixed  $A_{foot}$ ), a foot sinks less on a stronger granular substrate (larger  $\alpha$ ) than on a weaker substrate, and thus loses less energy to the substrate.

## CHAPTER III

### SUBSURFACE FOOT KINEMATICS AND FORCE GENERATION OF THE ZEBRA-TAILED LIZARD (*CALLISAURUS DRACONOIDES*) RUNNING ON GRANULAR MEDIA

#### *3.1 Summary*

For animals running on substrates that can deform and flow like water and sand, there is a dilemma: while foot penetration is required for locomotion, penetrating too deeply can decrease locomotor performance by reducing stride length and inducing body/limb drag. In a previous study of the zebra-tailed lizard running on granular media, we hypothesized that its hind foot must rotate (paddle) subsurface to generate thrust for locomotion. Such kinematics appear similar to the slap and stroke motion of the foot under water during water-running of the basilisk lizard [19, 20]. However, due to the opacity of the grains and lack of comprehensive force equations for granular media, well-established techniques for observing animal kinematics and water flow and measuring/calculating forces within fluids cannot be readily applied to studies of locomotion on granular media. In this study, we used x-ray high speed videos to capture the subsurface foot kinematics of the zebra-tailed lizard running on granular media, and tested a foot rotation (paddling) hypothesis proposed in a previous study [85]. We classified and analyzed the foot-ground interaction which occurred in four stages: impact, vertical penetration, rotation, and retraction. Using force models obtained from physics experiments, we determined the respective contributions of these four stages to the total vertical thrust required to balance the weight of the animal. While the kinematics and force contribution portions of these stages appear similar to those of the slap and stroke phases during water-running in the basilisk lizard, the physical mechanisms governing the forces are distinctly different. Unlike for water-running where the majority of thrust is gained by the momentum transfer from the rapidly accelerated water under the paddling foot, on granular media, thrust is dominated by speed-independent, frictional

forces, which increase hydrostatic pressure and thus foot depth. These differences suggest different movement control strategies for the water-running basilisk lizard and the sand-running zebra-tailed lizard.\*.

---

\*This Chapter is part of a paper by Chen Li, S. Tonia Hsieh, Paul B. Umbanhowar, and Daniel I. Goldman, to be submitted to The Journal of Royal Society Interface [131].

### 3.2 Introduction

Unlike rigid, non-slip ground, deformable substrates like granular media present unique challenges for a locomoting animal like a zebra-tailed lizard (Fig. 49A) as it must intrude its feet into the substrate to generate sufficient forces. Having a foothold below the surface could reduce stride length [38] and induce drag on the legs and the belly of the animal [92, 96]. In addition, energy is lost due to irreversible work done on the substrate [17, 18, 98]. Thus while foot penetration is required for locomotion, penetrating too deeply can be detrimental to locomotor performance. As a result, on a granular surface it is crucial for animal to possess appropriate foot morphology and use appropriate kinematics so that in the process of generating the required forces for locomotion the legs and body do not penetrate too deeply into the deformable substrate [92, 97, 98, 85].

This is much like the water-running of the basilisk lizard (*Basiliscus basiliscus* and *Basiliscus plumifrons*) (Fig. 49B), in which feet must also penetrate the surface to generate thrust but at the same time avoid sinking too deeply into water [19, 49, 20, 47]. In addition, the foot-ground interaction of the zebra-tailed lizard running on the granular surface [85] is kinematically similar to that of the basilisk lizard running on water [19, 20]. In both cases, the hind foot touches down the surface with a plantigrade foot posture. During stance,

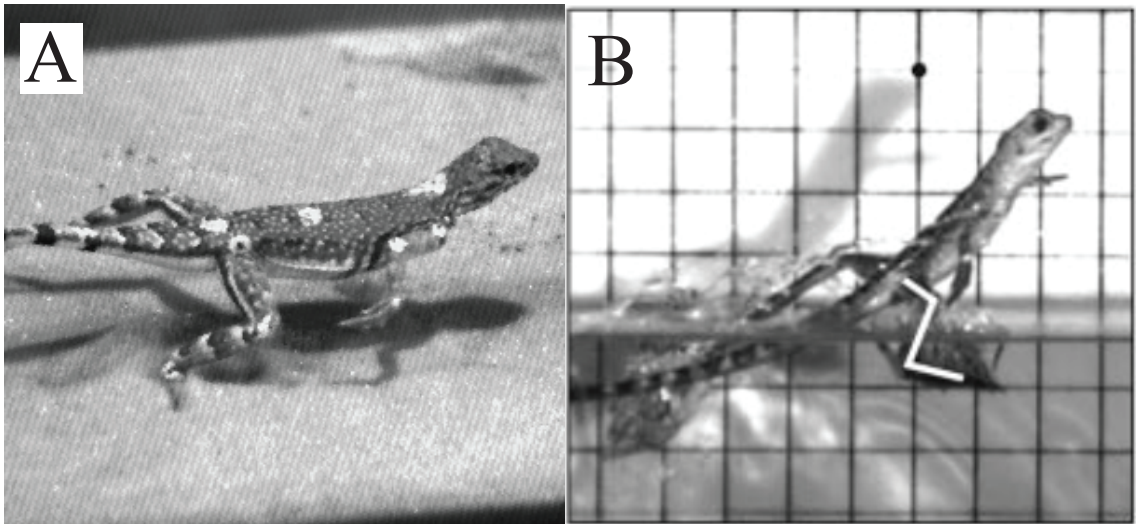


**Figure 49:** The sand-running zebra-tailed lizard (A) and the water-running basilisk lizard (B). Both snapshots are taken at mid-stance. Reproduced from [85] and [47].

the zebra-tailed lizard’s foot rotates (paddles) within the granular substrate to generate force (inferred from above surface kinematics and a granular penetration force model) [85], which appears similar to the slap and stroke of the foot under water in the basilisk lizard. Furthermore, both the zebra-tailed lizard and the basilisk lizard have elongate body and limbs, and an large, elongate hind foot. These similarities lead us to speculate that the zebra-tailed lizard may have similar kinematics and force generation strategies as those of the basilisk lizard.

For the basilisk running on the surface of water, foot kinematics during stance can be observed using high-speed video [19, 20], and the forces can be estimated from well-established hydrodynamic and hydrostatic equations [19]. In addition, the vortex rings formed within the water during footsteps can be visualized by Digital Particle Imaging Velocimetry (DPIV) (Fig. 17A), and the forces exerted by the water on the foot can be calculated from vortex ring orientation and momentum via Computational Fluid Dynamics (CFD) [132, 47] (Fig. 17B,C). However, the forces and flow during intrusion of a foot by zebra-tailed lizard running on granular media cannot be readily studied by these techniques, due to opacity of the grains and the lack of comprehensive equations governing the forces in granular media. Recently high speed x-ray imaging was successfully employed to reveal the subsurface kinematics of a desert-dwelling lizard (the sandfish) swimming within granular media [95], and by empirical force measurements and theoretical force models, the mechanics of sand-swimming was revealed [95, 125].

In this study, we use x-ray high speed videos to capture the subsurface foot kinematics of the zebra-tailed lizard running on granular media, and test the foot rotation (paddling) hypothesis proposed in the previous study of this lizard running on granular surface [85]. Based on the observed kinematics, we perform physics experiments to measure and model the different intrusion forces relevant to the foot-ground interaction on granular media, and determine their respective contributions to total vertical thrust. We compare kinematics and force generation of the zebra-tailed lizard with those of the water-running basilisk lizard (which have been studied in detail [19, 49, 48, 20, 47]) to reveal similarities and differences in these two animal species which both experience large foot penetration.

### 3.3 *Materials and methods*

#### 3.3.1 **Animals**

We collected eleven adult zebra-tailed lizards from the Mojave Desert under California Scientific Collecting Permit (SC 10901) in 09/2009 for x-ray subsurface foot kinematics experiments. Housing procedures were the same as described in the previous study [85].

#### 3.3.2 **X-ray subsurface kinematics capture**

We used x-ray high-speed video to capture 2-D sagittal subsurface foot kinematics on the granular surface (Fig. 50). For enhanced contrast, radio-opaque markers were glued to the skin near the joints. Due to high x-ray absorption and low shutter speed, we were unable to obtain enough data to be statistically meaningful using 0.27 mm diameter glass particles (density =  $2.5 \times 10^3$  kg/m<sup>3</sup>) even with large radio-opaque markers ( $\sim 2$  mm,  $\sim 0.1$  g). As a substitute, we obtained statistically meaningful data using poppy seeds (diameter  $\approx 1$  mm, density =  $1.0 \times 10^3$  kg/m<sup>3</sup>, Tasmanian Alkaloids Pty. Ltd., Tasmania, Australia) which had lower x-ray absorption, and through which small radio-opaque markers ( $\sim 0.5$  mm,  $\sim 0.001$  g,  $\ll$  foot weight  $\sim 0.3$  g) were visible. While the grain densities of these two media differ by a factor of two, their surface stiffnesses are comparable ( $\alpha \sim 10^5$  N/m<sup>3</sup>) and small compared to the  $\alpha > 10^{10}$  N/m<sup>3</sup> for the solid surface (estimated from Young's modulus of wood [133] and the dimension of the wood board). Because the observed phenomena (e.g., animal kinematics, foot intrusion, force profiles, etc.) on both granular media were qualitatively similar, we focus on presenting data obtained on poppy seeds. Additionally, a narrower fluidized bed trackway (150 cm long, 13 m wide)<sup>†</sup> was constructed to reduce the substrate width (and thus x-ray absorption) which still allowed the animals to run without interacting with the sidewalls.

During each trial, the x-ray source (Philips, Amsterdam, Netherlands) emitted x-rays (80 kV, 50 mA) horizontally across the width of the trackway for 6 s, during which the animal was induced to run (by a remotely-controlled small moving apparatus) across the range of

---

<sup>†</sup>This fluidized bed trackway was built by Loretta K. Lau.

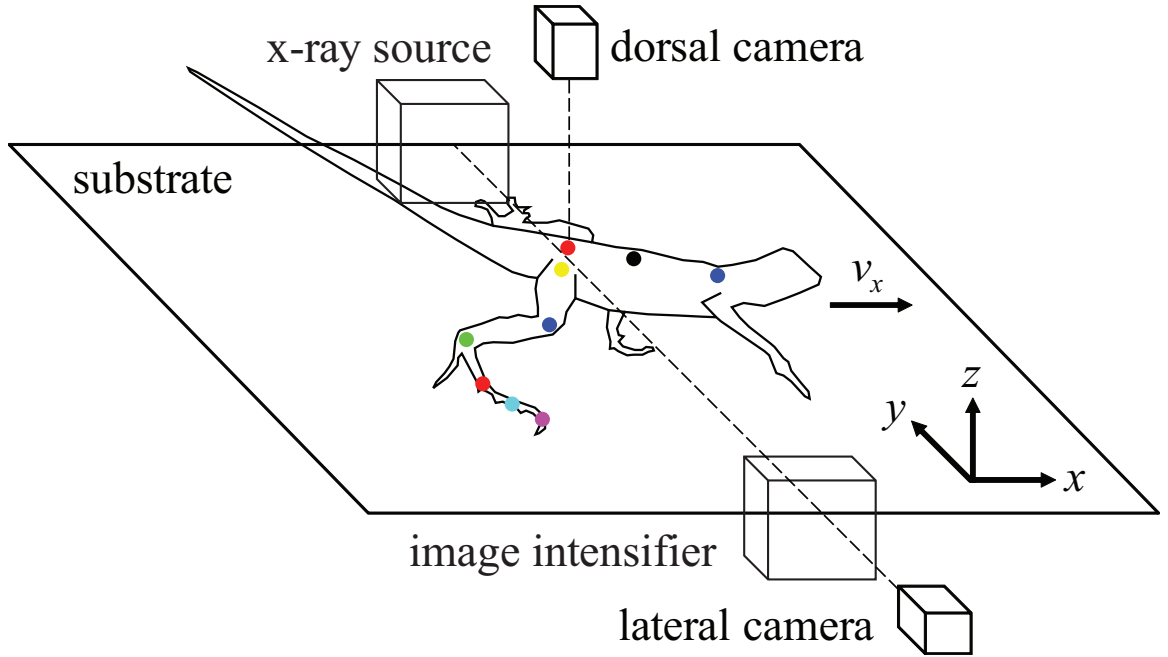


**Figure 50:** Experimental setup for subsurface foot kinematics capture using high speed x-ray imaging. A high-speed camera records the x-ray lateral view through the image intensifier as the lizard runs across a prepared substrate in the  $+x$  direction. A visible-light camera simultaneously records the dorsal view in visible-light. Colored circles show digitized points on the midline of the trunk, hind leg, and elongate hind foot, where radio-opaque markers were placed (similar to [85]).

view. An image intensifier transformed the x-rays into visible-light for capture with a high-speed camera (Photron, San Diego, CA, USA) from the lateral view at 500 frame/s with  $300 \mu\text{s}$  shutter speed. A second visible-light high-speed camera (AOS Technologies, Baden Daettwil, Switzerland) positioned directly above the trackway simultaneously captured the dorsal view at 500 frame/s for additional visible-light video analysis. Room temperature was  $25^\circ\text{C}$  during the test. Animals were permitted to rest at least five minutes between trials and for at least two days between sessions. Radio-opaque markers detached naturally after the experiment when the animals shed.

### 3.3.3 Kinematics analysis

We used the dorsal visible-light video to calculate running speed, and the lateral x-ray video to determine fore-aft ( $x$ ) and vertical ( $z$ ) positions of the foot. We also estimated the medio-lateral ( $y$ ) position in the x-ray subsurface foot kinematics data by conservation of body

segment lengths. Other analysis was performed with similar protocols as the visible-light 3-D kinematic data described in the previous study [85].

### 3.3.4 Granular force measurements

To model the forces relevant for running on granular media, we performed vertical impact, vertical penetration, and rotational intrusion experiments (Fig. 51). Before all trials, the granular medium was prepared to loosely packed state ( $\phi = 0.58$ ) using a fluidized bed ( $24 \times 22 \text{ cm}^2$  surface area, 12 cm depth).

For the impact experiment (Fig. 51A), we dropped a wood disc of 10.7 g and  $1 \text{ cm}^2$  area into the granular medium, from heights ranging from 0.76 cm to 20.32 cm such that impact speed  $v_c$  ranged from 0.4 m/s to 2 m/s to investigate impact force as a function impact speed. Balsa wood was used to reduce mass of the intruder. In addition, we varied disc mass from 5.4 g to 15.9 g for drops at 1 m/s to investigate the effect of mass of impact force. A camera recorded video of the entire impacting event (from pre-impact to full stop) at 80000 frame/s. Horizontal stripes marked on a lightweight (mass  $\ll 1 \text{ g}$ ) vertical rod rigidly attached to the disc were digitized, and image sequences were cross-correlated to obtain position, speed, and acceleration as a function of time [73]. Impact force and momentum transfer were calculated from acceleration and change in speed.

For the vertical penetration experiment (Fig. 51B), we pushed an aluminum disc of  $5 \text{ cm}^2$

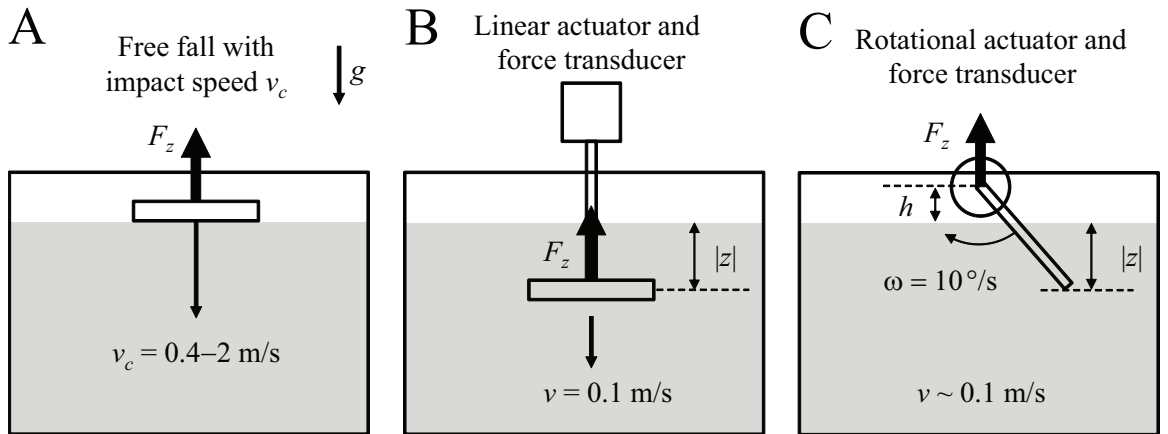


**Figure 51:** Experimental setup for granular force measurements. (A) Vertical impact. (B) Vertical penetration. (C) Rotational intrusion. Schematics are not to scale.

area downward at  $v = 0.1$  m/s into the granular medium and then retracted it. For the rotational intrusion experiment (Fig. 51C), we rotated an aluminum plate ( $7.5 \times 2.5 \times \text{cm}^2$ , 0.6 cm thickness) at angular velocity  $\omega = 10^\circ/\text{s}$  (corresponding to linear speeds of  $v \sim 0.1$  m/s) at hip height  $h = 2$  cm into the granular medium. Both vertical penetration and rotation were performed by a 6-DOF robotic arm (CRS robotics), and forces were measured by a 6-axis force/torque transducer (ATI).

### 3.4 Results

#### 3.4.1 Gait parameters

Out of the 27 runs from six individuals tested on 1 mm poppy seeds, we obtained seven usable runs from four individuals ( $N = 4$  animals,  $n = 7$  runs). These individuals (SVL =  $7.4 \pm 0.4$  cm,  $m = 12.5 \pm 1.2$  g) were collected later and were slightly larger than the individuals used in the visible-light 3-D kinematics experiment ( $P < 0.05$ , ANOVA). On poppy seeds in the narrower trackway these individuals ran with similar stride frequency ( $f = 10.1 \pm 0.9$  Hz) and duty factor ( $D = 0.40 \pm 0.02$ ) as the individuals in the visible-light 3-D kinematics ( $P > 0.05$ , ANOVA), but the forward speed ( $v_{x,CoM} = 1.93 \pm 0.22$  m/s) and stride length ( $\lambda = 0.19 \pm 0.01$  m) were larger ( $P < 0.05$ , ANOVA). We focused on observations of foot-ground interaction on poppy seeds, and discuss possible differences later.

#### 3.4.2 Foot curvature on the granular surface

The hind foot hyperextended less on a the granular surface than on solid surface. Digitized positions in the sagittal ( $x - z$ ) plane (Fig. 52C) from x-ray videos (Fig. 52A,B) showed

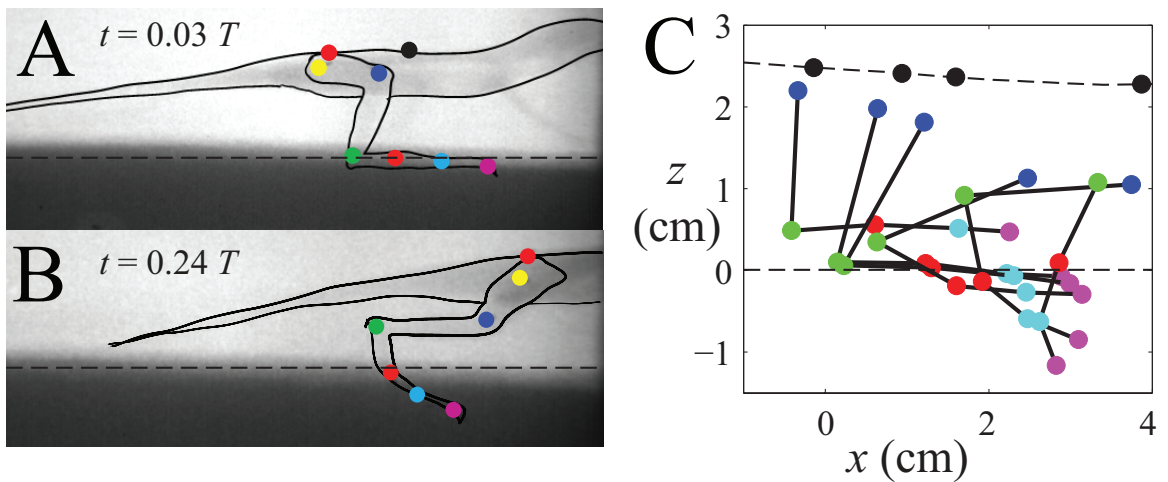


**Figure 52:** X-ray high speed videos revealed the lizard's subsurface foot kinematics on granular media. (A,B) X-ray videos from a representative shown at  $t = 0.03 T$  and  $0.24 T$ . (c) CoM (black), knee (blue), and foot (green, red, cyan, magenta for A, MP, PP, T markers) positions at  $t = -0.05, 0, 0.03, 0.13, 0.24,$  and  $0.35 T$ . The CoM positions are traced through time (dashed).

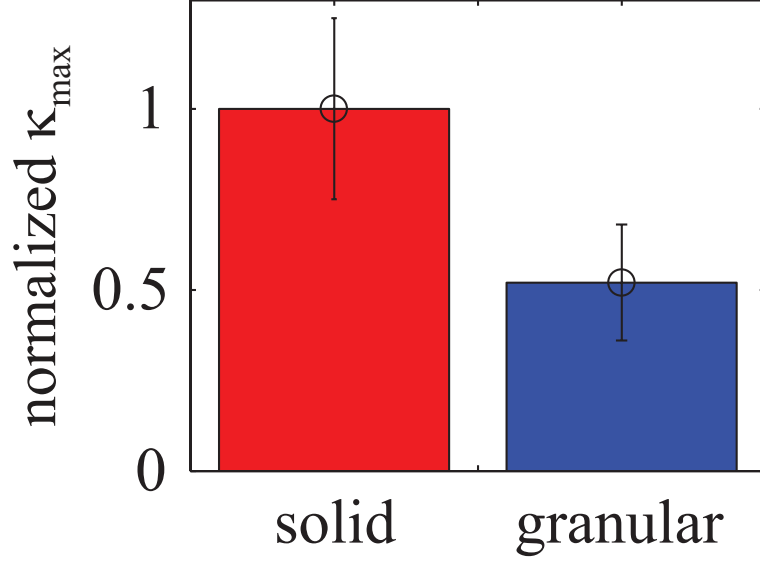


**Figure 53:** Comparison of foot curvature on solid (red) and granular (blue) surfaces. Foot curvatures are normalized to the maximal value  $\kappa_{max}$  on the solid surface. Error bars indicate  $\pm 1$  s.d.

that in contrast to on the solid surface, on the granular surface the foot was held relatively straight during early stance. The foot hyperextended after it had penetrated deeply into the substrate. 3-D foot positions (with  $y$  component estimated by conservation of foot segment lengths) confirmed that maximal foot hyperextension on poppy seeds was half that on the solid surface ( $\kappa = (0.52 \pm 0.16)\kappa_{max}$  at  $t = 0.32 \pm 0.02T$ ) (Fig. 53) .

### 3.4.3 Foot-ground interaction on the granular surface

Foot speeds (Fig. 54) showed that on the granular surface foot-ground interaction occurred in four stages (Fig. 54B,C, Table 6). Immediately before touchdown ( $t = -0.05T$ ), the

**Table 6:** Four stages of foot-ground interaction on the granular surface.

| Variable                      | Stage (1)       | Stage (2)       | Stage (3)       | Stage (4)       |
|-------------------------------|-----------------|-----------------|-----------------|-----------------|
| Start ( $T$ )                 | 0               | $0.03 \pm 0.01$ | $0.14 \pm 0.02$ | $0.35 \pm 0.01$ |
| End ( $T$ )                   | $0.03 \pm 0.01$ | $0.14 \pm 0.02$ | $0.35 \pm 0.01$ | $0.40 \pm 0.02$ |
| Duration ( $T$ )              | $0.03 \pm 0.01$ | $0.11 \pm 0.03$ | $0.21 \pm 0.03$ | $0.05 \pm 0.03$ |
| Duration (ms)                 | $3 \pm 1$       | $11 \pm 3$      | $21 \pm 3$      | $5 \pm 3$       |
| Foot speed $v_{foot}$ (m/s)   | $\sim 1.0$      | $\sim 0.1$      | $< 0.5$         | $\sim 1$        |
| Maximal foot depth $ z $ (cm) | $0.25 \pm 0.09$ | $0.50 \pm 0.17$ | $1.33 \pm 0.40$ | N/A             |

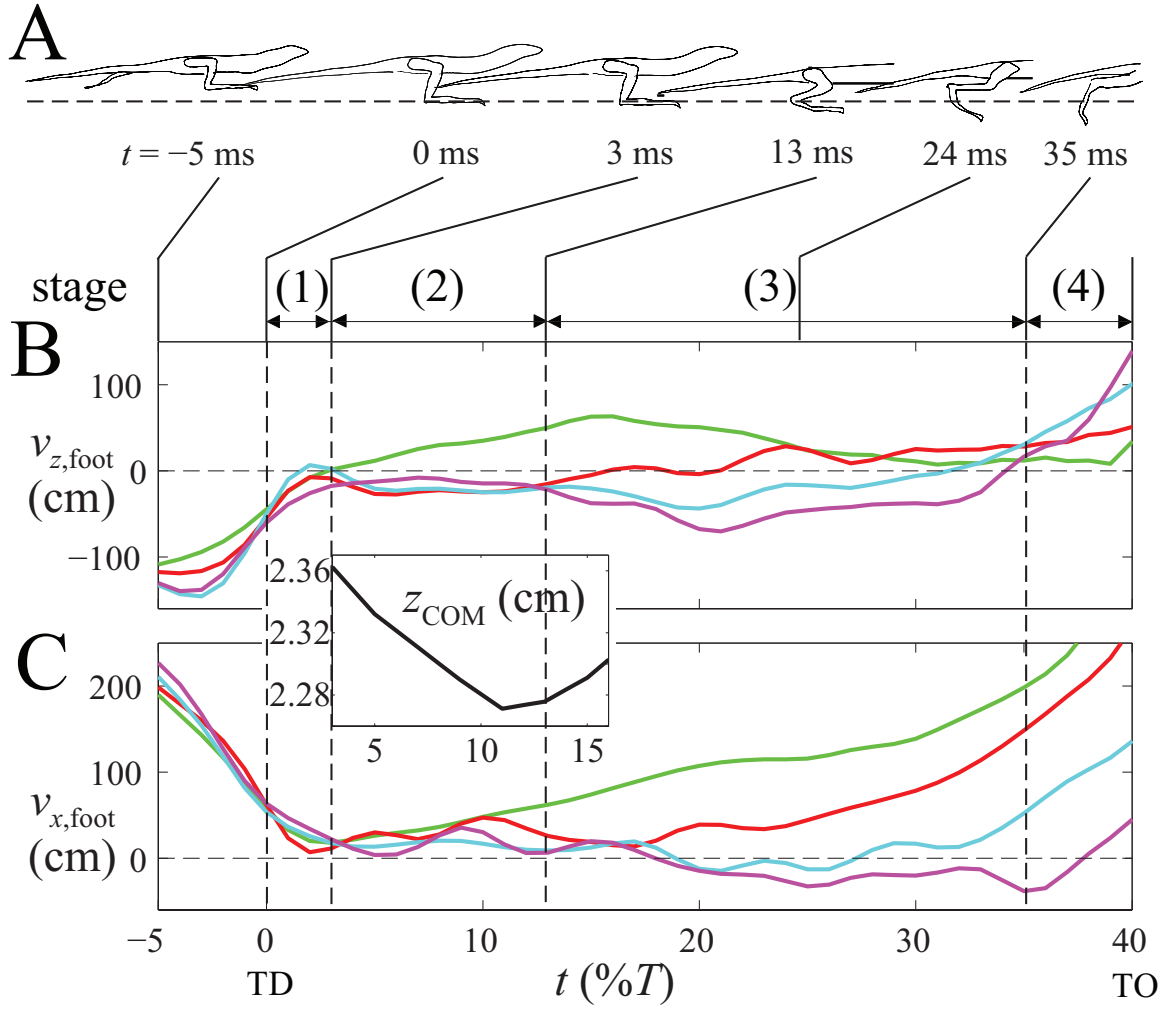


**Figure 54:** Subsurface foot kinematics during stance. (A) Body outline of a representative running lizard from video frames. Horizontal arrows and labels (1)-(4) indicate the four stages of foot-ground interaction. Tracings are shown at  $t = -0.05, 0, 0.03, 0.13, 0.24, 0.35T$ . (B) Vertical and (C) horizontal speeds of the foot as a function time during stance. Curve colors correspond to points in Fig. 52C. Inset: CoM vertical position as a function of time.

foot was above and parallel to the surface, and moved forward at  $v_{x,foot} \approx 2$  m/s and downward at  $v_{z,foot} \approx 1$  m/s. In stage (1) of foot ground interaction, the foot impacted the surface in a plantigrade posture and stopped ( $v_{x,z,foot} \approx 0$ ) within  $\approx 3$  ms at a depth of  $|z| \approx 0.25$  cm. In stage (2), the foot stayed roughly straight and horizontal, and penetrated further downward at  $v_{z,foot} \sim 0.1$  m/s to  $|z| \approx 0.50$  cm; the CoM moved downward and came to rest by the end of stage (2) (inset). In stage (3), the lower, more distal portion of the foot (toes) rotated about the metatarsus at  $v_{x,z,foot} < 0.5$  m/s deeper into the substrate

to a maximal depth of  $|z| \approx 1.33$  cm; the upper, more proximal portion of the foot (ankle) moved upward and forward; the CoM moved upward (inset). In stage (4), the entire foot moved upward and forward at  $v_{x,z,foot} \sim 1$  m/s and retracted from the substrate within  $\approx 5$  ms, with the toes collapsed together.

### 3.4.4 Granular force measurements

The impact force (Fig. 55A) on a disc displayed a large initial peak within the first  $\approx 2$  ms of impact, followed by a small, roughly constant decelerating phase. The magnitude of the peak force increased approximately quadratically with impact speed (Fig. 56). As the mass of the disc approached zero, the initial impact became the dominant force to stop the disc, and the ultimate penetration approached 1 mm. The penetration force (Fig. 55B) on a disc increased approximately linearly with depth, and corresponded to  $\alpha = 4.5 \times 10^5$  N/m<sup>3</sup> for poppy seeds using penetration force model  $F_z = \alpha Az$  [72, 92, 85]. The rotational (vertical) force (Fig. 55C) first increased with depth, then decreased as the plate approached maximal depth [97]. During vertical penetration and rotational intrusion, forces dropped by an order of magnitude during upward retraction. Both penetration and rotation forces were approximately independent of speed at low speeds  $v \sim 0.1$  m.

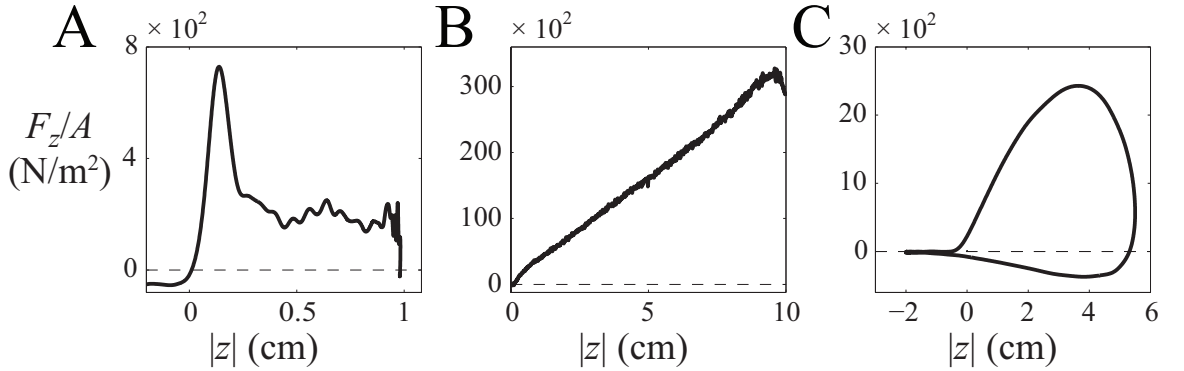


**Figure 55:** Vertical forces as a function of depth. (A) Impact force (measured by acceleration). (B) Penetration force. (C) Rotation force. All the forces are normalized to the intruder area for ease of comparison. Impact force is from a disc of 10.7 g mass impacting at speed  $v_c = 1$  m/s.

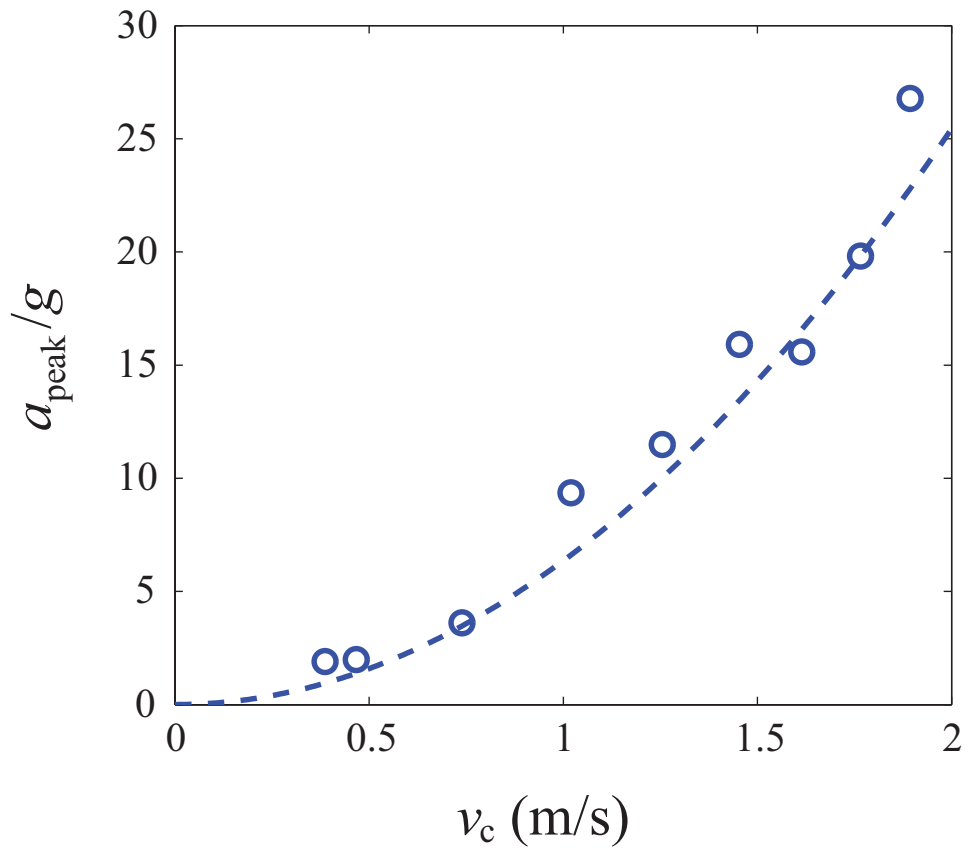


**Figure 56:** Peak impact force (measured by acceleration) as a function of impact speed. Dashed curve is a quadratic fit crossing the origin.

### 3.5 Discussion

#### 3.5.1 Reduced energy savings by foot tendons on the granular surface

We investigate whether the hind foot saved as much energy on the granular surface as on the solid surface. On the granular surface the observed maximal hyperextension of the hind foot at mid-stance was approximately half that on the solid surface ( $\kappa = (0.52 \pm 0.16)\kappa_{max}$ ) (Fig. 53). The relatively straighter foot configuration on the granular surface during stance was likely a result of the distributed ground reaction force over the foot segments. As the foot penetrated into the granular substrate, the ground reaction force (which must be about the same as on the solid surface since duty factor and CoM vertical oscillation were similar) was distributed over the entire subsurface portion of the foot. This resulted in a smaller torque and thus less foot hyperextension during stance on the granular surface. Because in our experiments poppy seeds had a larger  $\alpha$  ( $\approx 5 \times 10^5$  N/m<sup>3</sup>) than glass particles ( $3.5 \times 10^5$  N/m<sup>3</sup>), it is likely that on glass particles the foot would have to penetrate larger, which results in an even smaller torque and thus smaller foot curvature. This is in accord with the observed larger foot penetration and less curvature on glass particles.

Because foot curvature and tendon spring deformation are positively correlated, assuming that tendon spring stiffness is the same on both substrates, the energy stored at mid-stance on the granular surface must be smaller than that on the solid surface. The energy saving could be even smaller if lower leg muscle activation levels were higher on the granular surface resulting in larger tendon spring stiffness  $k_{tendon}$  [32, 122]. This is likely the case considering the larger knee flexion and extension on the granular surface.

#### 3.5.2 Force generation on granular media

The subsurface foot kinematics observed by x-ray videos (Fig. 52) confirmed our hypothesis of foot rotation (paddling) proposed in the previous study [85]. In the previous study, we used vertical force balance to estimate subsurface foot kinematics. Here we estimate forces using the observed subsurface foot kinematics, with a focus on differentiating the relative contribution to the total required vertical impulse by each stage of the observed foot-ground interaction. When moving on a level surface a lizard does not move up or down after a cycle,

thus during each step a hind foot must generate an upward impulse that balances half the downward impulse from the animal weight, i.e.,  $I_{required} = \int_0^T F_z dt = \frac{1}{2}mgT \approx 0.005$  Ns; we neglected the smaller fore feet (area  $\approx 0.3$  cm<sup>2</sup>) because the larger hind feet (area  $\approx 1$  cm<sup>2</sup>) presumably generate most of the forces for locomotion [27].

Foot-ground interaction during stage (1) was dominated by impact force at high speeds [73, 74] (Fig. 55A). After touchdown, the foot impacted the surface at  $\sim 1$  m/s and came to rest within  $\approx 3$  ms with little foot penetration ( $\approx 2.5$  mm) (Fig. 54), whereas the rest of the body (CoM) continued to fall until mid-stance (Fig. 52 inset). This implies that the foot motion was decoupled from the motion of the much heavier body. Therefore we assume that the effective impactor mass [134] is the foot mass ( $= 3\%m$  estimated by foot dimensions). By calculating the impact force on the foot using the measured force vs. mass relation, we estimated that impact force provided an upward impulse of  $\approx 0.0001$  Ns, a small portion of the required vertical thrust ( $\approx 3\% I_{required}$ ). Although impact force only contributed a small portion of vertical thrust, it quickly stopped the foot at a shallow depth.

Foot-ground interaction during stage (2) was dominated by speed independent vertical penetration force [92] (Fig. 55B). As the animal weight and inertia were transferred to the foot, the foot slowly penetrated downward at  $\sim 0.1$  m/s from  $\approx 2.5$  mm to  $\approx 5$  mm within  $\approx 10$  ms (Fig. 54). In this process, vertical granular penetration force provided a significant portion of the vertical thrust to decelerate the CoM downward motion (Fig. 52 inset). Using the penetration force model  $F_z = \alpha Az$  [72, 92, 85] and the observed increase in penetration depth, a hind foot (area = 1 cm<sup>2</sup>) provided an upward impulse of 0.0011 Ns (22%  $I_{required}$ ). The total upward impulse ( $\approx 25\% I_{required}$ ) in stages (1) and (2) was about half that to stop the CoM downward motion (50%  $I_{required}$ ).

Foot-ground interaction during stage (3) was dominated by speed independent rotational intrusion force [97] (Fig. 55C). As the foot rotated deeply into the substrate at speeds of  $< 0.5$  m/s to a maximal depth of  $\approx 13.3$  mm (Fig. 54), the rotational intrusion force accelerated the CoM upward (Fig. 52 inset). Similar to the previous study [85], we approximate the rotation force by vertical penetration force  $F = \alpha Az$  on a foot with decreasing  $A$  during foot rotation. Integration of  $F = \alpha Az$  over a constant angular speed rotation of  $90^\circ$

angular displacement in the vertical plane gives an upper bound on the upward impulse of 0.004 Ns (80%  $I_{required}$ ); further considering the sprawled posture of the foot observed from kinematics (i.e., the foot rotated in a plane at a  $45^\circ$  angle relative to the vertical plane) gives a lower bound of upward impulse of 0.003 Ns (56%  $I_{required}$ ). Therefore, the rotational intrusion force during stage (3) provided a majority (56% – 80%  $I_{required}$ ) of the vertical thrust. It may also contribute to horizontal thrust considering the substantial horizontal force observed for rotational intrusion.

Overall, during stages (1-3), the hind foot generated most of the vertical thrust required (81% – 105%  $I_{required}$ ). This may be further complemented by the fore foot, whose area is about a third of that of the hind foot ( $\approx 0.3 \text{ cm}^2$  vs.  $\approx 0.1 \text{ cm}^2$ ).

During stage (4), the foot retracted rapidly at  $\sim 1 \text{ m/s}$  (Fig. 54). During upward retraction, there was little upward force on the foot because the granular material deformed plastically [91, 10]. Our vertical penetration and rotational intrusion data both showed small forces during upward motion of the intruder following downward intrusion (an order of magnitude smaller compared to force during downward intrusion) (Fig. 55B,C). Since foot retraction happened faster ( $\sim 0.01 \text{ s}$ ) than the grains could avalanche and refill ( $\sim 0.1 \text{ s}$ , lower bound estimated from free fall under gravity) and the toes are collapsed during retraction [85] (Fig. 52, the downward drag on the foot was likely small. Therefore, we approximate the force during this stage as zero.

### 3.5.3 Comparison to the water-running basilisk lizard

The foot-ground (water surface) interaction of the basilisk lizard consists of three phases with distinct forces [19]. First, an upward impulse (slap impulse) is produced as the lizard foot impacts the water surface and suddenly accelerates a volume of water downwards (Fig. 16A). Next, after impact, an air cavity is produced as the lizard strokes downwards and backwards while plantar-flexing the foot. Integrated over time, the upward component of the drag force helps to support the lizard’s body weight (stroke impulse) (Fig. 16B). Finally, the lizard minimizes the downward forces associated with foot protraction by pulling its foot upwards before the cavity collapses. Protraction drag is further minimized by the

**Table 7:** Comparison of contributions to total vertical impulse from different phases of foot-ground interaction between the basilisk lizard and the zebra-tailed lizard.

| Basilisk lizard                         |              |             |              |             |            |
|---|--------------|-------------|--------------|-------------|------------|
| Kinematic phase                         | Slap         |             | Stroke       |             | Retraction |
| Force                                   | Hydrodynamic |             | Hydrodynamic | Hydrostatic | N/A        |
| Contribution (% total vertical impulse) | 18           |             | 62           | 22          | 0          |
| Zebra-tailed lizard                     |              |             |              |             |            |
| Kinematic phase                         | Stage (1)    | Stage (2)   | Stage (3)    | Stage (4)   |            |
| Force                                   | Impact       | Penetration | Rotation     | N/A         |            |
| Contribution (% total vertical impulse) | 3            | 22          | 56 – 80      | 0           |            |

feathering of the lateral toe fringes and the reorientation of the foot such that its long axis is parallel with the direction of movement (Fig. 16C).

The total vertical force (impulse) on the basilisk lizard’s foot thus comes from three sources. During slap, as foot depth is small, force is dominated by the inertia of the water under the foot being accelerated downward rapidly (up to 3 m/s). This hydrodynamic impact force during slap contributes approximately 18% of the total vertical impulse needed to balance the weight of the lizard. During stroke, as the foot penetrates deeper ( $\sim 10$  cm) into water, both hydrodynamic force (due to the water under the foot being accelerated downwards and backwards at  $\sim 1$  m/s) and hydrostatic force (due to the pressure difference between the water surface and the bottom of the air cavity) contribute to total thrust. Impact experiments of discs and foot models [48, 49] and calculations using hydrostatic and hydrodynamic equations show that these forces together contribute a total of 84% of the required vertical thrust [19], with 22% from hydrostatic force, and 62% from hydrodynamic force.

For the zebra-tailed lizard running on the granular surface, we divided the foot ground interaction to four stages. Stage (1) and (2) kinematically resemble the slap phase of the basilisk lizard and contribute a total of  $3\% + 22\% = 25\%$  of the required vertical impulse (as compared to 18% from slap for the basilisk lizard). Stage (3) kinematically resembles the stroke phase of the basilisk lizard and contributes  $56\% - 80\%$  of the required vertical impulse (as compared to 84% from stroke for the basilisk lizard). Stage (4) resembled the retraction phase of the basilisk lizard which does not contribute to thrust.

While it appears that the zebra-tailed lizard’s slap-like Stages (1-2) and stroke-like Stage (3) have similar kinematics and force contributions to those of the slap and stroke phases in the basilisk lizard, the physical mechanisms governing the forces are quite different (Table 7). For the basilisk running on water, the majority of the thrust ( $18\% + 62\% = 80\%$ ) results from hydrodynamic forces, which increases quadratically with foot speed. Less than a quarter (22%) of the thrust results from the hydrostatic force, which is independent of speed and increases linearly with depth. However, for the zebra-tailed lizard running on granular media, only 3% of the thrust comes from impact force which increases quadratically with speed. Most thrust ( $22\% + (56 - 80)\% = (78 - 102)\%$ ) results from speed-independent penetration and rotation forces, which is dominated by grain friction (different from in fluids) and granular hydrostatic pressure (similar to in fluids) which increases approximately linearly with depth.

The differences in dominating forces suggest that these two species of lizards may employ different kinematic and muscle activation strategies during locomotion. To run on water, the basilisk lizard must slap and stroke the foot rapidly enough to generate enough hydrodynamic forces using the inertia of water. Simply by penetrating the foot deeply without high speed paddling results in a small buoyant force (i.e.,  $\rho_{water}gV_{foot}$ , which is similar to the foot weight) and contributes a small portion of the total thrust. To run on granular media, however, the zebra-tailed lizard must instead penetrate the foot deeply enough to generate enough frictional forces, utilizing the increasing granular hydrostatic pressure as depth increases. Muscles do not necessarily need to work at high rates as do for basilisk lizard, which may affect muscle activation strategies (in consideration of muscle force-rate relationship) [5].

### 3.5.4 Recapitulation

(Figure 57) summarizes our observations and models of the CoM motion, trunk and upper leg function, and hind foot function of the zebra-tailed lizard during running on the solid surface and the granular surface obtained from this and the previous studies [85, 131]. On both substrates (Fig. 57A,B), the CoM falls during landing and rises during push-off in

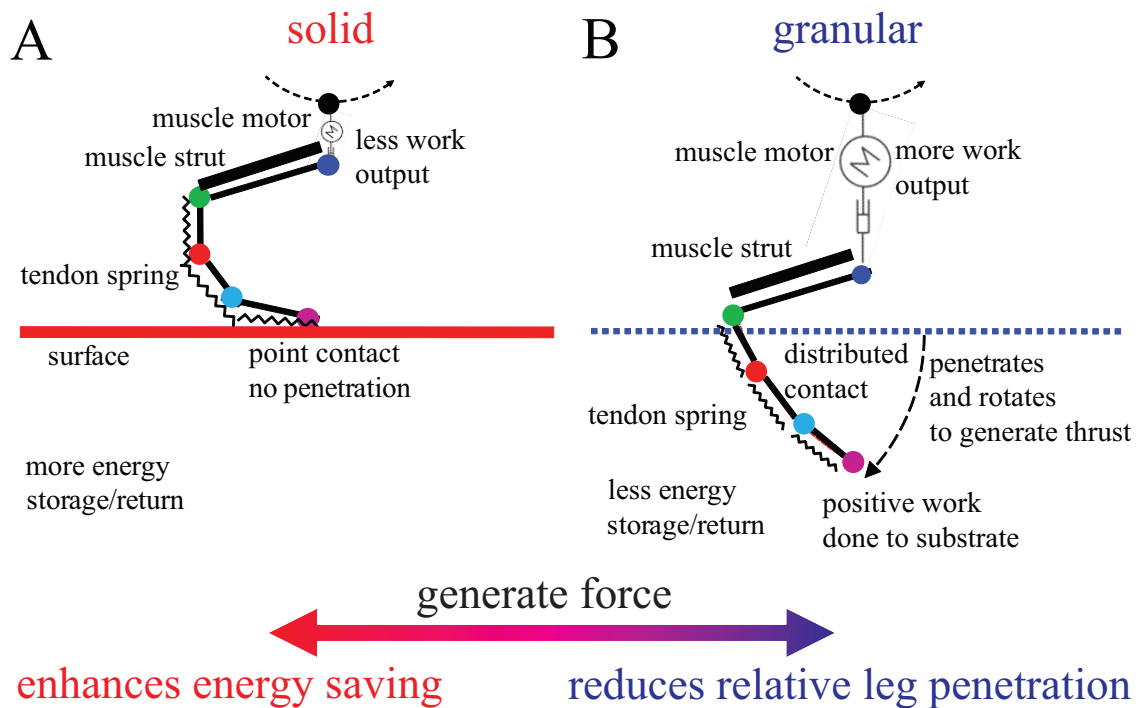


**Figure 57:** Summary of CoM motion, hind leg function, and hind foot function on the solid surface and the granular surface. On both substrates, the CoM oscillates during a stride, reaching its lowest point at mid-stance (dashed arrow). On the solid surface (a), the hind foot functions mainly as an energy-saving spring. On the granular surface (b), the foot hind functions mainly as a penetration-reducing support to reduce limb penetration. The upper leg and trunk function as a muscle motor to compensate for knee deflection and energy loss, which differ between the two substrates.

accord with the SLIP model. On the solid surface (Fig. 57A), the hind foot functions as an energy-saving spring. The foot engages ground with point contact, and the ground reaction force is concentrated at the digit tip. Larger torque on the foot results in larger foot hyperextension, and thus higher energy storage and return. On the granular surface (Fig. 57B), the dominant function of the hind foot becomes reduction of relative leg penetration. The foot penetrates into the substrates and rotates downwards, during which energy is lost to the substrate. Foot hyperextension is smaller due to the distribution of ground reaction force over the subsurface foot segments, and thus energy storage and return is lower. On both substrates, the upper leg and trunk function as a muscle motor which actively extends and adjusts to compensate for knee deflection and energy loss. On the granular surface, the upper leg and trunk produce more muscle work.

### ***3.6 Conclusions***

In this study, we used x-ray high speed videos to capture the subsurface foot kinematics of the zebra-tailed lizard running on granular media, and confirmed the foot rotation (paddling) hypothesis proposed in the previous study [85]. We found that the foot-ground interaction occur in four stages, namely impact, vertical penetration, rotation, and retraction. Using force models obtained from physics experiments, we determined the respective contributions of these four stages to the total vertical thrust required to balance the weight of the animal. While the kinematics and force contribution portions of these stages appear similar to those of the slap and stroke phases during water-running in the basilisk lizard, the physics of forces are distinctly different. Unlike for water-running where the majority of thrust is gained by the momentum transfer from the rapidly accelerated water under the paddling foot, on granular media, thrust is dominated by speed-independent, frictional forces, which increase hydrostatic pressure and thus foot depth. These differences suggest different movement control strategies for the water-running basilisk lizard and the sand-running zebra-tailed lizard.

## CHAPTER IV

### SENSITIVE DEPENDENCE OF THE MOTION OF A LEGGED ROBOT ON GRANULAR MEDIA

#### 4.1 *Summary*

Legged locomotion on flowing ground (e.g., granular media) is unlike locomotion on hard ground because feet experience both solid- and fluid-like forces during surface penetration. Recent bioinspired legged robots display speed relative to body size on hard ground comparable with high-performing organisms like cockroaches but suffer significant performance loss on flowing materials like sand. In laboratory experiments, we study the performance (speed) of a small (2.3 kg) 6-legged robot, SandBot, as it runs on a bed of granular media (1-mm poppy seeds). For an alternating tripod gait on the granular bed, standard gait control parameters achieve speeds at best 2 orders of magnitude smaller than the 2 body lengths/s ( $\approx 60$  cm/s) for motion on hard ground. However, empirical adjustment of these control parameters away from the hard ground settings restores good performance, yielding top speeds of 30 cm/s. Robot speed depends sensitively on the packing fraction  $\phi$  and the limb frequency  $\omega$ , and a dramatic transition from rotary walking to slow swimming occurs when  $\phi$  becomes small enough and/or  $\omega$  large enough. We propose a kinematic model of the rotary walking mode based on generic features of penetration and slip of a curved limb in granular media. The model captures the dependence of robot speed on limb frequency and the transition between walking and swimming modes but highlights the need for a deeper understanding of the physics of granular media.\*

---

\*This Chapter is a published paper by Chen Li, Paul B. Umbanhowar, Haldun Komsuoglu, Daniel E. Koditschek, and Daniel I. Goldman, The Proceedings of the National Academy of Sciences (2009) [92].

## 4.2 Introduction

Compared to agile terrestrial organisms, most man-made vehicles possess limited mobility on complex terrain [11] and are easily thwarted by materials like rubble and sand. Increased locomotive performance of engineered platforms demands better understanding of interaction with complex environments. At the same time, there is increasing evidence that small legged machines can have greater maneuverability than large wheeled vehicles in many natural environments [135]. However, while wheeled and treaded locomotion on sand has been well studied by pioneers like Bekker [64], study of the interaction of animals or legged devices with complex media like sand is in its infancy [136], in part because the physics of penetration and drag in granular media is largely unexplored for realistic conditions. Nearly all previous experiments and models of terrestrial locomotion were developed for running and walking on rigid, flat, non-slip substrates in which the possibility of substrate flow has been ignored [137, 138, 139, 140, 89].

Rainforest, grassland, polar tundra, mountains, and desert are examples of complex Earth terrains where locomotion can be challenging, and the limited experience of the Mars Rovers supports the presumption that extraterrestrial landscapes will be even more daunting. Deserts, common in nature and occupying about 10 percent of land surface on Earth [25], consist largely of granular media, a representative complex substrate. Granular materials, generically defined as collections of discrete particles, can exhibit solid-like behavior below a critical yield stress [141, 10], while liquid-like [142], gas-like [143], and even glass-like [80] behaviors are possible during flow. Yet, compared to other complex materials like debris, mud or snow, granular materials are simple enough that fundamental understanding of the collective physics can be achieved through interplay of experiment and theory. Unlike more heterogeneous real-world environments, granular media can be precisely controlled using laboratory scale devices [80, 82] to create states of varying material strength that mimic different deformable flowing materials produced during locomotion on complex terrains.

Here we systematically explore the performance of a small legged device, SandBot, on granular media prepared in different packing states with volume fraction ranges typical

of desert sand [76]. Despite SandBot's (and its predecessor RHex [15]) ability to move nimbly and rapidly over a wide range of natural terrain, we find that on granular media the locomotion is remarkably sensitive to substrate preparation and gait characteristics, which points to both the need for a more sophisticated understanding of the physics of motion within granular media and the possibility of better robotic control paradigms for locomotion on complex terrains.

### 4.3 Materials and Methods

#### 4.3.1 SandBot

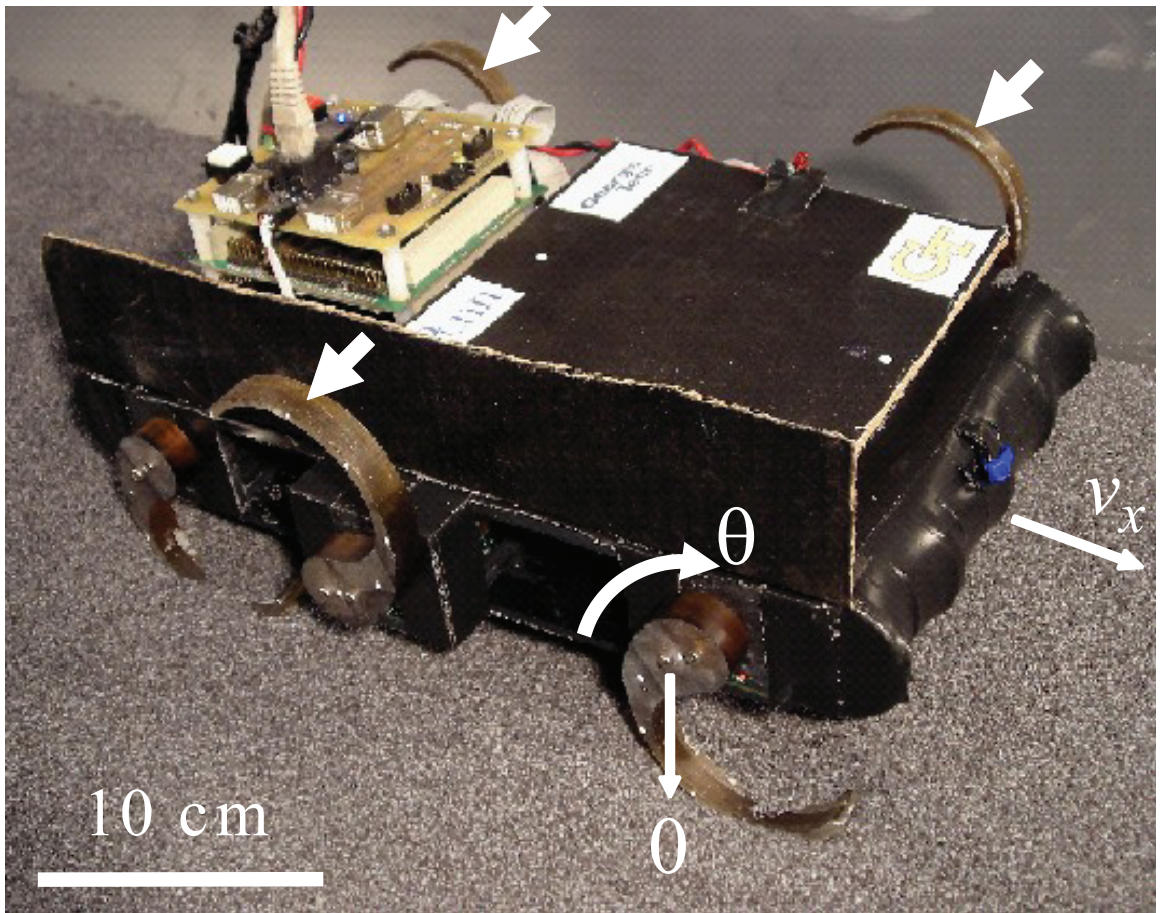


**Figure 58:** The six-legged robot, SandBot. SandBot moves with an alternating tripod gait (alternate triplets of limbs rotate  $\pi$  out of phase); arrows indicate members of one tripod.

The robot we study, SandBot<sup>†</sup> (Fig. 58), is the smallest (mass 2.3 kg) in a successful series of hexapedal robots, the RHex class [15]. RHex incorporates the pogo stick-like dynamics observed in a diversity of biological organisms running on hard ground [86]. This dynamics, called the Spring-Loaded Inverted Pendulum (SLIP) template [16], is hypothesized to confer passive self-stabilization properties to both biological and robotic locomotors [55]. RHex was the first legged machine to achieve autonomous locomotion at speeds over a fractional body length per second [15] and it and its “descendants“ such as Edubot/Sandbot, Whlegs [52] and

<sup>†</sup>This robot was developed by Haldun Komsuoglu and Daniel E. Koditschek.

iSprawl [51] are still the leaders in legged mobility (roughly, speed and efficacy) on general terrain. In fact, prior to the very recent development of BigDog [53], RHex remained the only class of legged machine with documented ability to navigate on complex, natural, outdoor terrain of any kind and has been used as the standard platform in comparisons with commercial wheeled and tracked vehicles like Packbot [54].

### 4.3.2 Limb kinematics

SandBot moves using an alternating tripod gait such that two sets of three approximately c-shaped limbs rotate synchronously and  $\pi$  out of phase. A controlling clock signal (Fig. 60A), prescribes the angular trajectory of each tripod. On rigid, no-slip ground SandBot's limb trajectories are tuned to create a bouncing locomotion [15] that generates speeds up to 2 body-lengths/sec. We initially used this clock signal on granular media, but found that the robot instead of bouncing adopts a swimming gait in which the legs always slip backward relative to the stationary bed and for which performance is reduced by a factor of 30. We surmised that this was due to an interval of double stance (both tripods in simultaneous contact with the ground), which is useful on hard ground during bouncing gaits but apparently causes tripod interference on granular media. Changes to the clock signal removed the double stance and slowed the initial leg impact. These parameter modifications allowed SandBot to move in the granular media at speeds up to 30 cm/s ( $\sim 1$  body-length/sec) in a walking gait that resembles the pendular gait of the robot on hard ground [144] but with important kinematic differences (discussed below). No amount of limb parameter adjustment produced rapid bouncing locomotion on granular media.

SandBot is a hexapedal robot platform that borrows its morphological design from the successful RHex class [15] [50]. SandBot's motors are controlled to follow the same prescribed kinematic path during each rotation and, as shown in previous work on RHex, changes in this kinematics have substantial effects on robot locomotor performance [57]. The kinematic angular trajectory consists of a fast phase and a slow phase with respective angular frequencies. Essentially, the fast phase corresponds to the swing phase (aerial phase), while the slow phase corresponds to the stance phase (ground phase). A set of

three parameters uniquely determines the clock signal configuration:  $\theta_s$ , the angular span of the slow phase;  $\theta_0$ , the angular position of the center of the slow phase; and  $d_c$ , the duty cycle of the slow phase. Specifying the cycle averaged limb angular frequency  $\omega$  fully determines the motion.

In our initial experiments we tested two sets of clock signals: a hard ground clock signal (HGCS) with ( $\theta_s = 0.85$  rad,  $\theta_0 = 0.13$  rad,  $d_c = 0.56$ ) which generates a fast bouncing gait (1 m/s) on hard ground [15] but very slow ( $\sim 1$  cm/s) motion on granular media, and a soft ground clock signal (SGCS) with ( $\theta_s = 1.1$  rad,  $\theta_0 = -0.5$  rad,  $d_c = 0.45$ ) which produces unstable motion on hard ground but regular motion on granular media. This confirmed that the locomotor capacity of SandBot is sensitive to the clock signal. Careful observation of limb kinematics revealed that the hard ground clock signal fails on granular media because of the simultaneous stance phase of two tripods. Also, the SGCS has a slower and delayed slow phase, which suggests that the speed and timing of limb placement may be critical to locomotion on granular media. In this study, we keep the clock signal fixed (SGCS), and explore robot performance as a function of limb frequency and substrate volume fraction.

Integrated sensors record the position and current (and thus torque) of Sandbot’s motors vs. the internal time. Comparison of the motor trajectory in experiment with the prescribed motion for both sets of timing parameters confirm a high degree of fidelity with an error of a few percent. Therefore, SandBot’s change in performance between HGCS and SGCS timing comes from the physics of the substrate interaction.

### 4.3.3 Trackway volume fraction control

In the desert, robots can encounter granular media ranging in volume fraction from  $\phi = 0.55$  to  $\phi = 0.64$  [76]. To test the robot performance on controlled volume fraction granular media, we employ a 2.5 m long fluidized bed trackway (Fig. 59) [24], which allows the flow of air through a bed of granular media, in this case  $\sim 1$  mm poppy seeds. With initial fluidization followed by repeated pulses of air [79], we prepare controlled volume fraction states with different penetration properties [77]. In this study, we test the performance of SandBot with varied limb frequency for  $\phi$  states ranging from loosely to closely packed

( $\phi = 0.580$  to  $\phi = 0.633$ ). We hypothesized that limb frequency would be important to robot locomotion since the substrate yield strength increases with increasing  $\phi$  and the yield stress  $\times$  robot limb area divided by the robot mass  $\times$  velocity is proportional to the maximum limb frequency for efficient locomotion.

To systematically test SandBot’s performance vs. substrate volume fraction, we employ a 2.5 m long, 0.5 m wide fluidized bed trackway with a porous plastic (Porex) flow distributor (thickness 0.64 cm, average pore size 90  $\mu\text{m}$ ). Four 300 LPM leaf blowers (Toro) provide the requisite air flow. Poppy seeds were chosen as the granular media because they are similar in size to natural sand [145]. and are of low enough density to be fluidized. The air flow across the fluidized bed is measured with an anemometer (Omega Engineering FMA-900-V) and is uniform to within 10 percent.

A computer controlled fluidization protocol sets the volume fraction and thus the mechanical properties of the bed. A continuous air flow initially fluidizes the granular media in the bubbling regime. The flow is slowly turned off leaving the granular media in a loosely packed state ( $\phi = 0.580$ ). Short air pulses (ON/OFF time = 100/1000 msec) pack the bed [81]. Increasing the number of pulses increases  $\phi$  up to a maximum of  $\phi = 0.633$ . Volume fraction was calculated by  $\phi = m/\rho V$ . The mass was measured with a precision scale (Setra). The density of the granular media was measured by means of displacement in water. In experiment, since the area of the fluidized bed trackway is fixed, volume fraction is set by controlling the height of the granular media,  $\phi = m/\rho Ah$ .

#### 4.3.4 Kinematics measurements

To characterize SandBot’s motion, we record simultaneous dorsal and lateral views with synchronized high speed video cameras (AOS Switzerland) at 100 frames/s. The center of mass (dorsal landmark) and the axles of the right-side front and rear motors (lateral landmarks) are marked with reflective material (WhiteOut). A pulley/rail system allows the power and communication cables to follow the robot as it moves. For each trial, we prepare the trackway with the desired volume fraction and place the robot on the prepared granular media at the far end of the trackway with both tripods in the same standing

position. An LED on the robot synchronizes the video and robot motor sensor data. After each trial, Matlab (The MathWorks) is used to obtain landmark coordinates from the video frames and calculate the kinematic variables  $v$  and  $\beta$ . Three trials were run for each state of  $(\phi, \omega)$ .

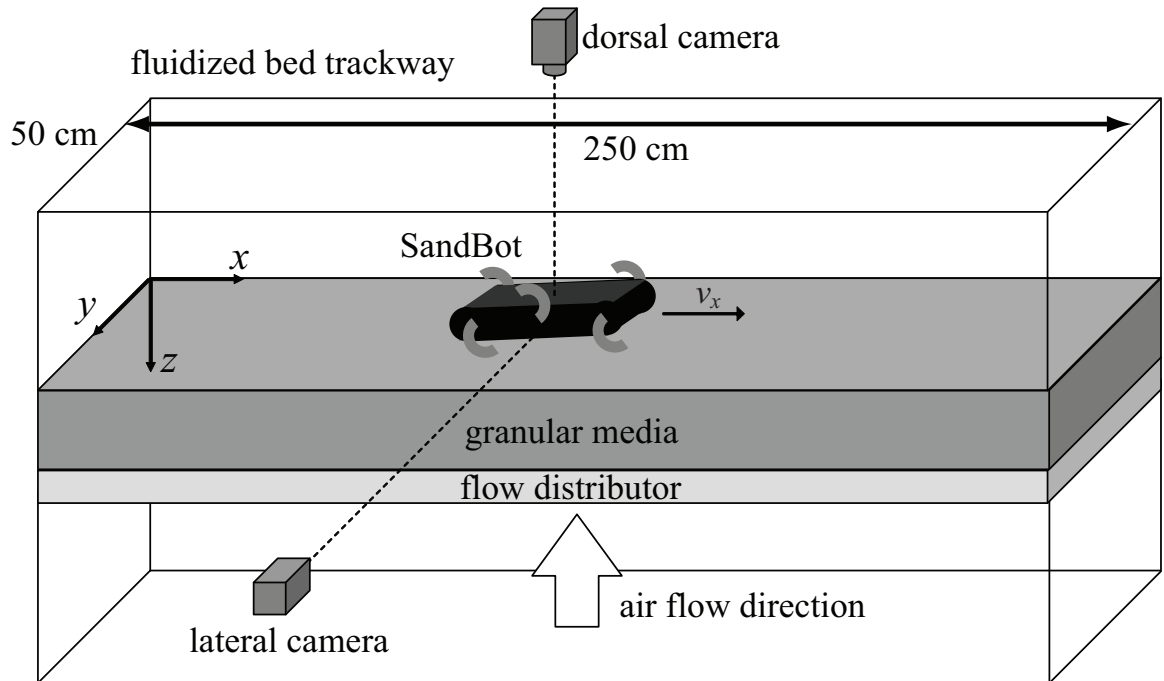


**Figure 59:** Experimental setup. Pulses of air through the bottom of the fluidized bed trackway control the initial volume fraction  $\phi$  of the granular substrate; air is turned off before the robot begins to move.

## 4.4 Results and Discussion

### 4.4.1 Sensitive dependence of speed on volume fraction

We find that robot performance is remarkably sensitive to  $\phi$ . For example, at  $\omega = 16$  rad/s the robot speed  $v(t)$  shows a change in average velocity  $\bar{v}_x$  of nearly a factor of five as  $\phi$  changes by just 5 % (Figs. 60B,C). For the closely packed state ( $\phi = 0.633$ ),  $\bar{v}_x$  was approximately 20 cm/s with  $\sim 5$  cm/s oscillations during each tripod rotation, whereas for

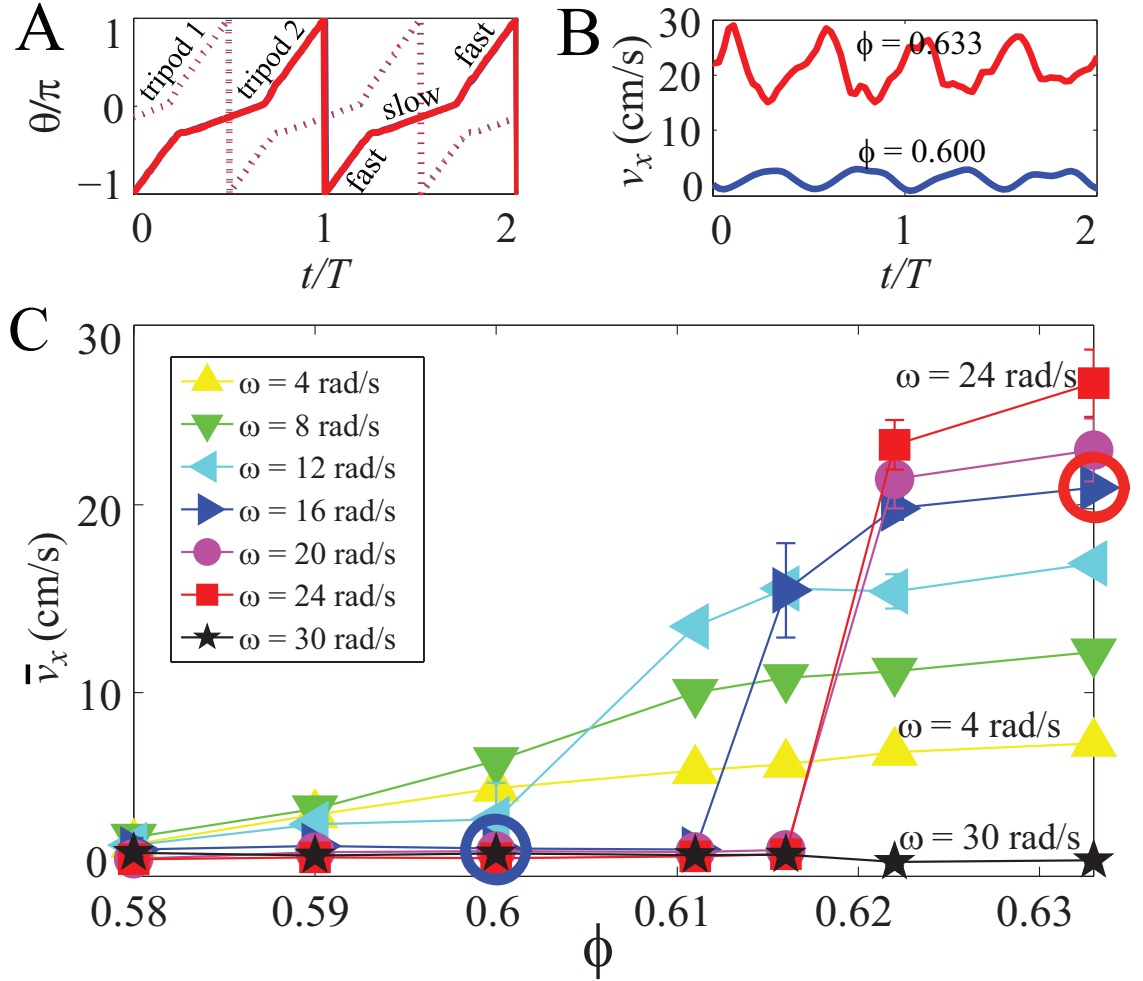


**Figure 60:** Locomotion of SandBot on granular media is sensitive to substrate packing and limb frequency. (A) Tripod leg-shaft angle vs. time is controlled to follow a prescribed trajectory with two phases: a slow stance phase and a fast swing phase. The trajectories of two trials,  $(\omega, \phi) = (16 \text{ rad/s}, 0.633)$  and  $(16 \text{ rad/s}, 0.600)$ , showing good repeatability. (B) Identical tripod trajectories produce different motion for  $\phi = 0.600$  and  $\phi = 0.633$ . (C) For given limb frequency ( $\omega = 4, 8, 12, 16, 20, 24,$  and  $30$  rad/s) the robot speed is remarkably sensitive to  $\phi$ . Red and blue circles show the corresponding states in (A) and (B).

a more loosely packed state ( $\phi = 0.600$ ),  $\bar{v}_x \approx 2$  cm/s with 1 cm/s variations in velocity.

This sensitivity to volume fraction is shown in the average robot speed vs. volume fraction (Fig. 60C). For fixed  $\omega$ ,  $\bar{v}_x$  is effectively constant for  $\phi$  above a critical volume fraction  $\phi_c(\omega)$ , but is close to zero for  $\phi$  below  $\phi_c(\omega)$ . For fixed  $\omega$ ,  $\phi_c(\omega)$  separates volume fraction into two regimes: the “walking” regime ( $\phi \geq \phi_c$ ,  $\bar{v}_x \gg 0$ ) and the “swimming” regime ( $\phi < \phi_c(\omega)$ ,  $\bar{v}_x \approx 2$  cm/sec).

#### 4.4.2 Rotary walking mode

The “walking” mode is dominant at low  $\omega$  and high  $\phi$ . In this mode, a tripod limb penetrates down and backward into the ground until the granular yield stress exceeds the limb transmitted inertial, gravitational, and frictional stresses at a depth  $d(\omega, \phi)$ . At this point, rather than rolling forward like a wheel, each limb abruptly stops translating relative to the grain bed and starts rotating about its now stationary center of curvature by slipping tangentially relative to the grains in the circular depression surrounding the limb (see Fig. 61). The simultaneous halt in both vertical and horizontal leg motion is apparently due to the large reduction in friction forces which occurs when the weight of the robot is supported by the limbs rather than the undercarriage. The ensuing rotary motion propels the axle and consequently the rest of the robot body along a circular trajectory in the  $x - z$  plane with speed  $R\omega$ , where  $R = 3.55$  cm is the c-leg radius. The forward body motion ends when, depending on  $\phi$  and  $\omega$ , either the second tripod begins to lift the robot or the underside of the robot contacts the ground.

With increased  $\omega$  limbs penetrate further as the requisite force to rapidly accelerate the robot body to the finite limb velocity increases. As the penetration depth approaches its maximum  $2R - h$ , where  $h = 2.5$  cm is the height of the axle above the flat undercarriage of the robot, the walking step size goes to zero since there is never a point in the cycle where the limb ceases its motion relative to the grain bed. Any subsequent forward motion is due solely to thrust forces generated by the swimming-like relative translational motion of the limb through the ground. Note that  $\phi_c(\omega)$  increases with  $\omega$ , and that the transition of  $\bar{v}_x$  from walking to swimming is sharper for higher  $\omega$  and smoother for lower  $\omega$ . The much

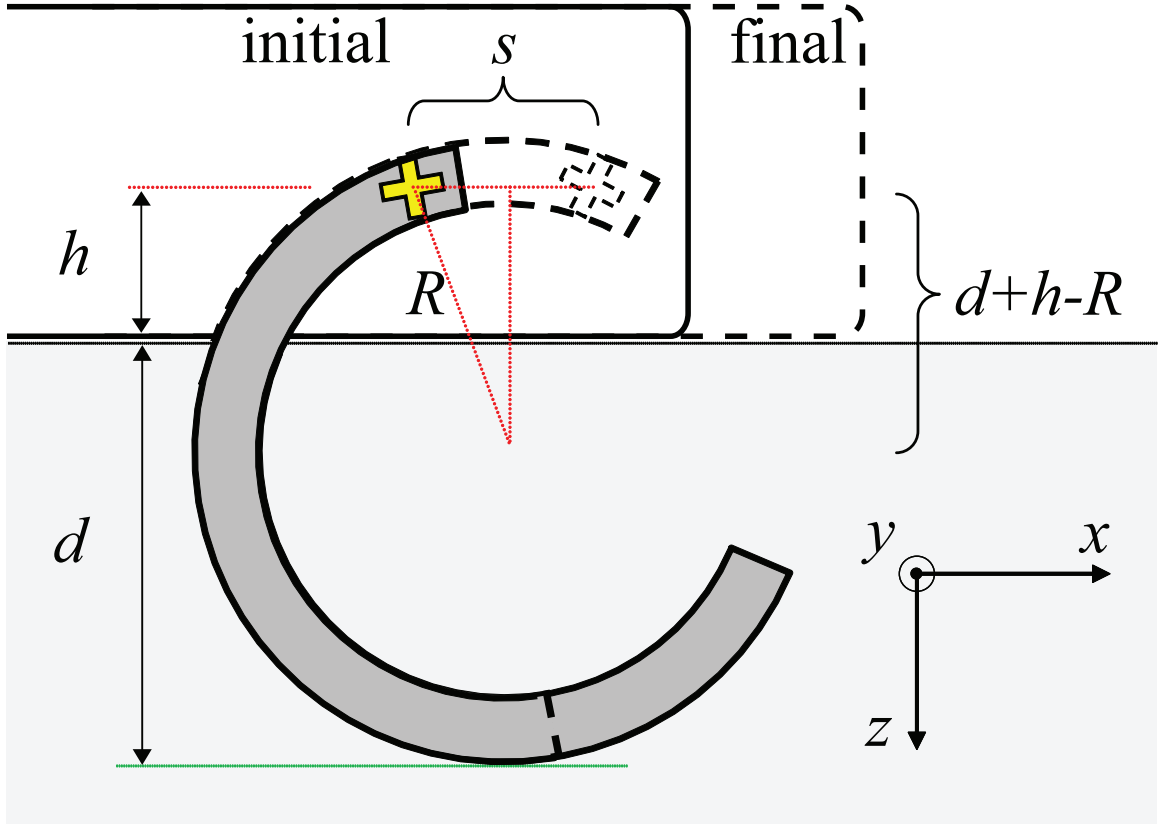


**Figure 61:** Schematic of a single robot leg rotary walking during a step in granular media. After reaching penetration depth  $d$ , the leg rotates about its center and propels the robot forward a step length  $s$ . The solid shape denotes the initial stage of the rotational motion and the dashed shape indicates when the limb begins to withdraw from the material (end of forward body motion).

slower swimming mode occurs for all volume fractions for  $\omega \geq 30$  rad/s.

#### 4.4.3 Sensitive dependence of speed on limb frequency

Plotting the average robot speed as a function of limb frequency (Fig. 62) shows how the robot suffers performance loss as its legs rotate more rapidly. For fixed  $\phi$ ,  $\bar{v}_x$  increases sub-linearly with  $\omega$  to a maximal speed  $\bar{v}_x^*$  at a critical limb frequency  $\omega_c$ , above which  $\bar{v}_x$  quickly decreases to  $\approx 2$  cm/s (swimming). Performance loss for  $\phi \gtrsim 0.6$  is more sudden (total performance loss within 1 rad/s) compared to performance loss for  $\phi \lesssim 0.6$ . Both  $\omega_c$  and  $\bar{v}_x^*$  display transitions at  $\phi \approx 0.6$  (Figs. 63A,B). The transition at  $\phi \approx 0.6$  for the rapidly running robot is noteworthy since it has been observed that granular media undergo a transition in quasi-static penetration properties for  $\phi \approx 0.6$  [77].

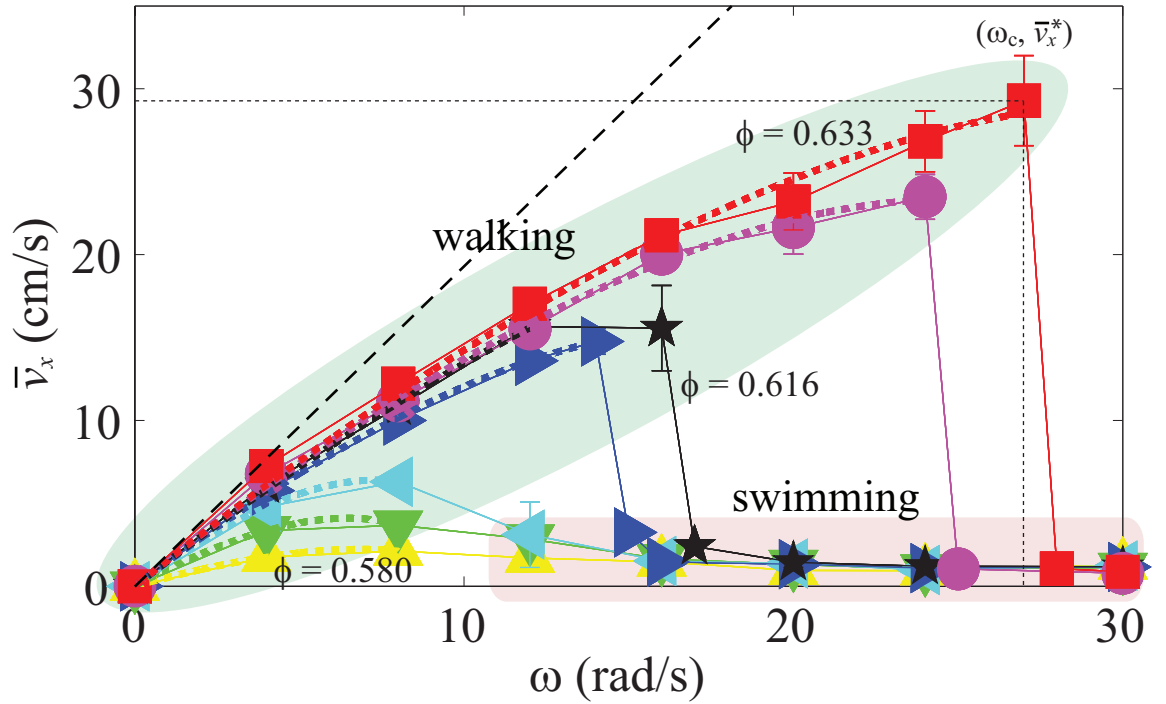


**Figure 62:** Average robot forward speed as a function of limb frequency. For a given volume fraction  $\phi$ ,  $\bar{v}_x$  increases sub-linearly with  $\omega$  to a maximal average speed  $\bar{v}_x^*$  at a critical limb frequency  $\omega_c$  above which the robot fails ( $\bar{v}_x < 2$  cm/s). The solid curves and symbols are for  $\phi = 0.580, 0.590, 0.600, 0.611, 0.616, 0.622$ , and  $0.633$ . The dashed curves are fits from a model discussed in the text. Dashed line indicates a linear speed vs. frequency relationship.

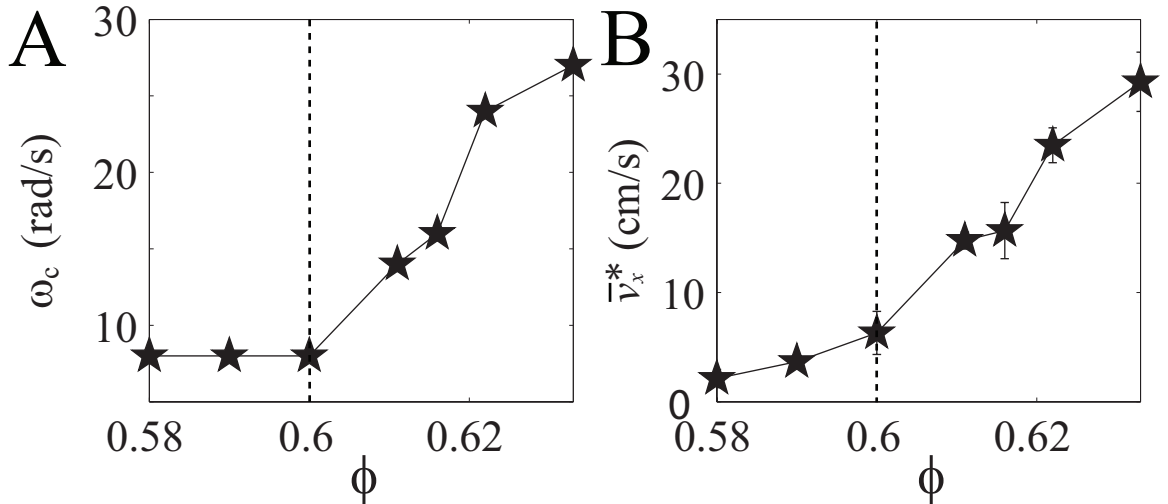


**Figure 63:** Signatures of phase transitions in robot performance. The dependence of (A)  $\omega_c$  and (B)  $\bar{v}_x^*$  on  $\phi$  shows transitions at  $\phi \approx 0.6$  (dashed lines).

#### 4.4.4 Rotary walking model captures robot performance

Starting with the observed kinematics of rotary walking with circular slipping, we constructed a straightforward two-parameter model<sup>‡</sup> that captures the essential elements determining granular locomotion for our legged device and agrees well with the data (dashed lines in Fig. 62). The model, which incorporates simplified kinematics and granular penetration forces while still agreeing well with a more realistic treatment (see Appendix), indicates that reduction of step length through increased penetration depth is the cause of the sub-linear increase in  $\bar{v}_x$  with  $\omega$  and the rapid loss of performance above  $\omega_c$ . The model assumes that the two tripods act independently, that the motion of each tripod can be understood by examining the motion of a single c-leg supporting a mass  $m$  equal to one-third of Sandbot’s total mass, and that the robot undercarriage rests on the surface at the beginning of limb/ground contact.

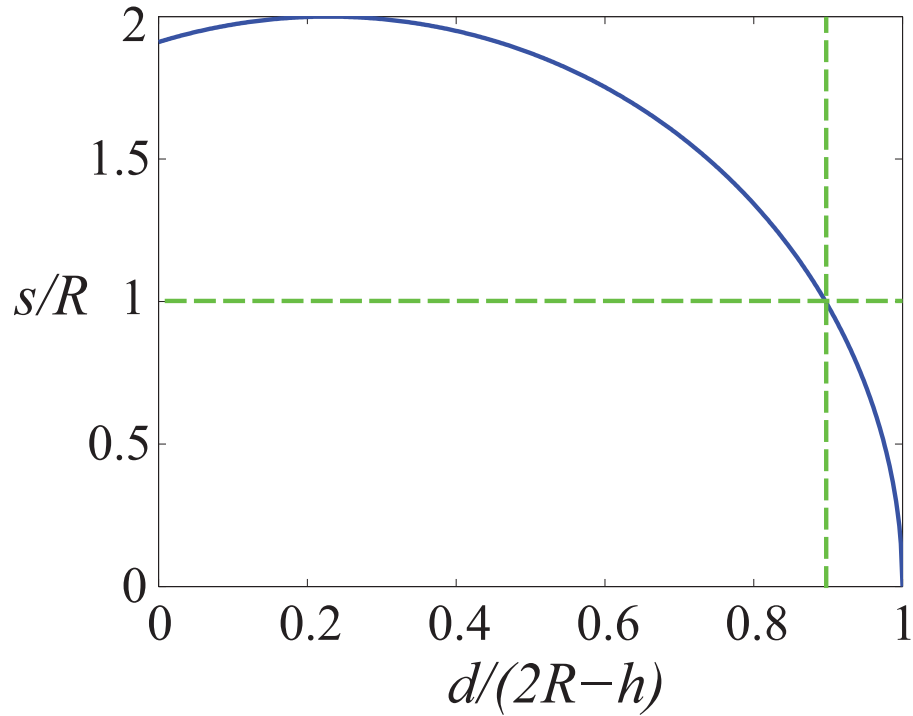


**Figure 64:** Step length as a function of penetration depth. Vertical and horizontal lines indicate critical step size and penetration depth.

<sup>‡</sup>This model was developed by Paul B. Umbanhowar.

Using the geometry of rotary walking (see Fig. 61), the walking step size per c-leg rotation is  $s = 2\sqrt{R^2 - (d + h - R)^2}$ , where  $d$  is the maximum depth of the lowest point on the leg. After the robot has advanced a distance  $s$ , the body contacts the ground and the c-leg moves upward. Since there are two leg rotations per control signal period (one for each tripod), the average horizontal velocity is  $2s \times$  gait frequency or  $\bar{v}_x = \frac{\omega s}{\pi}$ . The maximum limb penetration depth  $d$  is thus the key model component as it controls the stride length (see Fig. 64) and consequently the velocity. Maximum limb depth is determined by balancing the vertical acceleration of the robot center of mass  $ma$  with the sum of the vertical granular penetration force [72]  $kz$  and the gravitational force  $mg$  (Fig. 65), where  $g$  is the acceleration due to gravity, and  $k(\phi)$  is a constant characterizing the penetration resistance of the granular material.

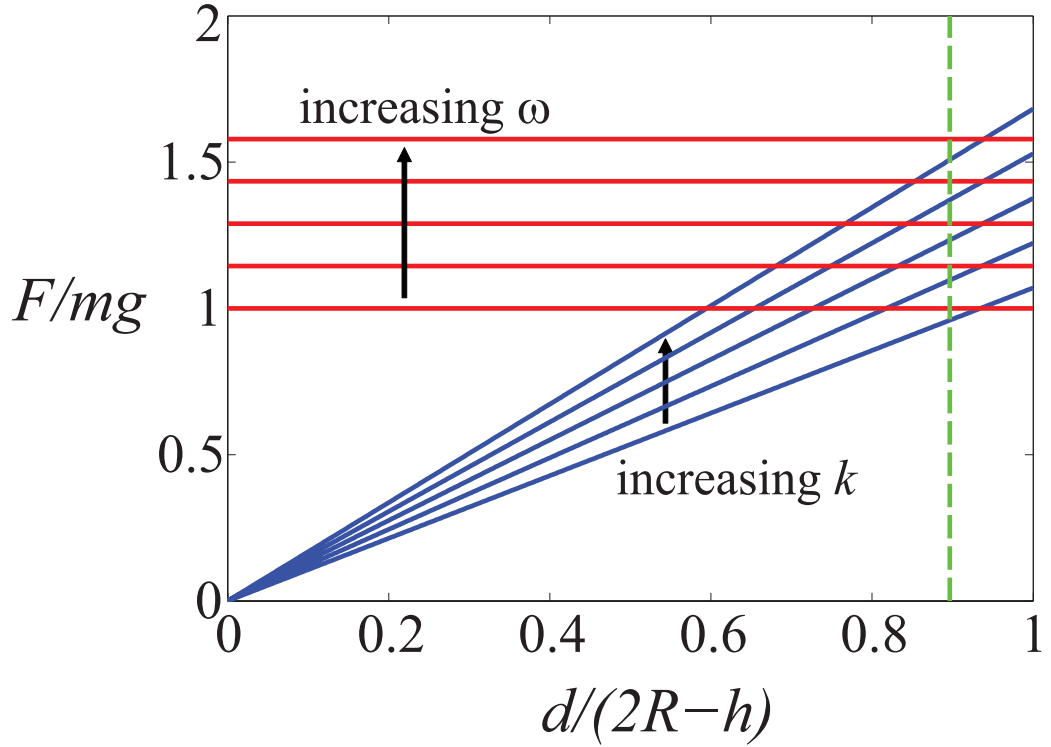


**Figure 65:** Vertical force balance during rotary walking. Granular penetration force for  $k = 1.75, 2.00, 2.25, 2.50,$  and  $2.75 \times 10^2$  N/m (blue) and force required to initiate rotary walking for various  $\omega$  (red) vs penetration depth. The penetration depth at constant  $\phi$  is determined by the intersections of the corresponding blue line with the red lines. Beyond the critical depth (green line) limbs encounter disturbed material and move to lower blue lines.

At low  $\omega$ ,  $ma \approx 0 = \sum F_i = mg - kd$  so  $d = mg/k$ , which is the minimum penetration depth. For finite  $\omega$  the penetration depth is greater since an additional force must be supplied by the ground to accelerate the robot body to the leg speed  $R\omega$  when the c-leg stops translating in the material. Taking  $a = \Delta v/\Delta t$ , with  $\Delta v = R\omega - 0$  and  $\Delta t$  the characteristic elastic response time of the limb and grain bed, gives the acceleration magnitude  $a = R\omega/\Delta t$ . The direction of the acceleration depends on the position of the c-leg. To keep the model simple we equate the vertical component of the acceleration with its magnitude (see discussion of the full model in Appendix). Equating the vertical forces with mass $\times$ acceleration,  $-m\frac{R\omega}{\Delta t} = mg - kd$ , gives c-leg penetration  $d = \frac{m}{k}(\frac{R\omega}{\Delta t} + g)$  with average horizontal velocity  $\bar{v}_x = \frac{2\omega}{\pi} \sqrt{R^2 - \left[\frac{m}{k(\phi)}(\frac{R\omega}{\Delta t} + g) + h - R\right]^2}$ . Fits to this model are indicated by dashed lines in Fig. 62. This expression captures the sub-linear increase in  $\bar{v}_x$  with  $\omega$  and the increase in velocity as the material gets harder (increasing  $k$ ) and indicates that the rotary walking velocity will go to zero when  $\omega$  is sufficiently large.

The parameter  $k$  characterizing the penetration resistance increases monotonically with  $\phi$  from 170 to 220 N/m and varies rapidly below  $\phi \approx 0.6$  and less rapidly above. Its average value of  $\approx 200$  N/m corresponds to a shear stress per unit depth of  $\alpha \approx 380$  kN/m<sup>3</sup> (Area

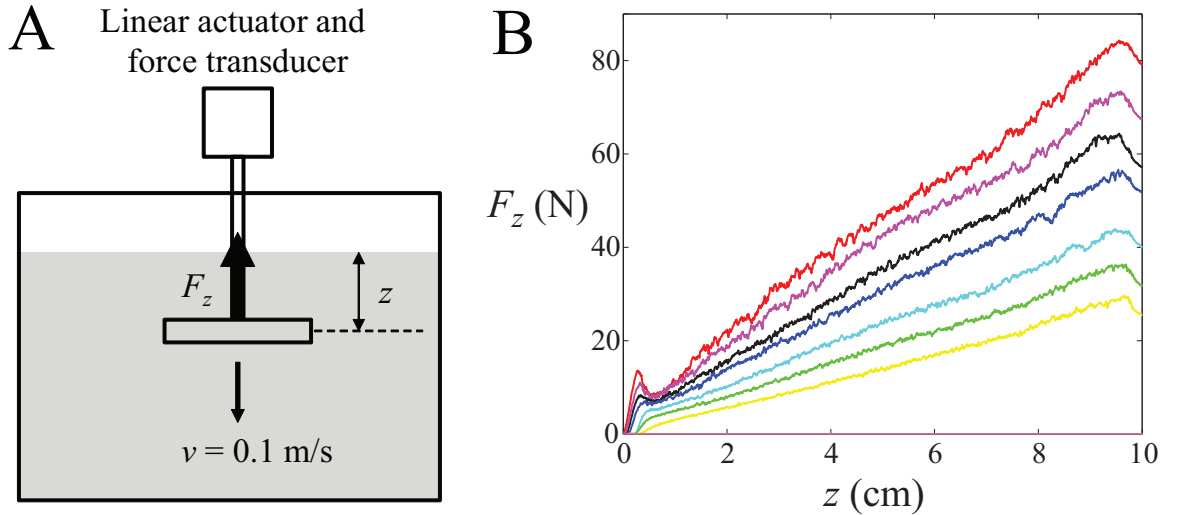


**Figure 66:** Granular penetration force measurements. (A) Experimental setup. (B) Measured granular penetration force as a function of depth for poppy seeds at  $\phi = 0.580, 0.590, 0.600, 0.611, 0.616, 0.622$ , and  $0.633$ .

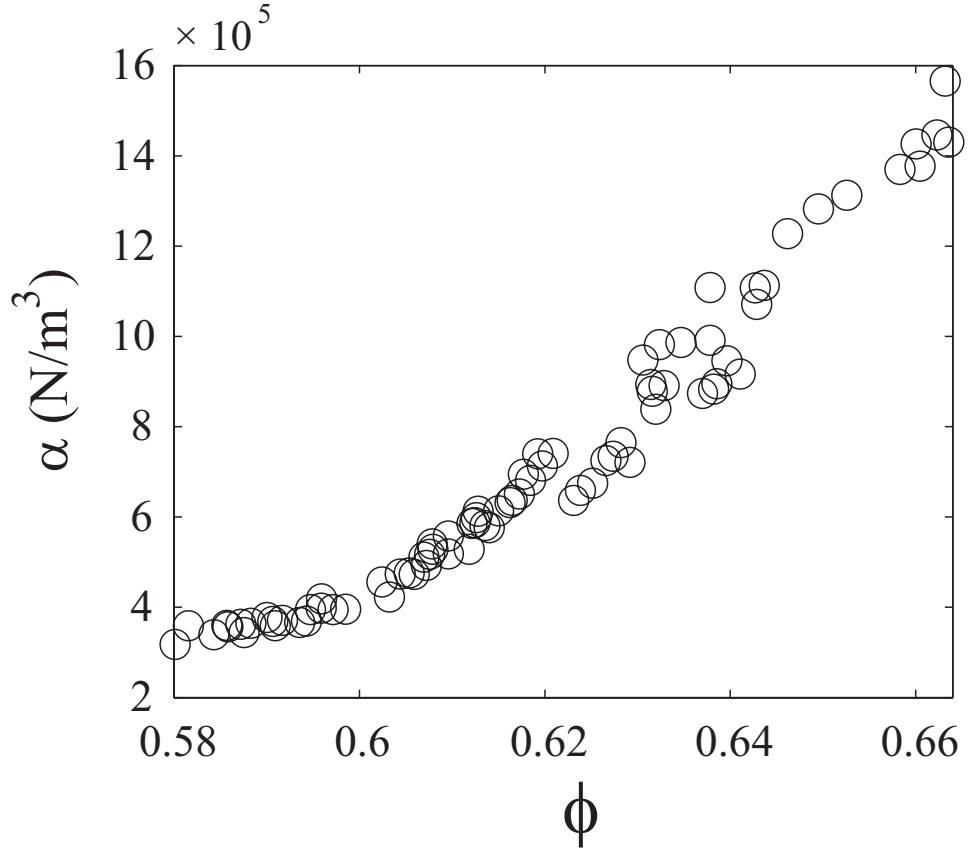


**Figure 67:** Measured yield stress ( $\alpha$ ) per depth as a function of volume fraction ( $\phi$ ) for poppy seeds.

= leg width  $\times R$ ) which is in good agreement with penetration experiments we performed on poppy seeds that yield  $\alpha = 300$  and  $480 \text{ kN/m}^3$  for  $\phi = 0.580$  and  $0.622$  respectively (Fig. 67) and is consistent with previous measurements of penetration into glass beads [146] where  $\alpha \approx 250 \text{ kN/m}^3$ . In contrast,  $\Delta t$  varies little with  $\phi$  and has an average value of 0.4 sec which compares favorably with the robot's measured hard ground oscillation period of 0.2 sec when supported on a single tripod. In our model we assume the two tripods do not simultaneously contact the ground, however, in soft ground this is not the case, which consequently reduces the effective step size per period from  $2s$  to a lesser value. The fit value of  $\Delta t$  is sensitive to this variation; reducing the step size per period by just 13 % decreases  $\Delta t$  to 0.2 sec while  $k$  is increased by less than 10 %.

Our model indicates that for deep penetration the walking step length is quite sensitive to penetration depth. As the walking step size goes to zero with increasing  $\omega$  or decreasing  $\phi$ ,

the fraction of the ground contact time that the leg slips through the grains (swimming) goes to one. Swimming in granular media differs from swimming in simple fluids as the friction dominated thrust and drag forces are largely rate independent at slower speeds [69, 70]. When thrust exceeds drag, the robot advances a distance proportional to the net force divided by  $\omega^2$  per leg rotation, and, consequently, velocity is proportional to  $\omega^{-1}$ . This explains the weak dependence of  $\bar{v}_x$  on  $\omega$  in the swimming mode. (The increase in robot velocity with decreasing  $\omega$  is bounded by the condition that the robot center of mass velocity in the ground (lab) reference frame cannot exceed the horizontal leg speed in the center of mass coordinates of the robot, which ensures the existence of and eventual transition to a walking mode as  $\omega$  is decreased.)

#### 4.4.5 Trigger of swimming mode

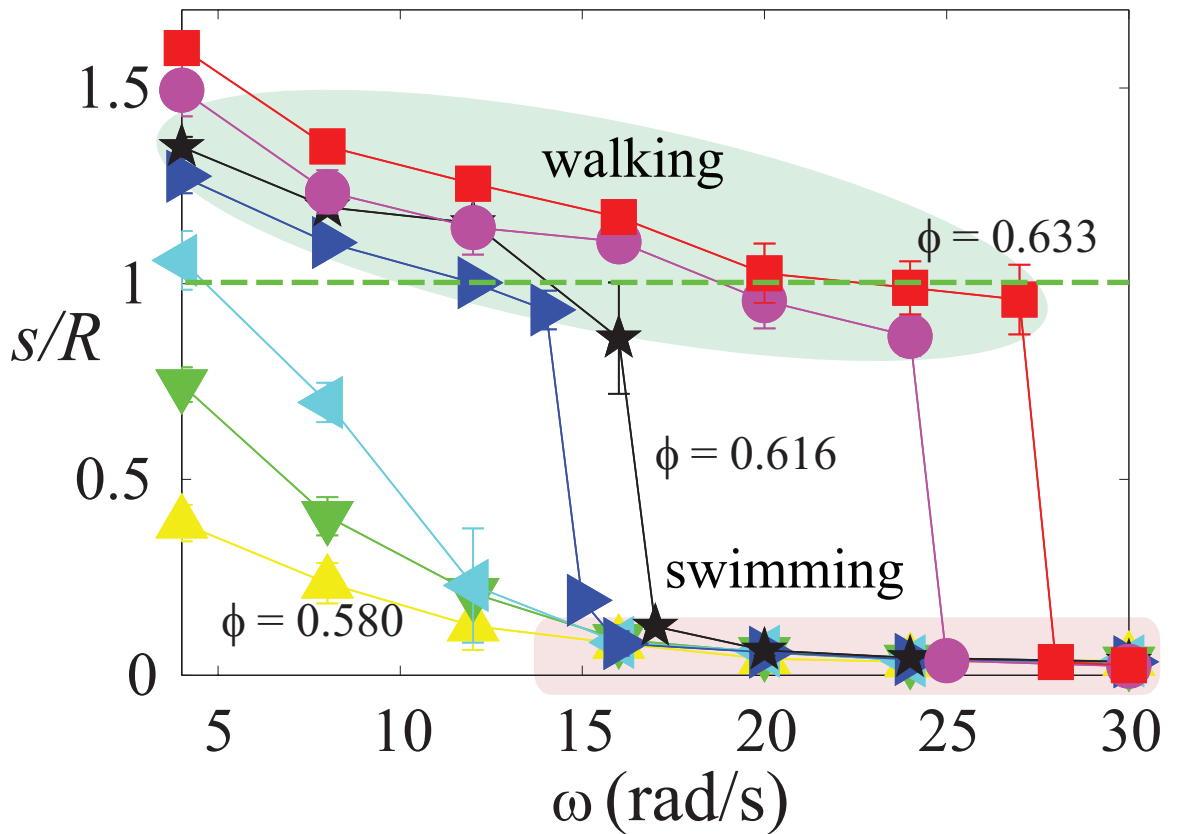


**Figure 68:** Step length as a function of limb frequency. Step length is derived from  $2s = 2\pi\bar{v}/\omega$  reveals the condition for the onset of swimming is  $s/R < 1$ . The solid lines and symbols are for  $\phi$  values of 0.580, 0.590, 0.600, 0.611, 0.616, 0.622, and 0.633.

The transition from walking to swimming appears gradual for  $\phi \lesssim 0.6$  since the penetration depth increases slowly with  $\omega$  at small  $\omega$  ( $R\omega/\Delta t \ll g$ ) and the  $\omega^{-2}$  contribution to the per step displacement from swimming is relatively large (see *e.g.* the data at  $\omega = 12$  rad/sec in Fig. 64). However, for  $\phi \gtrsim 0.6$ , the transition is abrupt. We hypothesize that this sharp transition occurs because the per step displacement is reduced sufficiently that the legs encounter ground disturbed by the previous step. At higher  $\phi$ , the volume fraction of the disturbed ground is significantly less compared to the bulk which increases penetration and consequently reduces the walking step size to near zero; this is not the case for the transition from walking to swimming at low  $\phi$  (and low  $\omega$ ) where the  $\phi$  of the disturbed material is relatively unchanged relative to its initial value. For the robot to avoid disturbed ground it must advance a distance  $R$  on each step, i.e.  $s \geq R$ , or in terms of the penetration depth,  $d \leq (\frac{\sqrt{3}}{2} + 1)R - h = 5.0$  cm. The disturbed ground hypothesis is supported by calculations of the step length derived from the average velocity  $2s = 2\pi\bar{v}_x/\omega$  which clearly show a critical step length near  $s/R = 1$  at the walking/swimming transition (Fig. 68). The somewhat smaller value of  $s/R \approx 0.9$  evident in the figure can be understood by recognizing that for  $s$  slightly smaller than  $R$  the majority of the c-leg still encounters undisturbed material.

At higher  $\omega$  in the swimming mode, the limbs move with sufficient velocity to fling material out of their path and form a depression which reduces thrust because the limbs are not as deeply immersed on subsequent passes through the material. However, as limb velocity increases, thrust forces becomes rate dependent and increase because the inertia imparted to the displaced grains is proportional to  $\omega^2$ . Between strokes, the excavated depression re-fills at a rate dependent on the difference between the local surface angle and the angle of repose [147] and the depression size. Investigating the competition between these different processes at high  $\omega$  and their consequences for locomotion could be relevant to understanding how to avoid becoming stranded or to free a stranded device.

## 4.5 Conclusions

Our study systematically investigates the performance of a legged robot on granular media, varying both properties of the medium (volume fraction) and properties of the robot (limb frequency and gait). Our experiments reveal how precarious it can be to move on granular media: changes in  $\phi$  of  $< 1\%$  result in either rapid motion or failure to move, and slight kinematic changes have a similar effect. A kinematic model captures the speed dependence of SandBot on granular material as a function of  $\phi$  and  $\omega$ . The model reveals that the sublinear dependence of speed on  $\omega$  and the rapid failure for sufficiently small  $\phi$  and/or large  $\omega$  are consequences of increasing limb penetration with decreasing  $\phi$  and/or increasing  $\omega$ , and changes to local  $\phi$  due to penetration and removal of limbs. Although detailed studies of impact and penetration of simple rigid objects exist [72, 70, 74], further advances in performance (including increases in efficiency) and design of limb morphology will require a more detailed understanding of the physics associated with penetration, drag, and crater formation and collapse, especially their dependence on  $\phi$ . Better understanding of this physics can guide development of theory of interaction with complex media advanced enough to predict limb design [148] and control [149] strategies, similar to the well-developed models of aerial and aquatic craft. Analysis of physical models such as SandBot can also inform locomotion biology in understanding how animals appear to move effortlessly across a diversity of complex substrates [6, 150]. Such devices will begin to have capabilities comparable with organisms; these capabilities could be used for more efficient and capable exploration of challenging terrestrial (e.g., rubble and disasters sites) and extraterrestrial (e.g., the Moon and Mars) environments.

## 4.6 Appendix

The model presented in the main body of the manuscript simplifies the underlying physics while capturing the essential features determining robot speed. Here, we describe a more complete model (which lacks a simple expression for  $\bar{v}_x$ ) and compare its predictions to those of the simple model<sup>§</sup>. The exact expression for the vertical acceleration component of the body when the limbs gain purchase is  $ma_z = ma\sqrt{\frac{2(h+z)}{R} - \left(\frac{h+z}{R}\right)^2}$  instead of the approximation  $ma_z = ma$  used in the simple model. Using the exact expression, the vertical granular force necessary for walking still has the same peak value of  $m(a+g)$  but decreases to  $mg$  when the limb is at its lowest point.

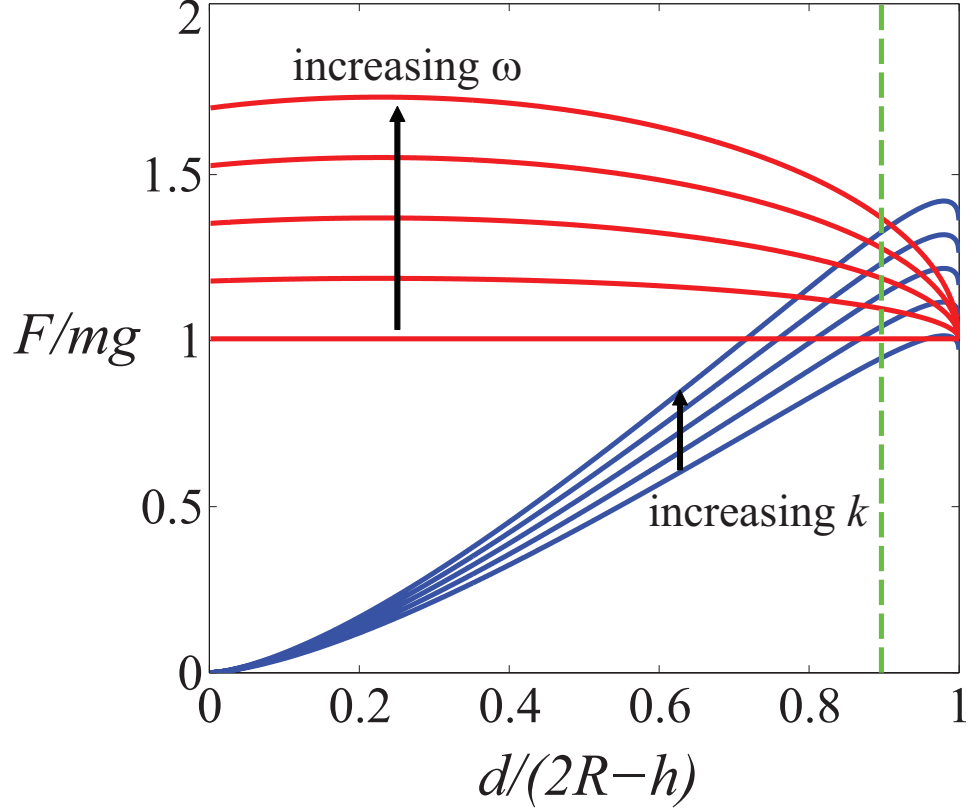
The second approximation we used in the simple model is that the grain force on the leg is  $kz$ . This expression is only strictly valid for a flat-bottomed vertically penetrating intruder [70]. Because the leg is a circular arc, the leg-grain contact area and the vertical component of the grain force are functions of limb depth and leg-shaft angle. Generalizing  $kz$  to a local isotropic yield stress given by  $\alpha z$  [10] Because the leg is a circular arc, the leg-grain contact area and the vertical component of the grain force are functions of limb depth and leg-shaft angle. Generalizing  $k_z$  to a local isotropic yield stress given by  $Rd\psi$  in length at depth  $z$  is  $dF_z = w\alpha z R d\psi \cos \psi$ , where  $w$  is the limb width and  $\psi$  is the angular position of the segment. The total vertical component of the force acting on the leg is then  $Rw\alpha \int_{-\psi_{min}}^{\psi_{max}} z \cos \psi d\psi$ . Substituting  $z(\psi) = R(\cos \psi - 1) + d$  and integrating gives  $F_z = Rw\alpha \left[ \frac{R}{2}(\psi + \cos \psi \sin \psi) + (d - R) \sin \psi \right]_{-\psi_{min}}^{\psi_{max}}$ , where  $\psi_{max} = \cos^{-1}(1 - d/R)$  and  $\psi_{min} = \psi_{max}$  when the leg tip is above the center of the c-leg and  $\cos^{-1}\left(\frac{d+h}{R} - 1\right) + \Delta\xi$  when it is below the center of the c-leg.  $\Delta\xi$  is the angular extent of the limb beyond  $\pi$  (e.g  $\Delta\xi = 0$  for a semi-circular limb).

Fig. 69 shows that the full model using realistic parameters shares the same essential physics as the simple model. For a given material strength (blue curves), the penetration depth increases with increasing  $\omega$  (intersection of blue and red curves) until the step length is reduced below the critical value (vertical green dashed line). Fig. 70 presents fits to the

---

<sup>§</sup>These models were developed by Paul B. Umbanhowar.

experimental data of the average speed  $\bar{v}_x$  vs.  $\omega$  for the full and simple models for  $\bar{v}_x \leq \bar{v}_x^*$  at each  $\phi$ . The fits and fit parameters for the simple ( $\bar{\Delta t} = 0.4$  s,  $\bar{\alpha} = 470$  kN/m<sup>3</sup>) and full ( $\bar{\Delta t} = 0.2$  s,  $\bar{\alpha} = 330$  kN/m<sup>3</sup>) models are in good agreement when the step length is less than the critical value  $s = R$ .



**Figure 69:** Vertical force balance during rotary walking from the full model. Non-dimensionalized granular force (blue curves) for  $\alpha = 250, 275, 300, 325,$  and  $350$  kN/m<sup>3</sup> and the required force to initiate rotary walking,  $a_z/g + 1$  (red curves) for  $\omega = 0, 7.5, 15, 22.5, 30$  rad/s for the full model as a function of limb penetration depth with a  $225^\circ$  c-leg arc angle and  $\Delta t = 0.15$  s. The intersection of the red and blue curves determines the penetration depth of the limb and consequently the step length. At constant material strength (blue)  $d$  increases with increasing  $\omega$ , whereas at constant  $\omega$ , increasing material strength reduces  $d$ . The vertical green dashed line indicates the critical penetration depth beyond which the leg encounters material disturbed by the previous step.

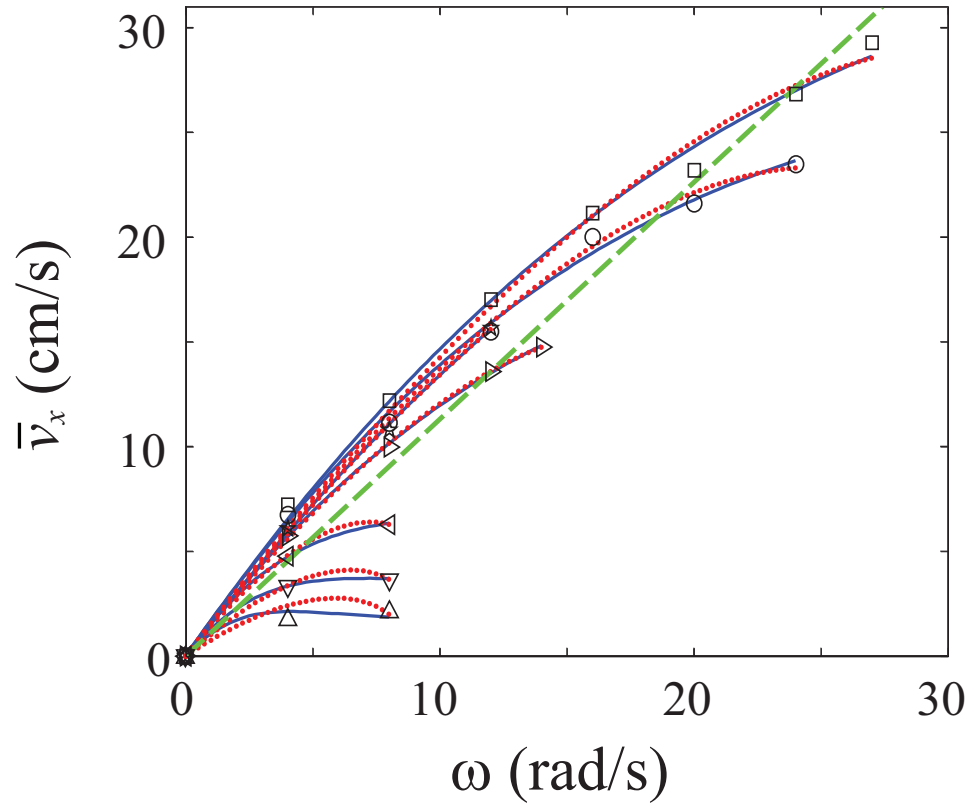


**Figure 70:** Comparison of full model predicted speed with simple model and experiment. Red dotted curve is from simple model, and blue solid curve is from full model. Models are fit to the measured robot speed (symbols) for  $\bar{v}_x \leq \bar{v}_x^*$ . The green dashed line indicates  $\bar{v}_x^* = R\omega/\pi$  or equivalently  $s = R$ . In A and B,  $h = 2.5$  cm,  $R = 3.55$  cm,  $w = 1.2$  cm, and  $m = 767$  g.

## CHAPTER V

### THE EFFECT OF LIMB KINEMATICS ON THE SPEED OF A LEGGED ROBOT ON GRANULAR MEDIA

#### *5.1 Summary*

Achieving effective locomotion on diverse terrestrial substrates can require subtle changes of limb kinematics. Biologically inspired legged robots (physical models of organisms) have shown impressive mobility on hard ground but suffer performance loss on unconsolidated granular materials like sand. Because comprehensive limb-ground interaction models are lacking, optimal gaits on complex yielding terrain have been determined empirically. To develop predictive models for legged devices and to provide hypotheses for biological locomotors, we systematically study the performance of SandBot, a small legged robot, on granular media as a function of gait parameters. High performance occurs only in a small region of parameter space. A previously introduced kinematic model of the robot combined with a new anisotropic granular penetration force law predicts the speed. Performance on granular media is maximized when gait parameters minimize body acceleration and limb interference, and utilize solidification features of granular media.\*

---

\*This Chapter is a published paper by Chen Li, Paul B. Umbanhowar, Haldun Komsuoglu, and Daniel I. Goldman, *Experimental Mechanics* (2010) [97].

## 5.2 Introduction

To move effectively over a wide range of terrestrial terrain requires generation of propulsive forces through appropriate muscle function and limb kinematics [1, 2]. Most biological locomotion studies have focused on steady rhythmic locomotion on hard, flat, non-slip ground. On these surfaces kinematic (gait) parameters like limb frequency, stride length, stance and swing durations, and duty factor can change as organisms walk, run, hop and gallop [1]. There have been fewer biological studies of gait parameter modulation on non-rigid and non-flat ground, although it is clear that gait parameters are modulated as the substrate changes during challenges like climbing [151, 150], running on elastic/damped substrates [128], transitioning from running to swimming [152], and running on different preparations of granular media [82]. Even subtle kinematic changes in gait can lead to major differences in limb function [153]. A major challenge is to develop models of limb interaction with complex substrates and to develop hypotheses for how organisms vary gait parameters in response to substrate changes.

The RHex class of model locomotors (robots) has proved useful to test hypotheses of limb use in biological organisms on hard ground [55] and recently on more complex ground with few footholds [6] or the ability to flow [92]. These hexapedal devices model the dynamically stable locomotion of a cockroach and were the first legged machines to achieve autonomous locomotion at speeds exceeding one body length/s. In these devices, complexity in limb motion is pared down to a few biologically relevant parameters controlling intra-cycle “stance” and “swing” phases of 1-dof rotating limbs (referred to as “gait” parameters hereafter; see detailed description in Methods and Results). When these gait parameters are appropriately adjusted, RHex shows performance comparable in speed and stability to organisms on a diversity of terrain [87]. However, because of the scarcity of existing models of limb interaction with complex substrates, adjustment of the gait parameters is typically done empirically [57, 50].

Sand, a granular medium [22], is of particular interest for studies examining the effects of limb kinematics on locomotor performance on yielding terrain. In a previous study [92]

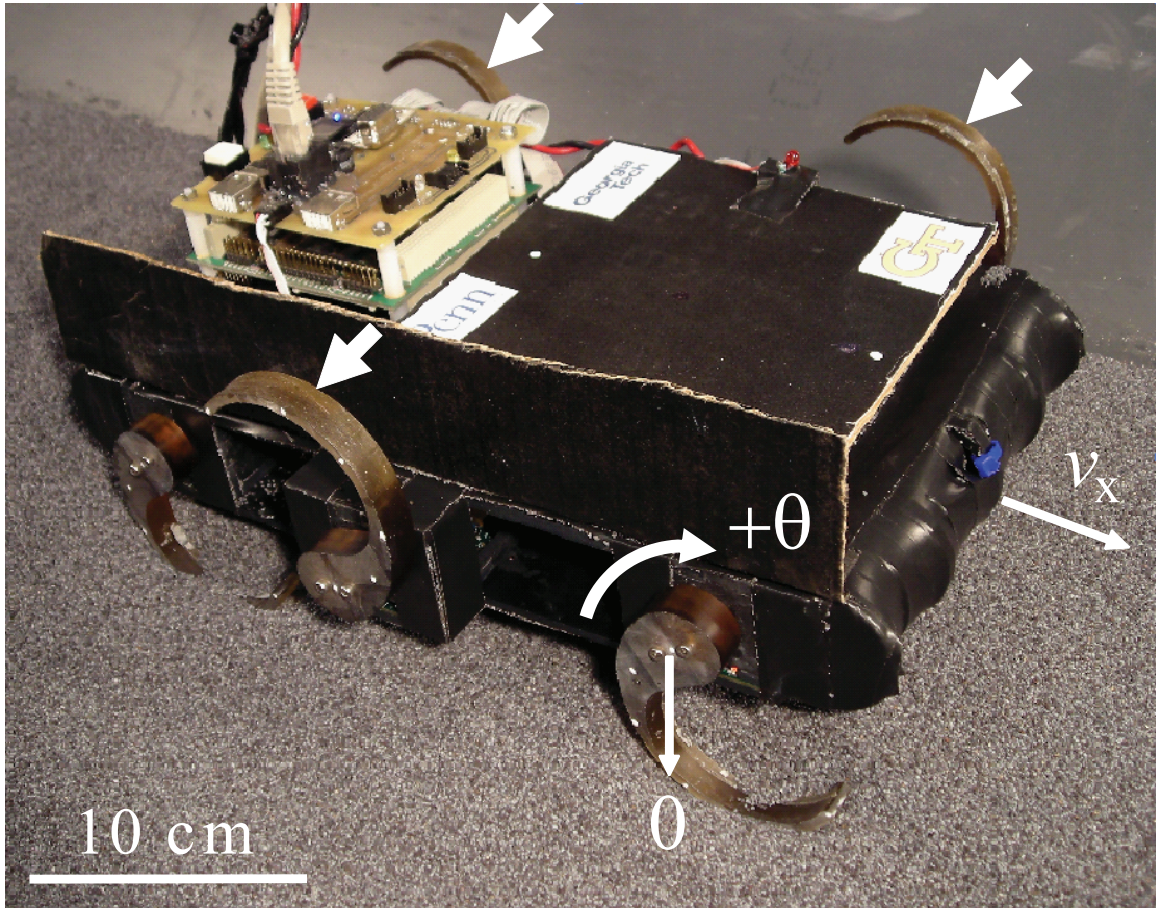


**Figure 71:** SandBot, a six-legged insect inspired robot, moves with an alternating tripod gait. The three arrows indicate the limbs of one tripod.

we found that minor changes in the limb kinematics of a small RHex-class robot, SandBot<sup>†</sup> (Fig. 71), produced major changes in its locomotor mode and performance (speed) on a granular medium, poppy seeds. This sensitivity occurs, in part, because forced granular media remain solid below the yield stress, but can flow like a fluid when the yield stress is exceeded [10]. We tested SandBot on granular media of different yielding properties (set by granular volume fraction) at various limb frequencies but with the other gait parameters fixed. While there is no fundamental theory at the level of fluid mechanics that accounts for the physics of the solid-fluid transition of granular media or the dynamics of the fluidized

<sup>†</sup>This robot was developed by Haldun Komsuoglu and Daniel E. Koditschek.

regime, empirical models of granular penetration force have proved useful to predict SandBot's speed [92]. SandBot's propulsion is determined by factors that control this transition during limb-ground interaction (limb penetration depth, limb speed, body mass, grain friction, volume fraction, etc.). Using a simplified equation describing the granular penetration force, we developed a kinematic model to explain the locomotion of SandBot.

In this study, we advance our understanding of the effects of limb kinematics on locomotor performance by testing SandBot with varying gait parameters on sand of fixed yield strength and at fixed limb frequency. We find that robot speed depends sensitively on limb kinematics; while the original model qualitatively captures this sensitivity, the penetration force used in the model and other assumptions need to be modified to explain some important features. Our study not only reveals the specific optimal kinematics for SandBot on granular media, but also advances our understanding of how in general to achieve effective legged locomotion on complex terrain.

### 5.3 Background and review of previous study

To understand the effect of limb kinematics addressed here, we first summarize the mechanism of SandBot locomotion on granular media (called rotary walking) discovered in our previous study [92]. In this section, we discuss the physics of granular media that controls the limb penetration depth (which governs locomotion performance) and then review our previous experiments and kinematic model.

#### 5.3.1 Physics of limb-granular media interaction

The physics that controls locomotor performance is the relative magnitude of the penetration resistance force (originating in the granular media) and the sum of the external forces (weight, inertial forces). When these balance, the granular media solidifies, allowing the robot to be supported at a fixed limb penetration depth.

The previous SandBot study [92] revealed that as the limb (or any simple intruder) vertically penetrates into the medium, the penetration force scales with  $z$ , the depth of the intruder below the surface [72], as  $F_p(z) = k(\phi)z$ , where  $\phi$  is the volume fraction, the ratio of the solid volume of the granular media to the volume that it occupies (for natural dry sand,  $0.55 < \phi < 0.64$ ). The constant,  $k(\phi)$ , characterizes the penetration resistance and increases with  $\phi$ . In this study we keep  $\phi$  fixed at approximately the critical packing state [154, 93, 10, 155] (which is close to the as-poured volume fraction) where granular media neither globally dilate nor compact in response to shear.

#### 5.3.2 Review of previous observations and model

In the previous study of SandBot [92], we fixed intra-cycle limb kinematics (by using gait parameters that produce consistent motion on granular media) and measured SandBot's average speed  $\bar{v}_x$  on poppy seeds as a function of volume fraction and the cycle-averaged limb frequency  $\omega$ . We observed a sensitive dependence of  $\bar{v}_x$  on both  $\phi$  and  $\omega$ , and developed a kinematic model which explained this dependence and revealed two distinct locomotor modes determined by whether the granular media solidifies during limb-ground interaction.

Our kinematic model describes the limb-ground interaction of SandBot by considering

the motion of just a single limb (Fig. 72). SandBot has six approximately c-shaped limbs (c-legs) divided into two alternating tripods. C-legs in the same tripod rotate in synchrony and each c-leg rotates about a horizontal axis normal to the robot body. We simplify the multi-leg ground interaction of each tripod to that of a single limb carrying  $1/3$  the total body mass  $3m$  (2.3 kg), as body weight is approximately uniformly distributed between each c-leg. We also considered a c-leg as a simple intruder ignoring its more complicated geometry, *i.e.*  $F_p(z) = kz$ . The previous study [92] showed that the simple intruder approximation gave approximately the same results as a more realistic treatment in which penetration force was integrated over the submerged leading surface of a c-leg. In this study we use the simple intruder approximation.

We make the approximation that SandBot's body is in stationary contact with the

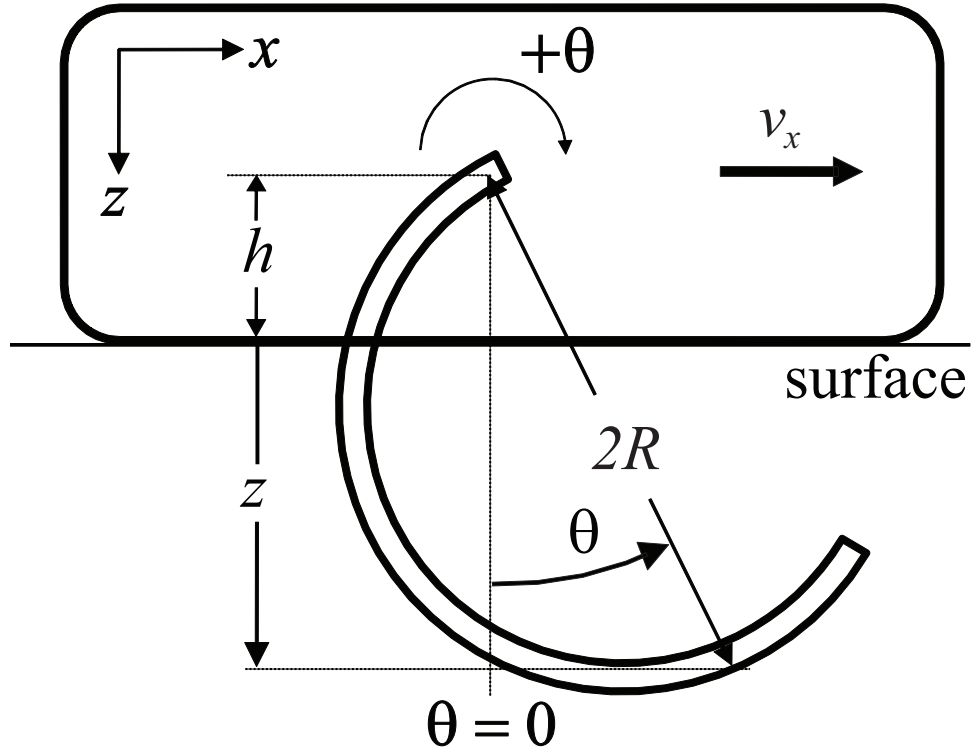


**Figure 72:** Schematic of single-leg representation of SandBot, with mass  $m = 1/3$  SandBot's total mass. With the body contacting the surface, the motor axle is height  $h = 2.5$  cm above the ground. The c-leg is approximately a circular arc (radius  $R = 3.55$  cm, arc span 225 degree). Leg angle  $\theta$  is measured clockwise about the axle and between the downward vertical and a diameter through the axle. Leg depth  $z = 2R \cos \theta - h$ .

surface at the onset forward motion in each cycle<sup>‡</sup>, and define the c-leg’s angular position,  $\theta$ , as the clockwise angular displacement from the configuration where the center of curvature of the c-leg is directly beneath the axle, see Fig. 72. During a full rotation, as  $\theta$  changes from  $-\pi$  to  $\pi$ , the c-leg initially contacts the ground at  $\theta = \alpha_i$  and loses ground contact at  $\theta = \alpha_i$ . Because leg depth can be approximated as  $z = 2R \cos \theta - h$  when the body is in contact with the surface<sup>§</sup>, penetration force can be written as  $F_p(\theta) = 2Rk [\cos \theta - \frac{h}{2R}]$  (blue curve in Fig. 73), where  $R = 3.55$  cm and  $h = 2.5$  cm are the radius of the c-leg and the hip height (*i.e.* distance from c-leg axle to underside of body) respectively.

Of prime importance in determining SandBot’s performance is the magnitude of the penetration force  $F_p(\theta)$  relative to the sum of the forces required to support the body weight and accelerate the body upward  $m(g + a)$  (red curve in Fig. 73), where  $g$  is the acceleration due to gravity and  $a$  the acceleration [92]. The relevant acceleration is given by the jump in robot speed when the granular media solidifies,  $R\omega$ , divided by the characteristic response time of the c-leg interacting with the granular media,  $\Delta t(\phi)$ , *i.e.*  $a = R\omega/\Delta t$ . Two distinct locomotor modes are possible depending on whether or not  $F_p(\theta = 0) > m(g + a)$ :

1. Rotary walking – movement with solidification (see Fig. 72, Fig. 73, Fig. 74): As the c-leg rotates into the ground after initial leg-ground contact at  $\theta = \alpha_i$ , the penetration force increases with increasing depth. In the rotary walking regime the material beneath the c-leg solidifies and leg penetration stops at an angle  $\theta = \beta_i$  when  $F_p(\beta_i) = m(g + a)$ , see Fig. 73, Fig. 74. Since the frictional force between the c-leg and granular material is insufficient for the leg to roll, the c-leg instead rotates about its center of curvature (green circle and arrow) lifting and advancing the robot in the process. Rotary walking continues until  $\theta = \beta_f$ , beyond which the c-leg again penetrates through the material since  $F_p(\theta) < m(g + a)$  and the body is again in contact with

---

<sup>‡</sup>When tripods move in phase (*e.g.*  $d_c = 1$ ) this approximation is exact as the body rests on the surface during the swing phase.

<sup>§</sup>In our previous study [92] we measured leg depth to the bottom of the c-leg; here we measure it to the point on the c-leg furthest from the motor axle to simplify the expression for penetration force vs. angle. As  $mg$  is comparable to  $kz$  for this study, the smallest penetration depth where rotary walking begins is close to the maximum possible value of  $2R - h$  so that the simplified expression for the leg depth is nearly identical to the exact value.

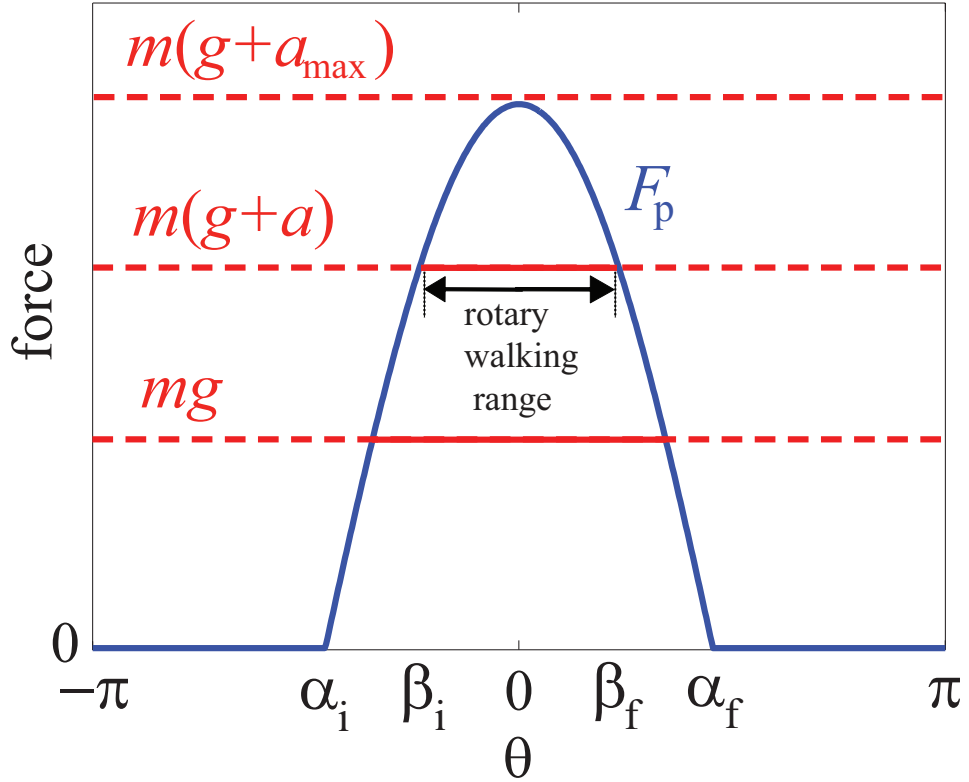


**Figure 73:** Vertical forces on SandBot during locomotion. Magnitude of penetration force  $F_p$  (blue curve) relative to force required for upward motion,  $m(g+a)$ , (red lines) determines the locomotor mode. The force required for quasi-static movement ( $mg$ ) is shown for reference. When  $F_p$  and  $m(g+a)$  intersect rotary walking occurs. When  $F_p$  and  $m(g+a)$  do not intersect (dashed red curve and above), the robot swims.

the ground (blue circle and arrow). Rotary walking thus occurs over a finite range of leg angle  $\beta_i < \theta < \beta_f$  or  $[\beta_i, \beta_f]$  (horizontal arrow in Fig. 73 and gray sector in Fig. 74) where  $\beta_i$  and  $\beta_f$  are determined by  $F_p(\beta_{i,f}) = 2Rk(\cos \beta_{i,f} - \frac{h}{2R}) = m(g+a)$ . For a given  $[\beta_i, \beta_f]$ , Fig. 74 shows that the robot advances a distance  $s = R(\sin \beta_f - \sin \beta_i)$ , where we call  $s$  the step size. During one complete gait cycle of period  $T$ , each alternating tripod advances the robot by  $s$ , giving an average robot speed of  $\bar{v}_x = 2s/T = s\omega/\pi$ .

2. Swimming – movement without solidification: When  $F_p(0) < m(g+a)$  (Fig. 73, dashed red curve), the granular material beneath the penetrating c-leg never solidifies and rotary walking does not occur, *i.e.*  $\beta_i = \beta_f = 0$ . Instead, the limb constantly slips

through the surrounding fluidized granular material, similar to a swimmer's arm in water, and the robot advances slowly ( $\bar{v}_x < 1$  cm/s). In this regime forward motion occurs when the frictional and inertial (drag) forces generated by the c-legs exceeds the frictional force between the robot body and the surface.

The two constants characterizing the interaction with the granular medium,  $k$  and  $\Delta t$ , together with limb frequency  $\omega$ , determine the relative magnitudes of  $F_p$  and  $m(g + a)$  and consequently control which locomotor mode the robot operates in. Reducing  $k$  (by decreasing  $\phi$ ) and/or increasing  $\omega$  reduces the rotary walking range; in other words, the less

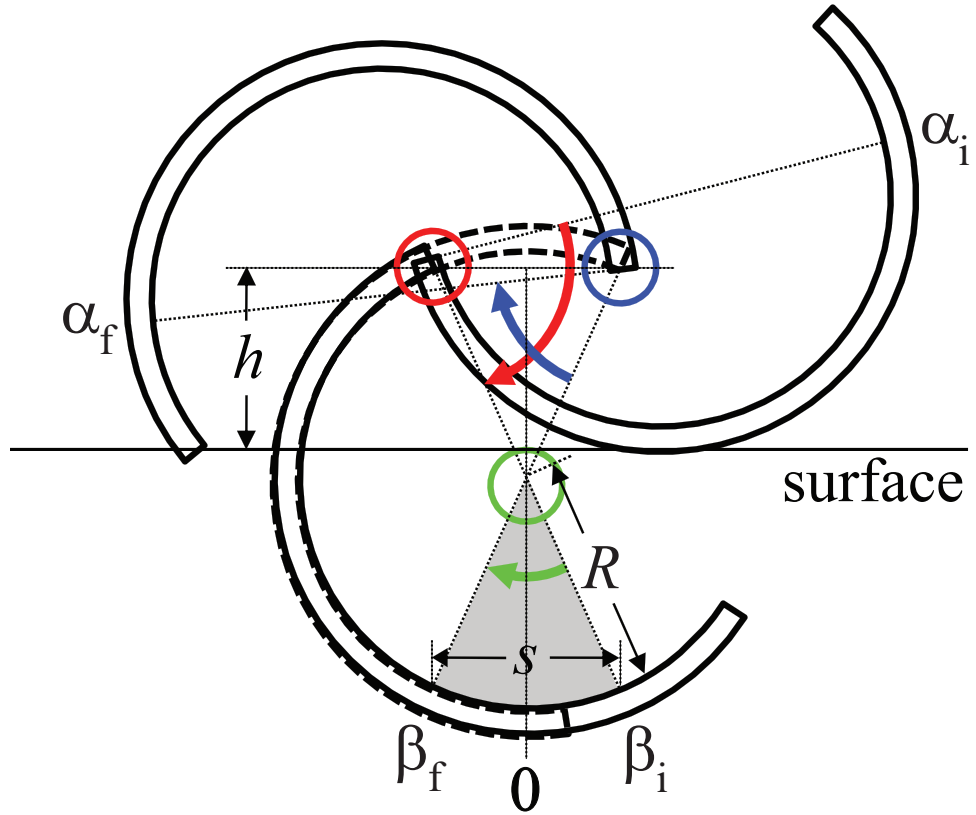


**Figure 74:** Schematic of rotary walking. The granular material flows in the intervals  $[\alpha_i, \beta_i]$  (red arrow) and  $[\beta_f, \alpha_f]$  (blue arrow) where  $F_p < m(g + a)$  and the c-leg rotates about the axle (red and blue circles). The material is a solid in the interval  $[\beta_i, \beta_f]$  (gray sector; line with arrows in Fig. 73) where  $F_p$  exceeds  $m(g + a)$  and the c-leg rotates about its center (green circle and arrow), lifting and propelling body forward by step length  $s = R(\sin \beta_f - \sin \beta_i)$ . The c-leg is above the ground in the interval  $[\alpha_f, \alpha_i + 2\pi]$ . Note that  $[\alpha_i, \alpha_f]$  in Fig. 73 is symmetric to vertical ( $\theta = 0$ ) as a result of assuming the force is isotropic.

compact the granular material is and/or the faster the limbs rotate, the deeper the c-legs have to penetrate before the granular material solidifies and rotary walking begins, and the more susceptible the robot is to entering the slow swimming mode. This simple kinematic model captures the observed sensitive dependence of  $\bar{v}_x$  on  $\phi$  and  $\omega$ , with  $k(\phi)$  and  $\Delta t(\phi)$  as two fitting parameters.

In summary, our previous study of SandBot [92] showed that to locomote effectively on granular media, limbs kinematics that access the solid phase of granular media should be employed.

## 5.4 Methods and Results

The limb kinematics of each tripod during one cycle are parameterized by three “gait parameters”, see Fig. 75A,B. The kinematics of both tripods are periodic (with period  $T$ ) and offset by half a period  $T/2$  but are otherwise identical. For the conditions in this and previous experiments, a motor controller in the robot ensures that the target kinematics are achieved. Limb kinematics consist of a “swing” phase (orange), which is typically faster, and a “stance” phase (green), which is typically slower, with respective frequencies  $\omega_f$  and  $\omega_s$ .

During hard ground locomotion in the RHex-class of Robots (and for animal locomotion in general), “swing” and “stance” phases typically correspond to off-ground and ground-contact phases, respectively. But because during locomotion on granular media this correspondence is not necessarily true, we simply call them fast and slow phases. In practice the fast and slow phases are implicitly defined by the triplet  $\{\theta_s, \theta_0, d_c\}$  where  $\theta_s$  is the angular extent of the slow phase,  $\theta_0$  is the angular location of the center of the slow phase, and  $d_c$  is the duty cycle of the slow phase (the fraction of the period in the slow phase). Specifying the cycle averaged limb frequency  $\omega$  fully determines the motion of the limbs in the robot

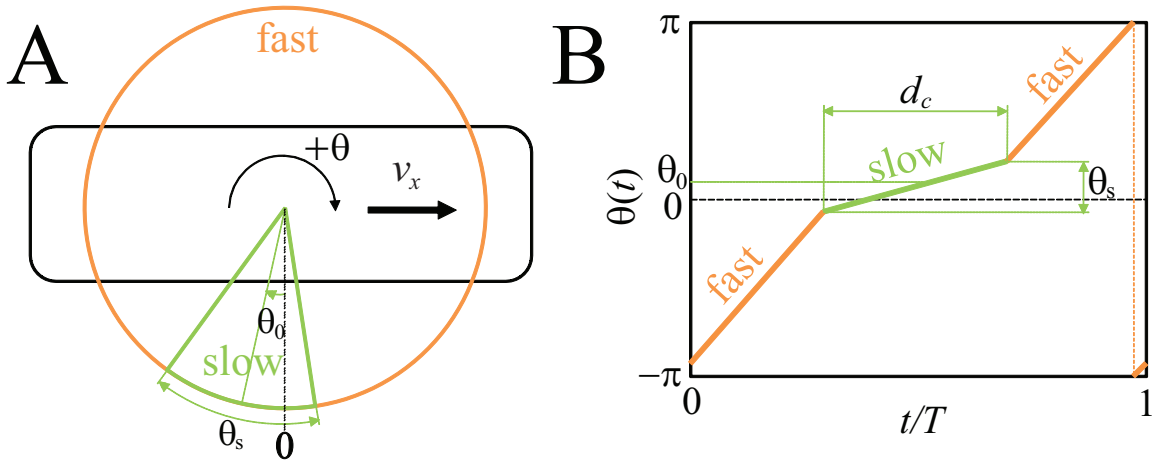


**Figure 75:** SandBot’s intra-cycle limb kinematics. (A) Each leg rotation is composed of a fast phase (orange) and a slow phase (green).  $\theta_s$  and  $\theta_0$  define the angular extent and center of the slow phase respectively. (B) Leg angle  $\theta$  as a function of time during one cycle (normalized to  $T$ ).  $\theta(t)$  of the other tripod is shifted by  $T/2$  but otherwise identical.  $d_c$  is the duty cycle of the slow phase, *i.e.* fraction of the period spent in the slow phase.

frame. By definition,  $\omega_s = \frac{\theta_s}{Td_c}$ ,  $\omega_f = \frac{2\pi - \theta_s}{T(1-d_c)}$ , and  $\omega = \frac{2\pi}{T}$ . Typically, gait parameters are set so that  $\omega_s < \omega < \omega_f$ , but the reverse is possible when  $\theta_s$  becomes large enough and/or  $d_c$  small enough.

In the first tests of SandBot on granular media (Fig. 76), we found that kinematics tuned for rapid stable bouncing motion on hard ground (HGK:  $\{\theta_s, \theta_0, d_c\} = \{0.85, 0.13, 0.56\}$ ) produced little motion on granular media (red curve). Empirical adjustment to soft ground kinematics (SGK:  $\{\theta_s, \theta_0, d_c\} = \{1.10, -0.50, 0.45\}$ ) restored effective (walking) locomotion on granular media (blue curve).

In the previous study [92], we used SGK to test  $\bar{v}_x(\phi, \omega)$ . Now armed with the understanding of how SandBot moves on granular media gained from this work, we set out to determine the effects of limb kinematics in detail. We set  $\phi = 0.605$  and  $\omega = 8$  rad/s, and measure SandBot's average speed on granular media as we systematically vary gait parameters, i.e.  $\bar{v}_x = \bar{v}_x(\theta_s, \theta_0, d_c)$ . We pick  $\omega = 8$  rad/s because at this intermediate frequency SandBot displays both rotary walking and swimming as the clock signal is varied. We pick  $\phi = 0.605$  to remove the effect of local volume fraction change which causes a premature transition from rotary walking to swimming<sup>¶</sup> and adds to the complexity of the problem.

We first test the effect of the extent and location of the slow phase for fixed  $d_c = 0.5$ , measuring speed  $\bar{v}_x = \bar{v}_x(\theta_s, \theta_0)$ . We vary the parameters between  $0 \leq \theta_s \leq 2$  and  $-2 \leq \theta_0 \leq 2$ , which are the limits set by the robot's controller. We choose  $d_c = 0.5$  because it is close to the  $d_c$  values of both HGK and SGK. This gave us an easy way to project HGK ( $d_c = 0.56$ ) and SGK ( $d_c = 0.45$ ) onto the  $\bar{v}_x = \bar{v}_x(\theta_s, \theta_0)$  plot ( $d_c = 0.5$ ), assuming that a small change of  $d_c$  near  $d_c = 0.5$  does not affect speed significantly (see Fig. 85 which supports this assumption).

Measurements of  $\bar{v}_x = \bar{v}_x(\theta_s, \theta_0)$  (Fig. 77) show a single sharp peak in speed near  $\{\theta_s, \theta_0\} = \{1.5, -0.5\}$ . High speeds only occur within a small island of  $-1 < \theta_0 < 0$  and  $\theta_s > 0.5$

---

<sup>¶</sup>In rotary walking when  $s < R$ , a limb encounters material disturbed by its previous step. If the initial volume fraction exceeds the critical value  $\phi \approx 0.605$ , disturbed granular material dilates to a lower volume fraction after each step; if initially  $\phi < 0.605$ , disturbed granular material compacts to a higher volume fraction after each step [154]. The dilation of disturbed granular material above  $\phi \approx 0.605$  results in premature transition from rotary walking to swimming if  $s < R$  as the disturbed granular material is weaker which increases penetration and reduces step length. Here we choose  $\phi = 0.605$  which ensures that the  $\phi$  encountered by the leg is unchanged even for  $s < R$ .

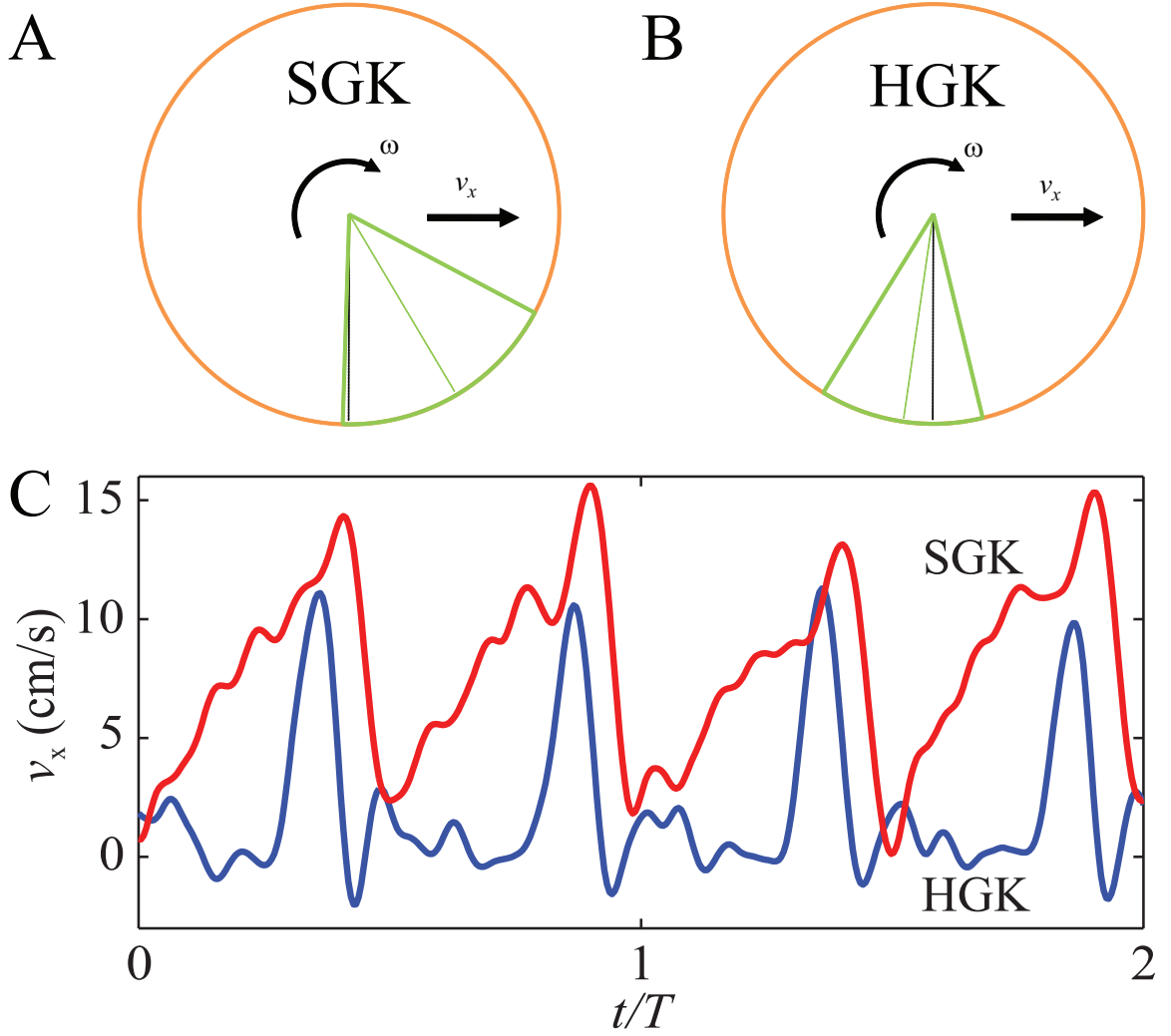


**Figure 76:** SandBot’s speed depends sensitively on intra-cycle limb kinematics. (A) Hard Ground Kinematics (HGK). (B) Soft Ground Kinematics (SGK). (C) Instantaneous speed of SandBot on granular media with hard ground clock signal (HGK:  $\{\theta_s, \theta_0, d_c\} = \{0.85, 0.13, 0.56\}$ ; red) and soft ground clock signal (SGK:  $\{\theta_s, \theta_0, d_c\} = \{1.10, -0.50, 0.45\}$ ; blue). With HGK SandBot moves slowly ( $\bar{v}_x \approx 2$  cm/s) on granular media, but with SGK (red), it advances rapidly ( $\bar{v}_x \approx 8$  cm/s).

surrounding the peak; lower speeds fill the remainder of the space. The drop in speed is rapid as  $\theta_0$  is varied away from the peak, and is less so when  $\theta_s$  is varied away from the peak; this is also evident in cross sections through the peak (blue circles in Fig. 77 and Fig. 84, respectively). Ignoring the effect of  $d_c$ , the SGK parameters (blue dot) lie close to the peak while the HGK parameters (red dot) are in the low speed region. The optimal gait parameters which we found for SandBot locomotion on poppy seeds at  $\phi = 0.605$  and

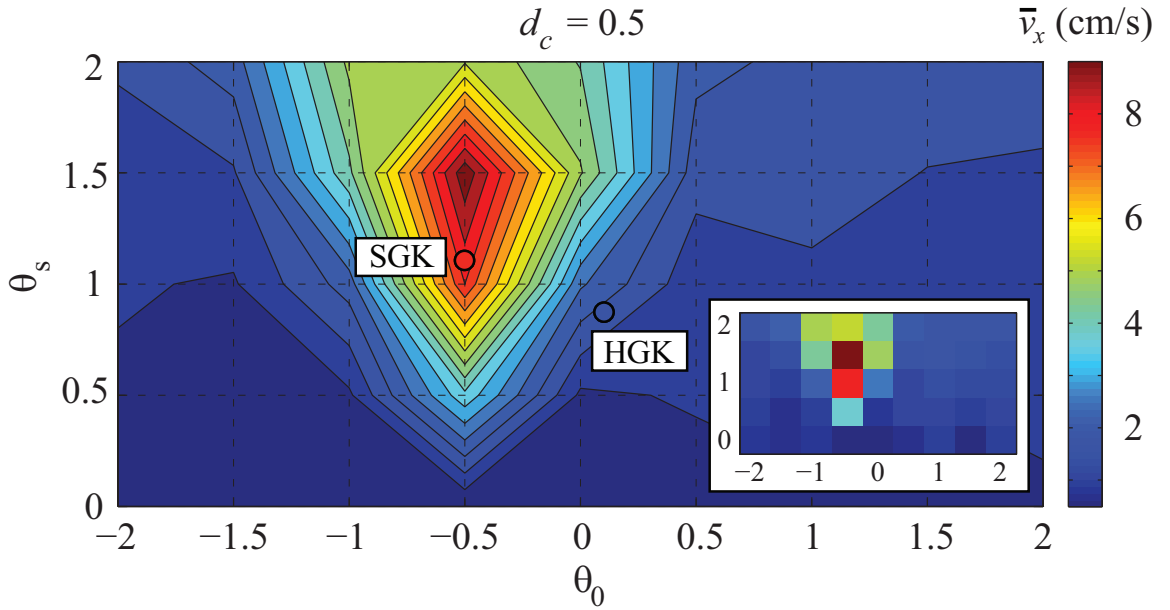


**Figure 77:** SandBot’s speed as a function of slow phase extent and location. Average speed  $\bar{v}_x$  of SandBot on granular media ( $\phi = 0.605$ ) as a function of  $(\theta_s, \theta_0)$  for  $d_c = 0.5$  and  $\omega = 8$  rad/s has a localized region of high speeds with peak  $\bar{v}_x \approx 9$  cm/s near  $\{\theta_s, \theta_0\} = \{1.5, -0.5\}$ . Circles show that  $\bar{v}_x$  for SGK (red) and HGK (blue) matches data for  $d_c = 0.5$  despite the formers slightly different  $d_c$  values. Inset: original data from which main figure is interpolated.

$\omega = 8$  rad/s are:  $\{\theta_s, \theta_0, d_c\} = \{1.5, -0.5, 0.55\}$ . These gait parameters generate about 20% higher speed than the previously used SGK parameters.

Variation of the duty cycle at fixed  $\{\theta_s, \theta_0\} = \{1.5, -0.5\}$  also has a substantial influence on speed. Data (blue circles in Fig. 85) show a well defined peak at  $d_c \approx 0.5$ . Speed drops off relatively slowly for  $d_c > 0.55$ , and more quickly to small (swimming) speeds for  $d_c < 0.5$ .

## 5.5 Discussion

### 5.5.1 Application of model to slow phase extent and location variation

To apply our kinematic model to SandBot locomotion with varied limb kinematics, we must consider the effects of variable limb kinematics during limb-ground interaction. Depending on the gait parameters during ground contact, the limbs could be rotating in the fast phase, in the slow phase, or in a combination of both. In our previous study, the kinematic model ignored limb frequency variability during ground contact and only considered the robot limb rotating at the constant cycle averaged limb frequency  $\omega$ .

However, as limb kinematics change, the variability of limb frequency in ground contact needs to be taken into account. For our test of  $\bar{v}_x = \bar{v}_x(\theta_s, \theta_0)$  within  $0 \leq \theta_s \leq 2$  and

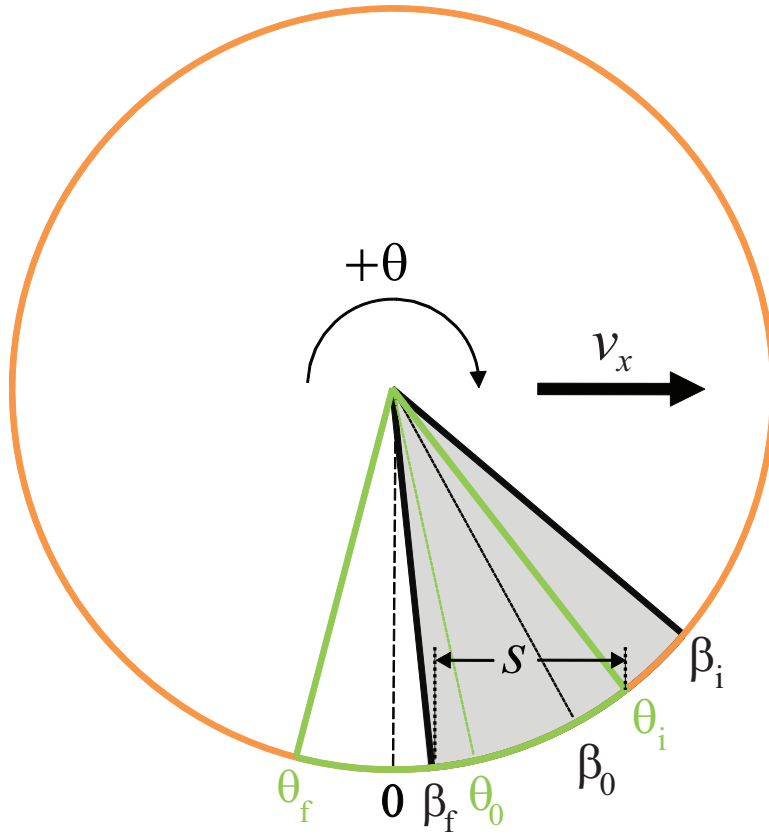


**Figure 78:** Schematic of overlap of the slow phase (green) and the rotary walking range (gray). Overlap of  $[\theta_i, \theta_f]$  and  $[\beta_i, \beta_f]$  determines step length  $s$  and thus speed  $\bar{v}_x$ . For the configuration shown,  $s = R(\sin \beta_f - \sin \theta_i)$ .  $\theta_0$  and  $\beta_0$  are centers of the slow phase and the rotary walking range, respectively.

$-2 \leq \theta_0 \leq 2$  and at  $d_c = 0.5$ ,  $\omega_f \gg \omega_s$  so that only the slow phase can possibly achieve rotary walking, as fast limb rotation results in swimming. In this case  $\omega_s$  (instead of  $\omega$ ) controls acceleration  $a$  and thus determines the rotary walking range<sup>||</sup>.

For fixed  $d_c$ , varying  $[\theta_s, \theta_0]$  changes the extent and location of the slow phase; the angular extremes of the slow phase are  $\theta_{i,f} = \theta_0 \pm \frac{\theta_s}{2}$ , see Fig. 78. Varying  $\theta_s$  also changes  $\omega_s$  which controls the rotary walking range. Therefore varying  $[\theta_s, \theta_0]$  affects where the slow phase overlaps with the rotary walking range. The step length  $s$  is given by  $s = R(\sin \psi_f - \sin \psi_i)$  where  $\psi_i = \max(\beta_i, \theta_i)$  and  $\psi_f = \min(\beta_f, \theta_f)$  if there is overlap or  $s = 0$  if there is no overlap. The larger the overlap, the further the robot moves forward in a cycle.

The rotary walking range  $[\beta_i, \beta_f]$  is given by solving the equation  $F_p(\theta) = 2Rk(\cos \beta_{i,f} - \frac{h}{2R}) = m(g+a)$ , with  $a$  given by  $a = \frac{m\omega_s}{\Delta t}$ . We can evaluate how  $[\theta_i, \theta_f]$  overlaps with  $[\beta_i, \beta_f]$  to determine  $s$ , and calculate the robot speed using  $\bar{v}_x = \frac{2s}{T} = \frac{s\omega}{\pi}$ . For fixed  $\omega$ , speed  $\bar{v}_x$  scales with step length  $s$ .

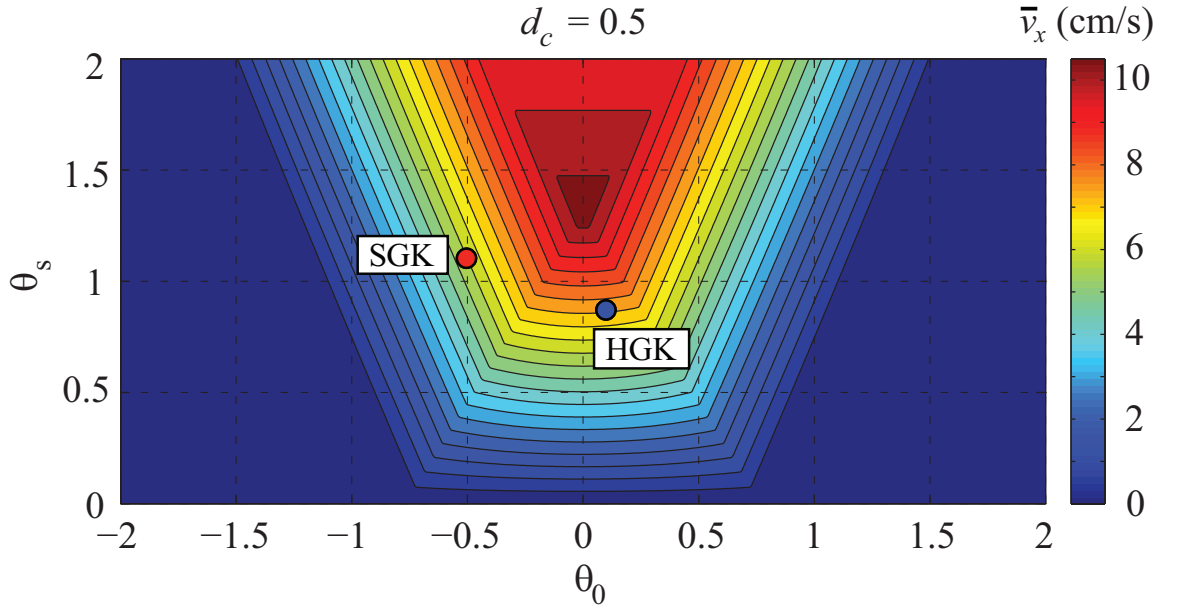


**Figure 79:** Model prediction of speed as a function of slow phase extent and location using the original penetration force law. Predicted  $\bar{v}_x(\theta_s, \theta_0)$  from the kinematic model with  $F_p = kz$  captures the single peak but predicts a lower speed for SGK than for HGK contrary to observation and fails to account for the observed peak in speed at  $\theta_0 \approx -0.5$ .

<sup>||</sup>The previous study did not err in considering  $\bar{v}_x$  as a function of  $\omega$  alone since for fixed clock parameters  $\omega_s$  scales with  $\omega$ . The only difference would be  $\Delta t(\phi) \rightarrow \Delta t\omega_s/\omega$ .

Figure 79 shows the model prediction of  $\bar{v}_x$  using fitting parameters  $k = 210$  N/m,  $\Delta t = 0.37$  s. Comparing prediction with observation (Fig. 77), the model captures the peak and predicts similar magnitudes of speeds. However the predicted peak is symmetric about  $\theta_0 = 0$  while the observed peak is symmetric about  $\theta_0 \approx -0.5$ .

### 5.5.2 Anisotropic penetration force law

If the penetration force of the granular material increased like  $kz$  as assumed in the model, we would expect  $\theta_0 = 0$  as this value would give the largest overlap between the slow phase and the rotary walking range as determined by the material strength (see scheme in Fig. 78). To investigate why the robot performs best with  $\theta_0 \approx -0.5$  we attached a c-leg to

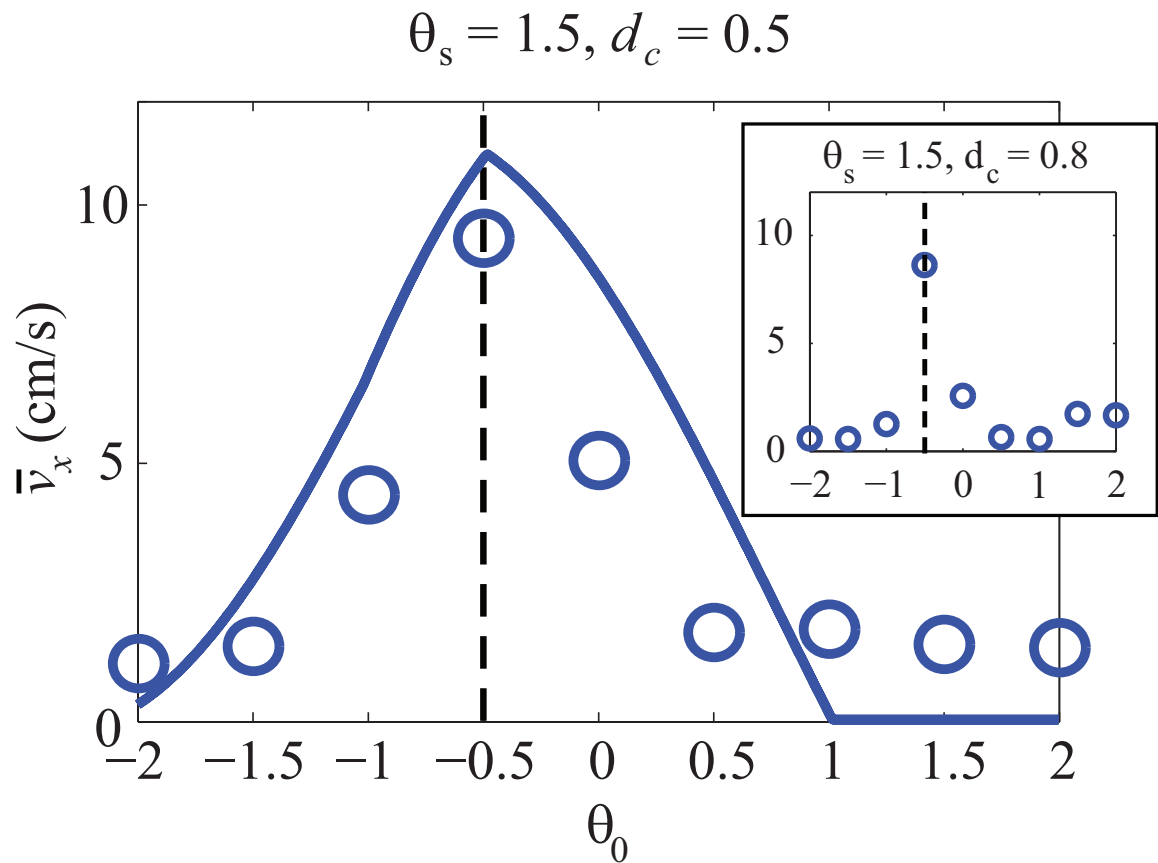


**Figure 80:** Asymmetry of speed as a function of slow phase location. For all  $\theta_s$  at  $d_c = 0.5$ ,  $\bar{v}_x(\theta, \theta_0)$  (Fig. 75) is maximal (dashed vertical black line) at  $\theta_0 \approx -0.5$  ( $\theta_s = 1.5$  shown). Inset: peak location  $\theta_0 \approx -0.5$  does not change for  $d_c = 0.8$ . Solid blue curve is prediction from the model with anisotropic penetration force.

a force/torque sensor and measured the grain resistance as the c-leg was rotated through the granular media at  $\omega = 0.35 \text{ s}^{-1}$  (the horizontal rotation axis of the c-leg was positioned the same distance  $h = 2.5 \text{ cm}$  above the grain surface as when it is mounted on the robot). Figure 81 shows a clear asymmetry in the penetration (vertical) force with the measured peak force occurring near  $\beta_0 = -0.75$ ; penetration force during rotation peaks before the intruder reaches the maximum depth. We confirmed that the measured anisotropy in the penetration force is intrinsic to our granular medium and is not an artifact of the particular shape of the c-leg by additionally rotating a rectangular bar and a sphere into granular media at the same hip height: both objects exhibited a peak force at  $\beta_0 = -0.75$ .

We speculate that the asymmetry in penetration force during rotation into granular media is a result of the changing limb orientation during rotational intrusion. For vertical penetration (which we considered in the model in the previous study), the intruder is

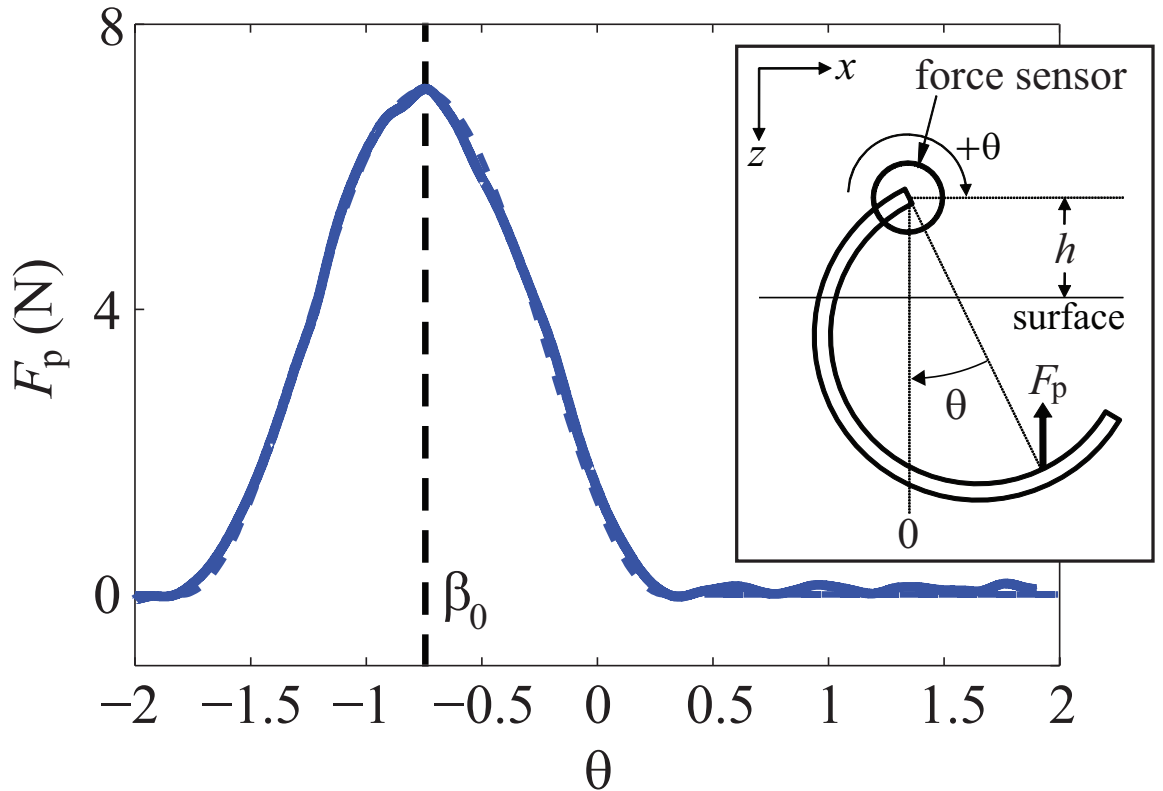


**Figure 81:** Anisotropic penetration force. Vertical penetration force  $F_p$  (solid blue curve) during c-leg rotation into poppy seeds reaches maximum at  $\beta_0 = -0.75$  (dashed black line) and is asymmetric to  $\theta_0 = 0$ . Inset: force measurement schematic.

constantly pushing down on the granular material. The grain contact network generated in granular material in response to intrusion [61] forms a downward pointing cone which generates a force symmetric to the vertical ( $\theta = 0$ ). In rotational intrusion, however, the direction of intrusion is constantly changing; the direction of the force cone should change as well and correlate with the instantaneous direction of intrusion.

We hypothesize that the force during rotational intrusion is maximal at  $\beta_0 = -0.75$  because for larger angles part of the cone reaches the surface and/or terminates on the horizontal walls of the container and can no longer support the entire grain contact network, thus reducing the maximal yield force. We also note that the angle at which maximal force is developed is close to the angle of repose 0.52 that we measure for the poppy seeds. This angle is the same as the internal slip angle in cohesionless granular material [10] which plays an important role in the formation of the grain contact network, supporting the plausibility of our speculation.

To account for the measured angular offset in peak force from vertical (Fig. 77 and Fig. 80), we modify the original penetration force law in our model to

$$F_p(\theta) = 2Rk' \{ \cos [b(\theta - \beta_0)] + 1 \}$$

for  $F > 0$ , where  $\beta_0 = -0.75$ , and  $k'$  and  $b$  are new fit parameters. Following the same procedure for the original force law, we find the robot speed by calculating  $[\beta_i, \beta_f]$ , the overlap between  $[\theta_i, \theta_f]$  and  $[\beta_i, \beta_f]$ , and the step size.

Figure 82 shows  $\bar{v}_x$  predicted by a fit to the model using the anisotropic penetration force law (fitting parameters  $k' = 65$  N/m,  $\Delta t = 0.4$  s, and  $b = 0.8$ ). Besides capturing the peak behavior of measured speed, the model also captures the shift in peak location to  $\theta_0 \approx -0.5$  (*i.e.* asymmetry to  $\theta_0 = 0$ ). For fixed  $\theta_s$ , speed is maximal when the center of the slow phase corresponds with the center of the rotary walking range (Fig. 78). If  $\theta_0$  is different from  $\beta_0 = -0.75$ , the overlap of the slow phase and the rotary walking range decreases, which reduces step length and thus speed. In accord with observation, SGK (red dot) lies near the peak while HGK (blue dot) lies in a region of low speeds. Figure 83 shows that SGK has higher speed than HGK because the overlap between the slow phase and the

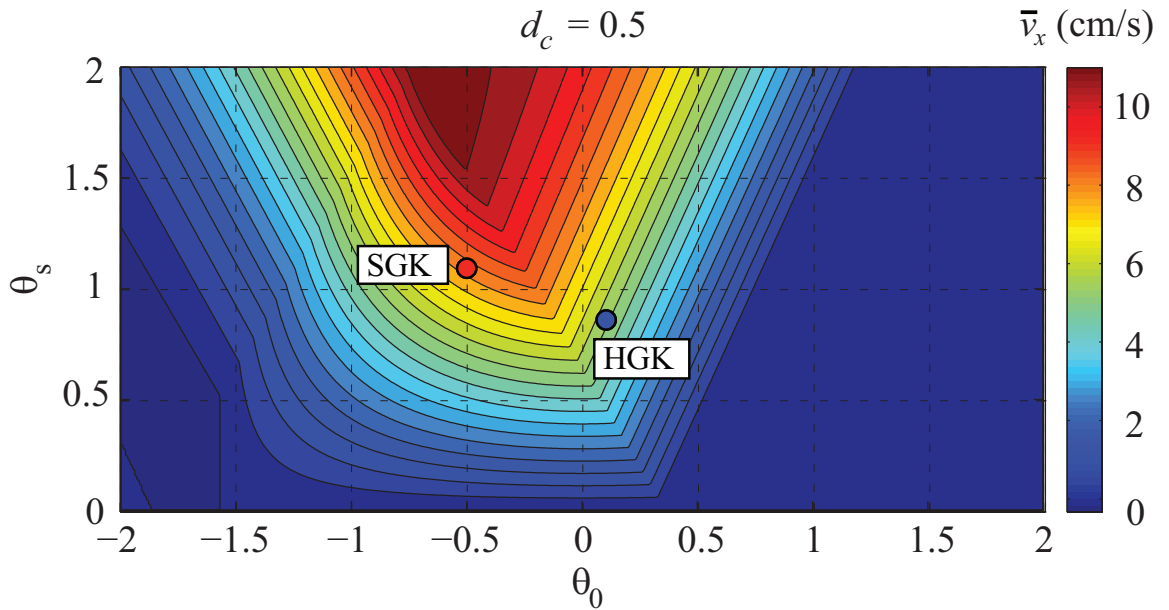


**Figure 82:** Anisotropic penetration force law better predicts speed as a function of slow phase extent and location. Prediction of  $\bar{v}_x(\theta_s, \theta_0)$  from the the model with the anisotropic penetration force for  $d_c = 0.5$  captures the asymmetry of  $\bar{v}_x$  with respect to  $\theta_0 = 0$  and predicts higher speed for SGK than for HGK. Fitting parameters:  $k' = 65$  N/m,  $\Delta t = 0.4$  s and  $b = 0.8$ .

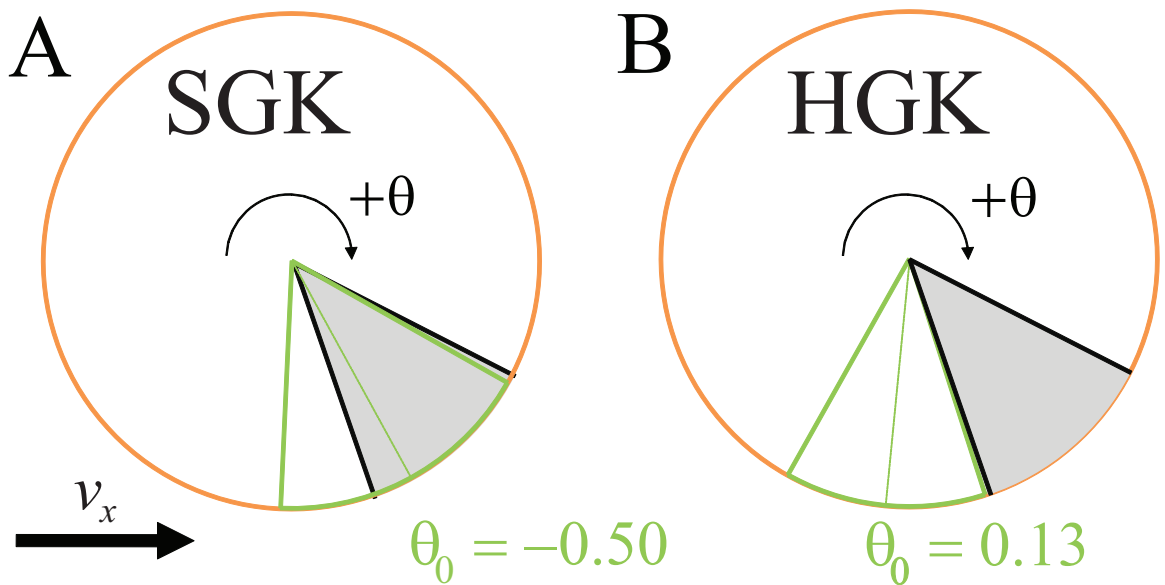


**Figure 83:** Comparison of overlap of the slow phase and the rotary walking phase between Soft Ground Kinematics and Hard Ground Kinematics. (A) In SGK the slow phase (centered at  $\theta_0 = -0.50$ ) overlaps nearly completely with the rotary walking range (centered at  $\beta_0 = -0.5$ ), explaining its high speed as compared to HGK (centered at  $\theta_0 = 0.13$ ) which has little overlap.

rotary walking range (gray sector in Fig. 78) is significantly larger.

At fixed  $\theta_0 = \beta_0$ , increasing the extent of the slow phase (increasing  $\theta_s$ ) from zero initially increases speed as the extent of the slow phase increases within the rotary walking envelope (see Fig. 77 and Fig. 84). However,  $\omega_s$  increases with  $\theta_s$  which increases the acceleration and reduces the rotary walking range. For sufficient extent (near  $\theta_s = 1.5$  for the data shown in Fig. 77 and Fig. 84) the slow phase contains the rotary walking range and step length is determined by the latter. Further increase in  $\theta_s$  reduce the rotary walking range. Rotary walking is not possible for  $\theta_s \geq \frac{2\pi d_c \Delta t}{\omega} \left( \frac{4k'}{m} - \frac{g}{R} \right)$  as the material is never strong enough to both support and accelerate the robot. In Fig. 84 the experimental speed is noticeably lower than the model prediction at the largest  $\theta_s = 2$ . As we discuss below in regards to variation in  $d_c$ , this reduction is a apparently the result of tripod overlap (both

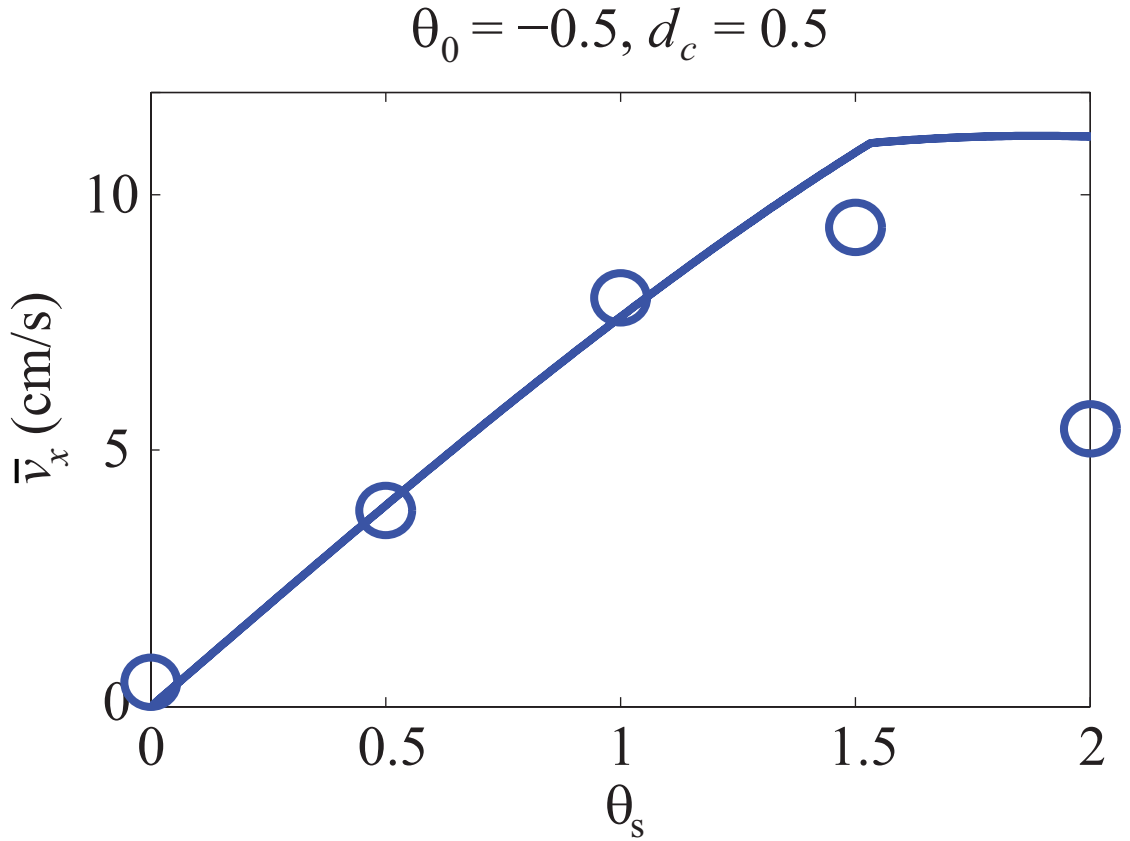


**Figure 84:** Speed as a function of slow phase extent. Measured  $\bar{v}_x(\theta_s, \theta_0 = -0.5)$  (blue circles) through the speed maximum (Fig. 77) deviates from the anisotropic force model prediction (blue curve) at large  $\theta_s$  due to limb overlap.

tripods simultaneously in ground contact) which occurs for a greater portion of the slow phase for larger  $\theta_s$ .

### 5.5.3 Effect of duty cycle

While the model prediction of  $\bar{v}_x(d_c)$  (blue curve in Fig. 85) matches the magnitudes of speeds at intermediate  $d_c \approx 0.5$ , it does not quantitatively match the shape of measured speed vs  $d_c$ . Below  $d_c \approx 0.5$ , the model predicts that  $\bar{v}_x(d_c)$  increases monotonically with increasing  $d_c$ . This trend is in accord with the experimental observations; however the model

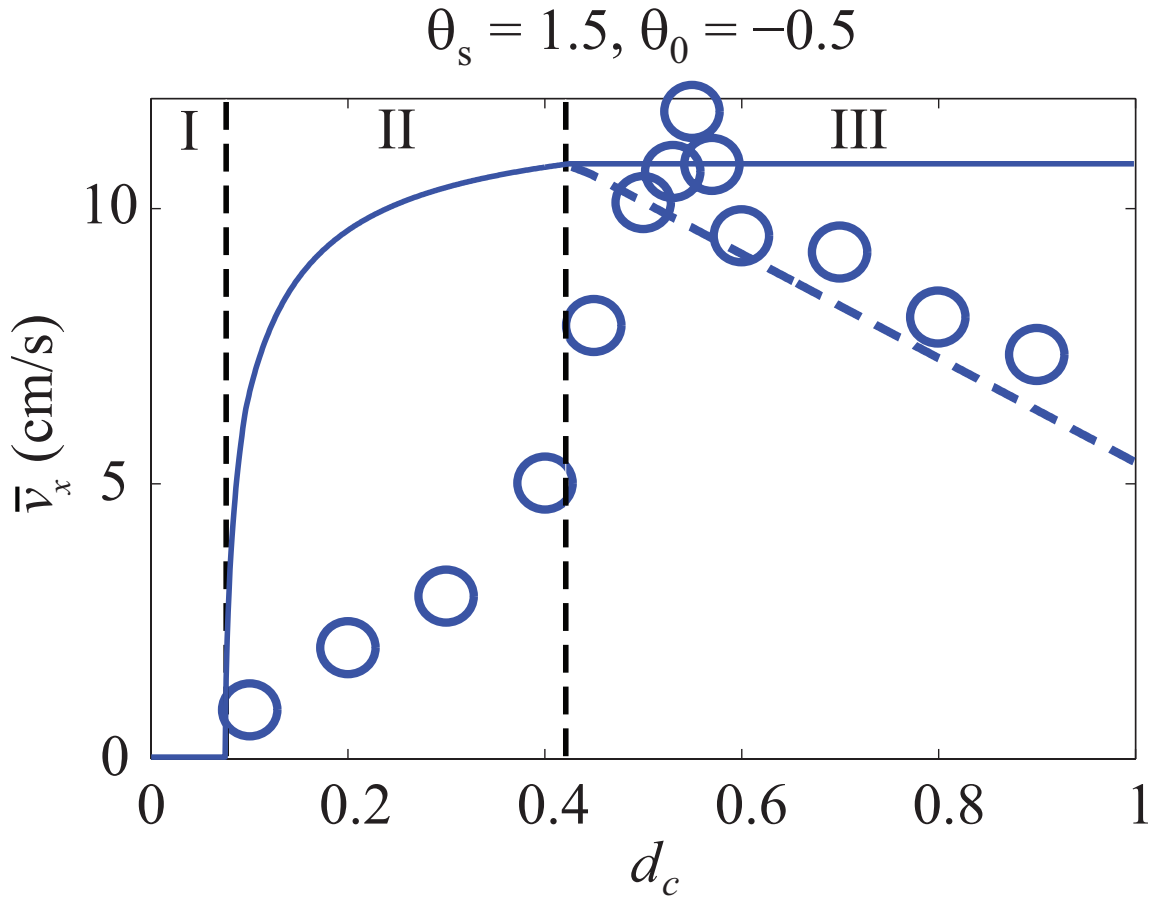


**Figure 85:** Speed as a function of duty cycle. Measured  $\bar{v}_x(d_c)$  (blue circles) for  $\{\theta_s = 1.5, \theta_0 = -0.5\}$  is maximum at  $d_c \approx 0.5$ . The model (solid blue curve) accurately predicts the speed for  $d_c \approx 0.5$  but is inaccurate elsewhere due to contributions of swimming neglected by the model (region I), a decrease in rotary walking range from cratering induced depth reduction and unequal penetration forces developed by c-legs on opposite sides of the body (II), and tripod overlap at high  $d_c$  (III). Model prediction with tripod overlap included (dashed blue line) better matches the data in region III.

prediction is consistently higher than measured speed. Above  $d_c \approx 0.5$ , the model predicts that  $\bar{v}_x(d_c)$  is independent of  $d_c$ , but the measured speed decreases with increasing  $d_c$  and is lower than the model prediction. We now discuss possible reasons for the discrepancies at low  $d_c < 0.1$  (labeled region I in Fig. 85), intermediate  $0.1 < d_c < \approx 0.5$  (region II) and high  $d_c > \approx 0.5$  (region III).

In region I,  $d_c$  is small so that  $\omega_s$  and thus  $a$  become large enough to ensure that the robot is in the swimming mode (i.e. movement without solidification). Here the model assumes rotary walking and predicts zero speed. In experiment, the robot can still advance slowly at each step due to thrust forces from continuously slipping limbs generated by frictional drag [70] and/or inertial movement of material. This thrust competes with friction from belly drag, and as in [92], we find that these result in low average speed of  $\bar{v}_x \approx 1$  cm/sec.

The model's overestimate of speed at high  $d_c$  (region III) is a result of tripod overlap and can be readily understood. When there is no tripod overlap (only one tripod with ground contact at any given time) each tripod advances the robot a distance  $s$  for a total displacement of  $2s$  per period. This is the case for  $d_c \leq \approx 0.5$ . However in the limit of  $d_c = 1$  both tripods are simultaneously in the slow phase as the duration of the fast phase is zero. The simultaneous slow phases generate a total displacement of just  $s^{**}$  instead of  $2s$  without tripod overlap. As a result, the predicted speed at  $d_c = 1$  must be halved (i.e.  $\bar{v}_x = \frac{s}{T} = \frac{s\omega}{2\pi}$ ). Lacking a way to quantify the tripod overlap effect, we assume that the reduction of step length from  $2s$  to  $s$  is linear with  $d_c$  for  $d_c > \approx 0.5$ ; the data is in good agreement with this prediction (dashed blue curve in Fig. 85). This reduction in speed is a purely kinematic effect that is inherent to the rotary walking gait at high  $d_c$ .

Two plausible mechanisms explain the model's overestimate of speed at intermediate  $d_c$  (region II): hole digging and uneven weight distribution. Lateral observations of the robot kinematics at low  $d_c$  show that the rapid motion of the c-leg during the slow phase throws significant numbers of particles out of the limb's path which creates a depression. For a

---

\*\*For  $d_c = 1$ , tripods are in phase so that each c-leg needs to provide just 1/6 the required total force compared to 1/3 when the tripods act independently which could affect the step size. However, we found that for  $\{\theta_s, \theta_0, d_c\} = \{1.5, -0.5, 1\}$ , decreasing  $m$  from 1/3 to 1/6 the body mass left the expression for  $s$  unchanged.

deep enough hole, rotary walking is impossible due to the reduced penetration depth of the leg below the now lower surface of the depression. The second mechanism concerns the model's assumption of uniform weight distribution between the three legs of the tripod. In the  $d_c$  range where the robot advances slower than predicted, observations show that the robot rotates in the horizontal plane. Rotation occurs in this transition region between pure swimming and pure rotary walking because the side of the robot with two c-legs in ground contact undergoes rotary walking while the opposite side is in the swimming mode. Due to the increased gravitational and inertial forces on the single c-leg, the penetration forces are never sufficient to achieve ground solidification under the leg even at the maximum penetration depth.

## 5.6 Conclusions

We have built upon our previous experiments and models of a legged robot, SandBot, to explore how changes in limb kinematics affect locomotion on granular media. We found that even when moving on controlled granular media of fixed volume fraction at fixed cycle-averaged limb frequency, speed remains sensitive to variations in gait parameters that control angular extent, angular location, and temporal duty factor of the slow phase of the limb cycle. We showed that the assumptions in a previously introduced model (which accurately predicted speed as a function of limb frequency and volume fraction) had to be modified to incorporate an anisotropic penetration force during rotational intrusion into granular media as well as changes in acceleration of the leg as gait parameters were varied. With these modifications the model was able to capture speed as a function of angular extent and angular location. The model also indicates that as duty cycle is changed, effects due to simultaneous limb pairs (tripods) in ground contact, rapid limb impact into sand, and unequal weight distribution on limbs become important.

Our experiments and modified model explain why gait parameters that allow the robot to rapidly bounce over hard ground lead to loss of performance on granular media. They demonstrate how the angular extent and location of the slow phase must be adjusted to optimize interaction with granular media by minimizing inertial force and limb interference, and maximizing the use of solid properties of granular media. Further studies of SandBot guided by our kinematic model should reveal how physical parameters of both robot (mass distribution, limb compliance, limb shape, belly shape) and the environment (grain friction, density, incline angle, gravity) control the solid-fluid transition and thus affect the limb-ground interaction and performance. However, advances are required in theory and experimental characterization of complex media. Otherwise we must continue to rely on empirical force laws specific to particular geometries, kinematics and granular media.

The existence of a speed optimum in gait parameter space implies that control of limb kinematics is critical to move effectively on granular media, whether actively through sensory feedback, and/or passively through mechanical feedback. Future work should compare these results to investigations of gait optimization on hard ground [57]. The differences in

limb kinematics on sand compared to hard ground are intriguing because on hard ground performance is optimized by making the robot bounce. However, this carries with it the risk of yaw, pitch and roll instability due to mismanaged kinetic energy. On granular media such instabilities appear rare; instead most gait parameters (see Fig. 77) result in little or no forward movement due to mismanaged fluidization of the ground. Thus, our results could have a practical benefit as they suggest strategies for improving the performance of current machines [156, 157, 12] on variable terrain via new limb and foot designs and control strategies.

Finally, an enormous number of organisms contend with sand [158], moving on the surface (or even swimming within it [95]). While the observed phenomena and proposed locomotion modes (e.g. rotary walking) appear specific to SandBot and its c-shaped limbs, the underlying principles could apply to locomotion of organisms on yielding substrates. For example, our recent work on terrestrial hatchling sea turtle locomotion demonstrates that their effective movement on sand proceeds through solidification of the granular medium [96]. Integrated studies of biological organisms and physical models can provide hypotheses [16] for passive and active neuromechanical [13] control strategies as well as better understanding of energetics [18] for movement on complex terrain.

## CHAPTER VI

### SYSTEMATIC STUDY OF THE PERFORMANCE OF SMALL ROBOTS ON CONTROLLED LABORATORY SUBSTRATES

#### *6.1 Summary*

The design of robots able to locomote effectively over a diversity of terrain requires detailed ground interaction models; unfortunately such models are lacking due to the complicated response of real world substrates which can yield and flow in response to loading. To advance our understanding of the relevant modeling and design issues, we conduct a comparative study of the performance of DASH and RoACH, two small, biologically inspired, six legged, lightweight ( $\sim 10$  cm,  $\sim 20$  g) robots fabricated using the Smart Composite Manufacturing (SCM) process. We systematically examine performance of both robots on rigid and flowing substrates. Varying both ground properties and limb stride frequency, we investigate average speed, mean mechanical power and cost of transport, and stability. We find that robot performance and stability is sensitive to the physics of ground interaction: on hard ground kinetic energy must be managed to prevent yaw, pitch, and roll instability to maintain high performance, while on sand the fluidizing interaction leads to increased cost of transport and lower running speeds. We also observe that the characteristic limb morphology and kinematics of each robot result in distinct differences in their abilities to traverse different terrains. Our systematic studies are the first step toward developing models of interaction of limbs with complex terrain as well as developing improved limb morphologies and control strategies.\*

---

\*This Chapter is a published paper by Chen Li, Aaron M. Hoover, Paul Birkmeyer, Paul B. Umbanhowar, Ronald S. Fearing, and Daniel I. Goldman, Proceedings of SPIE (2010) [98].

## 6.2 Introduction

In nature, animals display high mobility on terrains ranging from hard surfaces like rocks to deformable substrates like sand and rubble [159], snow [160], or even the surface of water [19]. In contrast, while man made wheeled and treaded vehicles demonstrate excellent mobility and low energy cost on rigid ground like paved roads, they often suffer total performance loss in deformable terrains like sand [11]. The main challenge of moving on deformable ground is that the locomotor can experience both solid- and fluid-like forces during substrate interaction depending on the magnitude of normal and shearing forces [10].

Granular material [22], which is common in nature, proves a good model substrate for studying locomotion on deformable ground [92, 95, 97, 96]. Granular media display the solid-fluid transition during limb-ground interaction, and are at the same time simpler than most other deformable and/or flowing substrates. Another advantage of using granular media as test substrates is that their mechanical properties are readily and precisely controlled by varying the volume (packing) fraction of their constituent particles (see Experiments section).

There is increasing evidence that small, legged machines can have greater maneuverability than large wheeled vehicles in many natural environments [135]. For example, recent studies of the legged RHex-class robot SandBot [92, 97] demonstrate that effective locomotion on deformable substrates like granular media is possible when stride frequencies and limb kinematics are appropriate for ground properties. In particular, these studies suggest that the ability of limbs to generate adequate ground thrust relative to gravitational and inertial forces is the key to effective locomotion on deformable substrates. Other factors, such as limb morphology and compliance [9] and neurosensory control [3], may also substantially effect locomotion on deformable substrates.

The DASH and RoACH robots<sup>†</sup> used in this study are small, biologically inspired, six-legged, lightweight ( $\sim 10$  cm,  $\sim 20$  g) robots (Fig. 86). Because their mass is  $\sim 100$  times smaller than earlier top performing devices like the RHex class of robots [15], DASH and

---

<sup>†</sup>These robots were developed by Aaron M. Hoover, Paul Birkmeyer, and Ronald S. Fearing.

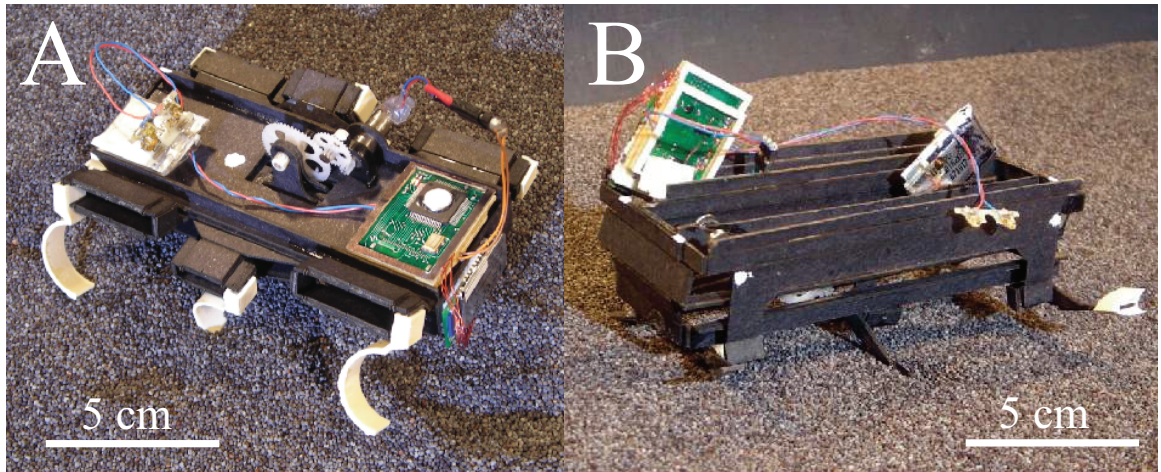


**Figure 86:** RoACH (A) and DASH (B) standing on loosely packed poppy seeds.

RoACH should traverse varied terrains with higher mobility and lower energy cost than any previous legged devices due to their potentially much larger thrust-to-gravity ratio. Although similar in size and composition, each robot has distinct limb morphology and kinematics and, as such, provide excellent test platforms for assessing benefits and tradeoffs of these factors on a variety of substrates. In addition, the robots are simple and inexpensive to construct, have relatively high power densities, and can survive collisions with the ground at their terminal velocities [59].

To probe the locomotor capabilities of small lightweight robotic platforms on differing terrains and to examine benefits and tradeoffs of different limb morphologies and kinematics, we systematically test the locomotor performance (average speed, mean mechanical power and cost of transport, and stability) of DASH and RoACH as they move on two distinct types of substrates, hard ground and deformable granular media. We vary by open loop control the robot stride frequency on prepared substrates of well defined mechanical properties and compare performance across robotic platforms and substrates.

## 6.3 *Materials and Methods*

### 6.3.1 **Experiment Design**

The volume (packing) fraction  $\phi$  of a granular material is defined as the ratio of the solid volume of the grains forming the media to the volume they occupy. Higher volume fraction indicates grains are more densely packed. In nature and under gravity, dry, spherical, granular media exist in a range of volume fraction  $0.55 < \phi < 0.64$  [76]. Granular media of different volume fraction often exhibit very different mechanical properties. For example, we find that as a bed of poppy seeds is compacted from  $\phi = 0.58$  to  $\phi = 0.64$ , reaction force during constant velocity vertical penetration increases approximately five-fold. The dynamics of ballistic impact under gravity also differ dramatically [154] with varying volume fraction.

An apparatus known as a fluidized bed can precisely control the volume fraction and thus the mechanical properties of granular media and has been used successfully for this purpose in physics and locomotion biology studies [80, 82, 92]. A sufficient counter flow of air through the grain bed against gravity brings the grains into a fluidized state with neutral buoyancy. Upon cessation of the air flow, the granular media settles to a loosely packed state of low volume fraction. Subsequent repeated air pulses (or vibration aided by small air flow) compacts the grains to higher  $\phi$ .

In this study, we use a fluidized bed trackway to prepare the granular media in a loosely packed state ( $\phi = 0.580$ ). As previously discovered [92], locomotion at low  $\phi$  is more challenging than at high  $\phi$  as limbs can easily fluidize the grains during ground interaction. By comparing the performance of small lightweight robotic platforms on rigid ground and on loosely packed granular media we sample two representative extremes from the spectrum of terrestrial substrates a mobile device could encounter. By comparing performance across RoACH and DASH platforms, we assess the benefits and tradeoffs of different limb morphology and kinematics on these two distinct substrates.

### 6.3.2 Experimental Setup

Figure 87 illustrates the experimental setup. Hard ground was realized with a piece of drywall (120 cm  $\times$  50 cm  $\times$  1 cm) with uniform surface properties. Loosely packed granular media was realized using poppy seeds prepared with  $\phi = 0.580$  in our 2.5 m long, 0.5 m wide fluidized bed trackway. Poppy seeds were chosen as the granular material because their size is close to natural sand [145] and their density ( $\approx 1.0$  kg/cm<sup>3</sup>) low enough to be fluidized. The fluidized bed trackway has a horizontal porous plastic (Porex) flow distributor (thickness 0.64 cm, average pore size 90  $\mu$ m) on which the poppy seeds rest. By blowing air upward through the distributor with four 300 LPM leaf blowers (Toro) at maximum power, the entire bulk of granular media was fluidized into the bubbling regime. As the flow was slowly reduced to zero, the poppy seeds came to rest in a loosely packed state. The air flow

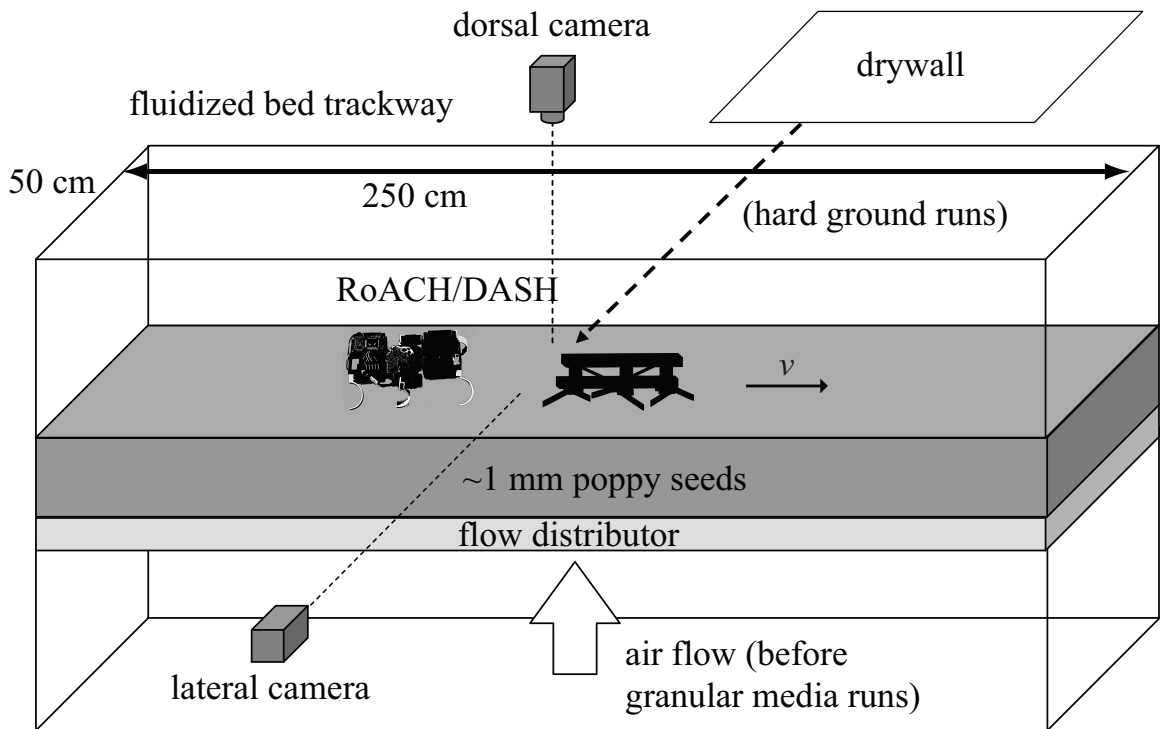


**Figure 87:** Experimental setup. (A) A fluidized bed trackway prepares the granular material,  $\sim 1$  mm diameter poppy seeds, into loosely packed states to create a deformable substrate with well defined mechanical properties. Hard ground is simulated by a piece of drywall. Dorsal and lateral cameras record high speed videos of the kinematics as DASH/RoACH moves on the substrate. Robot sensors record the back EMF and the control reference signal. (B) RoACH and (C) DASH stands on loosely packed poppy seeds.

across the fluidized bed is measured with an anemometer (Omega Engineering FMA-900-V) and is uniform to within 10 percent. Volume fraction was calculated as  $\phi = m/\rho V$ , where  $m$  is the total mass of the seeds,  $\rho$  the average solid density of each grain and  $V$  the bed volume.

The substrate was prepared before each run: for hard ground runs, the drywall rested horizontally on the flat granular media surface, and was wiped with a brush to remove any contaminants from the previous run (poppy seeds occasionally got onto the drywall when the robots ran off the end); for granular media runs, the poppy seeds were prepared into a loosely packed state with volume fraction  $\phi = 0.580$  using the fluidized bed trackway (air flow is turned off before the robot is run). The RoACH/DASH robot was carefully placed on the substrate at the same end of the trackway with one tripod entirely in contact with the surface while the other remained lifted above the substrate. On the granular media, DASH was placed with its stance with all six legs touching the surface. RoACH is run with the curvature of the legs pointing forward (rather than backward as is the case with the RHex and Sandbot robots) because this was observed to improve performance on hard ground.

A Python graphic user interface (GUI) is used to configure the robot via a 230 Kbps Bluetooth communication link. The robot's DC motor is controlled using a pulse width modulated (PWM) voltage, and the control reference signal sent to the robot is strictly an open loop, feedforward specification of the duty cycle of that signal (under open loop stride low frequency  $f < \sim 5$  Hz is not possible). The PIC microcontroller includes a 10-bit analog to digital converter that is used to sample the back EMF of the motor when the motor is switched off during the idle phase of the PWM cycle. Those measurements together with the voltage control reference signal are streamed back to the computer base station running the GUI for plotting and saving.

Simultaneous dorsal and lateral videos of the robot motion are recorded at  $1280 \times 1024$  resolution and 250 fps with high speed video cameras (AOS Switzerland) to capture the kinematics of the robot and its interaction with the substrate. The back and side of each robot is marked with reflective material (WiteOut). Lighting is provided by four overhead

work lights, a side work light (HomeDepot), and a high intensity HMI light (Arri). Videos and robot sensor data are synchronized by identifying the beginning of robot motion in the video and the beginning of the recording of the robot sensor data (which corresponds to the start of robot motion).

The stride frequency  $f$  of each run is measured from the lateral video frames. The average speed  $\bar{v}$  of each run is calculated using distance traveled and elapsed time from the dorsal video frames. The mean mechanical power  $\bar{P}_{mechanical}$  is averaged from  $P_{mechanical} = N\omega$ , where  $N = K_t I$  is the motor torque, and  $\omega = 2\pi V_{EMF}/K_e$  is the motor angular velocity, with the motor torque constant  $K_t = 0.00683$  Nm/A, and the motor back EMF constant  $K_e = 0.15$  V/Hz. The motor current  $I = (V_{ref} - V_{EMF})/R$  is determined from the back EMF  $V_{EMF}$  and the voltage control reference signal  $V_{ref}$  recorded by the motor sensors using the motor resistance  $R = 4.2 \Omega$ . The mean metabolic power  $\bar{P}_{metabolic}$  is averaged from  $P_{metabolic} = I^2 R$ . The mean mechanical and metabolic cost of transport is given by  $\overline{COT}_{mechanical} = \bar{P}_{mechanical}/m_R \bar{v}$  and  $\overline{COT}_{metabolic} = \bar{P}_{metabolic}/m_R \bar{v}$ , where  $m_R$  is the mass of the robot. Both the mechanical power and cost of transport characterize only the mechanical energy and do not include heat dissipation in the electronics and the motor. We verified that the calculated motor frequency  $\omega/2\pi$  and the stride frequency  $f$  determined from the lateral video are the same (within 5% deviation). Averaging of all data was performed on the second half of each run where the robot reached a steady state speed.

#### 6.4 Results and Discussions

Figure 88 shows average speed as a function of stride frequency for both robotic platforms on both substrates. On hard ground, both DASH and RoACH achieve high speeds, e.g. at  $f \approx 15$  Hz,  $\bar{v} \approx 80 - 100$  cm/s or  $\sim 10$  bodylength/s (as compared to the peak performance of  $\sim 1$  bodylength/s for the RHex class robots). DASH displays a roughly proportional  $\bar{v}$ - $f$  relationship (solid green line is a linear fit with zero intercept) indicative of a constant stride length for all stride frequencies. On the other hand, RoACH has a more irregular  $\bar{v}$ - $f$  pattern on hard ground, which may be a result of RoACH's more erratic vertical bouncing dynamics as observed in the lateral videos.

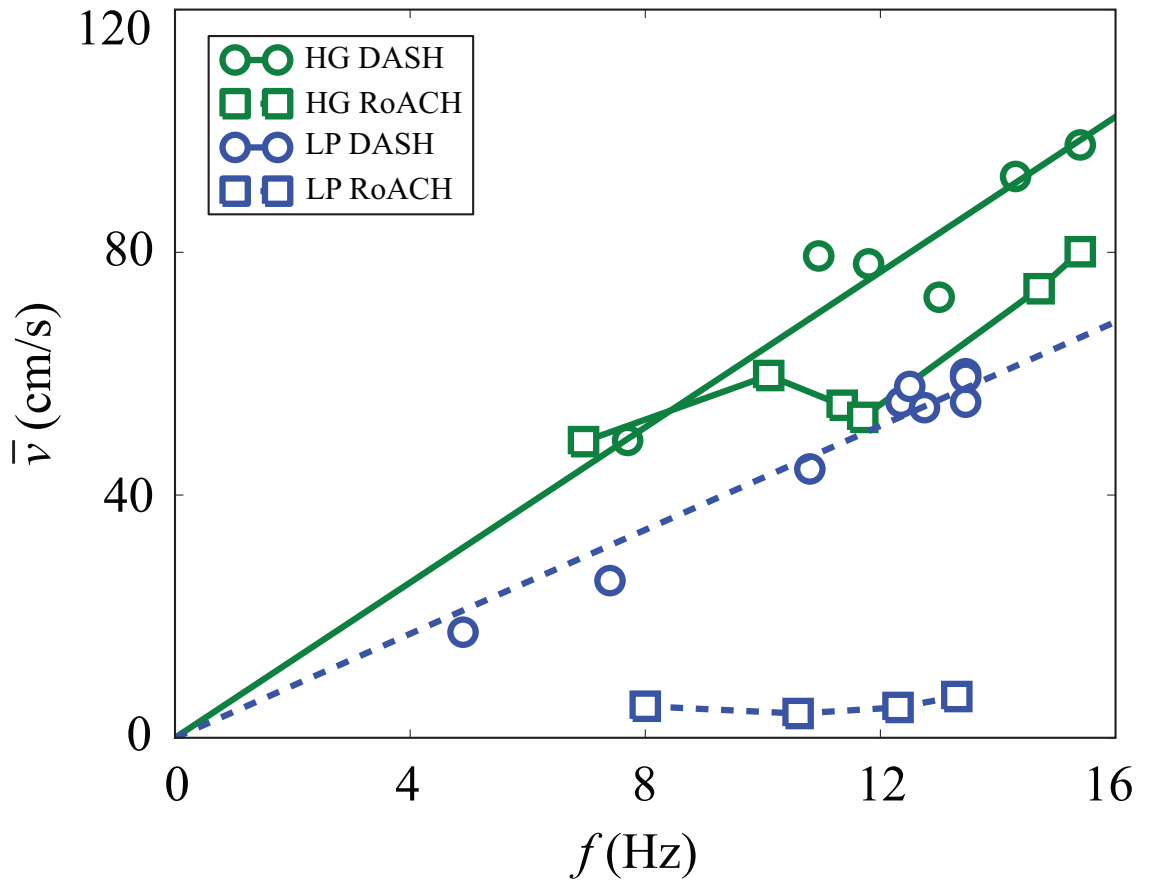
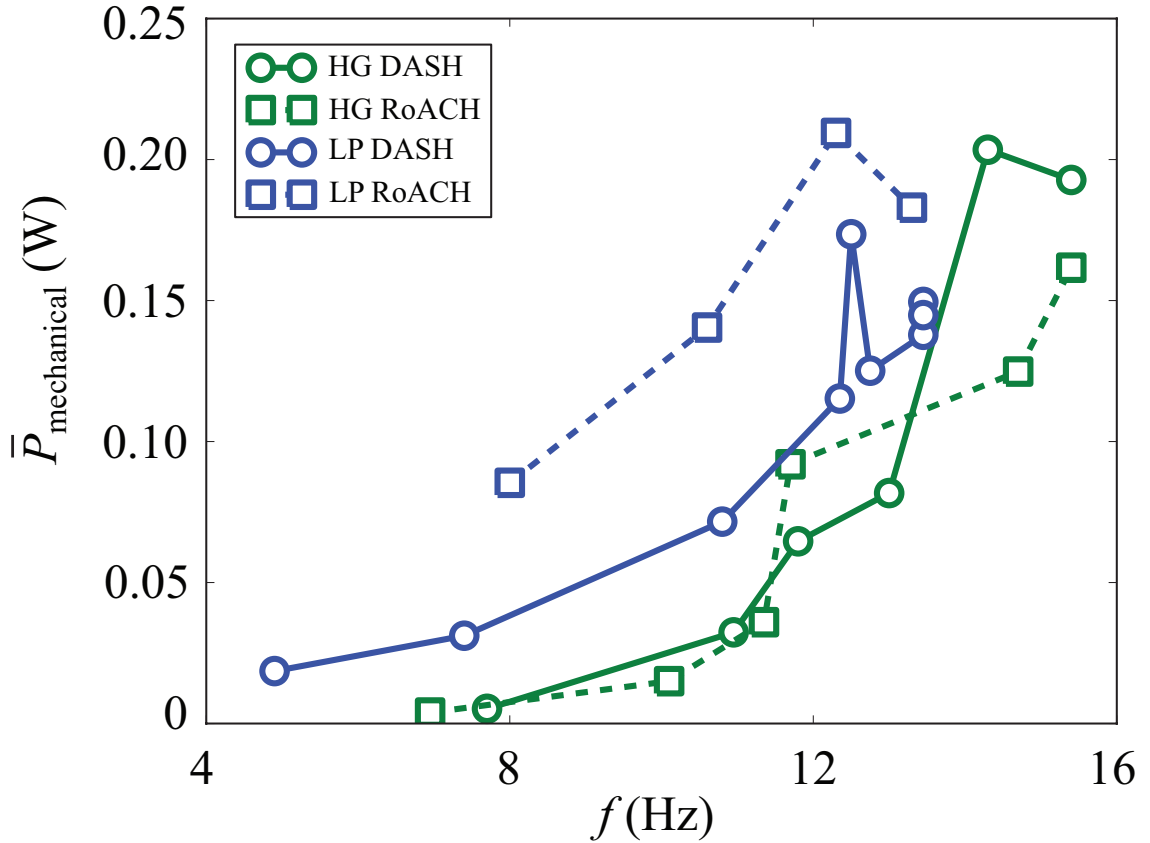


**Figure 88:** Average speed as a function of stride frequency of DASH (circles) and ROACH (square) on hard ground (HG, green) and loosely packed granular media (LP, blue). Lines are linear fits to the DASH data assuming a linear  $\bar{v}$ - $f$  relationship with an intercept of zero.

On loosely packed granular media, both robots suffer substantial performance loss. DASH’s speed drops by  $\sim 40\%$  for all frequencies, but maintains a proportional  $\bar{v}$ - $f$  relationship (dashed blue line). The slope of the  $\bar{v}$ - $f$  relationship is lower as compared to hard ground data, suggesting that there is more slip during each stride, although stride length remains independent of stride frequency. On the other hand, RoACH suffers near total ( $> 90\%$ ) performance loss, with  $\bar{v} \approx 5$  cm/s and roughly independent of frequency.

The difference in performance loss can be explained by the different limb morphology and kinematics of both robots. Closer observation of the robot kinematics from lateral high speed videos show that RoACH, due to its upright posture combined with its compliant limbs and kinematics (the curvature of the legs pointing forward), cannot effectively retract its limbs from the grains; instead, RoACH’s limbs penetrate deep into the substrate and constantly move back and forth within the fluidized grains with the body lying on the surface, resulting in tripod interference and large belly drag. The inability to retract limbs causes RoACH to “swim” at low speeds in fluidized granular media via frictional drag on the limbs similar to how SandBot swims in granular media [92]. DASH’s sprawled limb posture and kinematics, on the other hand, prevents it from getting trapped in the swimming regime for the parameters studied here and enables it to achieve  $\sim 5$  bodylength/s on loosely packed poppy seeds, a huge improvement from SandBot’s  $\sim 0.1$  bodylength/s [92]. This confirmed our speculation that on deformable substrates such as granular media, small lightweight robots of DASH’s scale can achieve higher mobility because of their high thrust-to-gravity ratio provided that limb morphology and kinematics are properly designed.

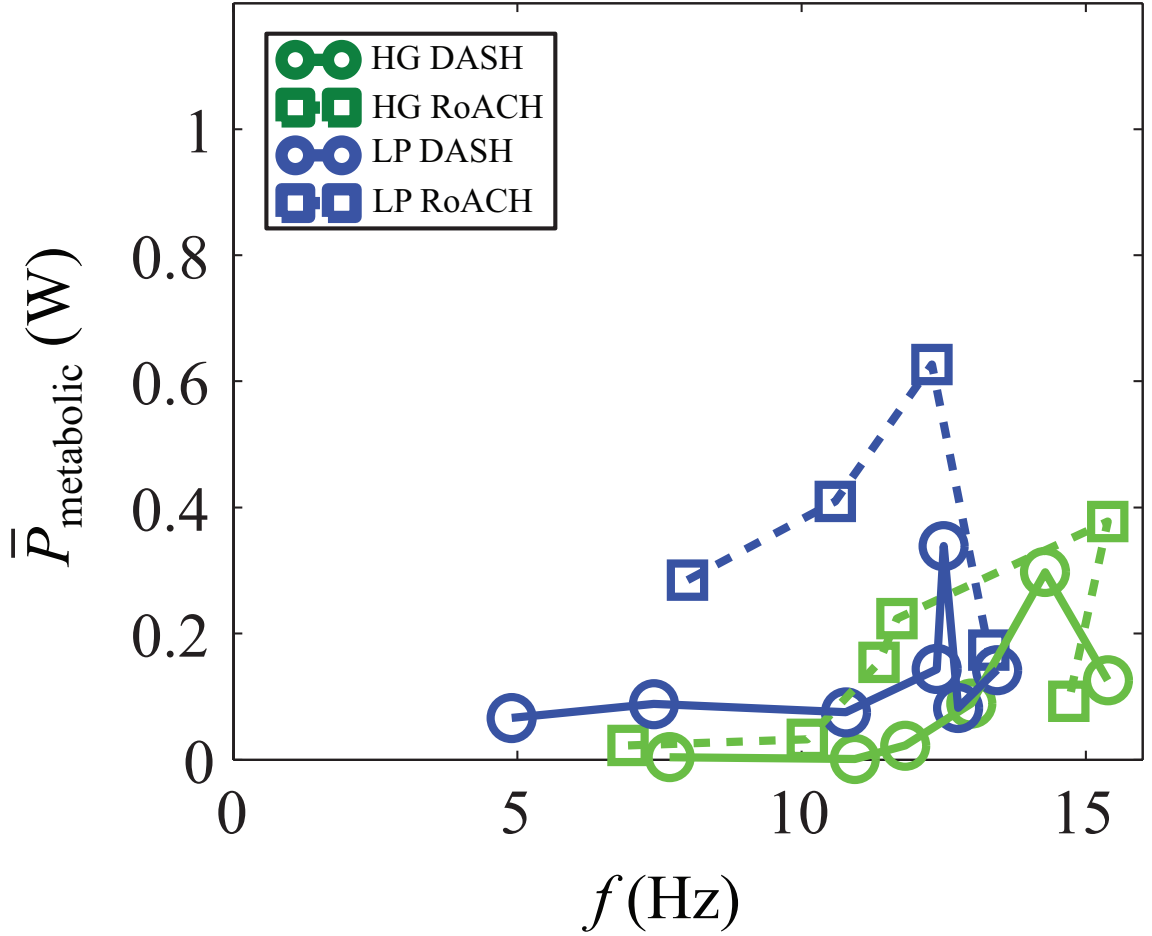
It is also worth noting from Fig. 88 that for DASH, run-to-run deviation from the linear  $\bar{v}$ - $f$  relationship is more pronounced on hard ground than on loosely packed granular media. The irregular  $\bar{v}$ - $f$  relationship for RoACH on hard ground also reduces to a roughly constant relationship on loosely packed granular media. We speculate that such reduction in run-to-run variation in speed originates from differences in stability on the two distinct substrates. On hard ground, while mobility is higher for both robots because of the larger ground reaction forces and reduced drag, their rapid bouncing motion can suffer greatly from yaw, pitch, and roll instabilities caused by non-periodic impacts and the large kinetic



**Figure 89:** Mean mechanical power as a function of stride frequency of DASH and RoACH moving on hard ground (green) vs. loosely packed granular media (blue).

energy associated with bouncing dynamics, which may result in large run-to-run variation in speed. On granular media, instability is rare because the “softer” dissipative granular media serves as a “buffer” to absorb any abrupt forces and accommodate a smoother motion at the cost of reduction in speed. This is consistent with previous observations in SandBot [92].

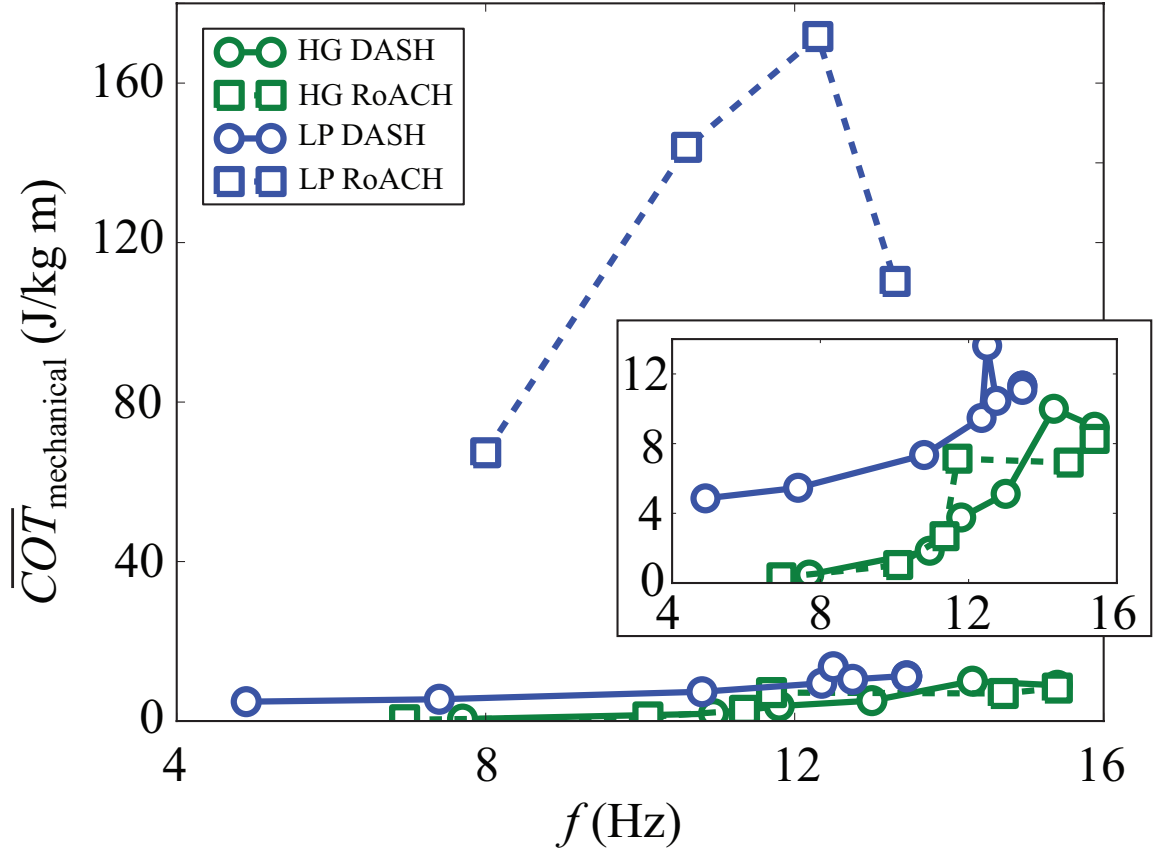
The distinct differences between foot-ground interaction with hard ground and with soft granular media is further revealed by the power consumption characteristics. As shown in Fig. 89, the mean mechanical power  $\bar{P}_{mechanical}$  for both robots is consistently higher on loosely packed granular media than on hard ground at all frequencies, with a smaller increase for DASH than for RoACH. This supports our speculation that DASH’s sprawled limb posture and kinematics is more effective for locomotion on granular media. Also noteworthy is the faster than linear increase of  $\bar{P}_{mechanical}$  with  $f$  for both robots on both substrates.



**Figure 90:** Mean metabolic cost of transport as a function of frequency of DASH and RoACH moving on hard ground (green) vs. loosely packed granular media (blue).

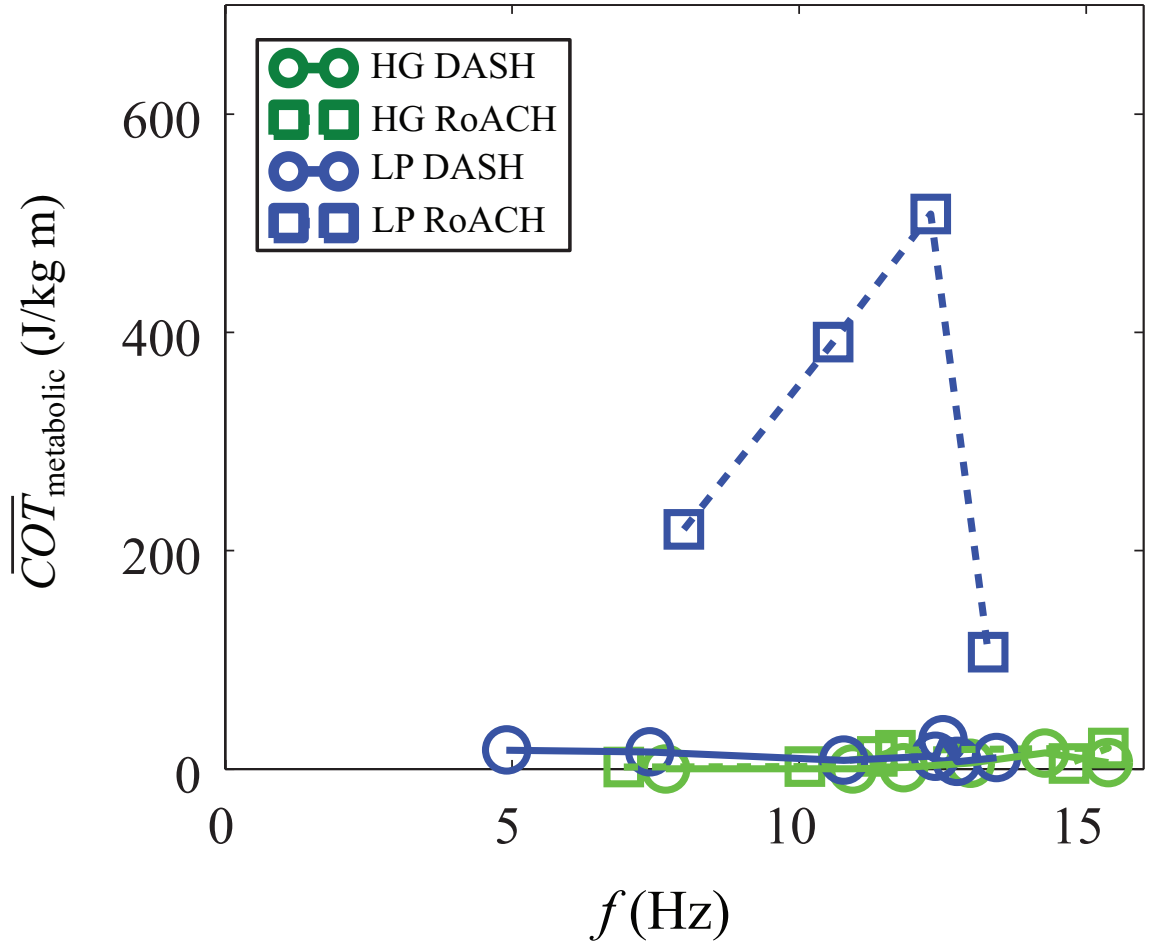
This may be an indication that the ground reaction force increases with frequency. Since in granular media, force is roughly rate-independent [69, 95], this implies that the granular reaction force may be dominated by the inertial force of translating the robot forward at each step (similar to [96]). In such locomotor mode we expect the power to increase as  $f^3$  and the data is not inconsistent with this prediction. It is noteworthy that even on loosely packed granular media, the mechanical power of DASH and RoACH is on the order of  $10^{-1}$  W, on the order of 100 times smaller than RHex's  $10^1$  W on hard ground [15].

Fig. 91 shows the mean mechanical cost of transport of both robots on both substrates. The most striking feature of the data is that RoACH on loosely packed granular media has very large mechanical cost of transport as compared to other cases ( $\sim 10$  times larger).



**Figure 91:** Mean mechanical cost of transport as a function of frequency of DASH and RoACH moving on hard ground (green) vs. loosely packed granular media (blue). Inset highlights the data in the main figure which is obscured by high  $\overline{COT}_{\text{mechanical}}$  of RoACH on loosely packed granular media.

This results directly from RoACH’s very slow “swimming” motion on loosely packed granular media, as  $COT \sim v^{-1}$ . During swimming motion, limbs constantly translate within fluidized grains and only generate net forward motion when the frictional drag on the limbs overcome that on the body. Most of the mechanical work is dissipated by the fluidized granular material which acts like a highly dissipative frictional fluid in which force is rate-independent [95] (this is different from the rate-dependent viscous dissipation of Newtonian fluids at low Reynolds number). The inset in Fig. 91 shows that  $\overline{COT}_{\text{mechanical}}$  increases with  $f$  faster than linearly for all other cases. Comparing DASH and RoACH, we see that locomotion speed and energy consumption on granular media are both greatly improved when the locomotor avoids operating in the swimming regime and instead makes use of



**Figure 92:** Mean metabolic cost of transport as a function of frequency of DASH and RoACH moving on hard ground (green) vs. loosely packed granular media (blue).

solidified granular media by adjusting morphology, kinematics, frequency, etc. This confirms the importance of utilizing the solidification properties of granular media for effective locomotion discovered in previous studies [92, 97, 96]. Compared to other animals [161] and legged robots [51, 162], both DASH and RoACH have relatively low minimal cost of transport on solid ground, and DASH also has relatively low cost of transport on loose ground (Fig. 93).

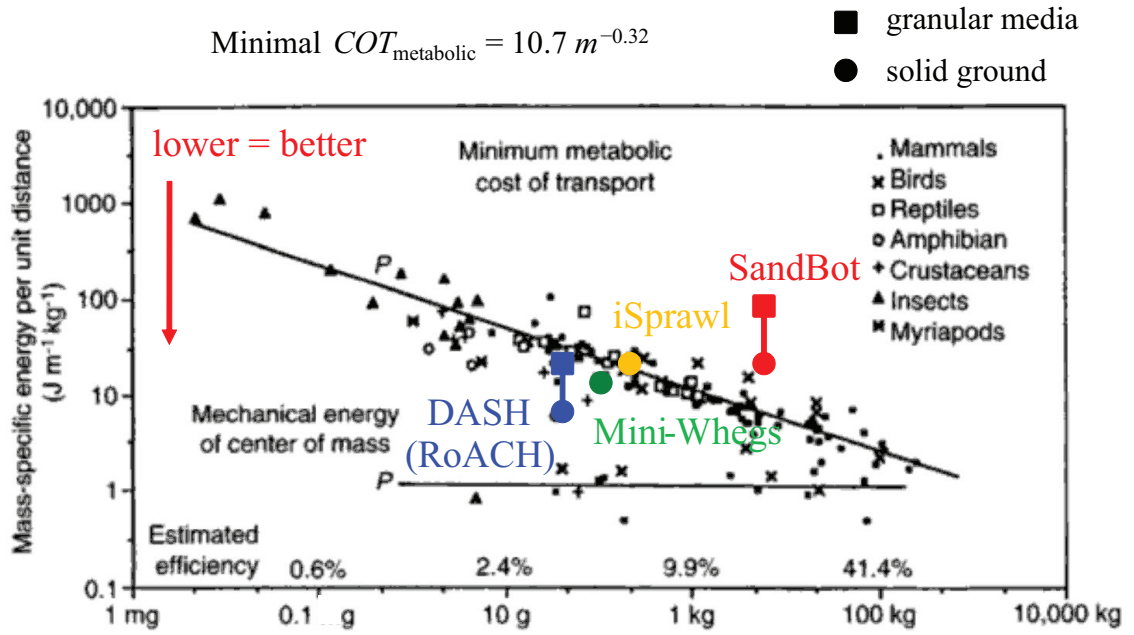


**Figure 93:** Comparison of minimal mechanical cost of transport to animals and other legged robots. Modified from [161]. Data of other robots are from [51, 162].

## 6.5 Conclusions

To probe the capability and assess the benefits and tradeoffs of various limb morphology and kinematics of small legged robotic platforms on a variety of terrains, we systematically tested the performance of the DASH and RoACH robots with different limb morphology and kinematics on hard ground and loosely packed granular media. We investigated how speed and power consumption characteristics vary with stride frequency under open loop control and compared performance across robotic platforms and substrates. We found that both robots suffer performance loss in the form of reduction in speed and increase in mechanical power and cost of transport as substrates weaken from rigid hard ground to deformable granular media, while the instability intrinsic to bouncing motion on hard ground is largely removed by the dissipative nature of granular media. We also found that differences in robot limb morphology and kinematics have a large impact on the platforms susceptibility to performance loss and instability. Future work could test sensitivity of performance to changes in limb morphology and kinematics by systematically varying these factors in analogy with the variation of SandBot’s kinematics [97].

Our study is among the first to investigate how the performance of small lightweight legged robots differs as the substrate changes from rigid to deformable ground. Our results show that when moving on deformable ground such as granular media, even for lightweight platforms with relatively large thrust to gravity ratio, precaution needs to be taken to avoid limbs getting caught and being trapped in the swimming regime. Traversing hard ground, on the other hand, requires careful management of kinetic energy and ground reaction dynamics for legged devices to minimize yaw, pitch, and roll instabilities.

Careful study of small physical models such as DASH and RoACH can also inform locomotion biology in understanding how small animals appear to move effortlessly across a diversity of complex substrates [150, 6]. Further studies of this kind can lead to systematic empirical laws (and ultimately comprehensive theory) of limb-ground interaction with a spectrum of substrates ranging from rigid ground to deformable grounds like granular media. Such advanced understanding will inform limb design and control methodologies, similar to the well-developed models of aerial and aquatic craft. Future devices will begin to

perform at levels comparable to organisms; these capabilities could be used for more efficient and capable exploration of challenging terrestrial environments (*e.g.* battlefields, building debris, and natural disasters sites).

## 6.6 Appendix

### 6.6.1 Performance on closely vs. loosely packed granular media

In addition to performance on hard ground vs. (loosely packed) granular media, both DASH and RoACH were also tested on closely vs. loosely packed granular media. Volume fraction was  $\phi = 0.580$  for loosely packed and  $\phi = 0.633$  for closely packed granular media. In these experiments, RoACH was run with the curvature of the legs pointing backward (similar to the case with the RHex and Sandbot robots).

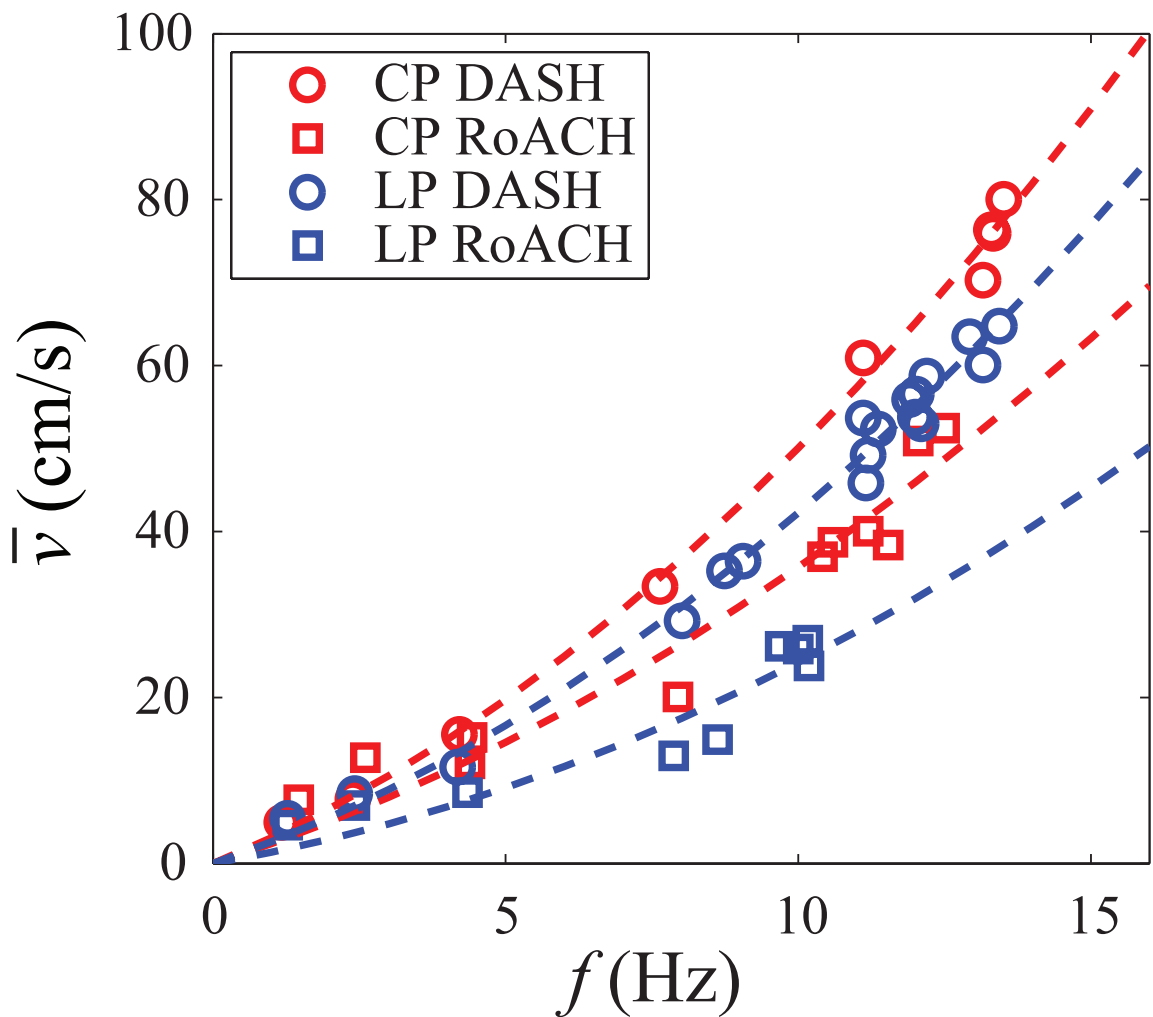


**Figure 94:** Average speed as a function of stride frequency of DASH (circles) and ROACH (square) on closely packed (red) and loosely packed granular media (LP, blue). Curves are fits to the data assuming a quadratic  $\bar{v}$ - $f$  relationship with an intercept of zero.

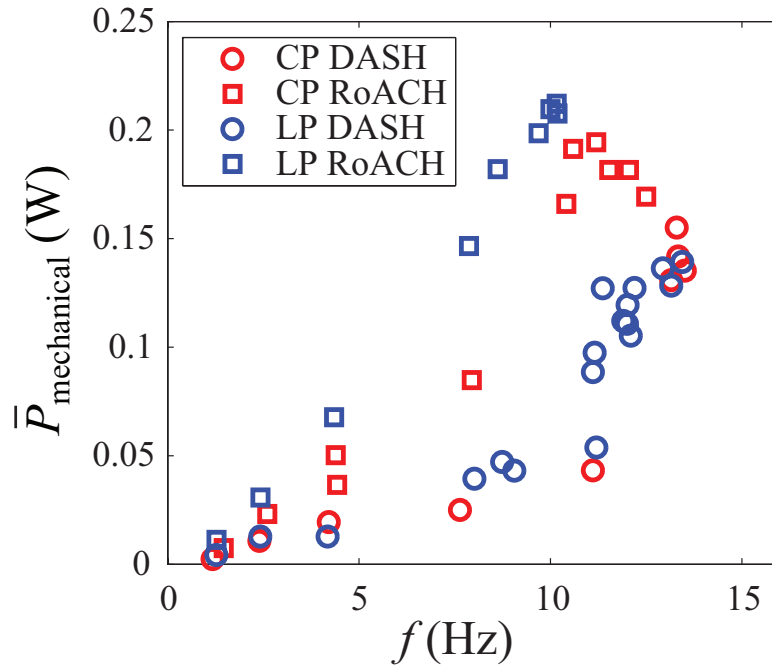


**Figure 95:** Mean mechanical power as a function of stride frequency of DASH and RoACH moving on closely packed (red) vs. loosely packed granular media (blue).

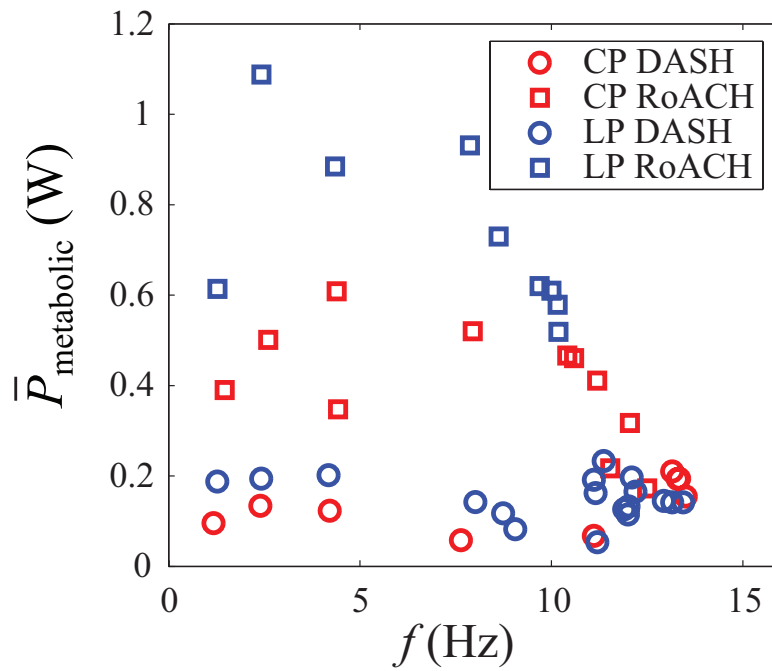


**Figure 96:** Mean metabolic cost of transport as a function of frequency of DASH and RoACH moving on closely packed (red) vs. loosely packed granular media (blue).

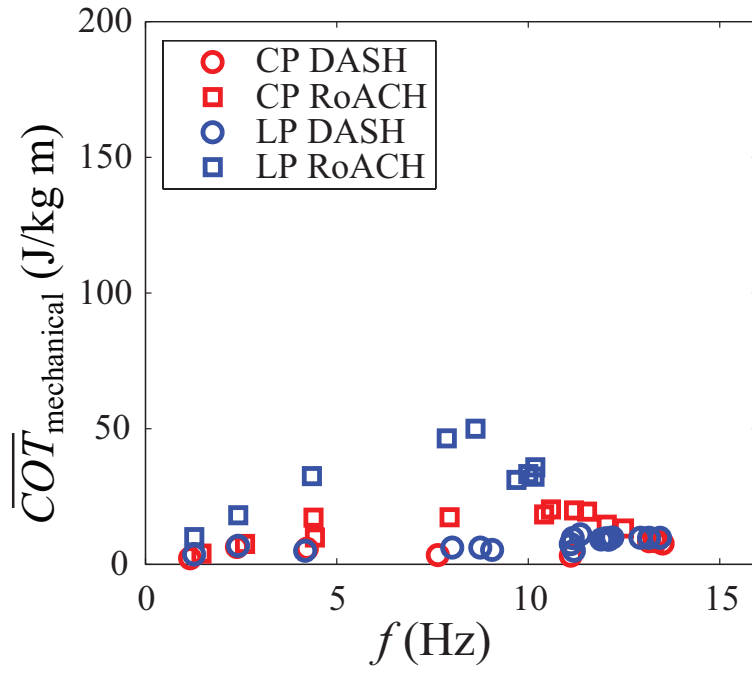


**Figure 97:** Mean mechanical cost of transport as a function of frequency of DASH and RoACH moving on closely packed (red) vs. loosely packed granular media (blue).

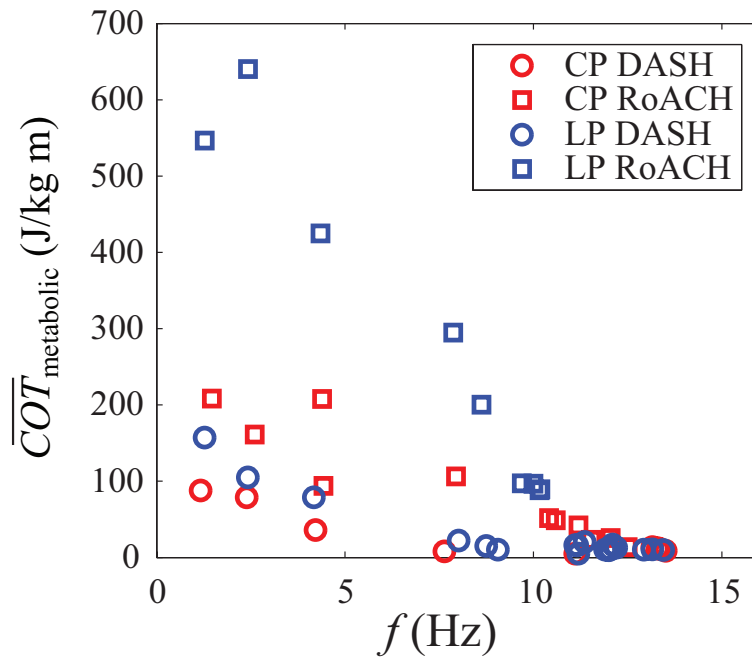


**Figure 98:** Mean metabolic cost of transport as a function of frequency of DASH and RoACH moving on closely packed (red) vs. loosely packed granular media (blue).

### 6.6.2 SCM process

The robotic platforms featured in these experiments are small, lightweight ( $\sim 10$  cm,  $\sim 20$  g) hexapedal robots that utilize alternating tripod gaits for horizontal locomotion. They both feature drive mechanisms which use a single 6 mm brushed DC motor (I-Fly Vamp) to drive all six limbs. Onboard lithium 90 mAh polymer battery (Fullriver), Bluetooth communications (Roving Networks RN-41), microcontroller (Microchip PIC dsPIC33), and motor driver allow the robots to run preprogrammed commands autonomously while sensors detect back electromotive force (back EMF) in the DC motor.

The robot fabrication process closely follows the Smart Composite Manufacturing (SCM) process[60], but instead of pre-impregnated composite fiber laminate, we substitute lightweight, double sided coated posterboard (Nature Saver posterboard, Officemax.com). For the polyimide flexure layer, we substitute a thicker polyethylene terephthalate (PET) film because thermal compatibility of the film is less of a concern than in the SCM process. In addition, the PET is less inert so it bonds better to various adhesive polymers. Just as in the SCM process, the posterboard is cut using a precision laser (VersaLaser VL200) according to a 2-dimensional design drawing. However, unlike with carbon fiber composites, the posterboard can be easily cut with an infrared laser. The steps for the prototyping process are outlined below with the step numbers corresponding to Fig. 99:

1. The process begins with a sheet of posterboard.
2. Gaps are laser-cut into the posterboard where flexures will be located in the final structure.
3. Two layers of adhesive polymer with one layer of flexural polymer (high melting point) are placed between two sheets of posterboard.
4. The resulting structure is rolled through heated rollers to apply pressure and melt the adhesive layers, bonding the structure.
5. Outlines of parts are then laser cut, releasing the parts from the original sheet.

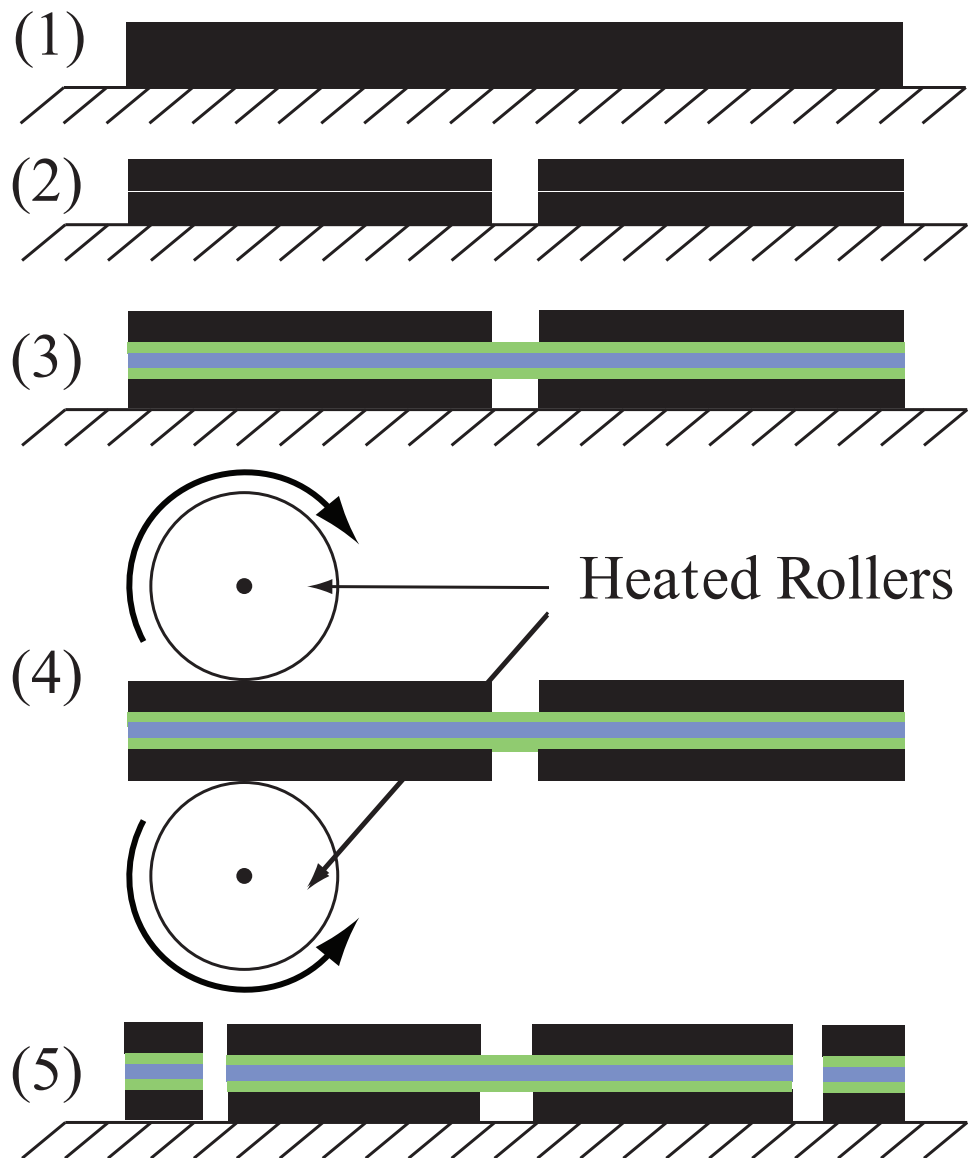


**Figure 99:** Step-by-step illustration of the posterboard link and hinge fabrication process [60].

Because the posterboard, unlike pre-impregnated composites, contains no adhesive, a simple thermoset polymer film for the flexure layer is insufficient. We must either add adhesive layers separately, or use a polymer film with an integrated adhesive to bond the structure. A carrier film with integrated adhesive is convenient because it is essentially monolithic. However, the standard thicknesses of such films limit the ability of the designer to change the stiffness of flexure hinges by using different thickness films. While it is possible

to use more than one layer of such a film, the interaction of the adhesive layers between the carrier film layers creates a noticeable viscoelastic response from the flexure hinges. In order to retain flexibility for the designer in the choice of flexure thickness, we have chosen to add a separate adhesive between the posterboard and the flexure film. For the the flexure film we use 25  $\mu\text{m}$  PET depending on the desired flexure stiffness. For the adhesive layer we use Otiva<sup>®</sup> hot mount adhesive (gbconnect.com), an unsupported, heat-activated mounting adhesive. Before the posterboard robot parts are cut, the hot mount is applied to one face of the posterboard and the liner film detached.

This fabrication method is appropriate for fabricating entire functional robots or simply mocking up a small mechanism to be integrated into a larger robot design. The process makes it possible to construct very lightweight robots with complex spatial kinematics that exhibit relatively high power densities. The posterboard SCM process also enables the designer to quickly try out a folded design and explore features such as alignment tabs or self-jamming flexures that can aid significantly in the final assembly process. For example, the designs presented below can be cut out and assembled in a matter of two to three hours. These hexapod crawler designs demonstrate the complicated 3D mechanisms that can result from folding a 2D design using this approach.

### **6.6.3 RoACH**

The Robotic Autonomous Crawling Hexapod (RoACH, Fig. 100) is a six-legged robot fabricated using the process described above. The kinematic design of the robot uses a combination of slider crank and four-bar linkages to create an alternating tripod gait that can be actuated using a single rotary input connected to a crank. The abduction and adduction degree of freedom is actuated by a slider crank mechanism. Protraction and retraction of the leg are achieved using a parallel four-bar linkage at the hip. Diagrams of the kinematics hip linkages of RoACH are shown in Fig. 101. As configured for this experiment, RoACH had a mass of 24.9 g.

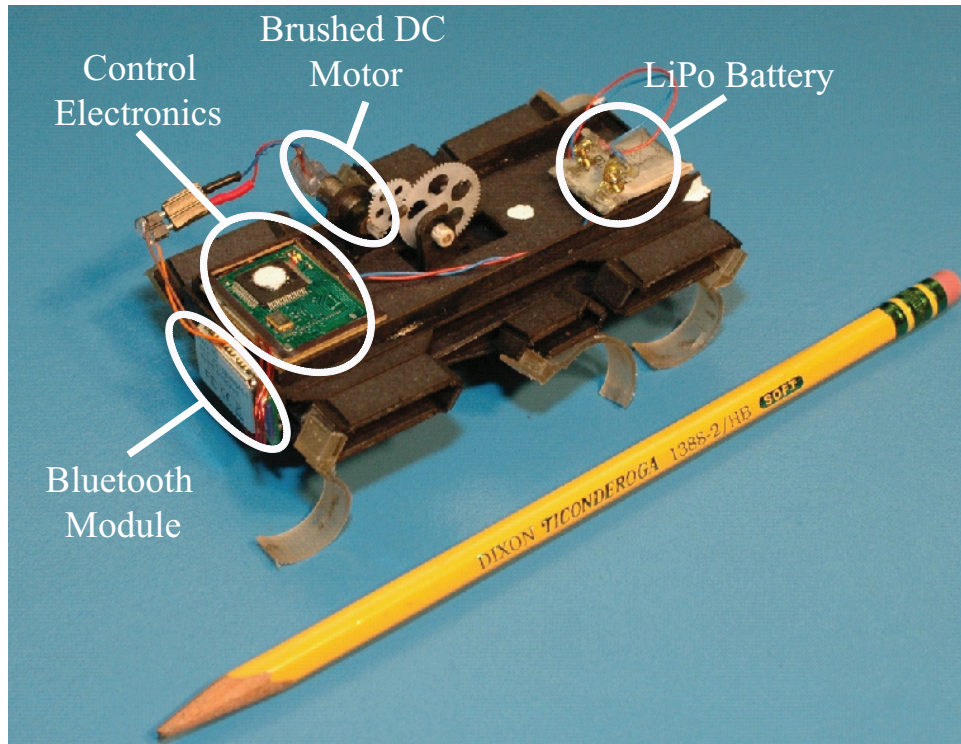


**Figure 100:** The RoACH robot shown with component parts of onboard power and electronics highlighted.

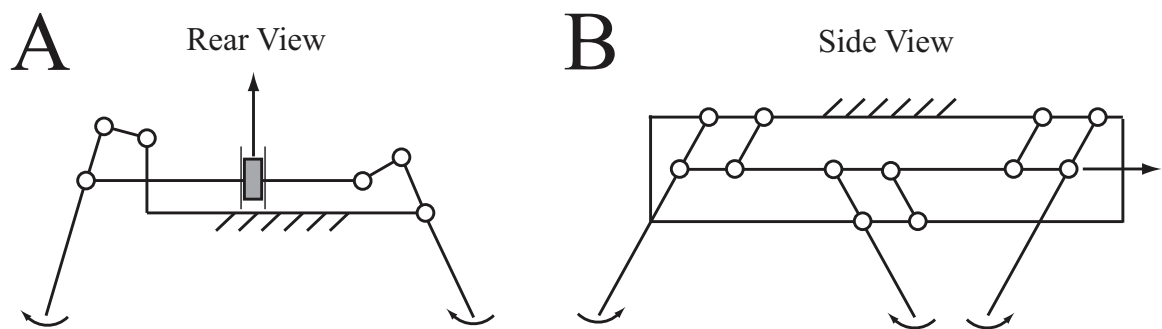


**Figure 101:** Linkage kinematics for RoACH's alternating tripod gait. (a) Vertical translation of the center link causes one tripod to engage the ground while the other is lifted. (b) Fore-aft translation of the central link causes the front and rear legs to rotate forward and the middle leg to rotate backward. Driving the center link in a circle in the sagittal plane creates the alternating tripod gait.

#### 6.6.4 DASH

A second robotic platform developed using the posterboard SCM process is the Dynamic Autonomous Sprawled Hexapod (DASH, Fig. 102) [59]. Like RoACH, DASH employs an

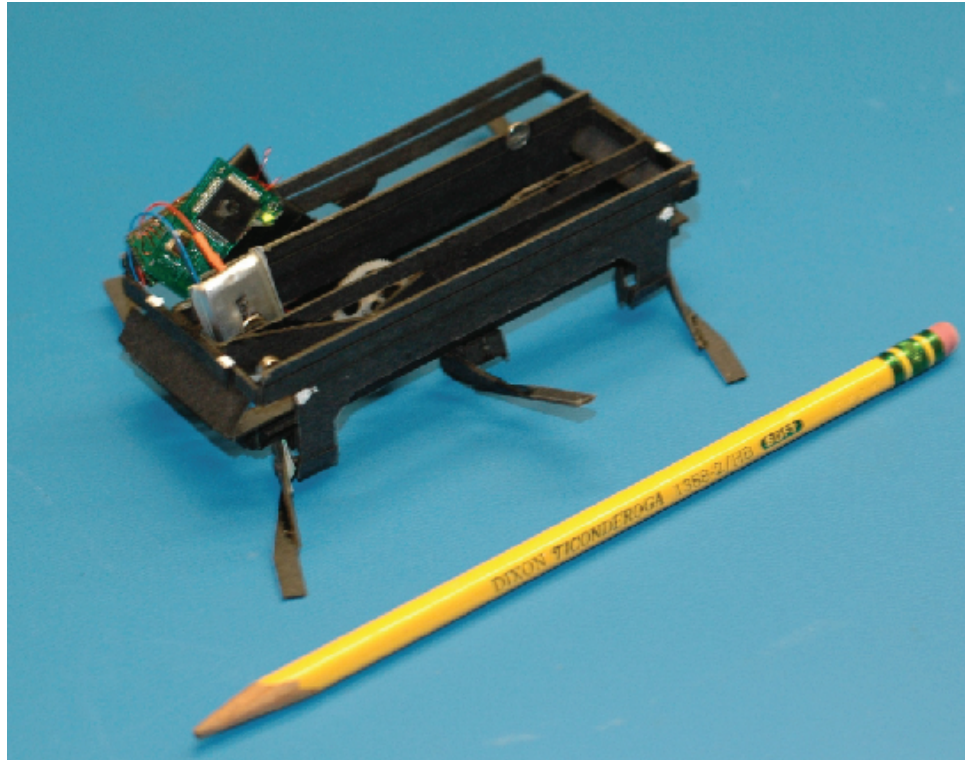


**Figure 102:** The DASH robot with component parts of onboard power and electronics (same as RoACH).

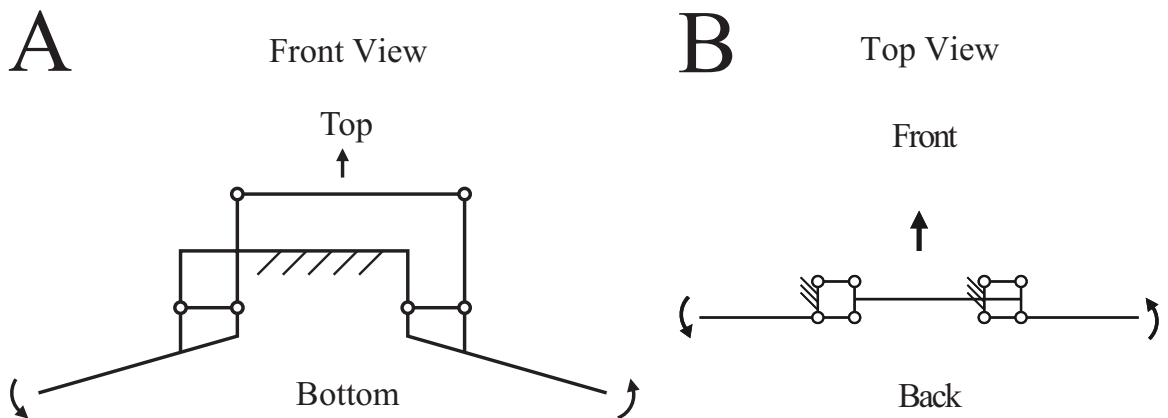


**Figure 103:** Linkage kinematics of DASH. (a) Vertical translation of top link causes one tripod to lift and the other to lower. (b) Fore-aft motion of the center link causes one tripod to rotate forward and the other to rotate backward.

alternating tripod gait which is driven by a single rotary input. The structure of DASH creates an oar-like transmission in which the circular input in the sagittal plane creates circular leg trajectories. The fore-aft displacement of the motor output rotates the four-bar

hip mechanisms, protracting one tripod and retracting the other. The vertical motion of the motor output angles the orientation of the hip four-bar mechanism which simultaneously lifts one tripod and lowers the other. Diagrams of the kinematics hip linkages of DASH are shown in Fig. 103. These vertical and fore-aft degrees of freedom are coupled together to enable a circular leg trajectory. With the battery and all onboard electronics for this experiment, DASH had a mass of 22.1 g.

While DASH and RoACH share a number of features such as their manufacturing process, electronics, motor, and even an alternating tripod gait, they have significant morphological differences. The most notable among these differences is their posture. DASH has a sprawled posture, with its legs directed outward nearly horizontally; RoACH has an upright posture with its legs directed almost vertically downward.

## CHAPTER VII

### TOWARDS A TERRAMECHANICS FOR LEGGED LOCOMOTION ON GRANULAR MEDIA

#### 7.1 *Summary*

During locomotion on sand, animals and robot models interact with granular substrates to generate thrust and lift. While resistance forces on simple shapes like discs and plates during intrusion along vertical or horizontal trajectories are well studied, no general model yet exists to predict resistance forces for intrusion along complex trajectories during footsteps. Recently a granular resistive force theory (RFT) was used to model forces on an intruder moving in the horizontal plane at a fixed depth, e.g. a sand-swimming lizard [95]. The RFT divides the intruder into small elements each generating forces that are assumed independent. Summation of the element forces predicts net thrust and drag. To begin to create a terramechanics for legged locomotion on granular media, we extend the RFT to intrusion in the sagittal plane. We measure the lift and drag on a small plate ( $3.8 \times 2.5 \times 0.6$  cm<sup>3</sup>) moving in granular media (1 mm diameter poppy seeds, 0.3 mm and 3 mm glass particles) of controlled compaction as a function of depth, angle of attack, and direction of motion. Both lift and drag increase with depth and depend sensitively on angle of attack and direction of motion at a given depth. Lift and drag are larger for intrusion into than out of the media due to symmetry breaking by gravity. For a model C-shaped limb rotating about a fixed axle, integration of plate forces captures the net lift and thrust measured in experiments. The RFT predicts that reversal of the C-shaped limb results in a smaller maximal lift with significant negative lift (suction) during the late phase of rotation, which is confirmed by experiments. In accord with the difference in lift, on poppy seeds a small bio-inspired legged robot (15 cm, 80 g) walks 50% faster at any frequency with C-shaped limbs than with reversed C-shaped limbs. Using the forces on the limbs calculated from the resistive force theory, a previously developed kinematic model based on vertical force balance

is used to predict robot performance. Model calculations show similar approximately linear speed vs. frequency relationships as observed, but under-predicts speeds at any frequency for both C-shaped and reversed C-shaped limbs. This highlights the need for improved models of legged locomotion on granular media which incorporate the dynamics of the locomotor and provide ways to predict forces on the intruder when granular media remain solid below yield stress\*.

---

\*This Chapter is part of a paper by Chen Li and Daniel I. Goldman, to be submitted to The Proceedings of the National Academy of Sciences [163].

## 7.2 Introduction

During locomotion on sand, animals and robot models interact with granular substrates to generate thrust and lift [92, 97, 98, 85]. Unlike fluids for which flow and forces can in principle be computed by Navier-Stokes Equations [21], no such comprehensive theory currently exists for granular media, particularly during localized intrusion [61]. While terramechanics has been around for a few decades and has guided the development of off-road vehicles [64, 65, 66, 67], it focused on the study of the overall performance of large wheeled and treaded vehicles with unprepared soil, and the locomotor-ground interaction involved largely concentrates on how normal stresses determine shear stresses. Due to the large size of the vehicle wheels and treads as compared to the size of the grains in a granular medium, this is mainly a global forcing problem. In addition, current terramechanics is largely based

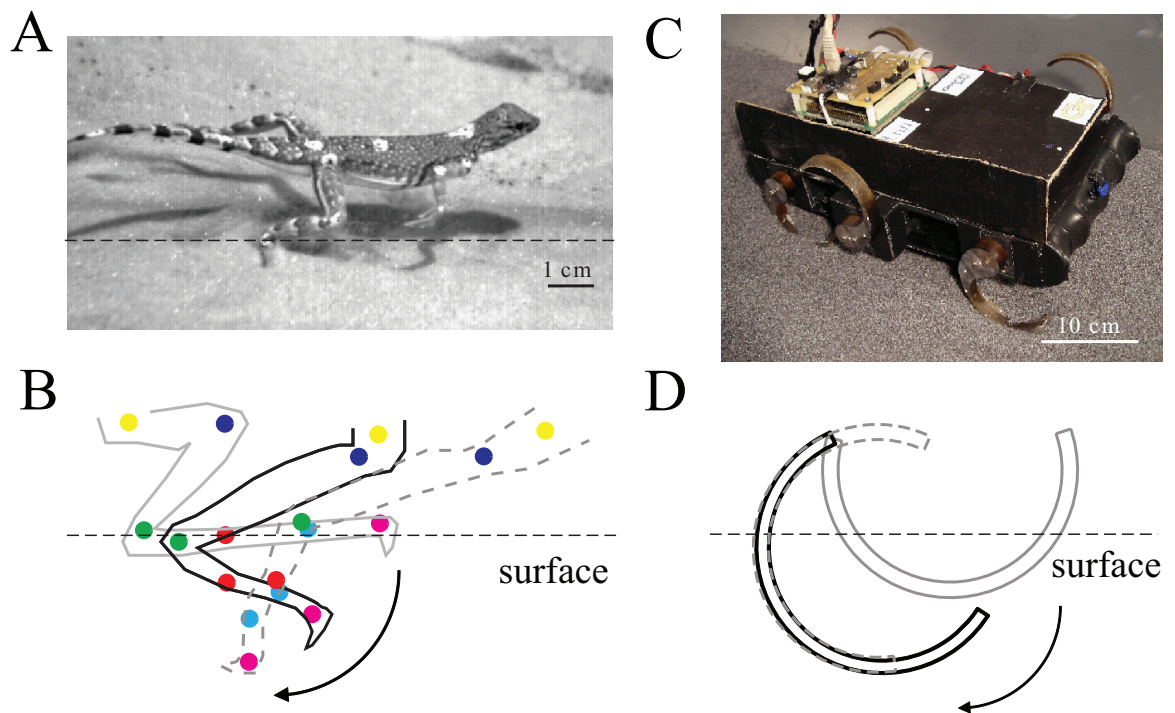


**Figure 104:** Relevance of rotational intrusion in locomotion. (A) The zebra-tailed lizard running on granular media (0.27 mm diameter glass particles). (B) Tracings of the lizard's hind limb from x-ray high speed video showed foot rotation subsurface. (C) A bio-inspired legged robot, SandBot, standing on granular media ( $\sim 1$  mm diameter poppy seeds). (D) SandBot's rotary walking: C-shaped legs rotate into granular media before the media solidify.

on empirical measurements and models, which has a major limitation that measurements must be performed on a case-by-case basis for different intruder shape and trajectory. No general models currently exist to predict resistance forces for localized intruder of complex geometry along complex trajectories during footsteps, particularly those relevant to legged locomotion.

Previous studies of resistance forces during localized intrusion into granular media have focused on simple intruders like discs and plates moving along simple trajectories like vertical or horizontal paths [70, 71, 72, 73, 74]. However recent locomotion studies have shown that the intrusions of body, limbs, and feet can be more complicated in that the geometry and trajectories of the intruder could both be complex (Fig. 104) [92, 97, 98, 85]. Therefore, it is crucial to develop a general model to describe granular forces during localized intrusion.

A promising candidate for such a general model is the resistive force theory (RFT) [164]. A granular resistive force theory in the horizontal plane<sup>†</sup> was recently used to model forces on a sand-swimming lizard, which swims in approximately in a horizontal plane by body undulation [95, 94, 125](Fig. 105). The resistive force theory was initially developed to describe forces on the spermatozoa which by body undulation swims in fluids at low Reynolds number (because the size and speed of the intruder is small) [164]. The resistive force theory divides the intruder moving in a medium into small elements each generating forces that are assumed independent. Summation of the element forces predicts net thrust and drag and captures the performance of the swimmer.

The assumption of independent forces on each element is valid for a thin, long undulatory swimmer (with low amplitude) in low Reynolds number Newtonian fluids, because viscous forces dominate (i.e., Stokes's law) and the inertia of the fluid is negligible [164, 165]. For the sandfish moving in granular media, whose body undulates at speeds of up to 0.4 m/s, the forces can also be described by the resistive force theory [95]. This is because, much like in low Reynolds number Newtonian fluids, in granular media at low intrusion speeds ( $< 0.5$  m/s) the inertia of the medium (grains) is small, and thus forces are friction-dominant and independent of speed [69, 70]. Because grain interactions are dissipative, disturbances

---

<sup>†</sup>This model was developed by Yang Ding.

typically dampen in short times, and thus changes in the static configuration dominate the forces [95].

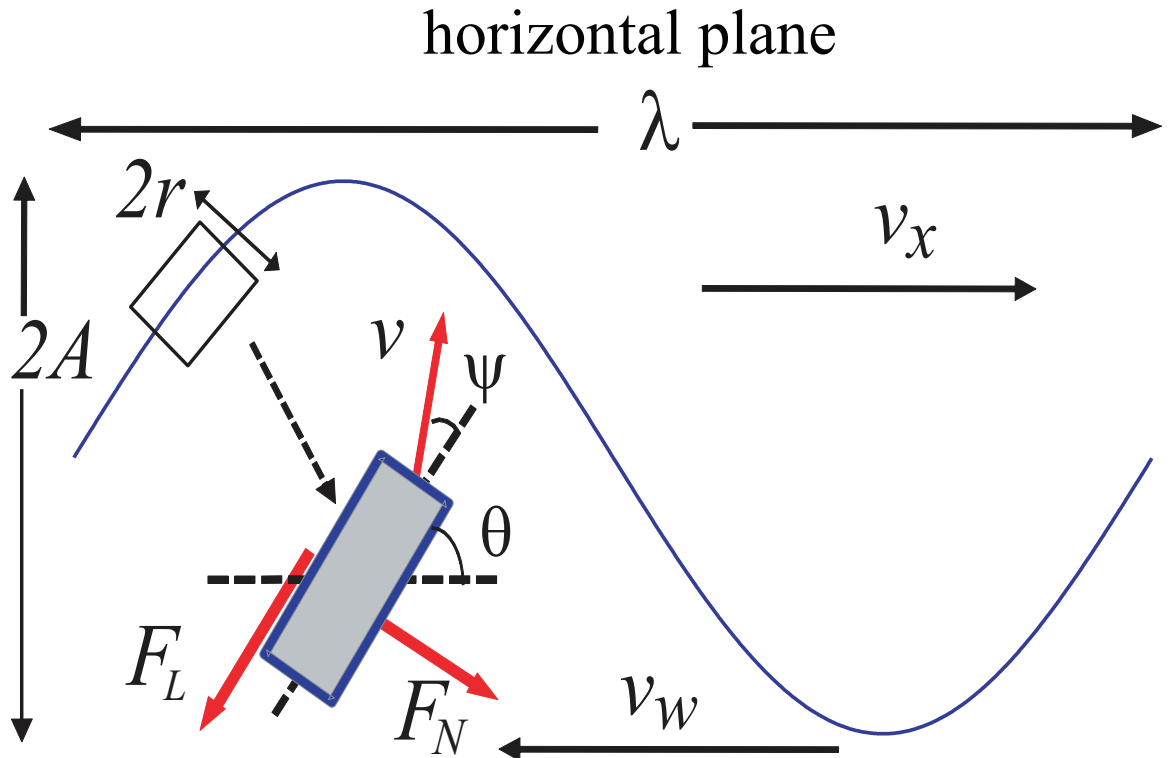


**Figure 105:** Granular resistive force theory in the horizontal plane, as applied on the body of the sand-swimming lizard, sandfish, which moves forward subsurface by undulating approximately with a traveling sinusoid wave down the body.  $F_N$  and  $F_L$  are normal and parallel forces on a given element of a sinusoidal traveling wave. Reproduced from [95].

### 7.3 Previous drag experiments in horizontal plane

To obtain empirical force laws for drag force on the sandfish, we moved a stainless steel cylindrical cylinder representing a body element through granular media at constant speed (10 cm/s) and measured the resulting normal and tangential forces for angles  $\psi$  between the element and its displacement direction ranging from 0 to  $\pi/2$  Fig. 107. We used a fluidized bed (22.8 cm  $\times$  22.8 cm) to set the initial volume fraction ( $\phi$ ) of the media. We chose stainless steel because a previous study [166] as well as our measurements showed that sandfish skin and stainless steel have about the same friction coefficient with sand ( $\sim 0.2$ ) [166]. The diameter of the cylinder ( $2r = 1.58$  cm) was similar to that of the sandfish body. The length of the cylinder is 3.8 cm. To avoid effects on the drag due to the finite size of the container, the cylinder was small compared to the size of the fluidized bed

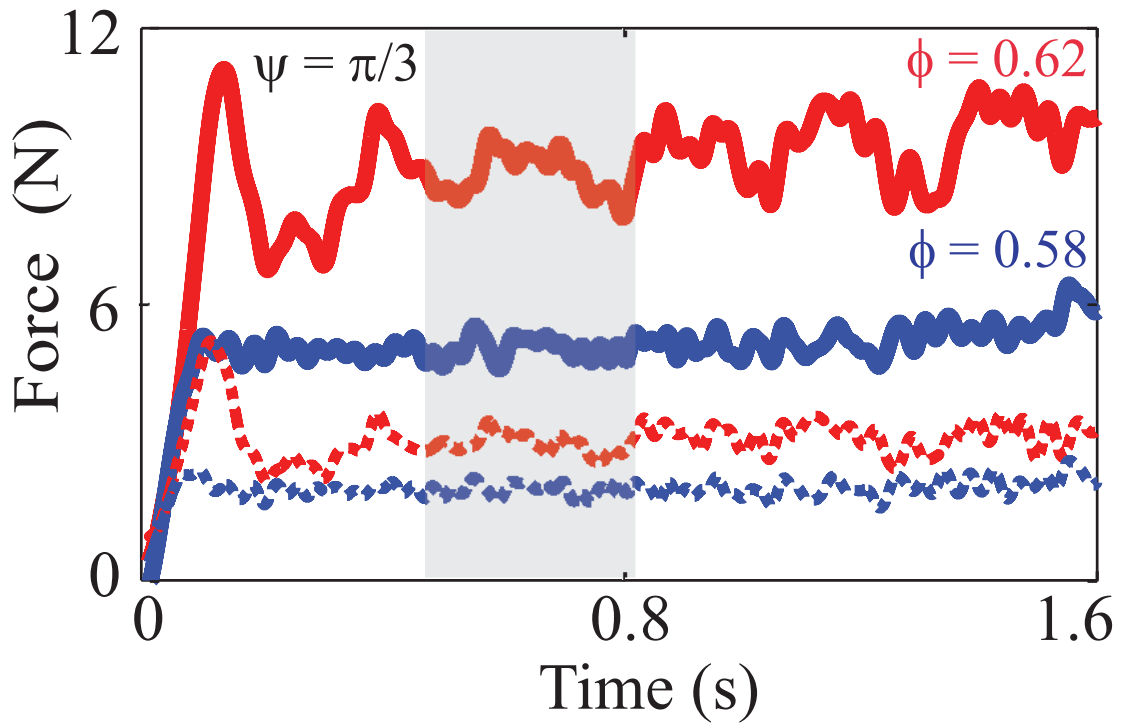


**Figure 106:** Representative total drag force (including sidewalls and end-faces) as a function of time. Intruder is a stainless-steel cylinder (diameter = 1.58 cm and length = 4.00 cm) oriented at an angle  $\psi = \pi/3$  to the direction of its forward speed (10 cm/s). The solid curves correspond to normal force  $F_N$  and the dashed to tangential force  $F_L$ . The red and blue colors correspond to closely and loosely packed media, respectively. The gray region indicate a steady-state region over which average force is calculated. Modified from [95].

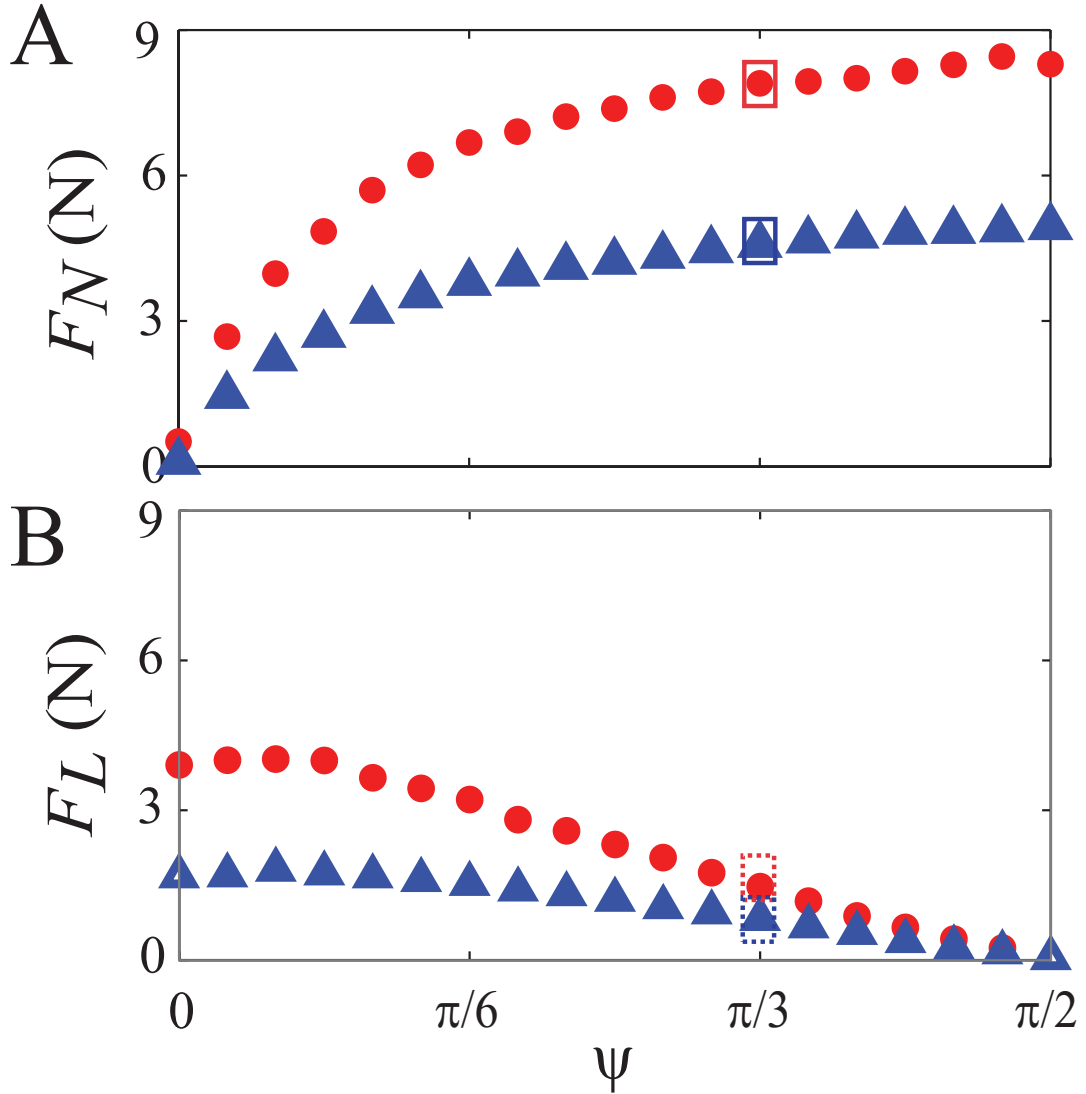


**Figure 107:** Drag force as a function of the angle between segment orientation and direction of motion. (A) Average normal ( $F_N$ ) and (B) tangential ( $F_L$ ) forces on the cylinder (removing force contribution from the end-faces); red circles and blue triangles correspond to closely and loosely packed preparations, respectively. In (A) and (B), the average forces corresponding to the force profiles in Fig. 106 are indicated with the respective rectangles. Modified from [95].

but large compared to the size of the grains. The cylinder was attached to a robotic arm (CRS Robotics) via a thin but stiff supporting rod which moved the structure at constant depth and speed while a 6-DOF force sensor (ATI industrial) mounted between the robotic arm and the supporting rod measured the net force generated during the drag motion (accurate to 0.06 N). The force on the supporting pole was also measured separately and

subtracted to obtain the force on just the cylinder.

Previous studies show that drag in granular media is independent of speed [69, 70] and increases approximately proportionally to depth [70]. To test if this effect persists in the regime relevant to the sandfish (0 – 40 cm/s), we dragged the cylinder perpendicular to speed at 1, 5, 10, 20, 30 cm/s (which covered the sandfish’s range of speeds) at a fixed depth of 7.62 cm and found that over an order of magnitude change in speed, force only changed by 10%; consequently we assumed force was independent of speed. We also dragged the cylinder oriented perpendicular to velocity at different depths (1.27, 2.54, 3.81, 5.08, 6.35, 7.62 cm) at 10 cm/s and confirmed that as seen previously [69] drag was proportional to depth. Therefore, we measured drag force on the cylinder as a function of angle  $\phi$  (for input into the Resistive Force Theory model) by dragging the cylinder at a fixed depth (7.62 cm) and a constant speed of 10 cm/s for different  $\phi$  (Fig. 107).

Before each trial, the initial state of the media was set using a fluidized bed and the test rod rotated to the desired angle using the robotic arm. For each angle the rod was pushed into the material to a depth of 7.62 cm and, after a 2 s pause, was dragged for 15.24 cm through the media and then extracted. Both the force and position of the rod were recorded at 140 Hz. The forces parallel ( $F_L$ ) and perpendicular ( $F_N$ ) to the surface of the rod were resolved by the force sensor and averaged over the steady state drag region (gray region in Fig. 106). The supporting rod was tested without the stainless steel test rod to remove the contribution from its drag force. Three trials were conducted for each  $\psi$ ,  $\phi$ .

These drag force measurements, coupled with a resistive force theory in the horizontal plane, successfully explained the undulatory motion of a sandfish lizard moving horizontally within granular media [95]. The agreement between the sandfish animal experiment and the RFT based model using drag force measurements demonstrated the predictive power of the RFT for locomotion in granular media, and indicated that the assumptions of speed independence, local interaction, and the use of the average  $F_N$  and  $F_L$  for all phases of the motion were good approximations at slow swimming speeds [95]<sup>‡</sup>.

---

<sup>‡</sup>This section is part of a published paper by Ryan D. Maladen, Yang Ding, Chen Li, and Daniel I. Goldman, *Science* (2009) [95].

#### 7.4 Measuring force on a small plate

To begin to create a terramechanics [67] for legged locomotion on granular media, we extend the RFT to intrusion in the sagittal plane. In the horizontal plane, because gravity is perpendicular to the plane, at a given depth, thrust and drag forces on an element depend only on the angle  $\theta$  between the direction of motion and orientation of the element [95]. In the sagittal plane, however, because gravity is within the plane and breaks symmetry, lift and drag forces should depend on both the orientation (angle of attack) and the direction of motion of the element. In granular media, forces increase approximately linearly with depth because the granular “hydrostatic” pressure increases with depth [69, 70, 71, 72]. Note that the RFT has been partially developed for the sagittal plane in a previous study to explain the drag induced lift force on an intruder moving horizontally at a fixed depth [94]; however, this study did not consider the possibility of changing direction of motion and changing depth. In addition, previous studies demonstrated that in many animals and

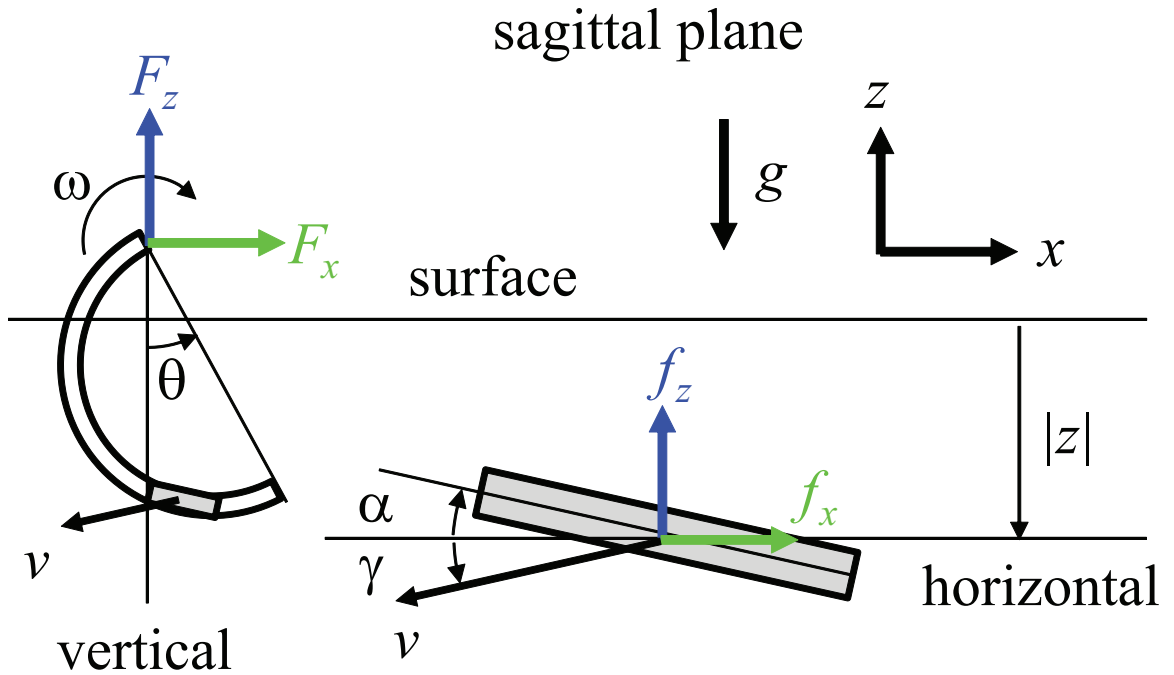


**Figure 108:** Granular resistive force theory in the sagittal (vertical) plane, as applied on the C-shaped leg of a bio-inspired robot, RHex, which rotates about a fixed axle through granular media.

robots moving on granular media, limbs/feet often intrude into the substrate at low speeds ( $v < \sim 0.5$  m/s). In this case, granular media behave like a “frictional fluid”: the inertia of the grains are small compared to grain friction, and intrusion forces are approximately speed independent [92, 95, 97]. Therefore, we perform intrusion force measurements at low speeds.

Therefore, we measured the lift and drag on a small plate ( $3.8 \times 2.5 \times 0.6$  cm<sup>3</sup>) moving in granular media at slow speeds ( $\sim 1$  cm/s) of controlled compaction as a function of depth ( $z$ ), angle of attack ( $\alpha$ ), and direction of motion ( $\gamma$ ) (Fig. 108). We performed the experiments in five different granular media/packing states, e.g., loosely (LP) and closely packed (CP) 1 mm diameter poppy seeds, loosely (LP) and closely packed (CP) 0.27 mm diameter glass particles, and closely packed (CP) 3 mm diameter glass particles (Table 8). Next we present experiments and results in LP poppy seeds (which was later used for robot experiments). The data for the other granular media are qualitatively similar to LP poppy seeds data, and are presented in Appendix.

**Table 8:** Granular media used for developing the resistive force theory in the sagittal plane.

| granular media          | diameter (mm)   | density ( $\times 10^3$ kg/m <sup>3</sup> ) | LP volume fraction | CP volume fraction |
|-------------------------|-----------------|---|--------------------|--------------------|
| 1 mm poppy seeds        | $0.7 \pm 0.1$   | 1.1   | 0.58               | 0.62               |
| 0.27 mm glass particles | $0.27 \pm 0.04$ | 2.5   | 0.58               | 0.62               |
| 3 mm glass particles    | $3.2 \pm 0.2$   | 2.6   | N/A                | 0.63               |

Before each trial, the granular medium (15 cm deep) was prepared by a fluidized bed ( $24 \times 22$  cm<sup>2</sup> area). A 6-DOF robotic arm (CRS robotics) pushed an aluminum plate ( $3.8 \times 2.5 \times 0.6$  cm<sup>3</sup>) oriented at angle of attack  $\alpha$  into the granular medium along direction of motion  $\gamma$ , and force during intrusion was measured by a 6-axis force/torque transducer (ATI). After the plate reached maximal depth, the granular medium was re-prepared into the same initial packing state while the plate was maintained stationary. The plate was then retracted along the same trajectory, and force during retraction was measured.  $\alpha$  and  $\gamma$  were set between trials.  $\alpha$  was varied between  $-\pi/2 \leq \alpha \leq \pi/2$  (between two opposite vertical plate orientations).  $\gamma$  was varied between  $0 \leq \gamma \leq \pi/2$  (from horizontal drag to

$$\alpha = \pi/6, \gamma = \pi/4$$

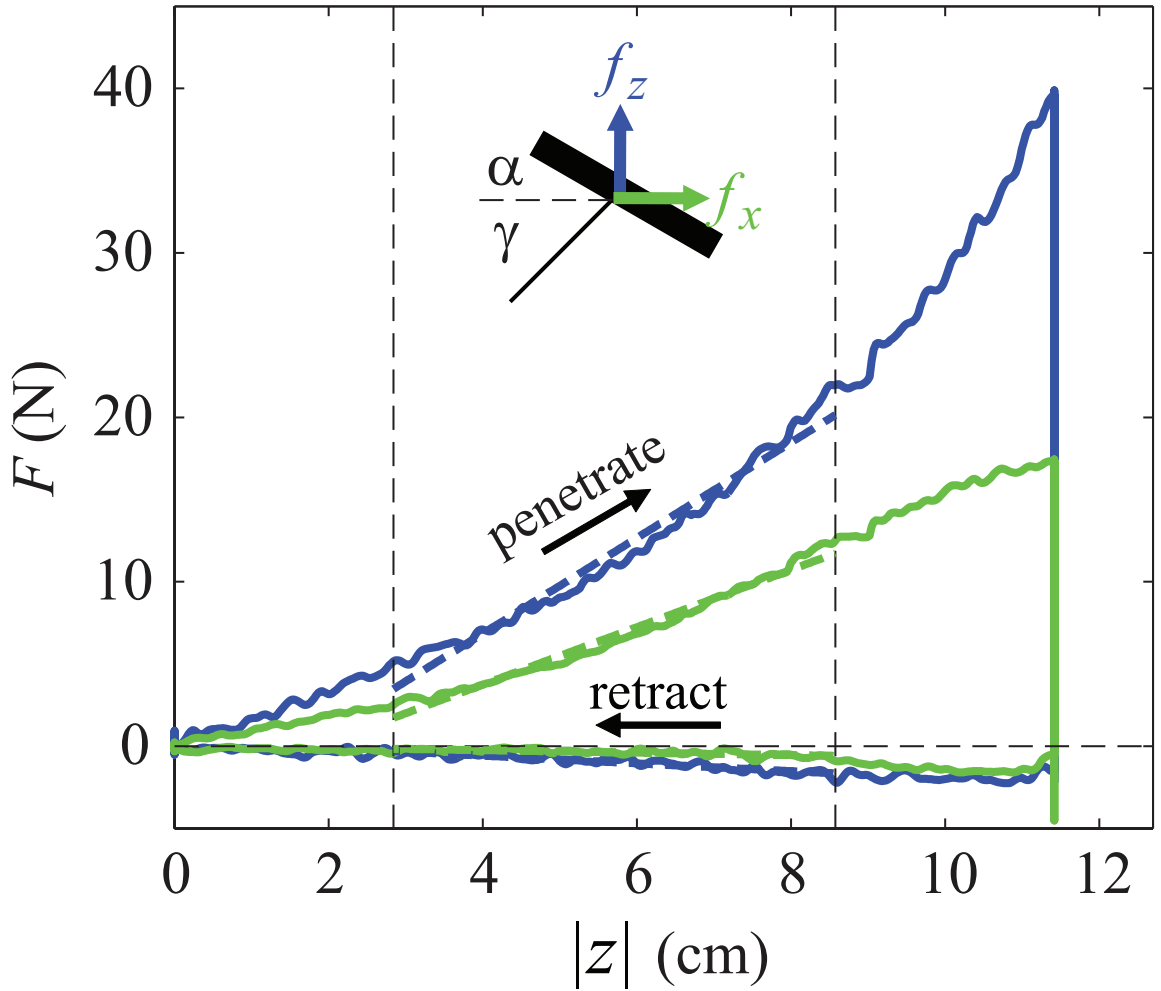


**Figure 109:** Representative force vs. depth measurements on the plate. Data shown is for LP poppy seeds with  $\alpha = \pi/6, \gamma = \pi/4$  (inset shows schematic). Blue curve indicates lift and green curve indicates drag. Higher curves are forces during penetration, and lower curves are forces during retraction. Dashed lines are linear fits to data over a depth range after yielding and before boundary effect becomes significant.

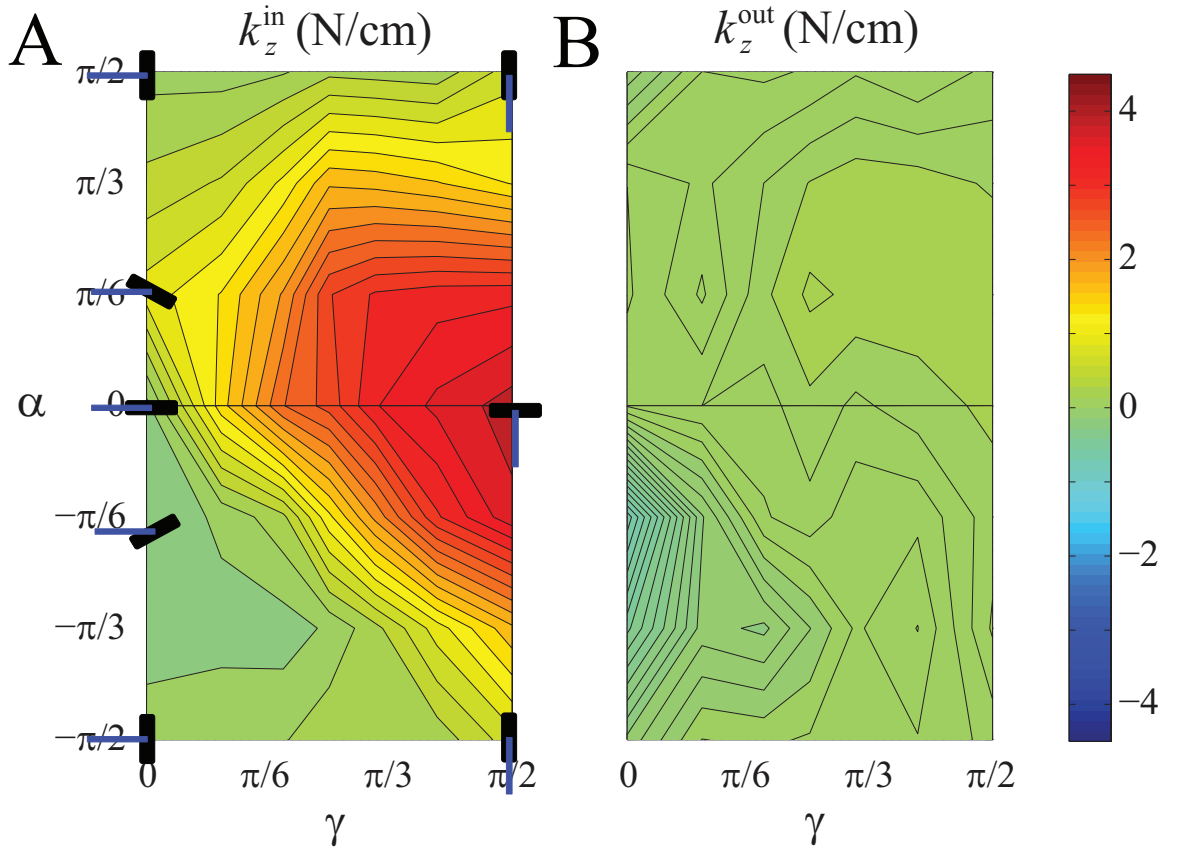
vertical penetration). For horizontal movement ( $\gamma = 0$ ), the plate was dragged at three different depths (2.54 cm, 5.08 cm, 7.62 cm). Forces during intrusion for  $\pi/2 \leq \gamma \leq \pi$  could be obtained from those in  $0 \leq \gamma \leq \pi/2$  by symmetry.

Figure 109 shows representative force as a function of depth for  $\alpha = \pi/6$  and  $\gamma = \pi/4$  (see inset for schematic) on LP poppy seeds. Both lift  $F_z$  and drag  $F_x$  were in most cases opposite to the direction of motion in the vertical and horizontal direction, and increased

approximately linearly with depth  $|z|$  during penetration and retraction during the steady state regions (Fig. 109). Therefore we fit a linear force relationship  $F_{x,z} = k_{x,z}|z|$  to the observed force vs. depth data over the steady state regions (dashed lines) and obtained force per depth as a function of angle of attack and direction of motion, i.e.,  $k_{x,z} = k_{x,z}(\alpha, \gamma)$ . For horizontal movement ( $\gamma = 0$ ),  $k_{x,z}$  was determined by fitting  $F_{x,z} = k_{x,z}|z|$  to average forces measured at the three depths.  $k_{x,z}$  were obtained for both intrusion (indicated by  $k_{x,z}^{in}$ ) into the granular medium (i.e.,  $v_z$  is downward) and retraction (indicated by  $k_{x,z}^{out}$ ) out of the granular medium (i.e.,  $v_z$  is upward). Positive values of  $k_{x,z}$  indicate that drag/lift force was opposite to the direction of motion along  $x, z$  axis. Negative values indicate that drag/lift force was in the same direction as the direction of motion along  $x, z$  axis.

### 7.5 Force per depth as a function angle of attack and direction of motion

Force per depth  $k_{x,z}$  depended sensitively on both angle of attack  $\alpha$  and direction of motion  $\gamma$  (Fig. 110, Fig. 111). For lift force during penetration into the granular medium (Fig. 110A),  $k_z^{in}(\alpha, \gamma)$  was maximal for  $\alpha = 0$  and  $\gamma = \pi/2$ , i.e., for a given depth the lift force was largest on a horizontally-oriented plate penetrating vertically downward. For a given  $\alpha$ ,  $k_z^{in}(\gamma)$  increased with  $\gamma$ , i.e., for a given depth the lift force on a plate at a given angle of attack was always larger when the plate moved more vertically than when the plate moved more horizontally. For a given  $\gamma$ ,  $k_z^{in}(\alpha)$  was always largest for  $\alpha \approx 0$  and diminished as  $\alpha$  approached  $\pm\pi/2$ , i.e., for a given depth the lift force was always larger on a plate



**Figure 110:** Lift force per depth (fitting parameter  $k$  in linear force fits, slope of dashed lines in Fig. 109) as a function of angle of attack ( $\alpha$ ) and direction of motion ( $\gamma$ ) for LP poppy seeds. (A)  $k_z$  during intrusion. (B)  $k_z$  during retraction. Stick figures in (A) indicate the angle of attack (black) and direction of motion (blue) in a few representative configurations.

oriented approximately horizontally and diminished as the plate became vertically oriented. However,  $k_z^{in}(\alpha)$  was symmetric to  $\alpha$  only at  $\gamma = \pi/2$  and became increasingly asymmetric to  $\alpha$  as  $\gamma$  approaches 0; i.e., for a given depth the lift force on a plate moving with a finite horizontal velocity component was different between positive and negative attack angles of the same value, because gravity breaks the symmetry.

Lift force per depth  $k_z^{out}(\alpha, \gamma)$  during retraction out of granular medium (Fig. 110B) displayed a qualitatively similar profile to  $k_z^{in}(\alpha, \gamma)$  during penetration into granular medium (Fig. 110A), but the magnitude was always smaller by an order of magnitude. This is likely a result of symmetry-breaking by gravity in the sagittal plane. Because of gravity, it is much more difficult for an intruder of a given attack angle to move downward into the granular medium than to move out of it.

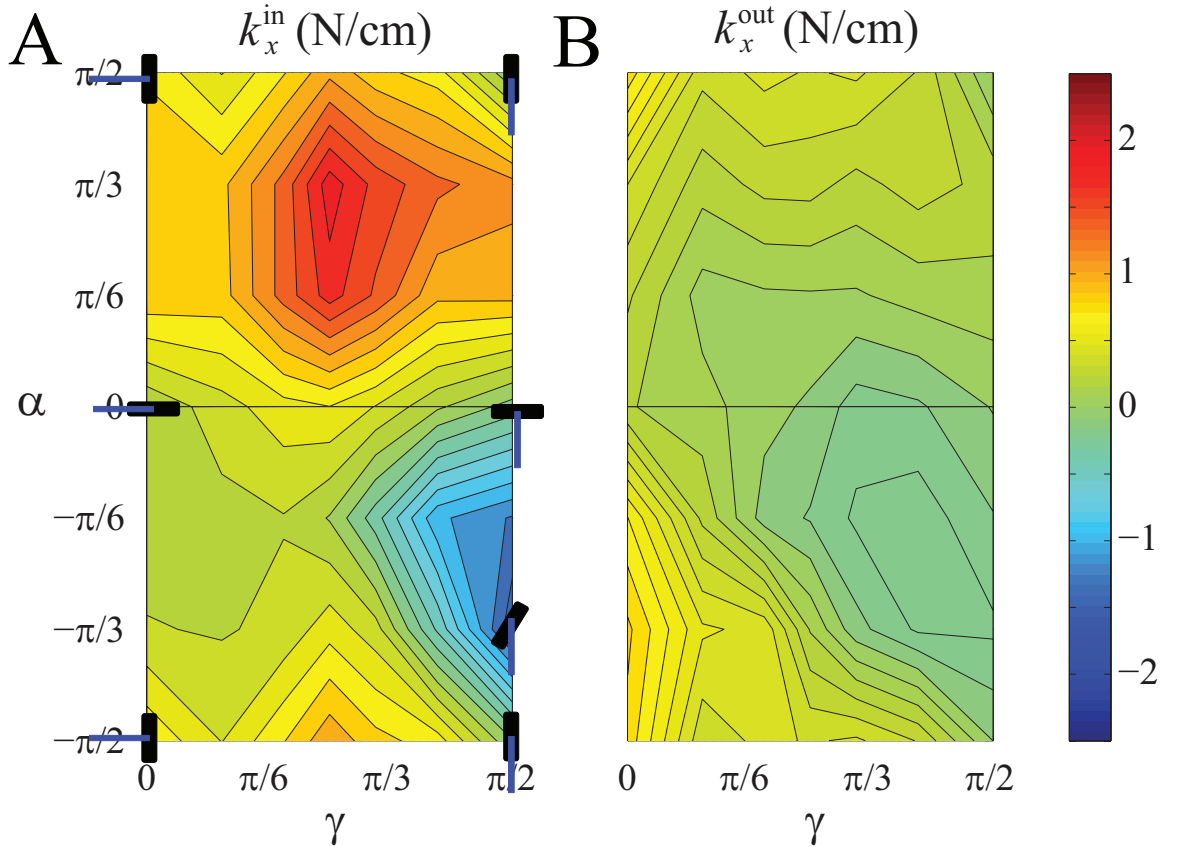


**Figure 111:** Drag force per depth (fitting parameter  $k$  in linear force fits, slope of dashed lines in Fig. 109) as a function of angle of attack ( $\alpha$ ) and direction of motion ( $\gamma$ ) for LP poppy seeds. (A)  $k_z$  during intrusion. (B)  $k_z$  during retraction. Stick figures in (A) indicate the angle of attack (black) and direction of motion (blue) in a few representative configurations.

Drag force per depth  $k_x$  also depended sensitively on both  $\alpha$  and  $\gamma$  (Fig. 111). It is worth noting that although  $k_x^{out}$  during retraction was also always smaller than that during intrusion  $k_x^{in}$ , the difference in force magnitude between intrusion and retraction was in most cases smaller for drag than that for lift ( $\sim 10$  times vs.  $\sim 3$  times). This is likely because horizontal drag is dominated by normal force on the sides of the intruder (friction-like), and thus the effect of symmetry breaking by gravity is less prominent than that on lift force.

## 7.6 Forces on rotating model legs of different geometry

Because previous studies suggested that in the speed range ( $v < \sim 0.5$  m/s) where most animals and robots locomote, granular media behave like a “frictional fluid” and the inertia of the grains are negligible [92, 95, 97], we assume that the forces on each element of an intruder are independent of each other both spatially and temporally. Therefore, with the measurements of forces as a function of depth, attack angle, and direction of motion, we can calculate (and thus predict) the force on an intruder of arbitrary shape moving along an arbitrary trajectory, by dividing an intruder into small plates and integrating forces on the plates:

$$F_{x,z} = \int_S f_{x,z} ds = \int_S k_{x,z}(\alpha_s, \gamma_s) \frac{A_s}{A_0} z_s ds$$

$$\begin{cases} k_{x,z} = k_{x,z}^{in}, & \text{if } v_z \text{ is downward for } ds; \\ k_{x,z} = k_{x,z}^{out}, & \text{if } v_z \text{ is upward for } ds; \end{cases} \quad (3)$$

where  $S$  denotes the intruder,  $ds$  denotes an element, and  $A_s$ ,  $z_s$ ,  $\alpha_s$ , and  $\gamma_s$  are the area, depth, angle of attack, and direction of motion of the element, respectively.

To test the predictive power of the resistive force theory, we investigated the lift and drag forces during rotation of intruders into granular media about a fixed axle, using model legs of three different geometries (Fig. 112): a C-shaped leg of a legged robot [92, 97, 98], an L-shaped leg, and a straight leg. The three legs had the same maximal length (3.8 cm, defined as the “diameter” of the leg), width (2.5 cm), and thickness (0.6 cm). The C-shaped and L-shaped legs were rotated with both the convex surface as the leading surface (called the positive curvature, indicated by “+”), and the concave surface as the leading surface (called the negative curvature, indicated by “−”). We selected these five geometries as they had the same cross-sectional area along the diameter, but displayed curvatures ranging from more negative curvature to more positive curvature.

The fluidized bed prepared the granular medium (15 cm deep) before each trial. The robotic arm then rotated the C-shaped leg into the granular medium as force was measured by the force/torque transducer. Angular velocity was  $\omega = 10$  degree/s (corresponding to speeds of  $v < \sim 10$  cm/s). Rotation was about a fixed axle at a hip height of  $h = 2$  cm

above surface within  $-3\pi/4 \leq \theta \leq 3\pi/4$ , where  $\theta$  is leg angle defined as the angle from the vertical to the diameter connecting center of rotation and the farthest point on the leg, similar to [92, 97]. The forces during rotation in the air were recorded and subtracted off to obtain ground reaction forces from the granular media during rotational intrusion.

For all the five geometries (Fig. 113, dashed curves), both lift (blue) and drag (green) as a function of leg angle displayed an asymmetric profile about the vertical downward direction ( $\theta = 0$ ), similar to previous observations [97]. However, lift was more asymmetric than drag as the peak locations of lift was farther away (more negative) from the vertical

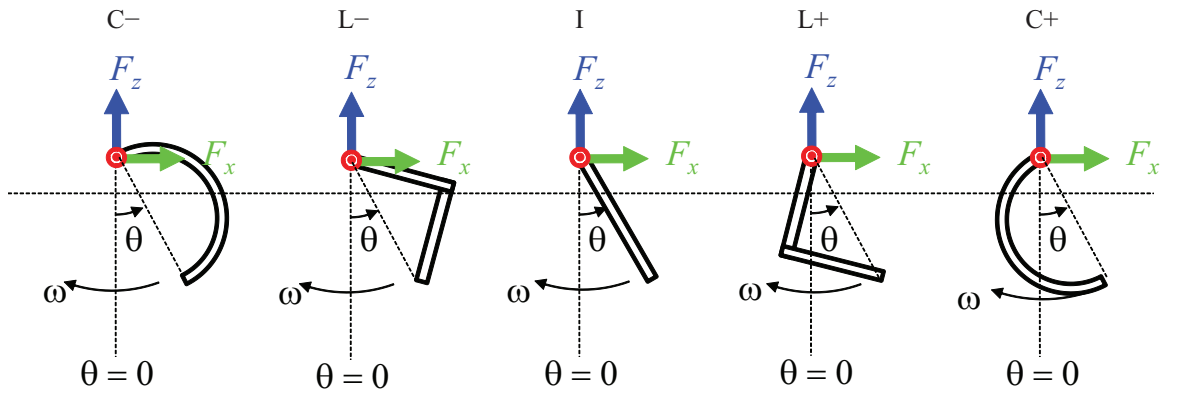


**Figure 112:** Experimental setup for rotation force measurements of model legs of five geometries into granular media. From left to right: C-shaped leg with the concave surface as the leading surface (C-), L-shaped leg with the concave surface as the leading surface (L-), straight leg (I), L-shaped leg with the convex surface as the leading surface (L+), C-shaped leg with the convex surface as the leading surface (C+). Center of rotation is at a fixed hip height  $h = 2$  cm.

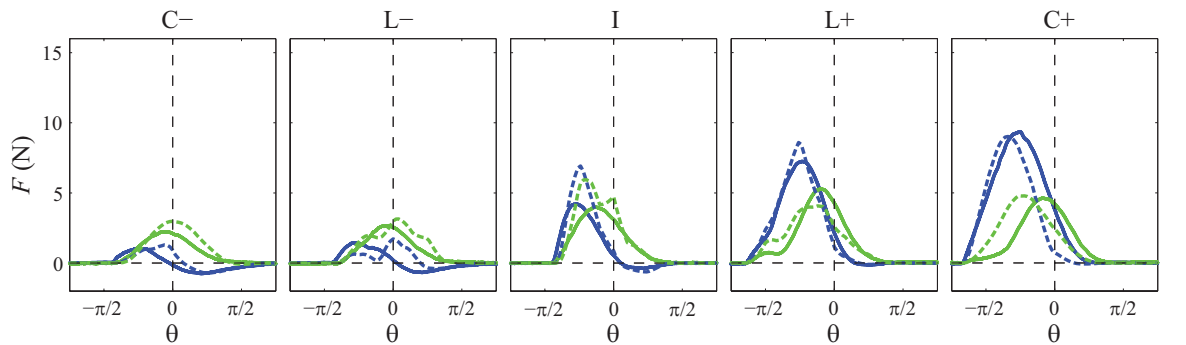


**Figure 113:** Net lift (blue) and drag (green) on the model legs of five geometries during rotation in LP poppy seeds. Solid curves are measurements and dashed curves are predictions from the resistive force theory.

( $\theta = 0$ ). In addition, the peak magnitude of lift increased by  $\sim 5$  times as the intruder curvature changed from the most negative (C-) to the most positive (C+), whereas the peak magnitude of drag increased only by  $\sim 2$  times. It is also worth noting that for negative curvature legs (C- and L-), lift is negative (suction) during the retraction phase of the rotation ( $\theta > 0$ ).

For all the five geometries, the lift and drag calculated from the RFT agreed reasonably well with the measurements (Fig. 113, solid curves). The fact both lift and drag were asymmetric is a result of the force per depth during intrusion ( $k_{x,z}^{in}$ ) being larger than that during retraction ( $k_{x,z}^{out}$ ). The higher asymmetry observed in lift compared to in drag is because the drop in force per depth between intrusion and retraction is larger for lift than for drag (i.e.  $k_z^{in}/k_z^{out} \sim 10$  vs.  $k_x^{in}/k_x^{out} \sim 3$ ).

The larger increase in peak lift and smaller increase in peak drag during intrusion as leg curvature changes from negative to positive are due to two reasons. First, at the same leg angle during intrusion ( $\theta < 0$ ), a positive curvature leg is deeper than a negative curvature leg. This explains the higher force magnitudes on positive curvature legs. Second, a positive curvature leg during intrusion orients its elements such that larger depth and larger force per depth occur together for lift, but not for drag. This can be understood by examination of the relation between  $k_{x,z}(\alpha(\theta), \gamma(\theta))$  and  $z(\theta)$  for each element. For lift on elements along a leg of positive curvature,  $k_z(\alpha(\theta), \gamma(\theta))$  is almost always large when  $z(\theta)$  is large, and  $k_z(\theta)$  is almost always small when  $z(\theta)$  is small. In contrast, for lift on elements along a leg of negative curvature,  $k_z(\alpha(\theta), \gamma(\theta))$  is almost always small when  $z(\theta)$  is large, and  $k_z(\theta)$  is almost always large when  $z(\theta)$  is small. Because the net lift  $F_z \propto \int_S k_z(\alpha(\theta), \gamma(\theta)) z_s(\theta) ds$ , the net lift is larger for the positive curvature than for the negative curvature. However, this is not the case for drag.

### 7.7 Application of the RFT to a legged robot

Previous studies [85, 92, 97] showed that vertical force balancing is crucial for legged locomotion on granular media, and a kinematic model qualitatively captured the performance of a legged robot using empirical vertical penetration force law [72, 92] and anisotropic penetration force law [97], with lift force per depth  $k_z$  as one of the two fitting parameters. Here we test the predictive power of the kinematic model using lift forces calculated from the resistive force theory. We studied the speed  $v_x$  as a function of stride frequency  $f$  in a RHex class legged robot, Xplorer (15 cm, 80 g) on LP poppy seeds. We tested the robot with C-shaped legs of both positive (C+, Fig. 115A) and negative (C-, Fig. 115B) curvatures. High speed videos were taken of the robot moving on the granular medium from both dorsal and lateral views, and speed and stride frequency were measured from the videos.

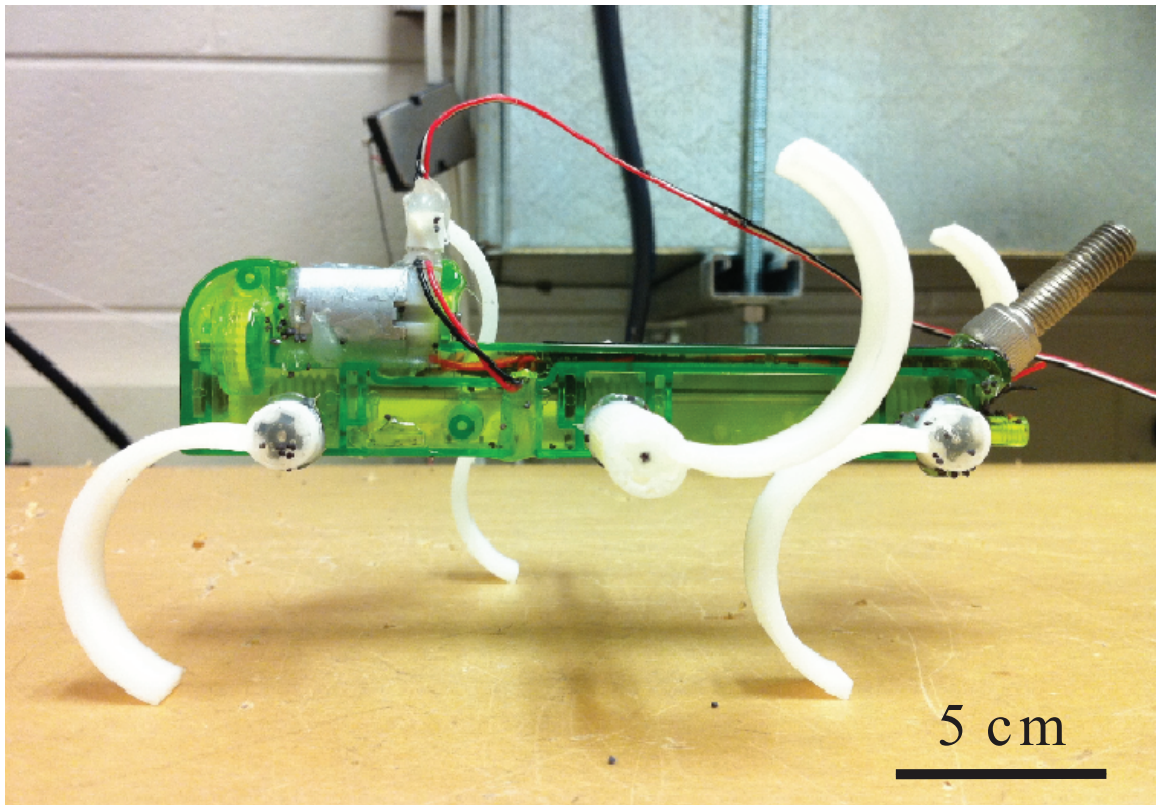


**Figure 114:** The Xplorer robot with C-shaped legs of positive curvature.

The robot moved rapidly on LP poppy seeds at  $\sim 1$  bodylength/s (Fig. 115C) using both “C+” (circles) and “C-” legs (squares). The average forward speed was about 50% faster

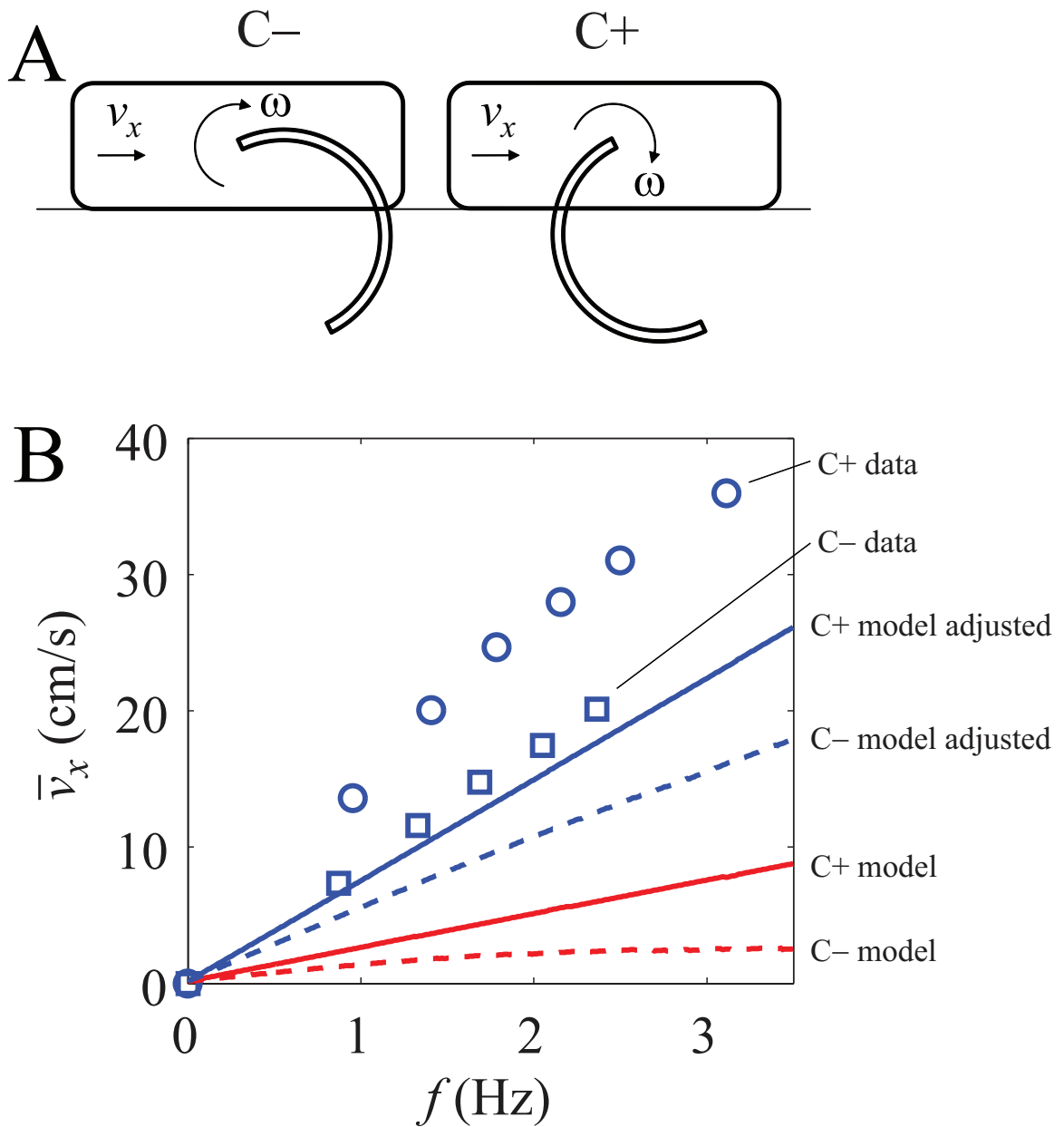


**Figure 115:** Robot performance on poppy seeds using C-shaped legs of positive and negative curvatures. (A) Single-leg representation of the robot using positive (C+) and negative (C-) curvature C-shaped legs. (B) Speed as a function of stride frequency on LP poppy seeds for positive and negative C-shaped legs. Circles (C+ data) and squares (C- data) are experimental data for the robot using positive and negative curvature C-shaped legs. Red solid (C+ model) and dashed (C- model) curves are predictions from the rotary walking model [92, 97] using lift forces as a function of leg angle calculated from the RFT. Blue solid (C+ model adjusted) and dashed (C- model adjusted) curves are predictions from the model using the actual end of the rotary walking phase, which the rotary walking model does not capture.

at any frequency with C-shaped limbs than with reversed C-shaped limbs. Lateral videos showed that the robot used “rotary walking” in both cases, as was previously found for SandBot. Speeds increased approximately linearly with frequency for both leg geometries.

Using the previously developed kinematic model [92, 97], we calculated the robot speed by:

$$\bar{v}_x = 2sf = 2R(\sin\beta_f - \sin\beta_i) \quad (4)$$

where  $\beta_{i,f}$  are determined by  $F_z = m(g+a)$ .  $F_z$  is calculated for the robot leg using Eqn. 3.  $m = 0.08/3 = 0.026$  kg is one third of the robot mass,  $g$  is gravitational acceleration,  $a = \frac{\omega R}{\Delta t} = \frac{2\pi f R}{\Delta t}$  is the acceleration due to leg rotation, and  $R = 0.02$  m is the leg radius. Leg width  $w = 0.01$  m and hip height  $h = 0.001$  m.  $\Delta t = 0.4$  s is a fitting parameter of the model determined in the previous studies for SandBot [92, 97]. Here we found that speed is insensitive to  $\Delta t$  for Xplorer, thus we take  $\Delta t = 0.4$  s for simplicity.

The average speed as a function of frequency calculated from the model using force predicted by the resistive force theory showed similar approximately linear trend as observations (Fig. 115C, red curves).  $\bar{v}_x$  was also higher at any  $f$  for the C+ legs (solid) than for the C− legs (dashed). However, the magnitudes of calculated robot speeds were 4 – 10 times lower than the data.

The discrepancy between data and model predictions is likely due to three reasons. First, the kinematic model in the previous studies [92, 97] did not use actual forces measured from experiment, but rather used the empirical force-depth/volume fraction relationships (i.e.,  $F_z = \alpha(\phi)Az$ ) determined from experiment, and used substrate strength ( $\alpha$ ) as fitting parameters. The model fitting parameter  $k_z$  to match the data was often larger than the  $k_z$  measured from experiments. Thus it is not surprising that with actual  $k_z$  measured from experiments, the model would under-predict speed. It is possible that the compaction of the granular media and the inertia of the grains being accelerated may play a role and contribute to forces, which are not captured by the RFT obtained from intrusions at low speeds.

Second, the kinematic model assumed that the rotary walking region (from  $\beta_i$  to  $\beta_f$ ) can be accurately determined by vertical force balance. Although this is largely true for

the start of the rotary walking regime  $\beta_i$  before which the robot legs rotate about a fixed axle, after rotary walking starts, the robot leg rotates about its geometric center within the cavity it has created, and no longer rotates about a fixed axle as assumed in the rotational intrusion. Thus the end of the rotary walking regime  $\beta_f$  is not accurately captured by vertical force balance. We observed the lateral videos of the robot moving and found that the actual end of the rotary walking regime  $\beta_f$  is approximately when the leg fully exited the granular surface, i.e., when leg diameter becomes horizontal ( $\theta = \pi/2$ ). By setting  $\beta_f = \pi/2$ , the predicted robot speed was higher and closer to observations (Fig. 115C, blue curves), but still smaller by  $\approx 40\%$ . This is an issue intrinsic to granular media: Granular media remain solid below the yield stress, but can flow like a fluid when the yield stress is exceeded [10]. The forces measured in the plate experiments are forces in flowing granular media, i.e., when the granular media have yielded. However, they do not necessarily equal forces when the granular media remain solid below yield stress, which could be arbitrary and depend on the intruder.

Thirdly, the kinematic model assumes that the forces on a robot leg is balanced at all instants of time (quasi-static), and calculates robot displacement purely by geometry. However, a locomoting animal or robot is a dynamical system, and the position of the center of mass at an instant of time is determined by its position at the previous instant and its velocity at that time (which is further determined by external forces). This will require integration of the resistive force theory with dynamical models of legged locomotion like the SLIP [86] and CT-SLIP models [167] and multi-body computer simulation [168, 125].

## 7.8 *Conclusions*

Our study demonstrated the applicability and predicative power of the resistive force theory for complex intrusions in granular media in the sagittal plane. Lift and drag forces on a small plate moving in granular media depend sensitively on the angle of attack and direction of motion, and increase approximately linearly with depth. Because of symmetry breaking by gravity, forces are larger during intrusion into the media than during extraction out of the media. Forces predicted from the resistive force theory on intruders of complex geometry moving along complicated prescribed trajectories match measurements reasonably well. The resistive force theory provides a general model for calculating granular forces for legged locomotion with morphology and kinematics of the animal or robot given as model inputs. This is a step forward with the advantage over previous techniques of empirical force measurements which must be performed for each and every intruder geometry and trajectory [69, 70, 71, 68, 72]. The discrepancy between the measured speed of a legged robot and model predictions using forces predicted by the resistive force theory highlights the need for improved models of legged locomotion which incorporate the dynamics of the locomotor and provide ways to predict forces on the intruder when granular media remain solid below yield stress.

## 7.9 *Appendix*

Below are lift and drag forces per depth as a function of angle of attack and direction of motion, for the other four granular media/packing states tested, as well as the measured vs. RFT-predicted forces as a function of leg angle on the five model legs in these granular media/packing states. For all cases,  $k_{x,z}$  displayed qualitatively similar profiles as those for LP poppy seeds. For a given granular medium, closely packed states had larger  $k_{x,z}$  than loosely packed states. Forces on model legs also showed qualitatively similar profiles as those for LP poppy seeds, and RFT-prediction matched measurements in most cases. However, in closely packed poppy seeds and 0.27 mm diameter glass particles, RFT-predicted forces were significantly higher than measurements for model legs of positive curvature.

7.9.1 CP poppy seeds

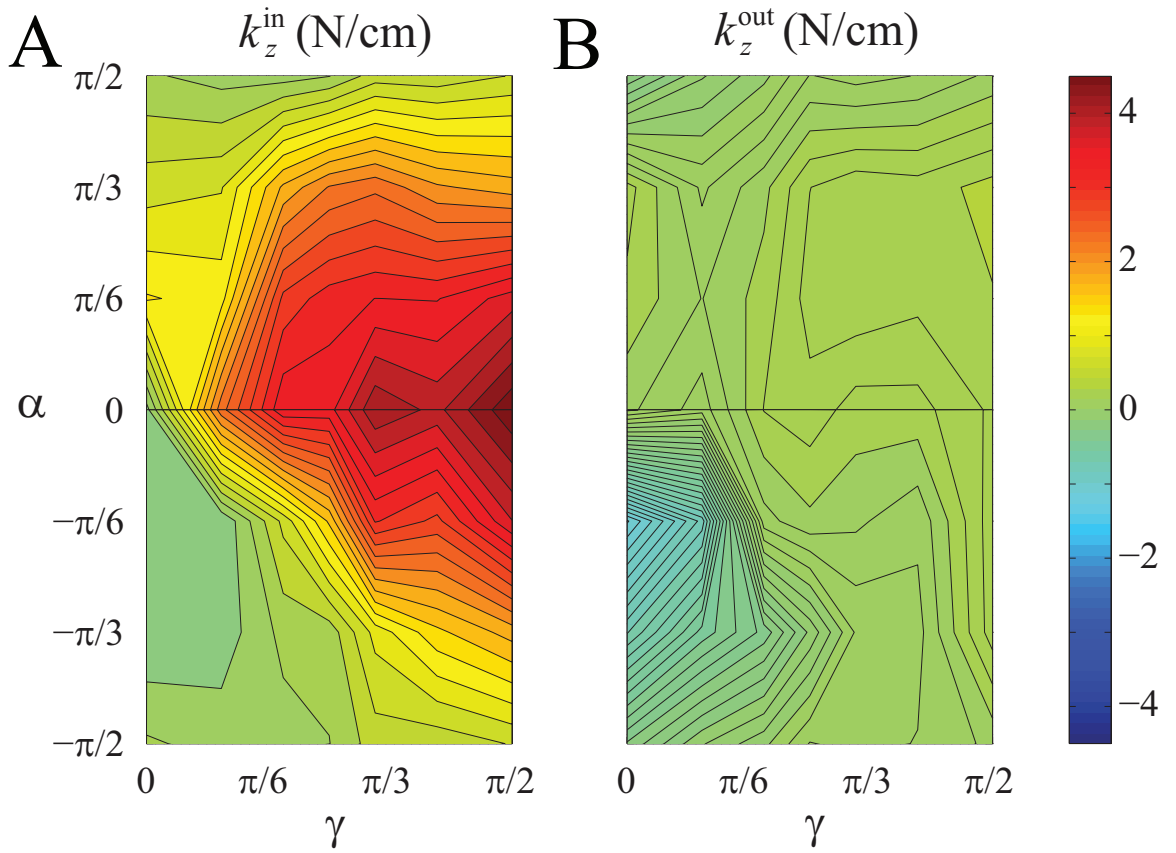


**Figure 116:** Lift force per depth (fitting parameter  $k$  in linear force fits, slope of dashed lines in Fig. 109) as a function of angle of attack ( $\alpha$ ) and direction of motion ( $\gamma$ ) for CP poppy seeds. (A)  $k_z$  during intrusion. (B)  $k_z$  during retraction.

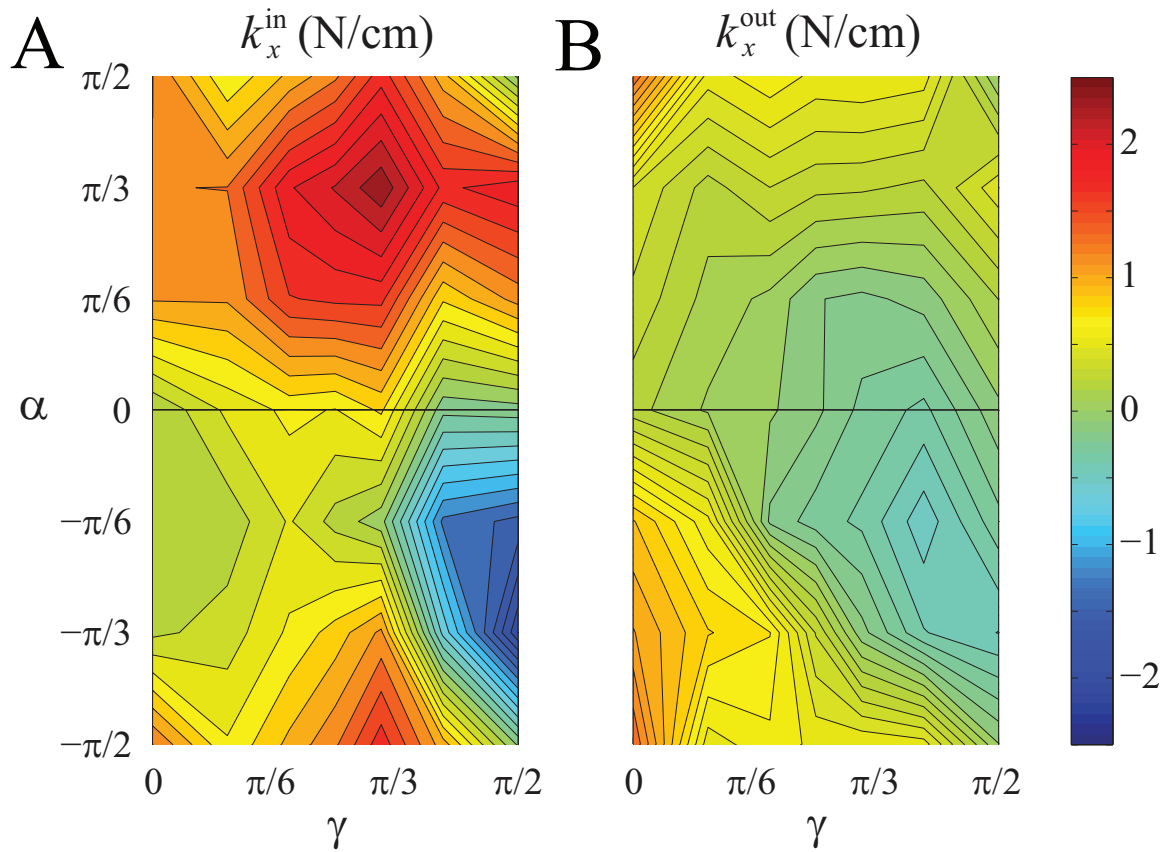


**Figure 117:** Drag force per depth (fitting parameter  $k$  in linear force fits, slope of dashed lines in Fig. 109) as a function of angle of attack ( $\alpha$ ) and direction of motion ( $\gamma$ ) for CP poppy seeds. (A)  $k_z$  during intrusion. (B)  $k_z$  during retraction.

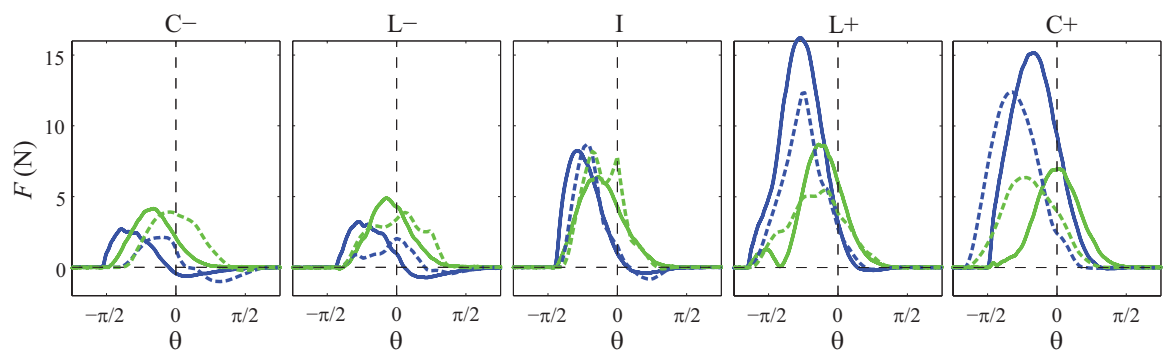


**Figure 118:** Net lift (blue) and drag (green) on the model legs of five geometries during rotation in CP poppy seeds. Solid curves are measurements and dashed curves are predictions from the resistive force theory.

### 7.9.2 LP 0.27 mm glass particles

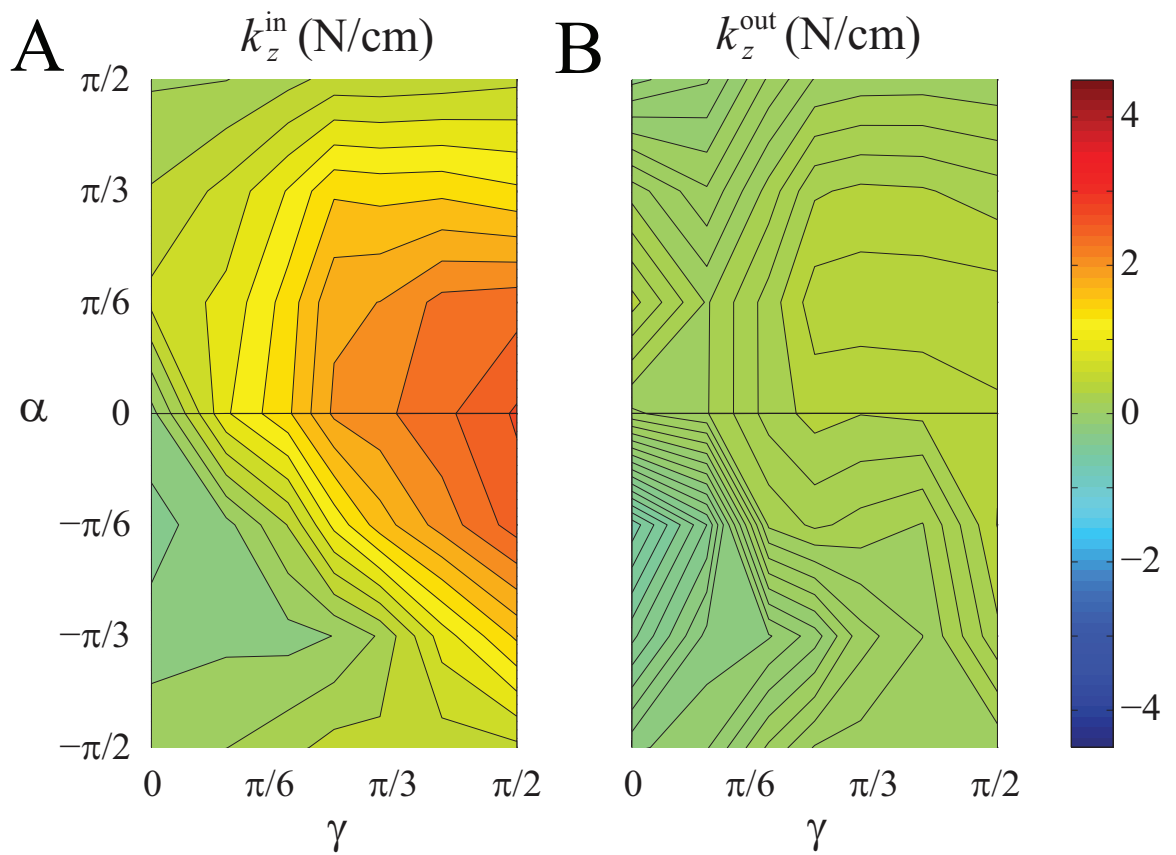


**Figure 119:** Lift force per depth (fitting parameter  $k$  in linear force fits, slope of dashed lines in Fig. 109) as a function of angle of attack ( $\alpha$ ) and direction of motion ( $\gamma$ ) for LP 0.27 mm glass particles. (A)  $k_z$  during intrusion. (B)  $k_z$  during retraction.

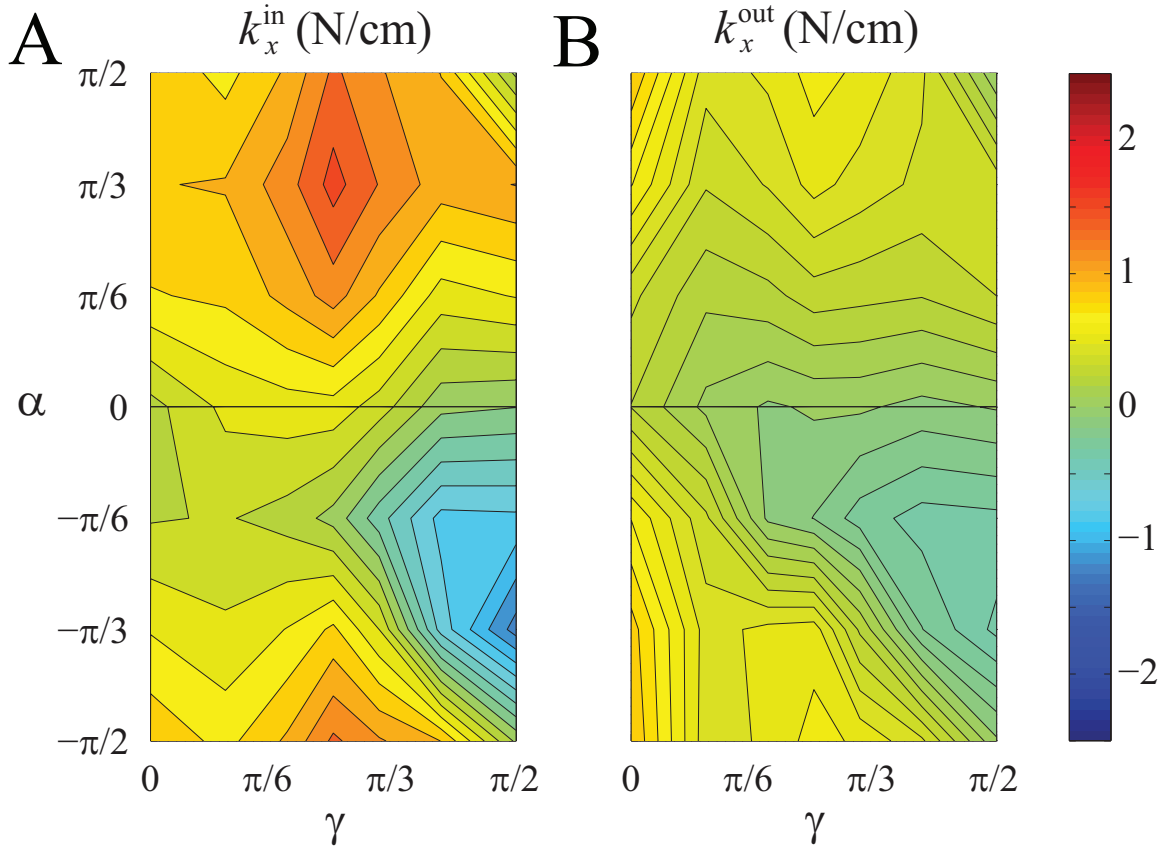


**Figure 120:** Drag force per depth (fitting parameter  $k$  in linear force fits, slope of dashed lines in Fig. 109) as a function of angle of attack ( $\alpha$ ) and direction of motion ( $\gamma$ ) for LP 0.27 mm glass particles. (A)  $k_z$  during intrusion. (B)  $k_z$  during retraction.

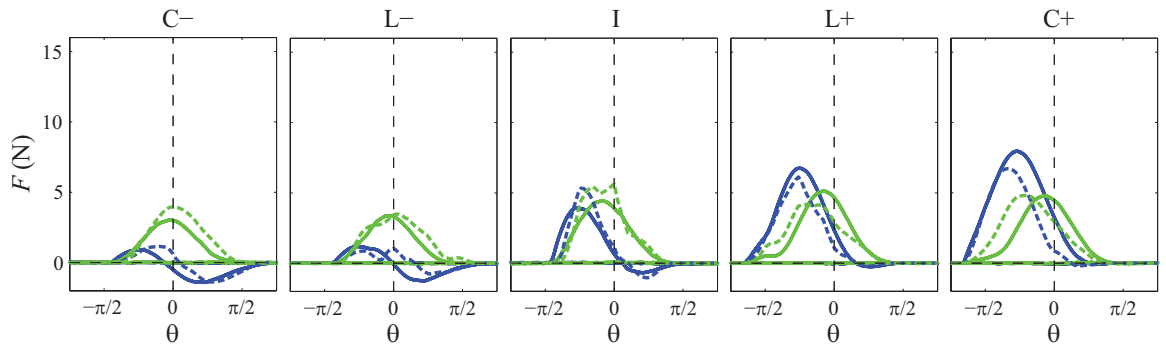


**Figure 121:** Net lift (blue) and drag (green) on the model legs of five geometries during rotation in LP 0.27 mm glass particles. Solid curves are measurements and dashed curves are predictions from the resistive force theory.

7.9.3 CP 0.27 mm glass particles

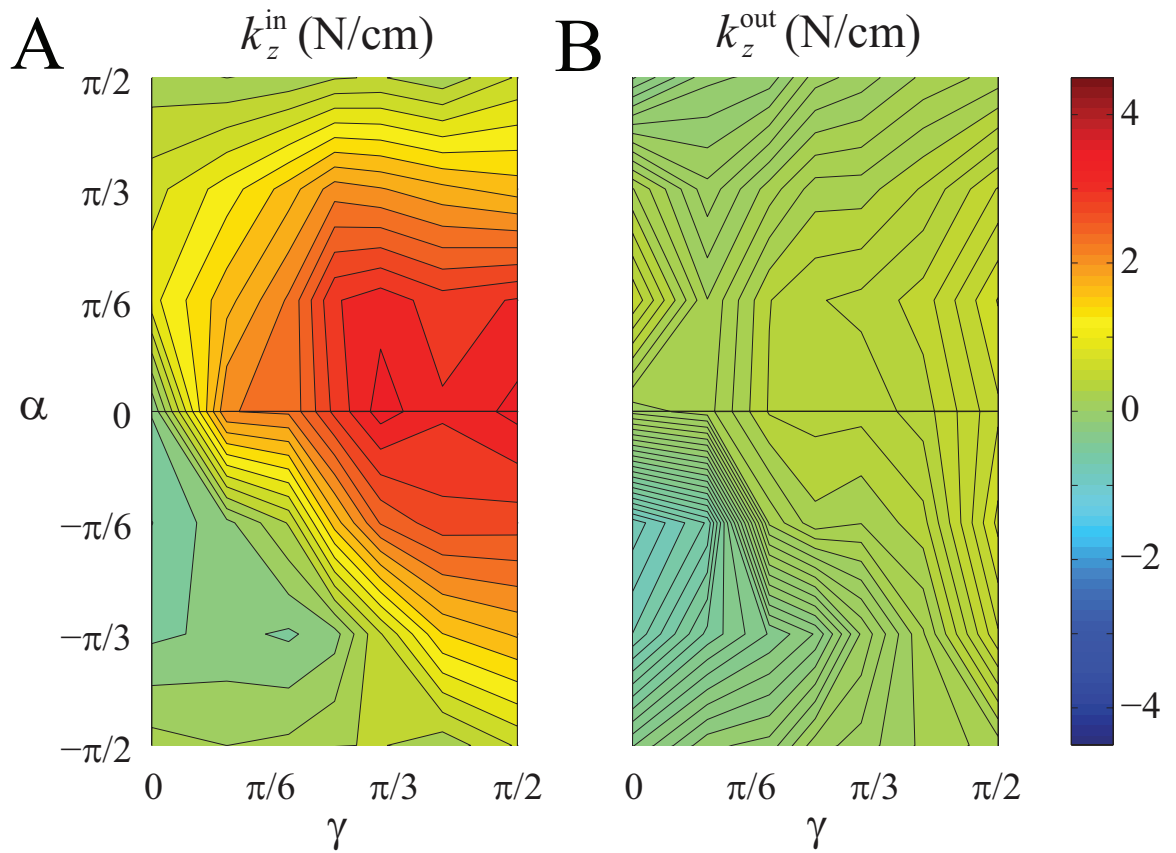


**Figure 122:** Lift force per depth (fitting parameter  $k$  in linear force fits, slope of dashed lines in Fig. 109) as a function of angle of attack ( $\alpha$ ) and direction of motion ( $\gamma$ ) for CP 0.27 mm glass particles. (A)  $k_z$  during intrusion. (B)  $k_z$  during retraction.

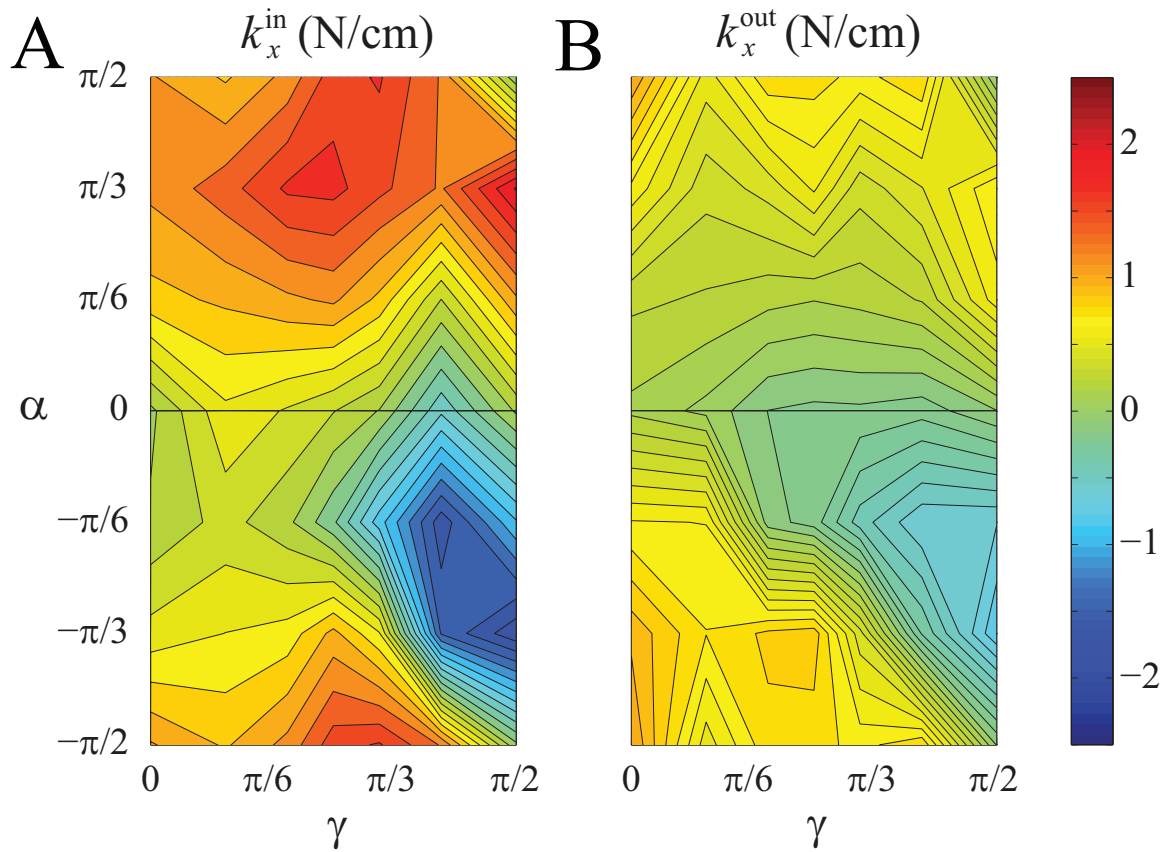


**Figure 123:** Drag force per depth (fitting parameter  $k$  in linear force fits, slope of dashed lines in Fig. 109) as a function of angle of attack ( $\alpha$ ) and direction of motion ( $\gamma$ ) for CP 0.27 mm glass particles. (A)  $k_z$  during intrusion. (B)  $k_z$  during retraction.

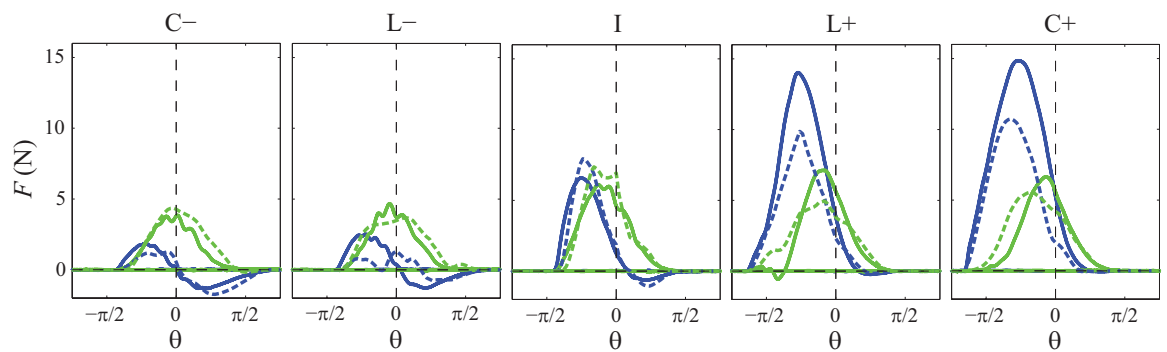


**Figure 124:** Net lift (blue) and drag (green) on the model legs of five geometries during rotation in CP 0.27 mm glass particles. Solid curves are measurements and dashed curves are predictions from the resistive force theory.

### 7.9.4 CP 3 mm glass particles

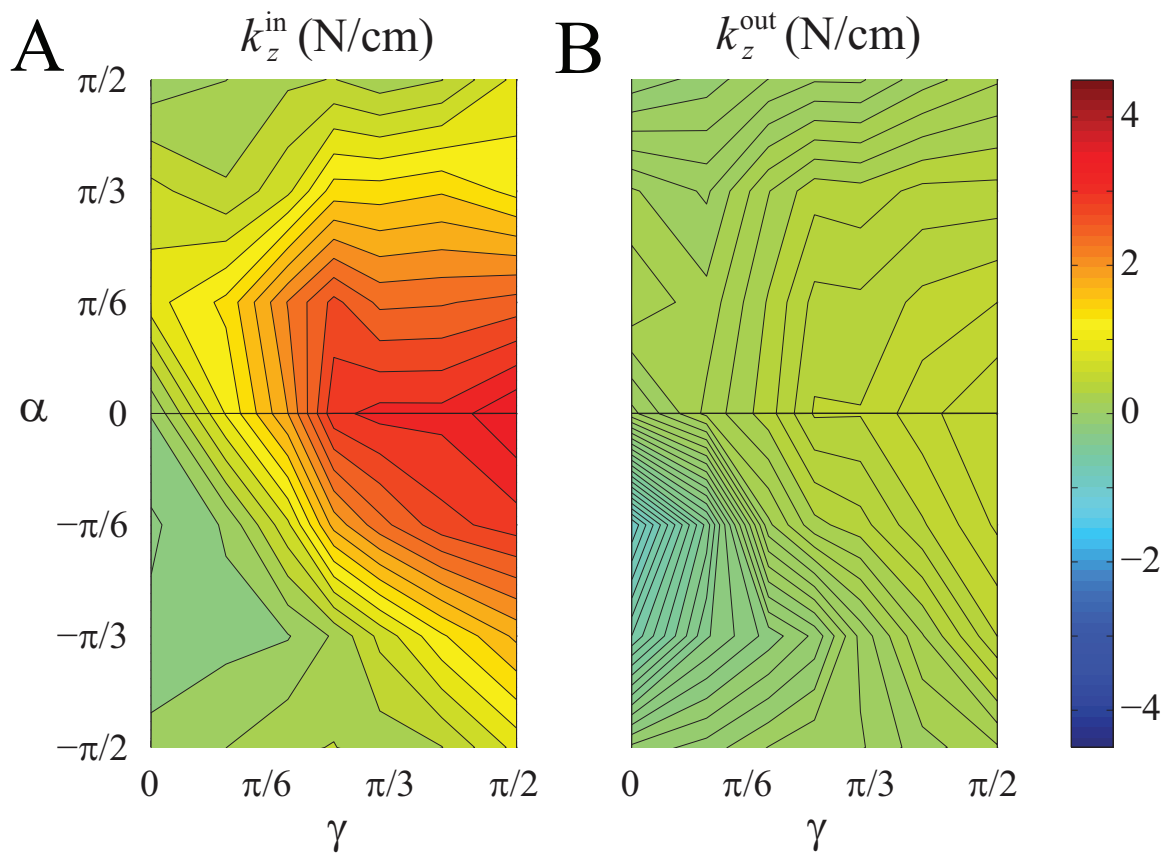


**Figure 125:** Lift force per depth (fitting parameter  $k$  in linear force fits, slope of dashed lines in Fig. 109) as a function of angle of attack ( $\alpha$ ) and direction of motion ( $\gamma$ ) for CP 3 mm glass particles. (A)  $k_z$  during intrusion. (B)  $k_z$  during retraction.

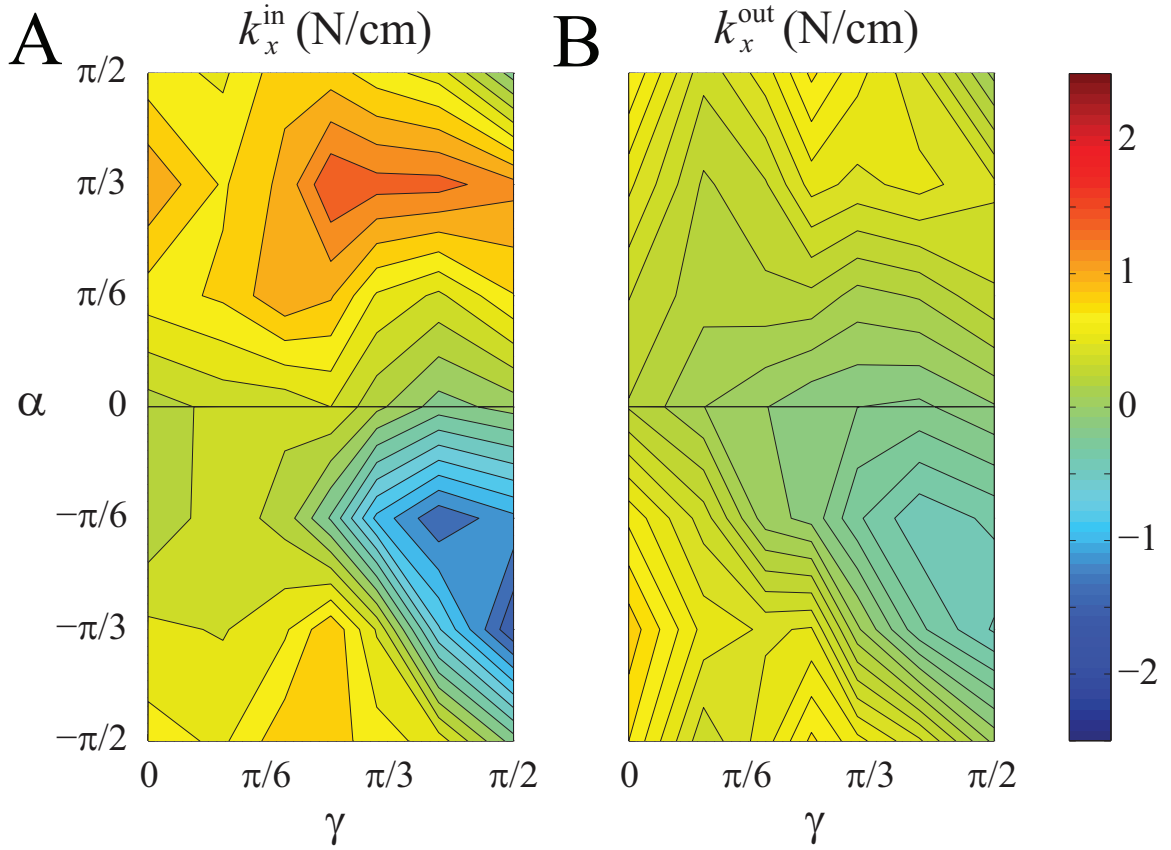


**Figure 126:** Drag force per depth (fitting parameter  $k$  in linear force fits, slope of dashed lines in Fig. 109) as a function of angle of attack ( $\alpha$ ) and direction of motion ( $\gamma$ ) for CP 3 mm glass particles. (A)  $k_z$  during intrusion. (B)  $k_z$  during retraction.

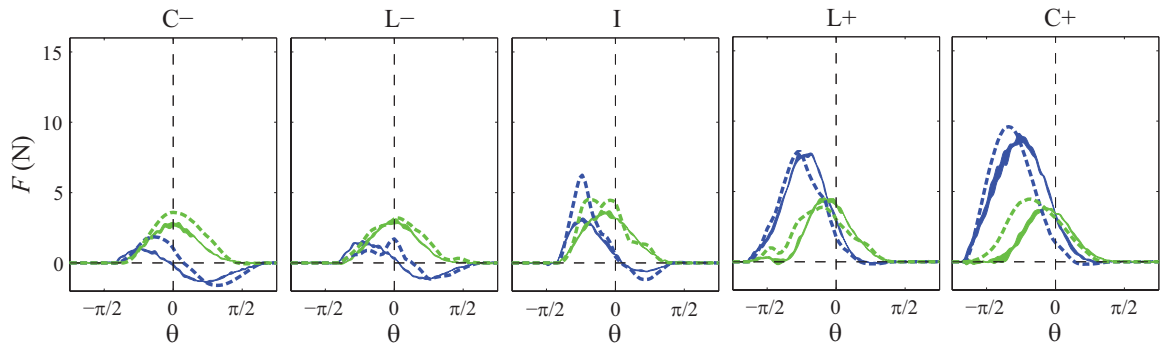


**Figure 127:** Net lift (blue) and drag (green) on the model legs of five geometries during rotation in CP 3 mm glass particles. Solid curves are measurements and dashed curves are predictions from the resistive force theory. Three runs per condition are taken for CP 3 mm glass particles, and the thickness of the solid curve indicates  $\pm 1$  s.d.

## CHAPTER VIII

### CONCLUSIONS

#### *8.1 General remarks*

In this dissertation, we integrated biological, robotic, and physics studies to discover principles of legged locomotion on granular media. We showed that for both biological organisms and bio-inspired robots, effective legged locomotion (walking and running) on granular surfaces could be achieved by generating sufficient vertical ground reaction force (lift) via leg/foot intrusion to balance the weight and inertial force of the body. In most cases leg/foot intrusion was slow enough ( $v < \sim 0.5$  m/s) that granular forces were dominated by granular hydrostatic pressure and grain-grain and grain-body friction, and were approximately independent of intrusion speed. Locomotor performance (speed) depended sensitively on kinematics, leg/foot morphology, and the strength of the granular substrate, because these parameters/properties determined the magnitude and direction of intrusion forces. Based on these findings, we developed a granular resistive force theory in the sagittal plane which provided a general model for calculating forces during locomotion relevant-low speed intrusions of complex intruders moving along complicated paths.

These studies demonstrated that a principled understanding of legged locomotion on yielding/flowing substrates can be achieved by creating lab controlled granular media as model substrates, studying the locomotor performance, kinematics, and mechanics of animals and legged robots on these substrates, and studying the physics of intrusion forces relevant to the leg/foot interaction. Results of this dissertation not only yielded testable hypotheses for locomotion studies, but also provided design principles and inspirations for the development of next generation legged robots capable of traversing terrains that can yield and flow like granular media.

## 8.2 *Specific accomplishments*

### **Biological studies:**

- Captured the kinematics and modeled the mechanics of a desert generalist, the zebra-tailed lizard running on solid and granular surfaces, and found that the lizard suffered little performance loss when substrate changed from solid to granular (**Chapter II**).
- Discovered that the lizard’s large, elongate hind foot served multi-functions during locomotion. On solid surface, the elongate foot tendons functioned as an energy-saving spring. On granular surface, the large foot functioned as a “snow shoe” to reduce leg penetration and energy loss to the granular substrate (**Chapters II and III**).
- Identified three phases of foot-ground interaction of the lizard running on granular media, slap, stroke (paddle), and retraction (**Chapter III**).

### **Robotic studies:**

- Discovered that the locomotor performance (speed) of a legged robot, SandBot, on granular media depended sensitively on both kinematics (including stride frequency and intra-cycle stance and swing configuration) and the surface strength of the granular substrate (indicated by packing fraction) (**Chapters IV and V**).
- Identified two modes of locomotion for SandBot on granular media. In walking, the legs pivoted about a fixed foothold atop solidified grains and speed was larger. In swimming, the legs paddled through fluidized grains and speed was smaller (**Chapter IV**).
- Discovered that small, lightweight robots (RoACH and DASH) with appropriate leg geometry suffered less performance loss compared to SandBot when substrates weakened. When leg geometry was not appropriate, speed dropped and cost of transport increased by an order of magnitude (**Chapter VI**).

## Physics studies:

- Demonstrated the importance of generating sufficient vertical ground reaction force to balance the weight and inertial force of the body during legged locomotion on granular media (**Chapters II–V**).
- Discovered that for the zebra-tailed lizard, impact force during foot slap only contributed a small portion of the required vertical thrust. Most vertical thrust were produced by foot stroke (paddling) through the media, during which vertical penetration and rotational intrusion forces are important (**Chapters II and III**).
- Utilized a quasi-static kinematic model to explain the observed locomotor performance of SandBot during walking (and swimming), by balance (or lack thereof) of the weight and inertial force of the robot body with empirically determined ground reaction forces during vertical penetration and rotational intrusion (**Chapters IV and V**).
- Developed a granular resistive force theory in the sagittal plane to determine forces for intruders of complex geometry moving along complicated trajectories in granular media (**Chapter VII**).

### 8.3 *Future directions*

As is often the case in initial investigations, many questions have been raised, and many interesting observations have not been thoroughly studied. Below are a few possible future directions which are natural extensions of the work presented in this dissertation and may be worth pursuing.

**Test of locomotor hypotheses.** The models of foot-ground interaction developed for the zebra-tailed lizard predicted that a large, elongate foot could increase energy saving on the solid surface, and reduce leg penetration and energy loss to the substrate on the granular surface. Similarly, the models of foot-ground interaction for SandBot suggested that interplay of locomotor parameters (e.g., body mass, limb/foot size and shape, kinematics) with substrate strength control the solid-fluid transition and resulting forces and thus affect the limb-ground interaction and performance. Future studies should systematically test these hypotheses, by comparative experiments of different animal species, legged robots, and computer simulation models [168, 125] of various body masses, leg lengths, foot sizes, and foot geometries, locomoting on granular media of variable properties which affect substrate strength, such as volume fraction, grain friction, density, incline angle, and even gravity.

**Role of grain inertial force during locomotion.** Our foot-ground interaction models for biological, robotic, and physics studies have largely focused on modeling granular intrusion forces at low speeds ( $< 0.5$  m/s). In this case, force was dominated by grain friction and approximately independent of speed, and increases approximately linearly with depth due to granular hydrostatic pressure. However, during locomotion legs and foot can sometimes move at high speeds ( $\sim 1$  m/s) where grain inertial forces may become significant. This may be particularly important for high speed runners, or for larger animals/robots, whose limbs could move much faster during locomotion. Future locomotion and physics experiments are needed to systematically investigate granular forces during high speed intrusion. This will complement the granular resistive force theory developed in this dissertation and lead us towards a comprehensive theory of granular forces for legged locomotion.

**Dynamical models of legged locomotion on granular media.** While the resistive force theory provided a good model for calculating granular forces on intruders of complex geometry moving along complicated trajectories, the kinematic model developed for Sand-Bot underpredicted locomotor performance with these forces. This highlights the need for dynamical models of legged locomotion on granular media, which incorporates the dynamics (i.e.,  $v(t + dt) = v(t) + a dt$ ) of the locomotion system. This is particularly important for running animals/robots. Future studies should combine the resistive force theory with dynamical models of legged locomotion like the SLIP [86] and CT-SLIP models [167] and multi-body computer simulation [168, 125].

**Creation of templates for legged locomotion on granular media.** The SandBot and zebra-tailed studies showed that walking (vaulting over a fixed foothold) and running (i.e., SLIP-like vertical CoM motion) on granular media were similar to those on solid surfaces. However, distinct differences existed—on granular media, CoM speed and height are not out of phase during walking and in phase during running, like found on solid surfaces [1]. These suggested that on granular media locomotor templates may be different. Future studies should examine the mechanics and energetics in more animal species/types of legged robots and determine appropriate templates for legged locomotion on granular media.

**Confirmation of muscle function and energy estimates.** In the studies of the zebra-tailed lizard, the estimates of elastic energy storage and return on the solid surface was based on the assumption of isometric contraction of lower leg muscles during stance. However, muscles have a finite stiffness and often do lengthen by a small amount under limb tension [105, 5]. In addition, the hind foot resilience was obtained from anesthetized lizards and was assumed to provide a good estimate for the hind foot resilience in running lizards. Future *in vivo* experiments, such as tendon buckles [107], sonomicrometry [107], ultrasonography [123], oxygen consumption measurement [124] are needed to determine the actual deformation of muscles and tendons during locomotion and resilience during locomotion, and confirm the proposed muscle/tendon function and energy estimates. Refinement

of experimental techniques such as running tracks with embedded force plate and miniature sensors suitable for this small animal (leg and toe diameter  $\sim 1$  mm) may help such advancements.

**More accurate measurements/calculation of granular forces.** The force and energy loss calculations on the granular surface were based on simplified foot kinematics (i.e., considering foot rotation as foot penetrating with reducing projected area) and used the vertical penetration force model. With the development of the resistive force theory in the sagittal plane, it will be useful to use the observed subsurface foot kinematics to calculate forces during foot rotation and examine the accuracy of the thrust estimates. Furthermore, integration of fluidized bed with techniques to directly measure ground reaction forces on granular media [18], as well as computational method like Discrete Element simulation [168, 125, 94] to calculate granular forces, will help improve models of granular forces proposed in this dissertation.

**Role of neural-sensory control.** Our models of the hind foot function of the zebra-tailed lizard assumed purely passive foot mechanics, and did not consider the role of active neural-sensory control. We observed that when confronted by a substrate which transitioned from solid into granular (or *vice versa*), the lizard displayed partial adjustment of foot posture during the first step on the new surface, and full adjustment of foot posture during the second step. Future studies using neuromechanics techniques [13] such as EMG [107, 126] and denervation/reinnervation [127] are needed to determine how neural-sensory feedback mechanisms are involved to control limb function to accommodate different substrates [128, 3].

**Creation of more neuromechanical templates.** While our studies of the zebra-tailed lizard focused on its foot function to generate force and enhance energy efficiency, they reveal many interesting foot properties and behaviors which may be beneficial for locomotion and worth further investigation. For example, the anisotropic stiffness of foot tendons (i.e., more stiff during hyperextension and less stiff during flexion) may facilitate firm ground engagement and thrust generation during stance and toe collapse during retraction to minimize drag. The relative lightweight of the foot enables rapid ground engagement

during high speed impact. The thin, long toes may also help an animal plant the foot into a deformable substrate more easily than would a large plate-like foot, which could slip more easily on the surface. While the damping properties of the foot reduce energy savings, they may also help the animal reset the foot to a desired posture and a straight shape quickly during swing to prepare for the next touchdown [100], and prevent muscle fatigue [169] from erratic vibrations possible in running on rough terrain. Future studies may these hypotheses to lead us towards template level models of legged locomotion on complex surfaces like those presented in this dissertation.

**Creation of a general locomotion model that unifies a variety of systems.** As revealed by the studies in this dissertation, there is a dilemma for animals/robots moving on granular media, i.e., foot penetration is required for locomotion while penetrating too deep can decrease locomotor performance by reducing stride length and inducing body/limb drag. While the animal and legged robots studied in this dissertation differ from each other in many aspects including mass, morphology, kinematics, and control strategies, it is plausible to speculate that there exists a generalized model of legged locomotion on granular media which could unify the many principles discovered (or yet to be discovered), because the underlying physics of granular forces appear similar. Such a generalized model should embed parameters of both the locomotor and the granular substrate, and predict qualitative transitions and quantitative changes in locomotor behavior and performance. For example, does increased mass and/or decreased foot area/leg length trigger transition of gait (and performance loss) from running, to walking, to swimming, and *vice versa*? Is there a critical pressure or yield stress (force/area) at which these transitions occur, given the leg/foot kinematics and morphology? If so, how do these transitions further depend on the properties of the granular media, such as friction, density, grain size, and volume fraction?

**Improvement of robot performance.** The principles of legged locomotion on granular media discovered in this dissertation suggested ways for enhancing ground reaction forces and improving the performance of legged robots on such surfaces. For example, because surface penetration is required for locomotion on granular media yet it reduces stride

length and causes increased drag, it is advantageous for a legged locomotor to have large feet and long legs and use appropriate kinematics to reduce relative leg penetration while generating the required thrust. The zebra-tailed lizard provides an excellent realization of these design criteria. Apart from its plantigrade foot posture, this lizard has a small mass to foot area ratio ( $\sim 10$  g vs.  $1 \text{ cm}^2$  by two, or  $0.5$  kPa pressure on the surface at rest). During running on granular media, the foot often sinks less than 40% of the vertical leg length, leaving the majority of the leg available for taking long strides and the body well above surface to avoid drag. By contrast, SandBot has a large mass to foot area ratio ( $\sim 2.3$  kg vs.  $5 \text{ cm}^2$  by three, or  $15$  kPa), and always penetrates  $> 70\%$  of the leg during locomotion. Recent small, lightweight robots like DASH and RoACH are approaching the organisms in locomotor performance, partly because of their relatively large feet for their body weight ( $\sim 20$  g vs.  $1 \text{ cm}^2$  by three, or  $0.7$  kPa). Future development of legged robots should incorporate such design principles (e.g., large foot area, long legs, small weight) and control strategies (e.g., slow down limb motion when a loose substrate is encountered) suggested by studies of this kind (Fig. 128).



**Figure 128:** Artist's concept of future legged robots that traverse granular surfaces, inspired from studies in this dissertation. Courtesy of IEEE Spectrum [56].

#### ***8.4 Final thoughts***

The projects in this dissertation have been fascinating and enjoyable to work on. The broad range in subjects, phenomena, and techniques has helped lead me to a large number of ideas and questions, and kept satisfying my scientific curiosity. I look forward to hearing about (and possibly working on) some of the projects outlined above.

## APPENDIX

Below are some examples of many additional efforts which did not end up in the previous chapters of this dissertation, but were enlightening to me or useful to other projects in the lab, and proved great intellectual, technical, or recreational exercises.

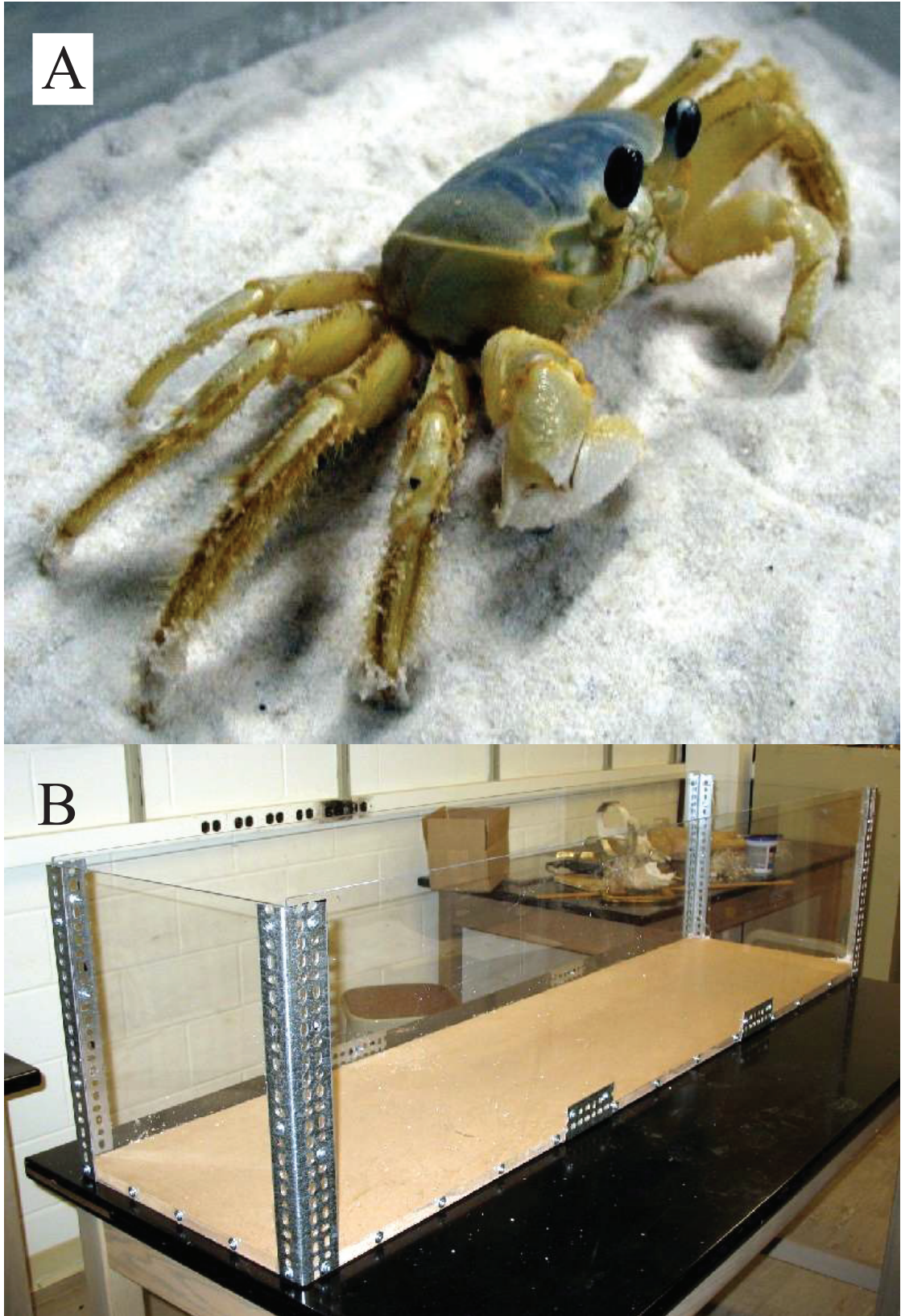


**Figure 129:** The ghost crab project. (A) A ghost crab (Genus *Ocypode*) sitting on sand. (B) A trackway which Ryan Maladen and I built together when we first started in the lab.

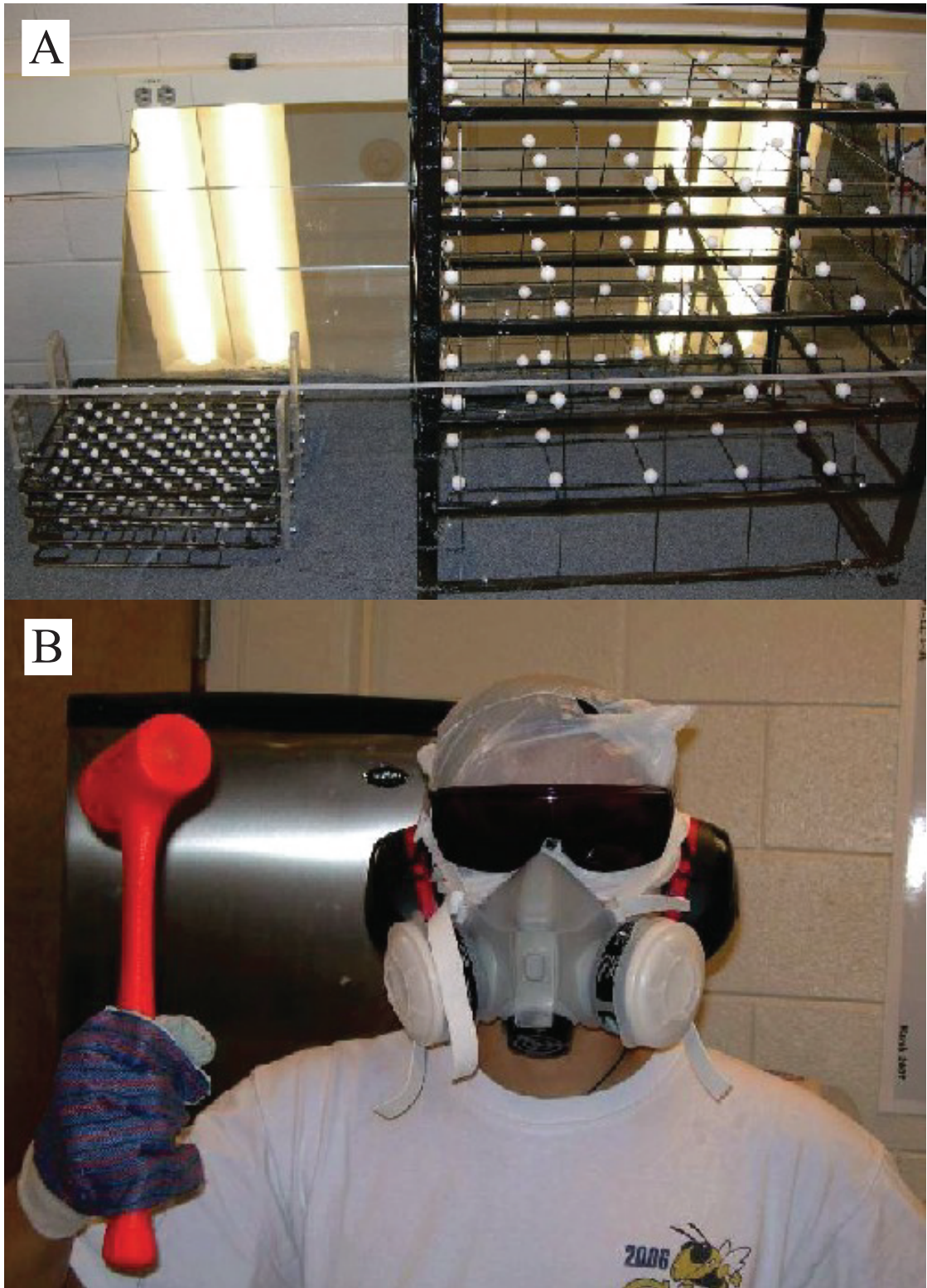


**Figure 130:** Calibration objects. (A) Two additional calibration objects which I built from HomeDepot shelving parts. (B) Me armed-to-teeth before cutting metal with Dremel Tools for making the calibration objects.

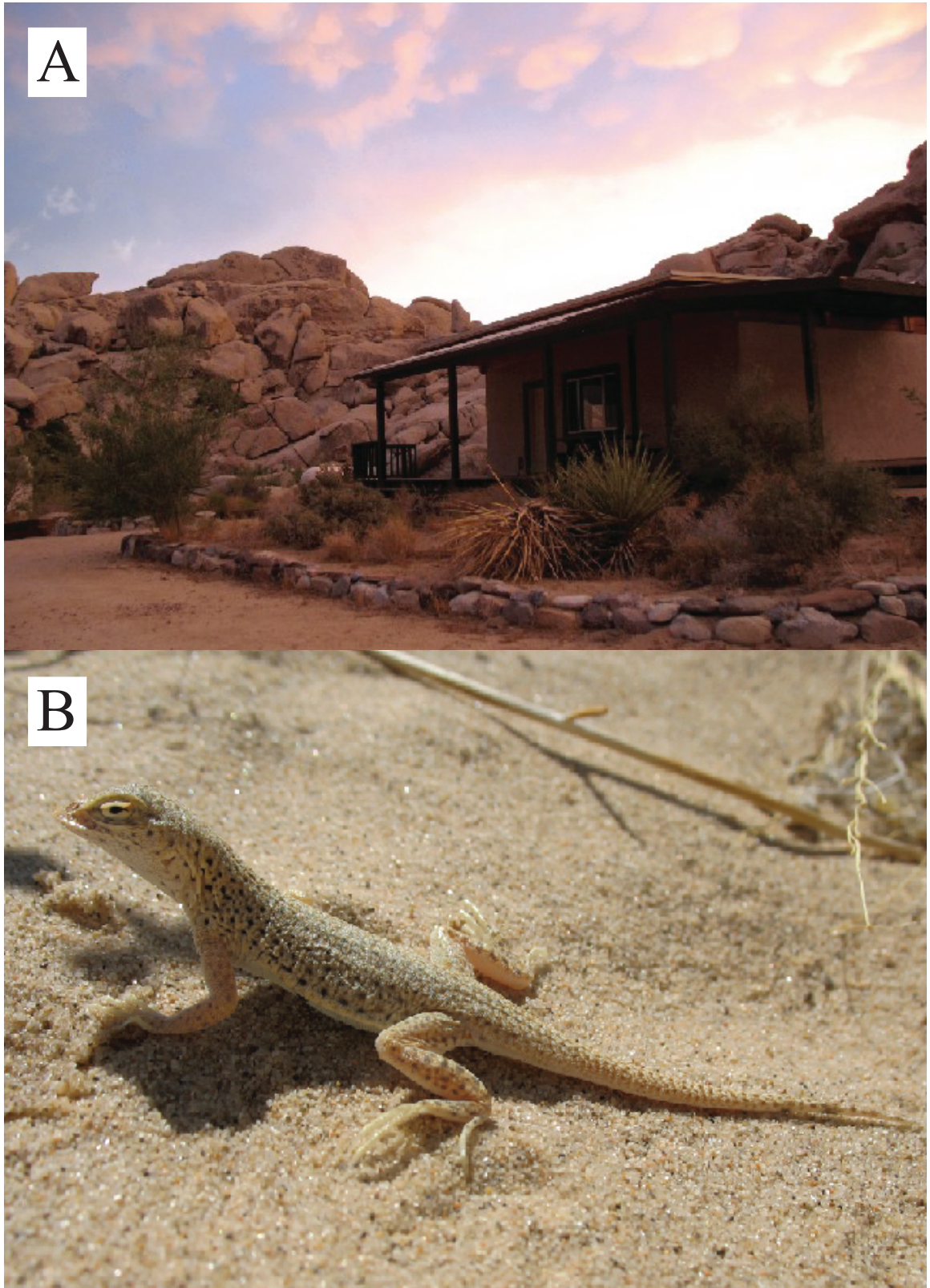


**Figure 131:** Natural beauty of the Mojave Desert. (A) A cabin surround by granite boulders under sunset clouds, in the Sweeney Granite Mountains Desert Research Center. (B) A baby fringe-toed lizard (Genus *uma*) I came across in the Kelso Dunes.

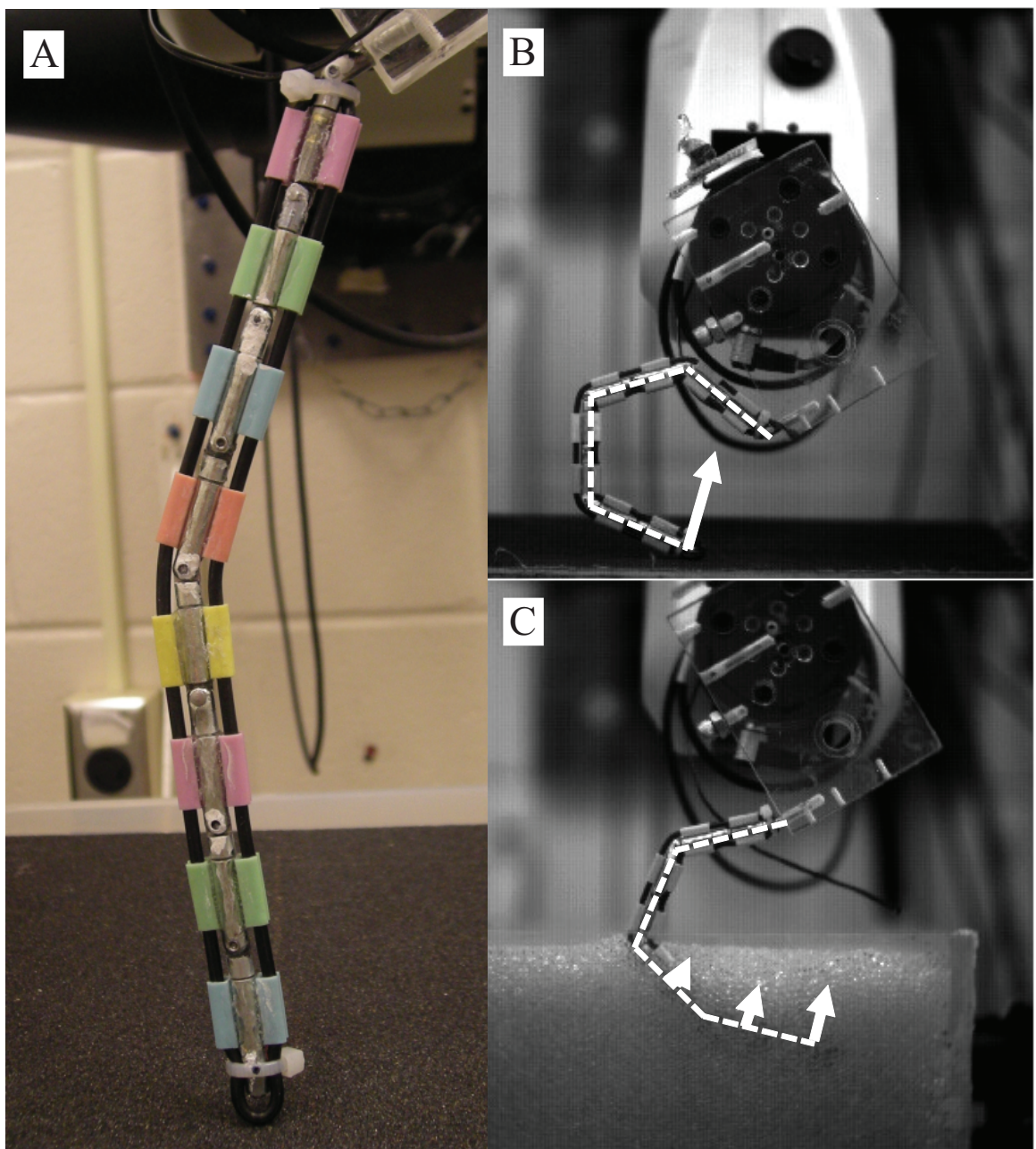


**Figure 132:** A physical model of the lizard foot to test the hypothesis of reduced foot curvature due to distribution of ground reaction force on granular media. (A) A physical model of the lizard foot inspired from the strut-spring model. When penetrated downwards into (B) solid and (C) granular surfaces to reach the same ground reaction force (not shown), the foot model curved less on the granular surface, presumably due to the smaller torque by distribution of ground reaction force along foot segments. Granular media was 3 mm diameter glass particles.

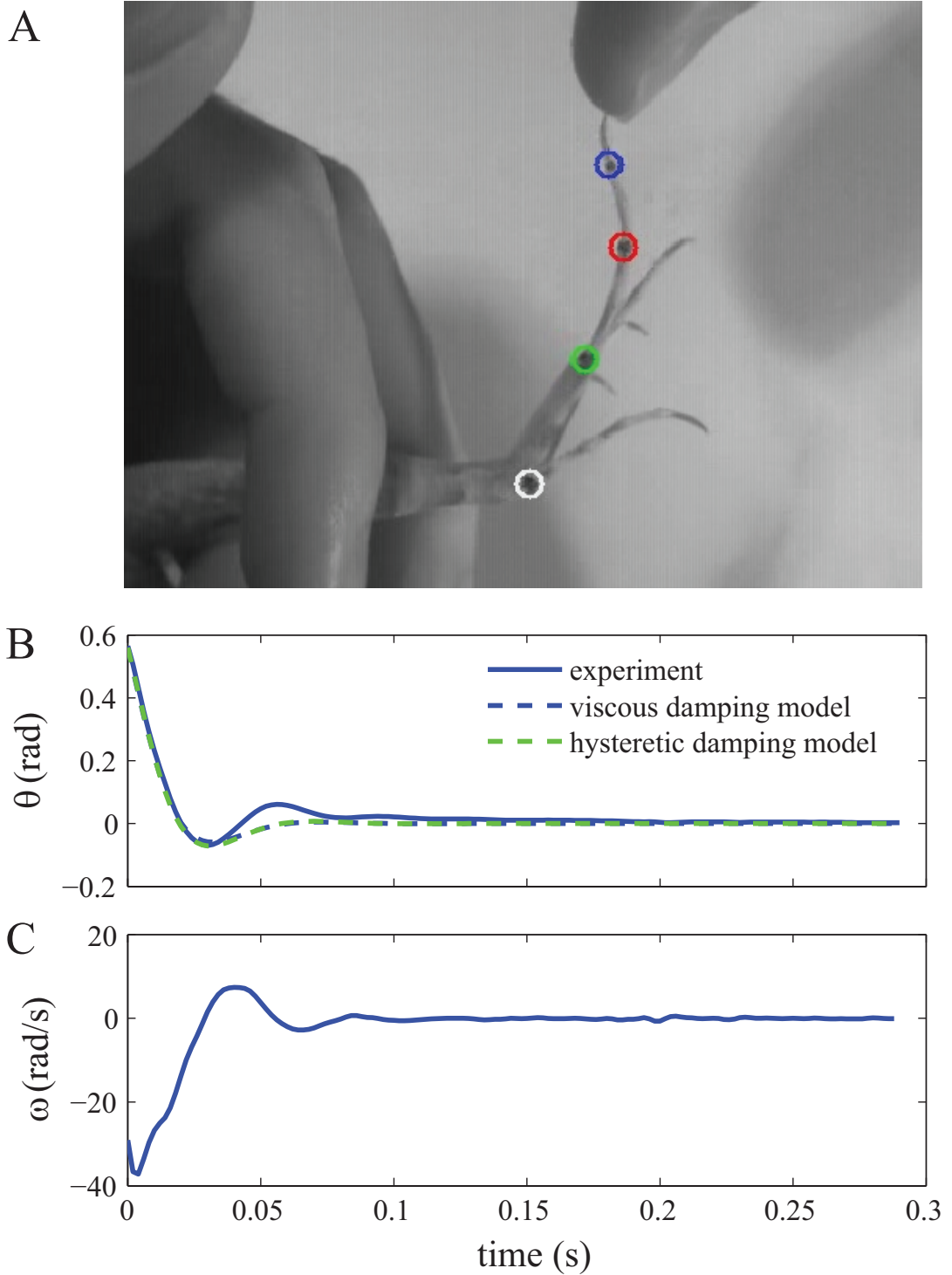
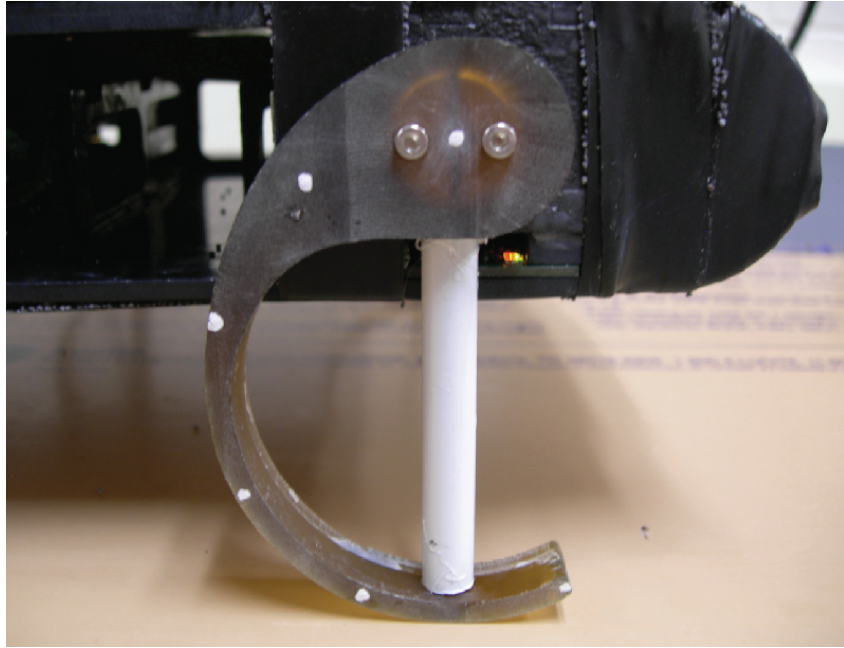


**Figure 133:** Measurements and modeling of the damping properties a hind foot of the zebra-tailed lizard during free vibration. (A) The hind foot of a lizard was hyperextended and released to vibrate freely. Snapshot shown before release. Colored circles indicate tracked marker positions. (B) Angular position and (C) angular velocity of the foot (measured at the toe tip relative to the ankle) as a function of time. Blue and green curves in (B) are fits from a viscous and a hysteretic damping model. The foot was underdamped and reached initial relaxed position within 0.1 s.

A



B

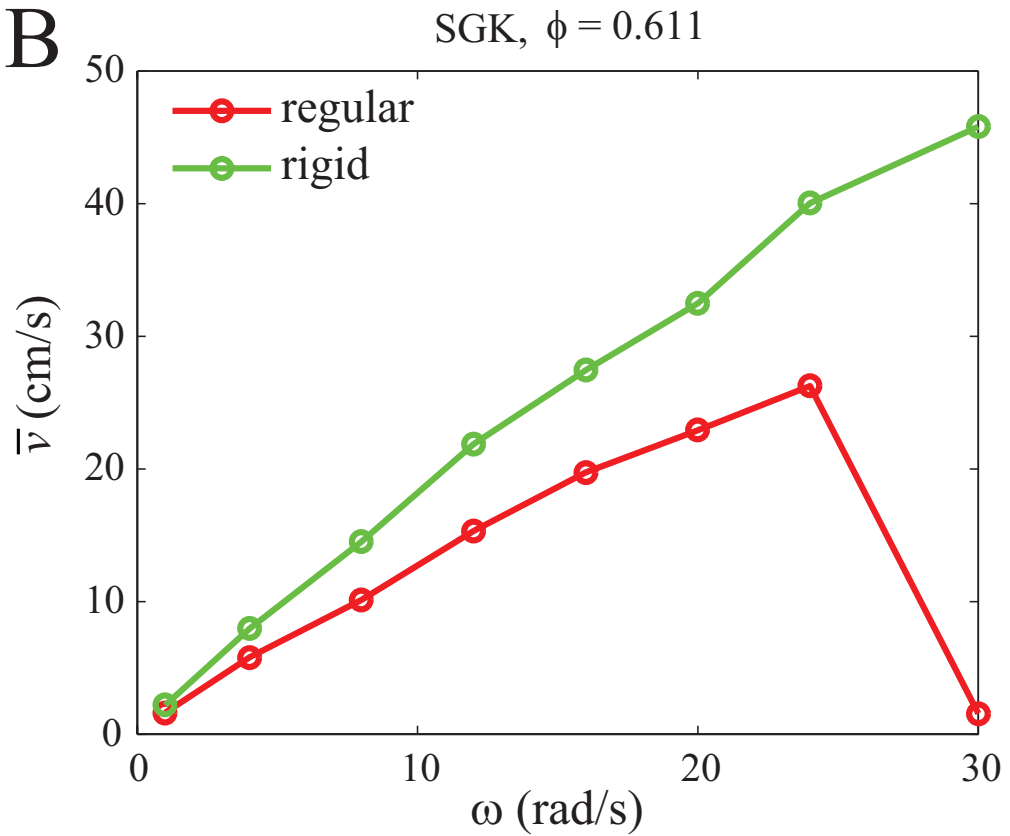
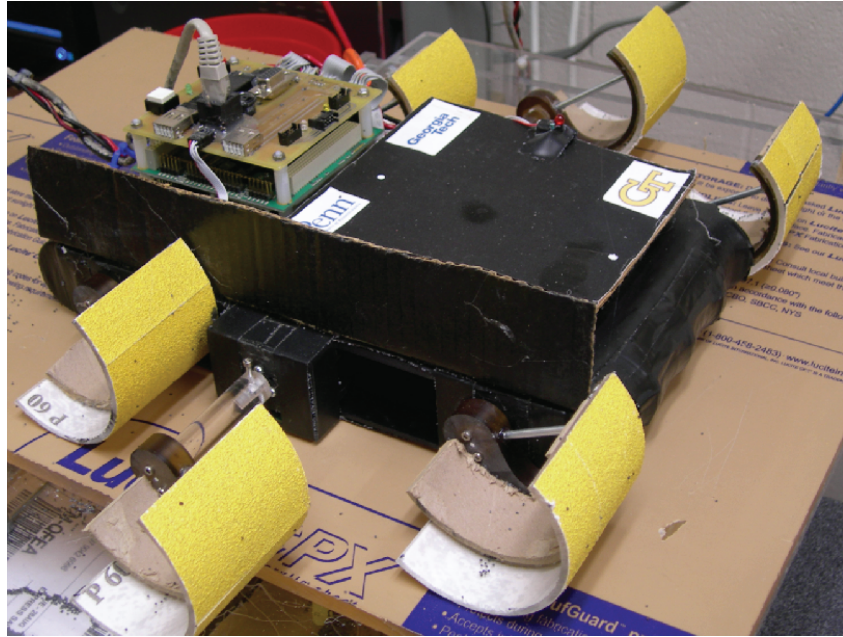
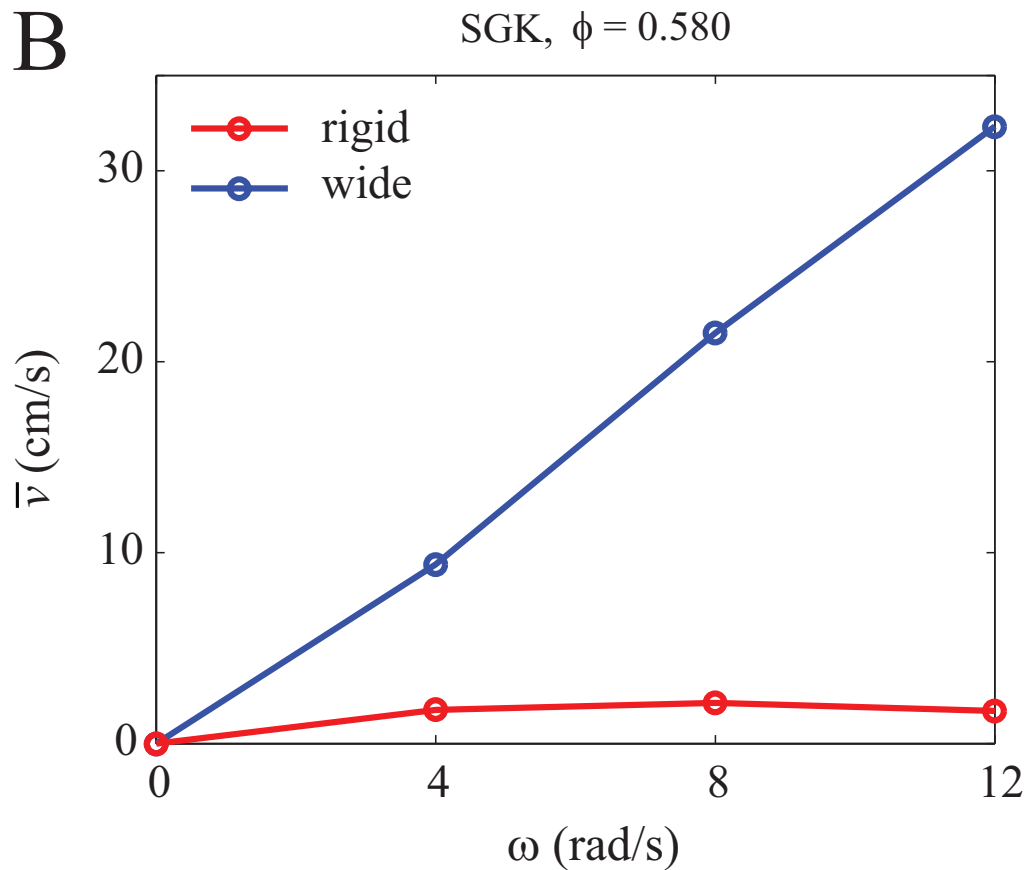


**Figure 134:** Enhancement of SandBot's performance by increasing leg rigidity. (A) SandBot with c-legs rigidified (by gluing a strut within the leg). (B) SandBot's speed on granular media (poppy seeds of  $\phi = 0.611$ ) using Soft Ground Kinematics increased significantly ( $\approx 40\%$ ) with rigid legs and did not enter swimming mode even at  $\omega = 30$  rad/s.

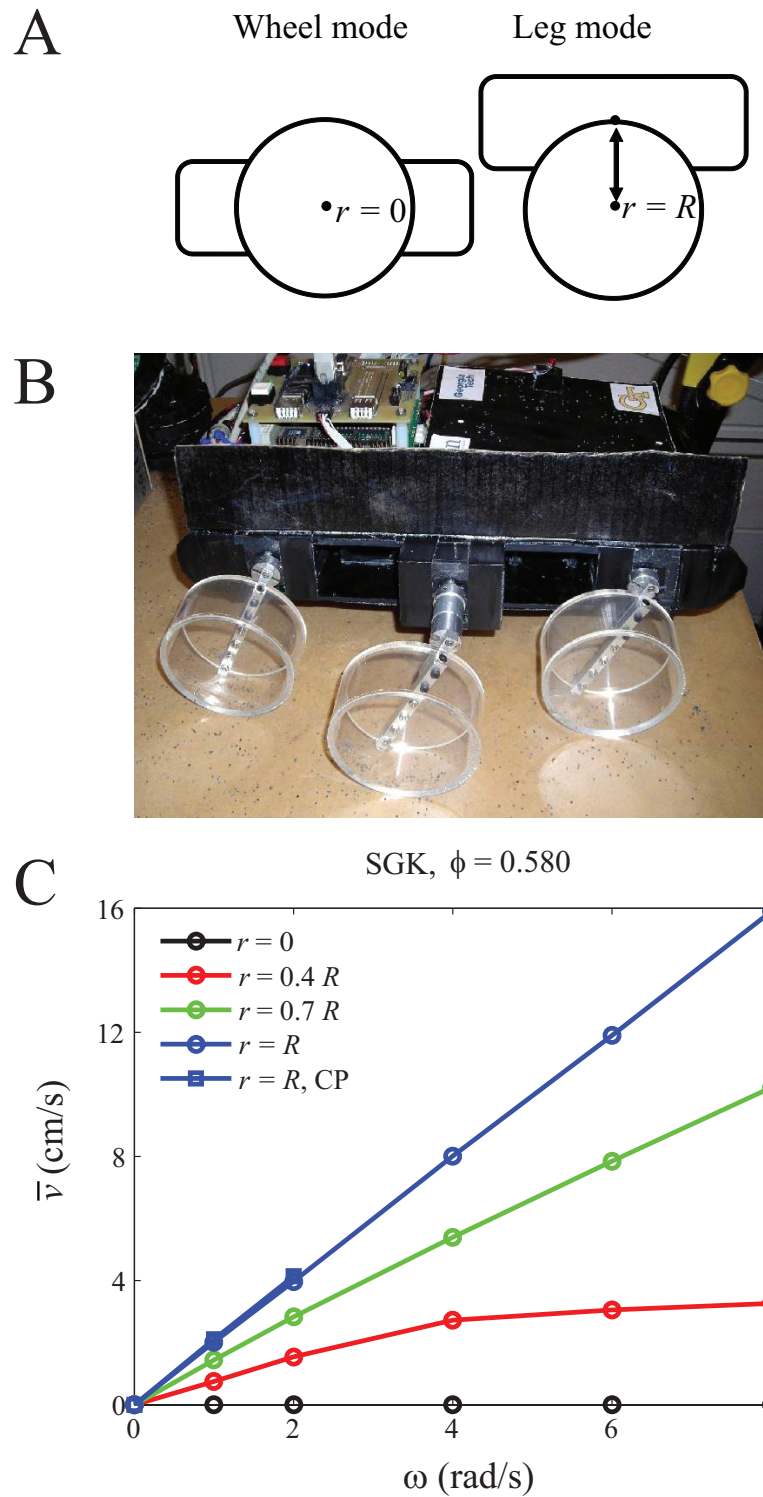
A



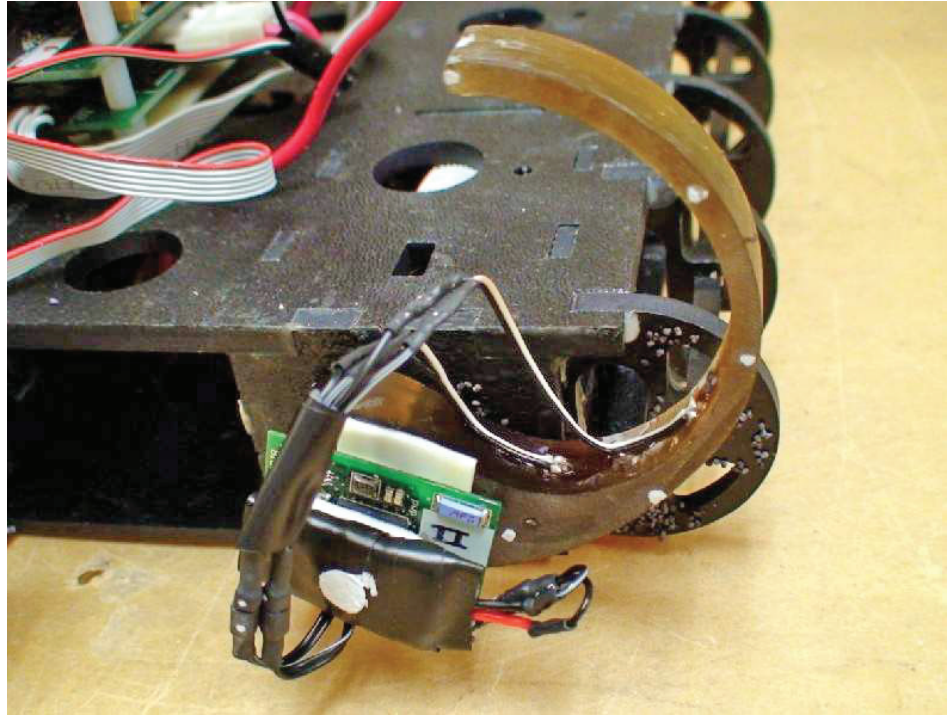
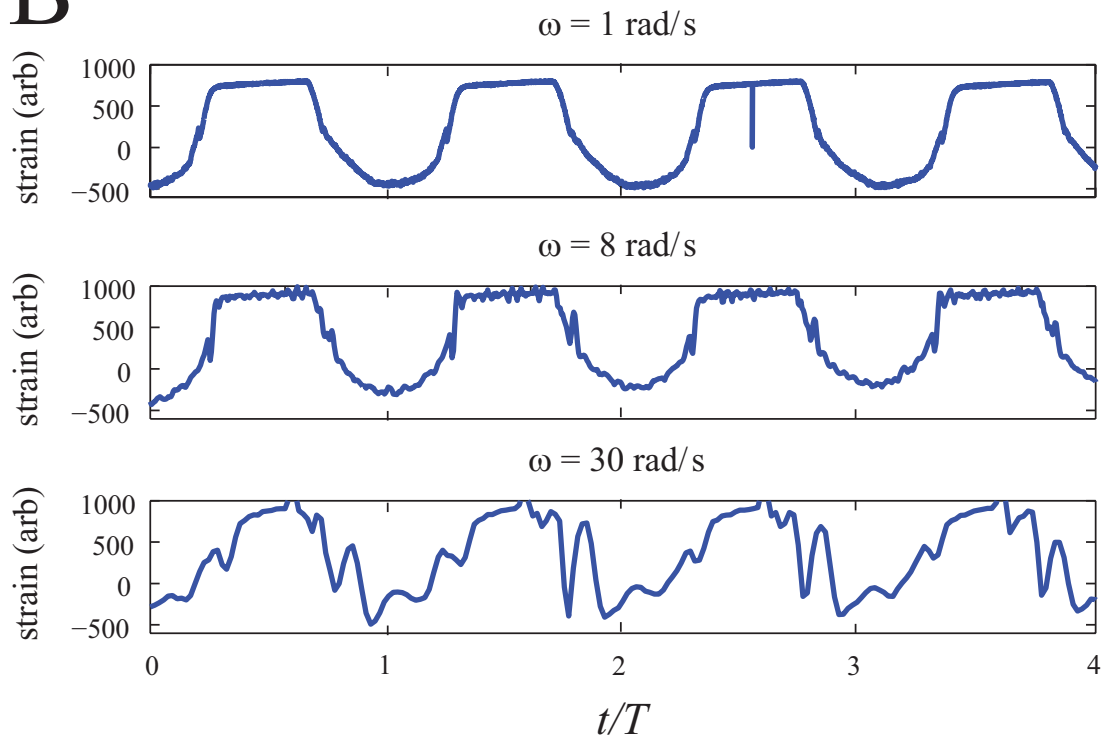
B



**Figure 135:** Enhancement of SandBot's performance by increasing leg area. (A) SandBot with wide legs (by gluing an extender onto the c-legs). (B) SandBot's speed on granular media (loosely packed poppy seeds,  $\phi = 0.580$ ) increased by an order of magnitude with wide legs and displayed linear speed-frequency relationship (i.e., fixed step length).



**Figure 136:** SandBot’s performance in wheel-leg transition. (A) Schematic of wheel mode and leg mode. (B) SandBot with circular legs I built, which could be mounted at different positions ranging from wheel mode to leg mode. (C) SandBot’s speed on granular media (loosely packed poppy seeds,  $\phi = 0.580$ ) as a function of stride frequency in wheel-leg transition using Soft Ground Kinematics. Blue squares are on closely packed ( $\phi = 0.622$ ) poppy seeds.

**A****B**

**Figure 137:** SandBot's leg strain during locomotion on granular media. (A) A bluetooth wireless strain gauge bonded to a c-leg of SandBot. Strain gauge was setup by Ryan Maladen. (B) SandBot's leg strain as a function of time for three stride frequencies on granular media (loosely packed poppy seeds,  $\phi = 0.580$ ).

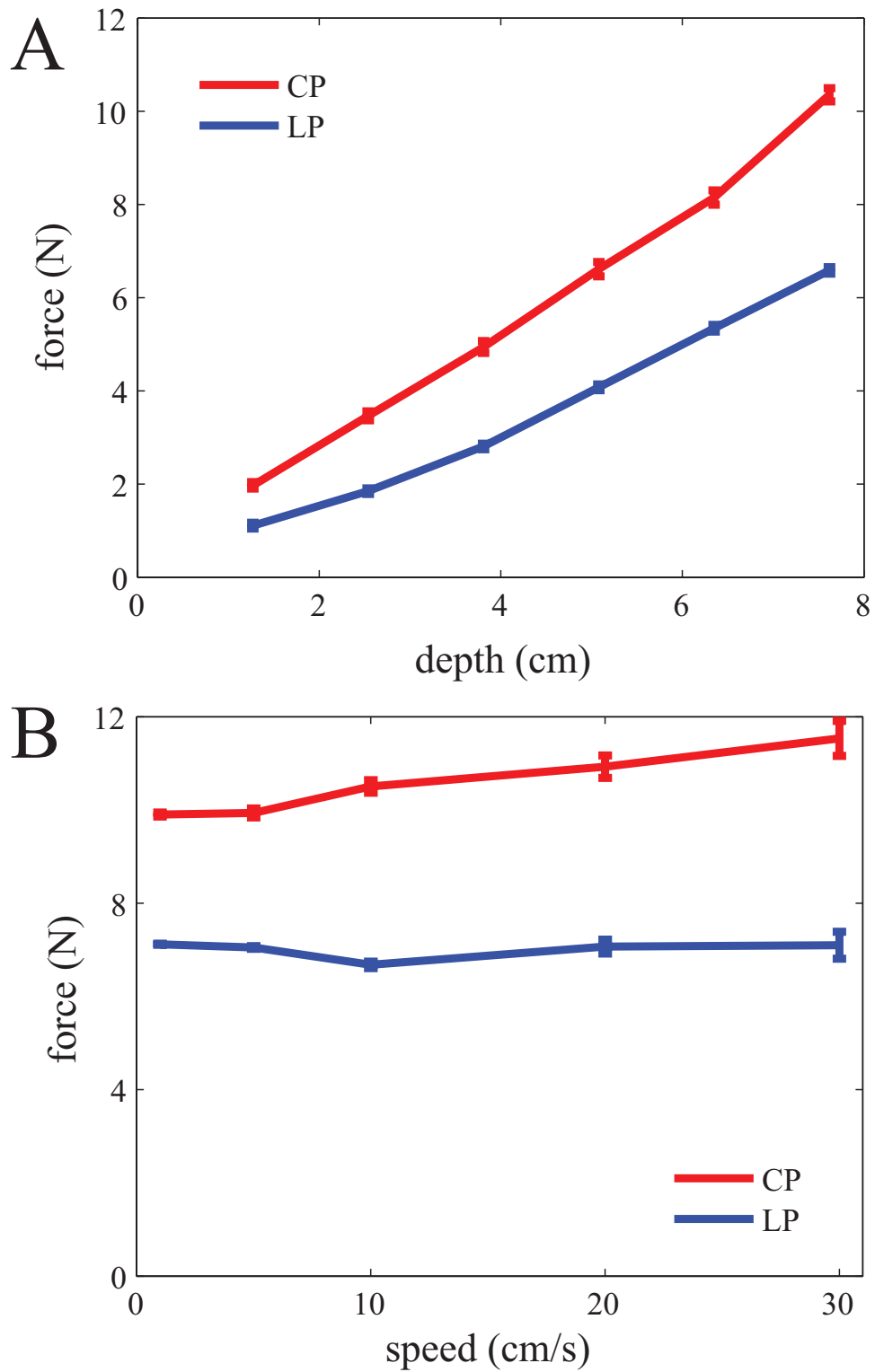


**Figure 138:** Mean drag force as a function of (A) depth and (B) speed in 0.27 mm diameter glass particles. Drag force is approximately independent of speed at low speeds ( $< 0.5$  m/s), and increases approximately linearly with depth. Blue and red curves are for loosely ( $\phi = 0.58$ ) and closely ( $\phi = 0.62$ ) packed states. Intruder was a stainless steel cylinder of 1.58 cm diameter and 3.8 cm length. Reproduced from [95].

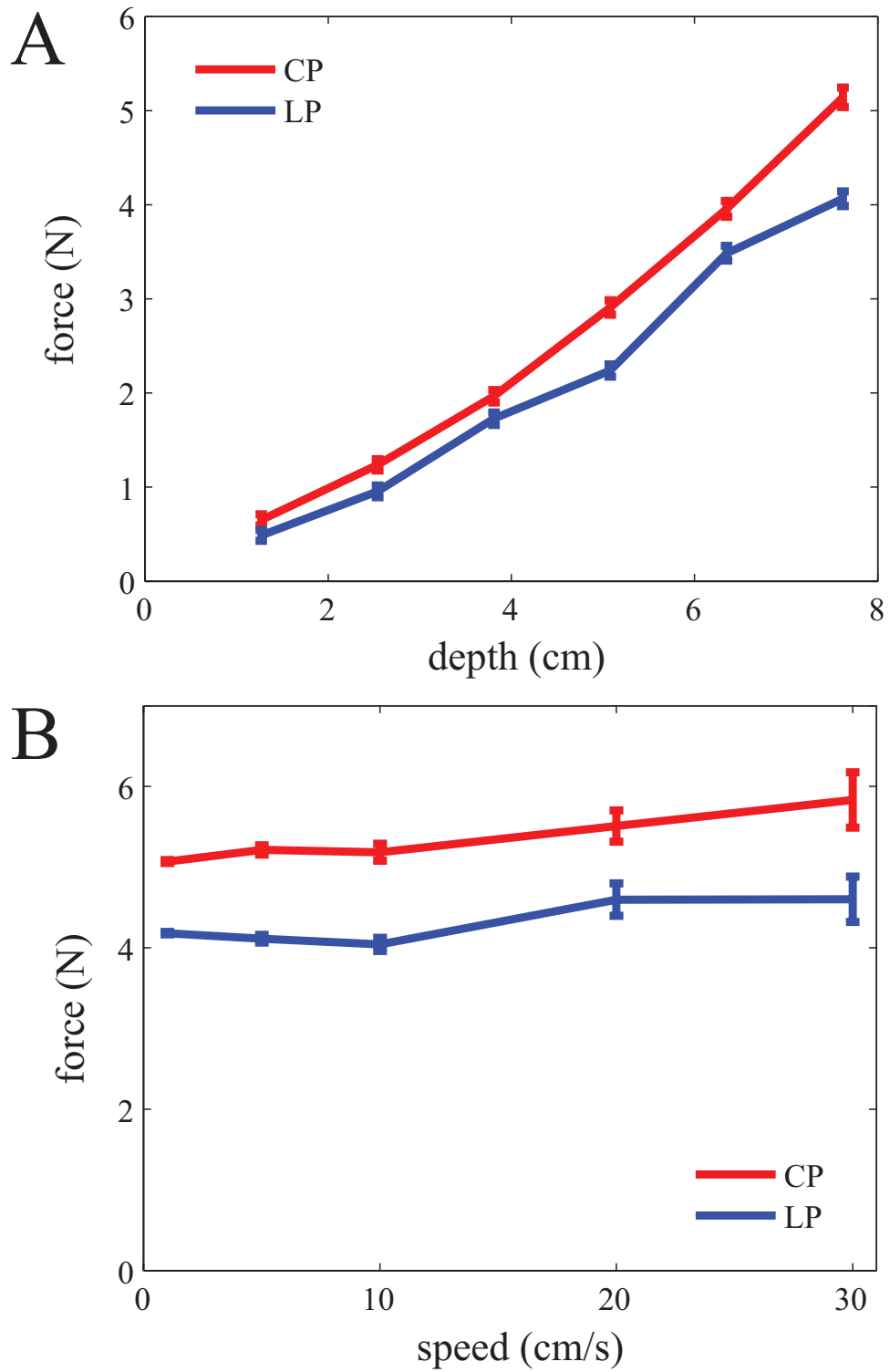


**Figure 139:** Mean drag force as a function of (A) depth and (B) speed in 3 mm diameter glass particles. Drag force is approximately independent of speed at low speeds ( $< 0.5$  m/s), and increases approximately linearly with depth. Blue and red curves are for loosely ( $\phi = 0.61$ ) and closely ( $\phi = 0.63$ ) packed states. Intruder was a stainless steel cylinder of 1.58 cm diameter and 3.8 cm length.

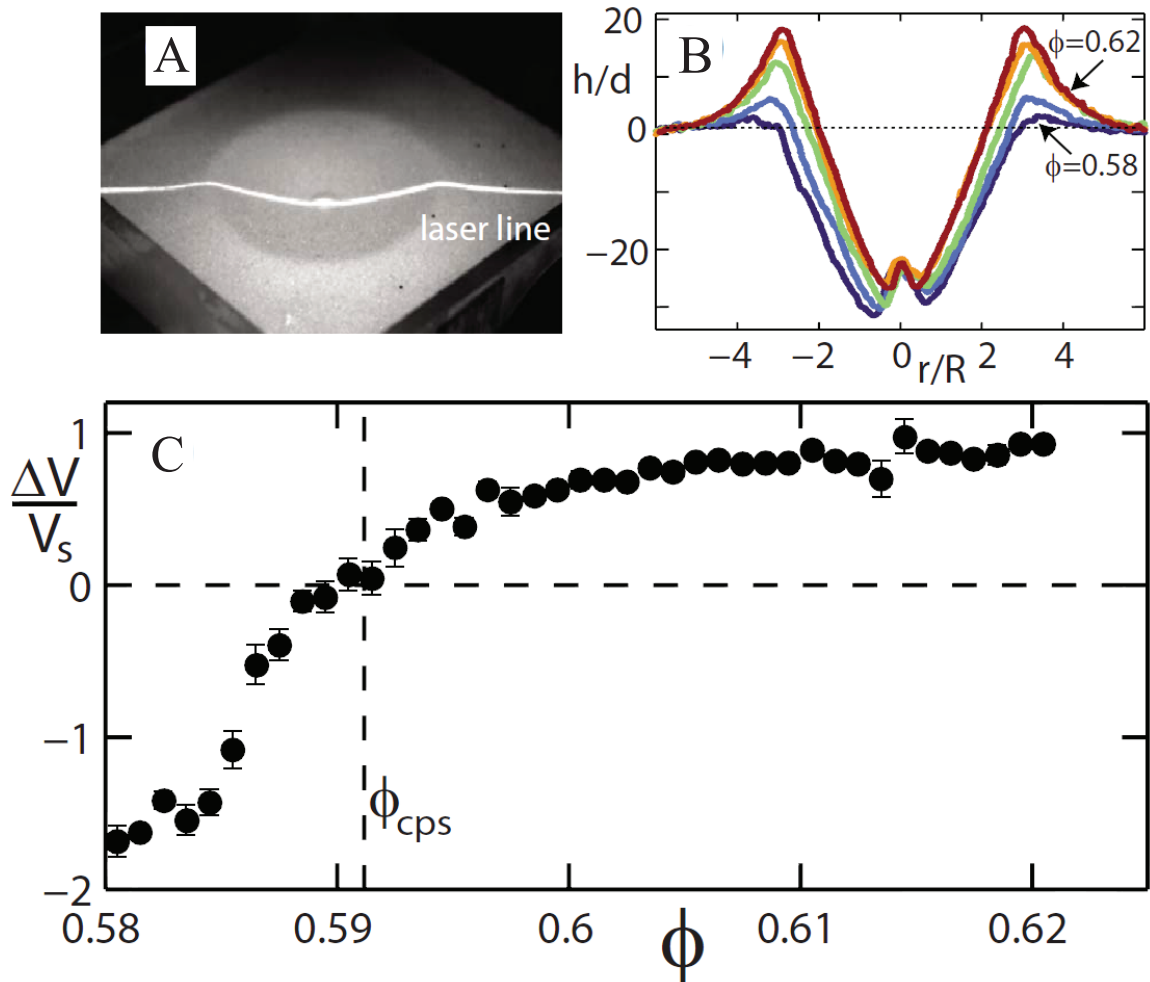


**Figure 140:** Influence of volume fraction on cratering at impact speed  $v_0 = 257 \pm 3$  cm/s. (A) Impact crater at  $\phi = 0.61$  and laser line. (B) Surface displacement  $h$  relative to grain diameter  $d$  increases with volume fraction ( $\phi = 0.579, 0.589, 0.600, 0.610$ , and  $0.622$ ). (C) Post impact change in bed volume  $\Delta V$  relative to sphere volume  $V_s$  vs.  $\phi$  is zero at critical packing state  $\phi_{cps} = 0.591$ , indicating the location of the critical packing state. Data analyzed by Paul B. Umbanhowar. Reproduced from [154].

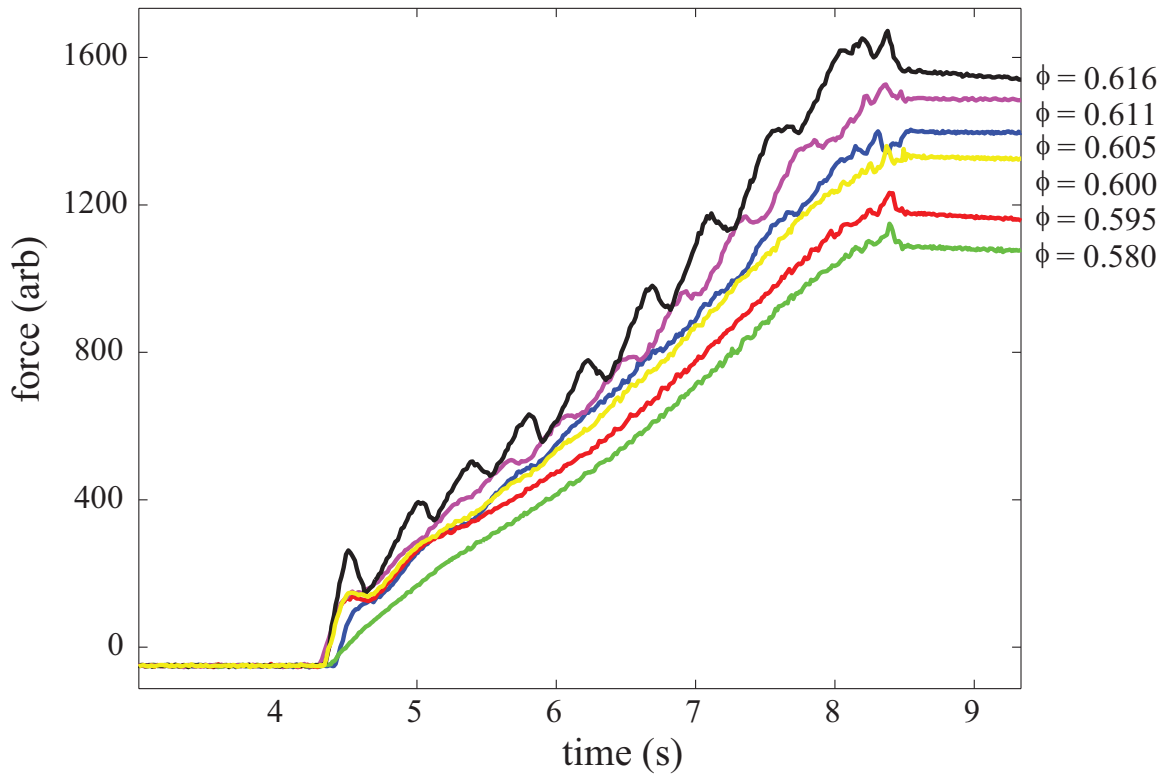


**Figure 141:** Force fluctuations during vertical penetration as a function of volume fraction. Force fluctuations increases with volume fraction, and the volume fraction onset of force fluctuation depends on the aspect ratio between the intruder and the container size. For the data shown, a disc of 4.4 cm diameter was intruded into granular media bounded by a tube of 10 cm diameter.

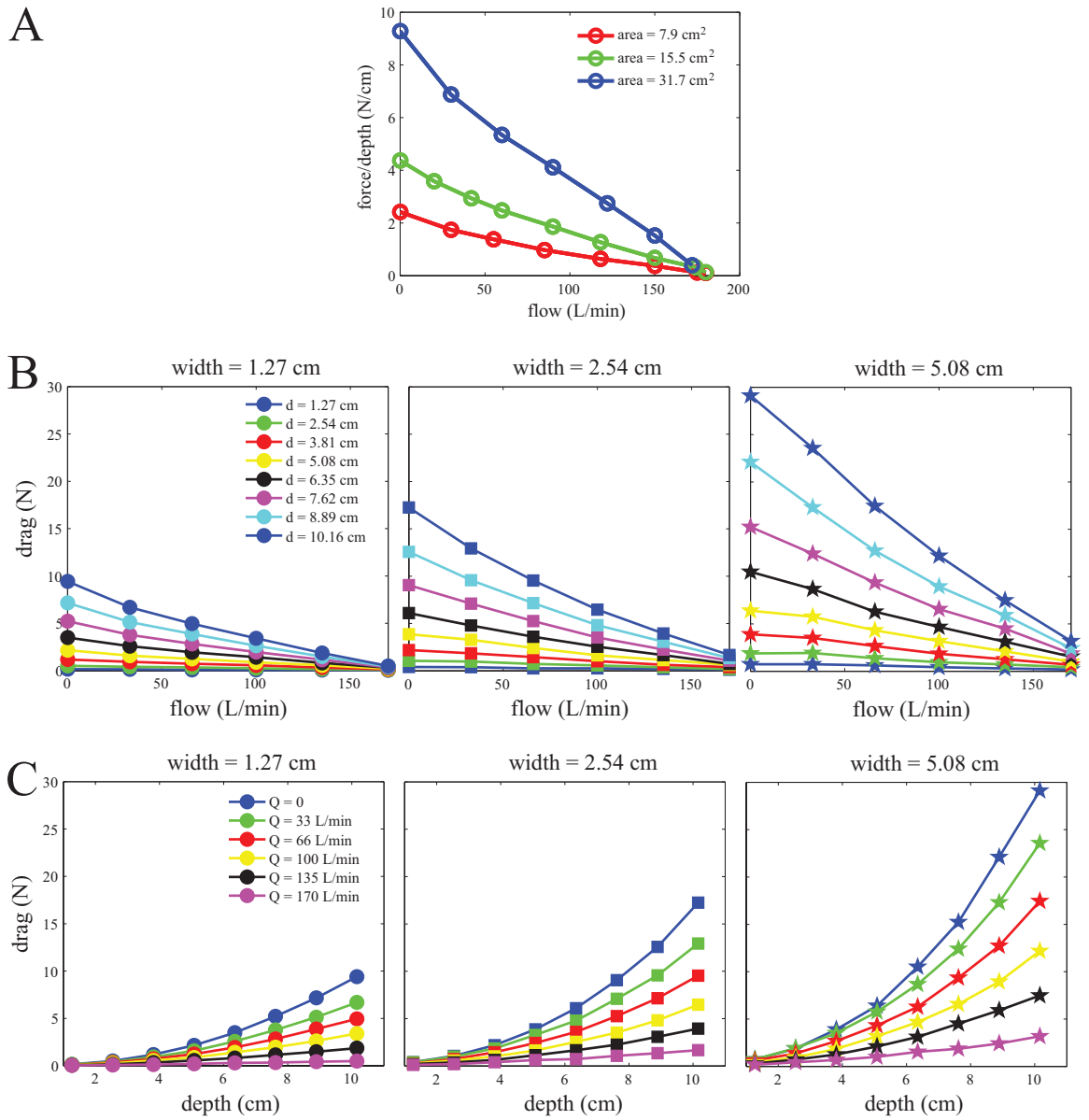


**Figure 142:** Granular force as a function of air flow rate through granular media. (A) Penetration force per depth decreases linearly with air flow and scales with intruder area. (B) Drag force on a plate (spanning from maximal depth to the surface) increases quadratically with the maximal depth ( $d$ ). (C) Drag force decreases linearly with air flow rate ( $Q$ ). In both (B) and (C), drag force scales with plate width. The fluidized bed has an area of  $24 \times 22 \text{ cm}^2$ .

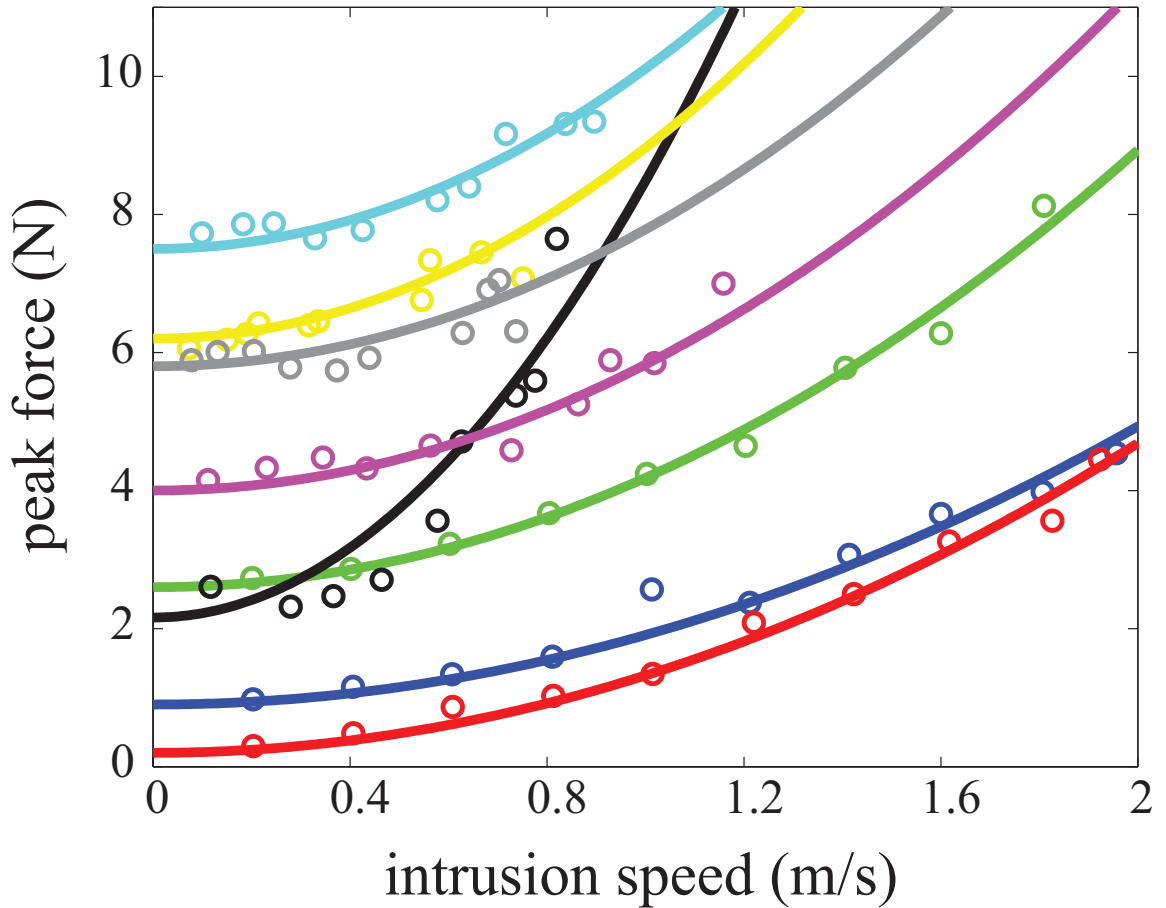


**Figure 143:** Effect of grain inertial force during intrusion at high speeds. Peak force during intrusion at high speeds ( $> 0.5$  m/s) increases approximately quadratically with intrusion speed. Solid curves are quadratic fits. Different colors are for: near horizontal drag of an intruder through loosely packed ( $\phi = 0.58$ ) 0.27 mm diameter glass particles at 1.9 cm depth (blue), 3.1 cm depth (green), and 3.1 cm depth with fluidization (red); near vertical penetration of an intruder into loosely packed ( $\phi = 0.58$ ) 0.27 mm diameter glass particles at a maximal depth of 6.6 cm (magenta), 9.1 cm (cyan), and 12.2 cm with fluidization (black); near vertical penetration of an intruder into loosely packed ( $\phi = 0.58$ ) poppy seeds at a maximal depth of 7.9 cm (yellow), and 9.1 cm (gray).

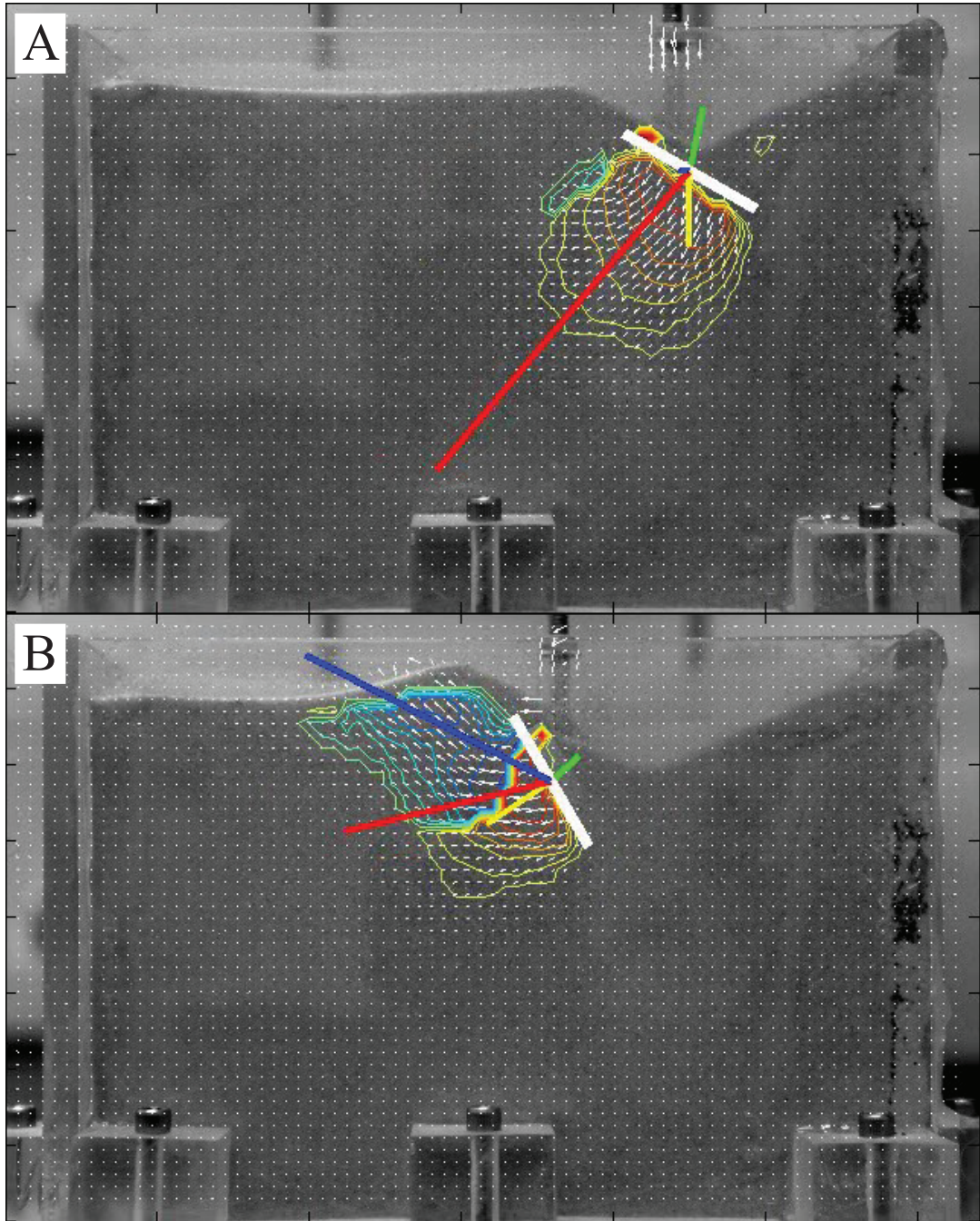


**Figure 144:** Granular Particle Imaging Velocimetry to capture the flow field during slow intrusion. Intruder was moved in the vertical plane while gently touching the sidewall of the fluidized bed, as grain motion was recorded by high speed video. (A) Intruder oriented at angle of attack  $\alpha = \pi/6$  moving along direction of motion  $\gamma = \pi/2$ . (B) Intruder oriented at  $\alpha = \pi/3$  moving along  $\gamma = 0.589$ . Granular media was loosely packed ( $\phi = 0.58$ ) 0.27 mm diameter glass particles. White, yellow, and green lines indicate plate orientation, direction of motion, and net force direction. White arrows indicate grain velocity. Colored contours indicate iso-speed layers, with the maximal contour at  $0.1 \times$  intrusion speed. Red and blue regions indicate grains with downward and upward velocity component. Red and blue lines indicate the total velocity of the red and blue regions.

## REFERENCES

- [1] R McNeil Alexander. *Principles of Animal Locomotion*. Princeton University Press, Princeton, 2003.
- [2] Michael H Dickinson, Claire T Farley, Robert J Full, M. A. R. Koehl, Rodger Kram, and Steven Lehman. How animals move: An integrative view. *Science*, 288(5463):100–106, April 2000.
- [3] Monica A Daley, James R Usherwood, Gladys Felix, and Andrew A Biewener. Running over rough terrain: guinea fowl maintain dynamic stability despite a large unexpected change in substrate height. *The Journal of Experimental Biology*, 209(Pt 1):171–87, January 2006.
- [4] S Sponberg and R J Full. Neuromechanical response of musculo-skeletal structures in cockroaches during rapid running on rough terrain. *The Journal of Experimental Biology*, 211:433–446, March 2008.
- [5] Thomas J. Roberts, Richard L. Marsh, Peter G. Weyand, and C. Richard Taylor. Muscular force in running turkeys: The economy of minimizing work. *Science*, 275(5303):1113–1115, February 1997.
- [6] J C Spagna, Daniel I Goldman, P-C Lin, D E Koditschek, and R J Full. Distributed mechanical feedback in arthropods and robots simplifies control of rapid running on challenging terrain. *Bioinspiration & Biomimetics*, 2(1):9–18, March 2007.
- [7] D P Ferris, M Louie, and C T Farley. Running in the real world: Adjusting leg stiffness for different surfaces. *Proceedings of the Royal Society B: Biological Sciences*, 265(1400):989–994, June 1998.
- [8] Andrew J Spence, Shai Revzen, Justin Seipel, Chris Mullens, and Robert J Full. Insects running on elastic surfaces. *The Journal of Experimental Biology*, 213(11):1907–1920, June 2010.
- [9] Chet T Moritz and Claire T Farley. Human hopping on damped surfaces: Strategies for adjusting leg mechanics. *Proceedings of the Royal Society B: Biological Sciences*, 270(1525):1741–1746, August 2003.
- [10] R M Nedderman. *Statics and Kinematics of Granular Materials*. Cambridge University Press, Cambridge, 1992.
- [11] Jean Kumagai. Sand Trap: Darpas 320-kilometer robotic race across the mojave desert yields no winners, but plenty of new ideas by jean kumagai. *Ieee Spectrum*, (June):44–50, 2004.
- [12] J Matson. Unfree Spirit: NASA’s Mars Rover Appears Stuck for Good. *Scientific American*, 302(4):16, 2010.

- [13] K. Nishikawa, Andrew A Biewener, P. Aerts, a. N. Ahn, H. J. Chiel, M. a. Daley, T. L. Daniel, R J Full, M. E. Hale, T. L. Hedrick, a. K. Lappin, T. R. Nichols, R. D. Quinn, R. a. Satterlie, and B. Szymik. Neuromechanics: an integrative approach for understanding motor control. *Integrative & Comparative Biology*, 47(1):16–54, May 2007.
- [14] Rolf Pfeifer, Max Lungarella, and Fumiya Iida. Self-organization, embodiment, and biologically inspired robotics. *Science*, 318(5853):1088–1093, November 2007.
- [15] Uluc Saranli, Martin Buehler, and Daniel E Koditschek. RHex: A Simple and Highly Mobile Hexapod Robot. *The International Journal of Robotics Research*, 20(7):616–631, July 2001.
- [16] R J Full and D E Koditschek. Templates and anchors: neuromechanical hypotheses of legged locomotion on land. *The Journal of Experimental Biology*, 202:3325–3332, December 1999.
- [17] P Zamparo, R Perini, C Orizio, M Sacher, and G Ferretti. The energy cost of walking or running on sand. *European Journal of Applied Physiology and Occupational Physiology*, 65(2):183–187, 1992.
- [18] T M Lejeune, P A Willems, and N C Heglund. Mechanics and energetics of human locomotion on sand. *The Journal of Experimental Biology*, 201:2071–2080, July 1998.
- [19] J W Glasheen and T A McMahon. A hydrodynamic model of locomotion in the Basilisk lizard. *Nature*, 380(6572):340–341, 1996.
- [20] S. T. Hsieh. Three-dimensional hindlimb kinematics of water running in the plumed basilisk lizard (*Basiliscus plumifrons*). *The Journal of Experimental Biology*, 206(23):4363–4377, December 2003.
- [21] S Vogel. *Life in moving fluids: the physical biology of flow*. Princeton Univ Pr, 1996.
- [22] H.M. Jaeger, S.R. Nagel, and R.P. Behringer. Granular solids, liquids, and gases. *Reviews of Modern Physics*, 68(4):1259–1273, 1996.
- [23] Pierre Jop, Yoël Forterre, and Olivier Pouliquen. A constitutive law for dense granular flows. *Nature*, 441(7094):727–730, June 2006.
- [24] R Jackson. *The Dynamics of Fluidized Particles*. Cambridge University Press, 2000.
- [25] E Ezcurra. Global Deserts Outlook. *United Nations Environmental Programme, Nairobi, Kenya*, 2006.
- [26] Douglas A Kelt, James H Brown, Edward J Heske, Pablo A Marquet, R Stephen, Julian R W Reid, A Kontantín, Georgy Shenbrot, Source Ecology, and No Apr. Community Structure of Desert Small Mammals : Comparisons Across Four Continents. *Ecology*, 77(3):746–761, 1996.
- [27] Walter Mosauer. Adaptive convergence in the sand reptiles of the Sahara and of California: A study in structure and behavior. *Copeia*, 1932(2):72–78, July 1932.
- [28] D.J. Germano and C.R. Hungerford. Reptile population changes with manipulation of sonoran desert shrub. *Great Basin Naturalist*, 41(1):129–138, 1981.

- [29] Clifford S Crawford. *Biology of Desert Invertebrates*. Springer, New York, 1981.
- [30] J L Cloudsley-Thompson. *Ecophysiology of Desert Arthropods and Reptiles*. Springer, New York, 1991.
- [31] Cameron W Barrows and Michael F Allen. Patterns of occurrence of reptiles across a sand dune landscape. *Journal of Arid Environments*, 74(2):186–192, February 2010.
- [32] Y C Fung. *Biomechanics: Mechanical Properties of Living Tissues*. Springer, New York, 1993.
- [33] R McNeil Alexander. Tendon elasticity and muscle function. *Comparative Biochemistry and Physiology Part A: Molecular & Integrative Physiology*, 133(4):1001–1011, December 2002.
- [34] NC Heglund, CR Taylor, and TA McMan. Scaling stride frequency and gait to animal size: mice to horses. *Science*, 186(4169):1112–1113, 1974.
- [35] R. Blickhan, Robert J Full, and Lena H Ting. Exoskeletal strain: evidence for a trot-gallop transition in rapidly running ghost crabs. *Journal of experimental biology*, 321(1):301–321, 1993.
- [36] Jonas Rubenson, Denham B Heliam, David G Lloyd, and Paul a Fournier. Gait selection in the ostrich: mechanical and metabolic characteristics of walking and running with and without an aerial phase. *Proceedings. Biological sciences / The Royal Society*, 271(1543):1091–9, May 2004.
- [37] Andrew A Biewener and Monica A Daley. Unsteady locomotion: integrating muscle function with whole body dynamics and neuromuscular control. *The Journal of Experimental Biology*, 210:2949–2960, September 2007.
- [38] D J Irschick and B C Jayne. Comparative three-dimensional kinematics of the hindlimb for high-speed bipedal and quadrupedal locomotion of lizards. *The Journal of Experimental Biology*, 202:1047–1065, May 1999.
- [39] L J Vitt and R D Ohmart. Ecology and reproduction of lower Colorado River lizards: I. *Callisaurus draconoides* (Iguanidae). *Herpetologica*, 33(2):214–222, 1977.
- [40] Wyatt L Korff and Matthew J McHenry. Environmental differences in substrate mechanics do not affect sprinting performance in sand lizards (*Uma scoparia* and *Callisaurus draconoides*). *The Journal of Experimental Biology*, 214:122–130, January 2011.
- [41] W H Karasov and R A Anderson. Correlates of average daily metabolism of field-active zebra-tailed lizards (*Callisaurus draconoides*). *Physiological Zoology*, 71(1):93–105, 1998.
- [42] D J Irschick and B C Jayne. A field study of the effects of incline on the escape locomotion of a bipedal lizard, *Callisaurus draconoides*. *Physiological and Biochemical Zoology*, 72(1):44–56, 1999.
- [43] C T Farley and T C Ko. Mechanics of locomotion in lizards. *The Journal of Experimental Biology*, 200:2177–2188, August 1997.

- [44] Dl Jindrich and R J Full. Many-legged maneuverability: dynamics of turning in hexapods. *The Journal of Experimental Biology*, 202:1603–1623, June 1999.
- [45] K Autumn, Y a Liang, S T Hsieh, W Zesch, W P Chan, T W Kenny, R Fearing, and R J Full. Adhesive force of a single gecko foot-hair. *Nature*, 405(6787):681–685, June 2000.
- [46] Daniel M Dudek and Robert J Full. Passive mechanical properties of legs from running insects. *The Journal of Experimental Biology*, 209:1502–1515, April 2006.
- [47] S Tonia Hsieh and George V Lauder. Running on water: Three-dimensional force generation by basilisk lizards. *Proceedings of the National Academy of Sciences of the United States of America*, 101(48):16784–16788, November 2004.
- [48] J W Glasheen and T A McMahon. Vertical water entry of disks at low Froude numbers. *Physics of Fluids*, 8(8):2078–2083, 1996.
- [49] J Glasheen and T McMahon. Size-dependence of water-running ability in basilisk lizards (*Basiliscus basiliscus*). *The Journal of Experimental Biology*, 199(Pt 12):2611–2618, January 1996.
- [50] Daniel E Koditschek, Robert J Full, and Martin Buehler. Mechanical aspects of legged locomotion control. *Arthropod structure & development*, 33(3):251–72, July 2004.
- [51] S. Kim, J E Clark, and M R Cutkosky. iSprawl: Design and tuning for high-speed autonomous open-loop running. *The International Journal of Robotics Research*, 25(9):903, September 2006.
- [52] R.T. Schroer, M.J. Boggess, R.J. Bachmann, R.D. Quinn, and R.E. Ritzmann. Comparing cockroach and Whegs robot body motions. *IEEE International Conference on Robotics and Automation, 2004. Proceedings. ICRA '04. 2004*, pages 3288–3293 Vol.4, 2004.
- [53] Marc Raibert, Kevin Blankespoor, Gabriel Nelson, Rob Playter, and Others. Bigdog, the rough-terrain quadruped robot. *Proceedings of the 17th International Federation of Automation Control*, pages 10822–10825, 2008.
- [54] Brian M. Yamauchi. PackBot: a versatile platform for military robotics. *Proceedings of SPIE*, 5422:228–237, 2004.
- [55] Philip Holmes, Robert J Full, Dan Koditschek, and John Guckenheimer. The dynamics of legged locomotion: Models, analyses, and challenges. *SIAM Review*, 48(2):207–304, 2006.
- [56] D Goldman, H Komsuoglu, and D Koditschek. March of the Sandbots. *Spectrum, IEEE*, 46(4):30–35, 2009.
- [57] J D Weingarten, G A D Lopes, M Buehler, R E Groff, and D E Koditschek. Automated gait adaptation for legged robots. volume Vol.3 of *2004 IEEE International Conference on Robotics and Automation (IEEE Cat. No.04CH37508)*, pages 2153–2158, Piscataway, NJ, USA, 2004. IEEE.

- [58] A M Hoover, S Burden, X Y Fu, S S Sastry, and R S Fearing. Bio-inspired design and dynamic maneuverability of a minimally actuated six-legged robot. In *Biomedical Robotics and Biomechanics (BioRob), 2010 3rd IEEE RAS and EMBS International Conference on*, pages 869–876. IEEE, 2010.
- [59] P Birkmeyer, K Peterson, and R S Fearing. DASH: A dynamic 16g hexapedal robot. In *Intelligent Robots and Systems, 2009. IROS 2009. IEEE/RSJ International Conference on*, pages 2683–2689. IEEE, 2009.
- [60] R J Wood, S Avadhanula, R Sahai, E Steltz, and R S Fearing. Microrobot Design Using Fiber Reinforced Composites. *J. Mech. Design*, 130(5), May 2008.
- [61] Junfei Geng, D. Howell, E. Longhi, R. Behringer, G. Reydellet, L. Vanel, E. Clément, and S. Luding. Footprints in Sand: The Response of a Granular Material to Local Perturbations. *Physical Review Letters*, 87(3):035506(1–4), July 2001.
- [62] Adrian Daerr and Stephane Douady. Two types of avalanche behaviour in granular media. *Nature*, 399(May):241–243, 1999.
- [63] D Coles. Transition in circular Couette flow. *Journal of Fluid Mechanics*, 21(03):385–425, 1965.
- [64] M G Bekker. *Theory of land locomotion: the mechanics of vehicle mobility*. University of Michigan Press, 1956.
- [65] M G Bekker. *Off-the-road locomotion, research and development in terramechanics*. University of Michigan Press, Ann Arbor, 1960.
- [66] J Y Wong. *Terramechanics and off-road vehicles*. Elsevier, 1989.
- [67] JY Y Wong. *Terramechanics and Off-Road Vehicle Engineering*. Butterworth-Heinemann, Oxford, UK, 2010.
- [68] I. Albert, J. Sample, A. Morss, S. Rajagopalan, A.-L. Barabási, and P. Schiffer. Granular drag on a discrete object: Shape effects on jamming. *Physical Review E*, 64(6):2–5, November 2001.
- [69] K Wiegardt. Experiments in granular flow. *Annual Review of Fluid Mechanics*, 7(1):89–114, 1975.
- [70] R. Albert, M. Pfeifer, A.-L. Barabási, and P. Schiffer. Slow drag in a granular medium. *Physical Review Letters*, 82(1):205–208, January 1999.
- [71] I. Albert, P. Tegzes, R. Albert, J. Sample, A. Barabási, T. Vicsek, B. Kahng, and P. Schiffer. Stick-slip fluctuations in granular drag. *Physical Review E*, 64(3):1–9, August 2001.
- [72] G Hill, S Yeung, and S. a Koehler. Scaling vertical drag forces in granular media. *Europhysics Letters (EPL)*, 72(1):137–143, October 2005.
- [73] Hiroaki Katsuragi and Douglas J. Durian. Unified force law for granular impact cratering. *Nature Physics*, 3(6):420–423, April 2007.

- [74] Daniel I Goldman and Paul B Umbanhowar. Scaling and dynamics of sphere and disk impact into granular media. *Physical Review E*, 77(2):021308(1–14), February 2008.
- [75] James G. Berryman. Random close packing of hard spheres and disks. *Physical Review A*, 27(2):1053–1061, 1983.
- [76] W W Dickinson and J D Ward. Low depositional porosity in eolian sands and sandstones, Namib Desert. *Journal of Sedimentary Research*, 64(2a):226–232, 1994.
- [77] Matthias Schröter, Sibylle Nägele, Charles Radin, and Harry L Swinney. Phase transition in a static granular system. *Europhysics Letters (EPL)*, 78(4):44004, May 2007.
- [78] Daniel I Goldman. Pattern formation and uidization in vibrated granular layers, and grain dynamics and jamming in a water uidized bed. *Doctoral Dissertation*, 2002.
- [79] Matthias Schröter, Daniel Goldman, and Harry Swinney. Stationary state volume fluctuations in a granular medium. *Physical Review E*, 71(3):1–4, March 2005.
- [80] Daniel Goldman and Harry Swinney. Signatures of Glass Formation in a Fluidized Bed of Hard Spheres. *Physical Review Letters*, 96(14):1–4, April 2006.
- [81] Edmund Nowak, James Knight, Eli Ben-Naim, Heinrich Jaeger, and Sidney Nagel. Density fluctuations in vibrated granular materials. *Physical Review E*, 57(2):1971–1982, February 1998.
- [82] D I Goldman, W L Korff, M Wehner, M S Berns, and R J Full. The mechanism of rapid running in weak sand. *Integrative & Comparative Biology*, 46:Suppl. 1, E50, 2006.
- [83] Tyson L Hedrick. Software techniques for two- and three-dimensional kinematic measurements of biological and biomimetic systems. *Bioinspiration & Biomimetics*, 3(3):034001(1–6), September 2008.
- [84] Y I Abdel-Aziz and H M Karara. Direct linear transformation from comparator coordinates in close-range photogrammetry. In *Proc. ASP/UI Symposium on Close-range Photogrammetry*, pages 1–18, 1971.
- [85] Chen Li, S. Tonia Hsieh, and Daniel I Goldman. The effect of substrate on the running mechanics of the zebra-tailed lizard (*Callisaurus draconoides*). *Journal of Experimental Biology*, 2011.
- [86] R. Blickhan. The spring-mass model for running and hopping. *Journal of Biomechanics*, 22(11-12):1217–1227, 1989.
- [87] J Schmitt, M Garcia, R C Razo, P Holmes, and R J Full. Dynamics and stability of legged locomotion in the horizontal plane: A test case using insects. *Biological Cybernetics*, 86(5):343–353, May 2002.
- [88] J J Chen, A M Peattie, K Autumn, and R J Full. Differential leg function in a sprawled-posture quadrupedal trotter. *The Journal of Experimental Biology*, 209:249–259, January 2006.

- [89] J Schmitt and P Holmes. Mechanical models for insect locomotion: dynamics and stability in the horizontal plane I. Theory. *Biological Cybernetics*, 83(6):501–515, December 2000.
- [90] J Schmitt and P Holmes. Mechanical models for insect locomotion: dynamics and stability in the horizontal plane-II. Application. *Biological Cybernetics*, 83(6):517–527, December 2000.
- [91] J R F Arthur, T Dunstan, Q A J L Al-Ani, and A Assadi. Plastic deformation and failure in granular media. *Géotechnique*, 27(1):53–74, 1977.
- [92] Chen Li, Paul B Umbanhowar, Haldun Komsuoglu, Daniel E Koditschek, and Daniel I Goldman. Sensitive dependence of the motion of a legged robot on granular media. *Proceedings of the National Academy of Sciences of the United States of America*, 106(9):3029–3034, 2009.
- [93] Nick Gravish, Paul B Umbanhowar, and Daniel I Goldman. Force and flow transition in plowed granular media. *Physical Review Letters*, 105(12):208301(1–4), September 2010.
- [94] Yang Ding, Nick Gravish, and Daniel I Goldman. Drag induced lift in granular media. *Physical Review Letters*, 106(2):028001(1–4), January 2011.
- [95] Ryan D Maladen, Yang Ding, Chen Li, and Daniel I Goldman. Undulatory swimming in sand: Subsurface locomotion of the sandfish lizard. *Science*, 325(5938):314–318, July 2009.
- [96] Nicole Mazouchova, Nick Gravish, Andrei Savu, and Daniel I Goldman. Utilization of granular solidification during terrestrial locomotion of hatchling sea turtles. *Biology letters*, 6(3):398–401, June 2010.
- [97] Chen Li, Paul B Umbanhowar, Haldun Komsuoglu, and Daniel I Goldman. The effect of limb kinematics on the speed of a legged robot on granular media. *Experimental Mechanics*, 50(9):1383–1393, April 2010.
- [98] Chen Li, Aaron M Hoover, Paul Birkmeyer, Paul B Umbanhowar, Ronald S Fearing, and Daniel I Goldman. Systematic study of the performance of small robots on controlled laboratory substrates. *Proceedings of SPIE*, 7679:76790Z(1–13), 2010.
- [99] Robert K Josephson. MECHANICAL POWER OUTPUT FROM STRIATED MUSCLE DURING CYCLIC CONTRACTION. *The Journal of experimental biology*, 512:493–512, 1985.
- [100] Thomas Libby and Robert J Full. Active muscle enhances rapid perturbation recovery in an insect limb. *Integrative & Comparative Biology*, 51:Suppl. 1, E81, 2011.
- [101] Andrew A Biewener and R Blickhan. Kangaroo rat locomotion: design for elastic energy storage or acceleration? *The Journal of Experimental Biology*, 140:243–255, November 1988.
- [102] R J Full and M S Tu. Mechanics of six-legged runners. *The Journal of Experimental Biology*, 148:129–146, January 1990.

- [103] R F Ker, M B Bennett, S R Bibby, R C Kester, and R McNeil Alexander. The spring in the arch of the human foot. *Nature*, 325:147–149, January 1987.
- [104] Anthony P. Russell. The aponeuroses of the lacertilian ankle. *Journal of Morphology*, 218(1):65–84, October 1993.
- [105] Andrew A Biewener. Muscle function in vivo: A comparison of muscles used for elastic energy savings versus muscles used to generate mechanical power. *Integrative & Comparative Biology*, 38(4):703–717, 1998.
- [106] R McNeil Alexander and A Vernon. The mechanics of hopping by kangaroos (Macropodidae). *Journal of Zoology*, 177(2):265–303, 1975.
- [107] Andrew A Biewener, D D Konieczynski, and R V Baudinette. In vivo muscle force-length behavior during steady-speed hopping in tammar wallabies. *The Journal of Experimental Biology*, 201:1681–1694, June 1998.
- [108] C P McGowan, J Skinner, and Andrew A Biewener. Hind limb scaling of kangaroos and wallabies (superfamily Macropodoidea): Implications for hopping performance, safety factor and elastic savings. *Journal of Anatomy*, 212(2):153–163, February 2008.
- [109] Andrew A Biewener, R McNeil Alexander, and N C Heglund. Elastic energy storage in the hopping of kangaroo rats (*Dipodomys spectabilis*). *Journal of Zoology*, 195(3):369–383, 1981.
- [110] D T Kirkendall and W E Garrett. Function and biomechanics of tendons. *Scandinavian Journal of Medicine & Science in Sports*, 7(2):62–66, April 1997.
- [111] R McNeil Alexander and A S Jayes. Fourier analysis of forces exerted in walking and running. *Journal of Biomechanics*, 13(4):383–390, January 1980.
- [112] Chet T Moritz and Claire T Farley. Human hopping on very soft elastic surfaces: Implications for muscle pre-stretch and elastic energy storage in locomotion. *The Journal of Experimental Biology*, 208:939–949, March 2005.
- [113] W P Coombs Jr. Theoretical aspects of cursorial adaptations in dinosaurs. *The Quarterly Review of Biology*, 53(4):393–418, 1978.
- [114] M Hildebrand. Walking and running. *Functional Vertebrate Morphology*, 3:38–57, 1985.
- [115] T. Garland Jr and C.M. Janis. Does metatarsal/femur ratio predict maximal running speed in cursorial mammals? *Journal of Zoology*, 229(1):133–151, 1993.
- [116] D Bauwens, T Garland Jr, A M Castilla, and R Van Damme. Evolution of sprint speed in lacertid lizards: morphological, physiological and behavioral covariation. *Evolution*, 49(5):848–863, 1995.
- [117] Andrew A Biewener. Biomechanical consequences of scaling. *The Journal of Experimental Biology*, 208(Pt 9):1665–1676, May 2005.

- [118] Jonas Rubenson, David G Lloyd, Denham B Heliam, Thor F Besier, and Paul a Fournier. Adaptations for economical bipedal running: The effect of limb structure on three-dimensional joint mechanics. *Journal of The Royal Society Interface*, 8(58):740–755, October 2011.
- [119] J Knapik, C Hickey, S Ortega, J Nagel, and R De Pontbriand. Energy cost of walking in four types of snowshoes. In *Human Factors and Ergonomics Society Annual Meeting Proceedings*, volume 41, pages 702–706. Human Factors and Ergonomics Society, 1997.
- [120] A A Biewener and T J Roberts. Muscle and tendon contributions to force, work, and elastic energy savings: a comparative perspective. *Exercise and Sport Sciences Reviews*, 28(3):99, 2000.
- [121] Y C Fung. Structure and stress-strain relationship of soft tissues. *American Zoologist*, 24(1):13–22, 1984.
- [122] P L Weiss, I W Hunter, and R E Kearney. Human ankle joint stiffness over the full range of muscle activation levels. *Journal of Biomechanics*, 21(7):539–544, January 1988.
- [123] Constantinos N Maganaris and John P Paul. In vivo human tendon mechanical properties. *Journal of Physiology*, 521(1):307–313, 1999.
- [124] R McNeil Alexander. *Energy for Animal Life*. Oxford University Press, New York, 1999.
- [125] R. D. Maladen, Y. Ding, P. B. Umbanhowar, A. Kamor, and Daniel I Goldman. Mechanical models of sandfish locomotion reveal principles of high performance sub-surface sand-swimming. *Journal of The Royal Society Interface*, 8(62):1332–1345, March 2011.
- [126] Sarah S Sharpe and Daniel I Goldman. Interaction with granular media influences muscle activation strategy during sand-swimming. *The Journal of Experimental Biology*, 2012.
- [127] Young-Hui Chang, Arick G Auyang, John P Scholz, and T Richard Nichols. Whole limb kinematics are preferentially conserved over individual joint kinematics after peripheral nerve injury. *The Journal of experimental biology*, 212(Pt 21):3511–3521, November 2009.
- [128] Daniel Ferris, Kailine Liang, and Claire T Farley. Runners adjust leg stiffness for their first step on a new running surface. *Journal of Biomechanics*, 32(8):787–794, August 1999.
- [129] R McNeil Alexander and A S Jayes. A dynamic similarity hypothesis for the gaits of quadrupedal mammals. *J Zool*, 201(1):135–152, 1983.
- [130] U Proske and D L Morgan. Tendon stiffness: Methods of measurement and significance for the control of movement. A review. *Journal of Biomechanics*, 20(1):75–82, January 1987.

- [131] Chen Li, S. Tonia Hsieh, Paul B. Umbanhowar, and Daniel I. Goldman. Comparison of kinematics and force generation between sand-running zebra-tailed lizard and water-running basilisk lizard. *Journal of The Royal Society Interface*, 2012.
- [132] Eg Drucker and George V Lauder. Locomotor forces on a swimming fish: three-dimensional vortex wake dynamics quantified using digital particle image velocimetry. *The Journal of experimental biology*, 202(Pt 18):2393–2412, January 1999.
- [133] David E. Kretschmann. *Wood Handbook, Chapter 05: Mechanical Properties of Wood*. Madison, WI: U.S. Department of Agriculture, Forest Service, Forest Products Laboratory, 2010.
- [134] Kai-Jung Chi and Daniel Schmitt. Mechanical energy and effective foot mass during impact loading of walking and running. *Journal of biomechanics*, 38(7):1387–95, July 2005.
- [135] M H Raibert. Legged robots. *Communications of the ACM*, 29(6):499–514, 1986.
- [136] LP P Kadanoff. Built upon sand: Theoretical ideas inspired by granular flows. *Reviews of Modern Physics*, 71(1):435, 1999.
- [137] R. Altendorfer. Stability Analysis of a Clock-Driven Rigid-Body SLIP Model for RHex. *The International Journal of Robotics Research*, 23(10-11):1001–1012, October 2004.
- [138] E. R. Westervelt, G. Buche, and J. W. Grizzle. Experimental Validation of a Framework for the Design of Controllers that Induce Stable Walking in Planar Biped. *The International Journal of Robotics Research*, 23(6):559–582, June 2004.
- [139] G A Cavagna, N C Heglund, and C R Taylor. Mechanical work in terrestrial locomotion: Two basic mechanisms for minimizing energy expenditure. *American Journal of Physiology- Regulatory, Integrative and Comparative Physiology*, 233(5):R243, 1977.
- [140] M D Berkemeier and R S Fearing. Sliding and hopping gaits for the underactuated acrobot. *Robotics and Automation, IEEE Transactions on*, 14(4):629–634, 1998.
- [141] K Terzaghi. Theoretical soil mechanics. 1943.
- [142] Patrick Heil, E. Rericha, Daniel Goldman, and Harry Swinney. Mach cone in a shallow granular fluid. *Physical Review E*, 70(6):1–4, December 2004.
- [143] J. van Zon, J. Kreft, Daniel Goldman, D. Miracle, J. Swift, and Harry Swinney. Crucial role of sidewalls in velocity distributions in quasi-two-dimensional granular gases. *Physical Review E*, 70(4):2–5, October 2004.
- [144] R Altendorfer, N Moore, and H Komsuoglu. Rhex: A biologically inspired hexapod runner. *Autonomous Robots*, 11:207–213, 2001.
- [145] R A Bagnold. The physics of blown sand and desert dunes. 1941.
- [146] M. Stone, R. Barry, D. Bernstein, M. Pelc, Y. Tsui, and P. Schiffer. Local jamming via penetration of a granular medium. *Physical Review E*, 70(4):1–10, October 2004.

- [147] Simon de Vet and John de Bruyn. Shape of impact craters in granular media. *Physical Review E*, 76(4):1–6, October 2007.
- [148] Daniel Santos, Matthew Spenko, Aaron Parness, Sangbae Kim, and Mark Cutkosky. Directional adhesion for climbing: theoretical and practical considerations. *Journal of Adhesion Science and Technology*, 21(12):1317–1341, October 2007.
- [149] J K Hodgins and M N Raibert. Adjusting step length for rough terrain locomotion. *Robotics and Automation, IEEE Transactions on*, 7(3):289–298, 1991.
- [150] Daniel I Goldman, Tao S Chen, Daniel M Dudek, and Robert J Full. Dynamics of rapid vertical climbing in cockroaches reveals a template. *The Journal of Experimental Biology*, 209(Pt 15):2990–3000, August 2006.
- [151] Bc Jayne and Dj Irschick. Effects of incline and speed on the three-dimensional hindlimb kinematics of a generalized iguanian lizard (*Dipsosaurus dorsalis*). *The Journal of Experimental Biology*, 202 (Pt 2):143–59, January 1999.
- [152] Andrew A Biewener and G B Gillis. Dynamics of muscle function during locomotion: accommodating variable conditions. *The Journal of Experimental Biology*, 202(Pt 23):3387–3396, December 1999.
- [153] K Autumn, S T Hsieh, D M Dudek, J Chen, C Chitaphan, and R J Full. Dynamics of geckos running vertically. *The Journal of Experimental Biology*, 209(Pt 2):260–72, January 2006.
- [154] Paul Umbanhowar and Daniel I Goldman. Granular impact and the critical packing state. *Physical Review E*, 82(1):1–4, July 2010.
- [155] A Schofield and P Wroth. Critical state soil mechanics. 1968.
- [156] Aaron M. Hoover, Erik Steltz, and Ronald S. Fearing. RoACH: An autonomous 2.4g crawling hexapod robot. *2008 IEEE/RSJ International Conference on Intelligent Robots and Systems*, pages 26–33, September 2008.
- [157] R. Playter, M. Buehler, and M. Raibert. BigDog. *Proceedings of SPIE*, 6230:62302O–62302O–6, 2006.
- [158] G W Brown. *Desert biology*. Academic Press, 1968.
- [159] R C Stebbins. *Amphibians and reptiles of California*, volume 31. Univ of California Pr, 1972.
- [160] K L Parker, C T Robbins, and T A Hanley. Energy expenditures for locomotion by mule deer and elk. *The Journal of wildlife management*, pages 474–488, 1984.
- [161] R J Full and M S Tu. Mechanics of a rapid running insect: Two-, four- and six-legged locomotion. *The Journal of Experimental Biology*, 156:215–31, March 1991.
- [162] J M Morrey, B Lambrecht, A D Horchler, R E Ritzmann, and R D Quinn. Highly mobile and robust small quadruped robots. In *Intelligent Robots and Systems, 2003.(IROS 2003). Proceedings. 2003 IEEE/RSJ International Conference on*, volume 1, pages 82–87. IEEE, 2003.

- [163] Chen Li and Daniel I Goldman. Towards a terramechanics for legged locomotion on granular media. *The Proceedings of the National Academy of Sciences*, 2012.
- [164] J Gray and G J Hancock. The propulsion of sea-urchin spermatozoa. *Journal of Experimental Biology*, 32(4):802, 1955.
- [165] Jeremie Korta, Damon a Clark, Christopher V Gabel, L Mahadevan, and Aravinthan D T Samuel. Mechanosensation and mechanical load modulate the locomotory gait of swimming *C. elegans*. *The Journal of experimental biology*, 210(Pt 13):2383–9, July 2007.
- [166] Werner Baumgartner, Florian Fidler, Agnes Weth, Martin Habbecke, Peter Jakob, Christoph Butenweg, and Wolfgang Böhme. Investigating the locomotion of the sandfish in desert sand using NMR-imaging. *PloS one*, 3(10):e3309, January 2008.
- [167] J. Seipel and P. Holmes. A simple model for clock-actuated legged locomotion. *Regular and Chaotic Dynamics*, 12(5):502–520, October 2007.
- [168] Andrew Slatton, Yang Ding, and PB Umbanhowar. Integrating a Hierarchy of Simulation Tools for Legged Robot Locomotion. *IROS*, 2008.
- [169] Robert F Ker. The implications of the adaptable fatigue quality of tendons for their construction, repair and function. *Comparative biochemistry and physiology. Part A, Molecular & integrative physiology*, 133(4):987–1000, December 2002.

## VITA

Chen Li was born in Wuhan, China on September 8, 1982, with a twin sister Li Chen, to Danhua Chen and Xiannian Li. He went to Beijing, China to attend Peking University in September 2001 and received a B.S. in physics and a B.S. in economics in 2005. He then moved to Atlanta, GA, USA in August 2005 to pursue graduate studies at Georgia Tech, and joined Professor Goldman's group in September 2006. In 2009, he was awarded an Amelio Fellowship for Excellence in Research from the School of Physics, and won the Best Student Paper in the Comparative Biomechanics Division at the annual meeting of Society for Integrative and Comparative Biology. He defended his PhD in physics in November 2011. Chen also met his wife Jin Liao at Georgia Tech in 2007, and they got married in 2010.